

Proceedings of

ICADD-3

**Third International Conference on
Analysis of Discontinuous Deformation
- from Theory to Practice -**

Edited by
Bernard Amadei

June 3 – 4, 1999
Vail, Colorado

Proceedings of

ICADD-3

**Third International Conference on
Analysis of Discontinuous Deformation**

Published by:

**American Rock Mechanics Association (ARMA)
600 Woodland Terrace
Alexandria, VA 22302 USA**

**Tel: 703 / 683-1808; Fax: 703 / 683-1815
email: arma@tmn.com**

June 1999

**© 1999 American Rock Mechanics Association
All rights reserved.**

**This book or any parts hereof may not be reproduced in any form without
permission in writing from the publisher.**

PREFACE

The third International Conference on Analysis of Discontinuous Deformation (*ICADD-3*) features the most recent developments in three methods of analysis of discontinuous deformation, namely, Key Block analysis, Discontinuous Deformation Analysis (DDA), and Manifold Method (MM). All three methods have undergone major developments over the past ten years and are now being used more frequently in engineering practice. The theme of *ICADD-3, From Theory to Practice*, was selected in order to promote dialog and exchange between academia and practice. The primary emphasis of *ICADD-3* is how to apply Key Block, DDA and MM in the practice of rock mechanics and rock engineering. For this reason, *ICADD-3* is held in conjunction with the 37th U.S. Rock Mechanics Symposium (*Vail Rocks '99*).

The proceedings of this conference contain a total of 25 regular papers and 3 keynote papers. The papers were selected to provide a good mix of case studies and applied research. The papers have been divided into five sections. The first section deals with recent developments in DDA methodology. New algorithms are proposed to make DDA analysis better. It is noteworthy that the development of many of these new algorithms has been driven by practical needs. The second section presents various civil engineering applications of DDA where it is used as a design tool. Both static and dynamic loading conditions are addressed. Through these applications, we now have a better perspective of the advantages and limitations of DDA. DDA has been found to be very powerful, but is still limited to modeling two-dimensional problems. We are looking forward with much anticipation to being able to address real-world three-dimensional problems in the future. This is obviously a formidable challenge which, when completed, will be a major step forward in the modeling of complex blocky systems.

The third and fourth sections in these proceedings deal with Key-Block analysis and Manifold Method. Two papers present engineering applications of the Key-Block analysis. The latter has been found to be very robust and ready to be used by practicing engineers, not only as a descriptive geometrical tool, but also in analysis and design. The use of interactive graphics software has contributed greatly to the success of this method of analysis. The papers on the Manifold Method reveal that this method is now in its full stage of development and is being used in a wide range of practical applications. Several papers in these proceedings address coupling phenomena and the complex problem of crack propagation. Finally, the last section of these proceedings deals with hybrid methods of analysis where more conventional numerical methods such as FEM, DEM, and BEM are combined with DDA or MM to solve complex problems. The main idea here is to combine the best assets of each method.

ICADD-3 was sponsored by the American Rock Association (ARMA) and the ARMA Foundation. It was supported financially by the U.S. Air Force Office of Scientific Research and RockSol Consulting Group, Inc. I wish to thank all the authors for their interest and contributions.

I am pleased to welcome you to Vail, Colorado.

Bernard Amadei
ICADD-3 Conference Chair

ORGANIZATION OF THE CONFERENCE

Conference Chair

Bernard Amadei, University of Colorado, Boulder, CO

International Advisory Committee and Session Chairs

Nenad Bicanic, University of Glasgow, Glasgow, UK
Yossef H. Hatzor, Ben-Gurion University, Beer-Sheva, Israel
Joseph T. Kottensette, U.S. Bureau of Reclamation, Denver, CO
Jeen-Shang Lin, University of Pittsburgh, Pittsburgh, PA
Max Ma, Golder Associates Inc., Redmond, WA
Mary M. MacLaughlin, Montana Tech., Butte, MT
Yuzo Ohnishi, Kyoto University, Kyoto, Japan
Ernian Pan, University of Colorado, Boulder, CO
Saeid Saeb, RockSol Consulting Group, Boulder, CO
M. Reza Salami, North Carolina Agricultural and Tech. State Univ., Greensboro, NC
Gen-Hua Shi, Consultant, Loyalton, CA
Edward C. Ting, Purdue University, West Lafayette, IN
John P. Tinucci, PanTechnica Corp., Eden Prairie, MN
M. Ronald Yeung, San Jose State University, San Jose, CA
Chung-Yue Wang, National Central University, Chungli, Taiwan, ROC
Weiyuan Zhou, Tsinghua University, Beijing, PRC

Sponsor

American Rock Mechanics Association and ARMA Foundation, Alexandria, VA
Peter Smeallie, Executive Director

Managed by

ExpoMasters, Inc., Englewood, CO
Mark Cramer, President

Contributors

U.S. Air Force Office of Scientific Research
RockSol Consulting Group, Boulder, CO

Disclaimer

The pages appearing in these proceedings have been produced directly from material provided by contributors without benefit of technical peer review or grammatical editing. It is the belief of the conference chair that these papers have technical merit, otherwise they would not have been accepted for publication. However, complete accuracy and technical viability cannot be assured. Neither the conference chair nor the American Rock Mechanics Association (ARMA) accepts responsibility or liability for misprints or falsehoods contained in these papers.

TABLE OF CONTENTS

Preface	iii
Organization of the Conference	v
Disclaimer	vi

Keynote Lectures

Applications of Discontinuous Deformation Analysis and Manifold Method <i>G.-H. Shi</i>	3
Development of Discontinuous Deformation Analysis: The First 10 Years (1986-1996) <i>M.Y. Ma</i>	17
Comparison between Physical and Manifold Method Models of Discontinuous Rock Masses <i>Y. Ohnishi, G. Chen, M. Ogawa, T. Itoh, and T. Nakai</i>	33

Discontinuous Deformation Analysis (DDA) - Methodology

An Efficient Adaptive Skyline Solver for Contact Dynamics in Discrete Body Systems <i>C.-Y. Wang, C.-C. Chuang, and J. Sheng</i>	47
A Non-Linear Model for Discontinuities in DDA <i>G. Chen and Y. Ohnishi</i>	57
A Gravity Turn-On Routine for DDA <i>M. M. MacLaughlin and N. Sitar</i>	65
Practical Computing Formulas of Simplex Integration <i>G. Chen and Y. Ohnishi</i>	75
A Method of Sub-Meshing in Discontinuous Deformation Analysis (DDA) <i>D. Clatworthy and F. Scheele</i>	85

Discontinuous Deformation Analysis (DDA) - Applications

Method of Stability Analysis of a Dam-Foundation-Plant System <i>J.-M. Pei</i>	97
---	----

Analysis of Cyclic Plastic Deformation of Railroad Ballast by DDA <i>T. Ishikawa and Y. Ohnishi</i>	107
The Voussoir Beam Reaction Curve <i>Y. H. Hatzor</i>	117
DDA Analysis of the RCC Modification for Pueblo Dam <i>J. T. Kottenstette</i>	127
On the DDA Framework for Modelling Concrete Fracture <i>C. Pearce, N. Bicanic, A. Thavalingam, and Z. H. Liao</i>	133
Analysis of Large Block Test Data Using the DDA Method <i>M. R. Yeung and S. C. Blair</i>	141
On the Methodology of Numerical Etching <i>X. Wang, K. Shyu, C.-T. Chang, and D. Zheng</i>	151
Modeling Excavation Induced Response of Jointed Rock Using DDA <i>C. T. Lin, S. Ouyang, C.-T. Huang, C. C. Chen, P.T.H. Huang, C.-C. Lee, and J. Liu</i>	159
 Key-Block Analysis	
Two Examples of the Application of Key-Block Theory in China <i>J.-M. Pei, X.-C. Pen, and S.-R. Hang</i>	171
Applications of Key Block Theory and DDA at Yerba Buena Island Tunnel Portals under Earthquake Loading <i>H. K. Law and I. P. Lam</i>	181
 Manifold Method	
Manifold Method with Complete First Order Displacement Function on Physical Cover <i>S. Wang, X. Ge, and G. Zhang</i>	193
Manifold Method with Four Physical Covers Forming an Element and Its Application <i>S. Wang and X. Ge</i>	203
Application of Manifold Method to Jointed Dam Foundation <i>G.-X. Zhang, Y. Sugiura, and K. Saito</i>	211
Manifold Method in Saturated-Unsaturated Unsteady Groundwater Flow Analysis <i>Y. Ohnishi, M. Tanaka, T. Koyama, and K. Mutoh</i>	221

Manifold Method Analysis of Rock Masses Containing Joints of Two Different Scales	231
<i>J.-S. Lin, C.-Y. Koo, and J.-C. Chern</i>	

Hybrid Numerical Analyses

Dynamic Behaviors in Discontinuous Elastic Media Using DDA	243
<i>K. Shyu, X. Wang, and C.-T. Chang</i>	
Soil and Rock Analysis by Mechanics of Multiple Continuous Bodies	253
<i>C. Shih, A. Altschaeffl, and E.C. Ting</i>	
Stability Analysis of the Ship-Lock Slopes of the Three Gorges Project by Three-Dimensional FEM and DEM Techniques	263
<i>W. Zhu, Q. Zhang, and L. Jing</i>	
Crack Propagation by Manifold and Boundary Element Method	273
<i>G.-X. Zhang, Y. Sugiura, and H. Hasegawa</i>	
Crack Propagation Using Manifold Method Coupled with Element Free Method	283
<i>W. Zhou, X. Kuo, and R. Yang</i>	

Keynote Lectures

APPLICATIONS OF DISCONTINUOUS DEFORMATION ANALYSIS AND MANIFOLD METHOD

Gen-hua Shi
P. O Box 640
Loyalton CA 96118, USA

ABSTRACT: Few recent applications of DDA and manifold method are presented in this paper. The applications are the backward DDA simulations, the static stability computations of DDA, the earth quake reaction computation of DDA and the dynamic rock deformation simulation by manifold method. The fields involved are nuclear waste disposal, dam foundations, slopes, tunnel portals, tunnels and tunnel lining. These applications can serve as references for similar cases.

1 BACKWARD DDA SIMULATIONS ON KAMAISHI MINE

Backward DDA is a backward numerical model for discontinuous deformation analysis of rock block systems. This backward analysis is a practical and unique method. It is different from all of the traditional stress-strain computation methods.

Modern instruments offer reliable displacement, distance or strain measurements in rock or structures; the question explored here is how to estimate the global discontinuous deformations based upon these reliable, local data. The backward analysis serves exactly this purpose. The input consists of measured data. The output will be displacements, rotations, and strains of each block and the sliding, opening and closing of interfaces between blocks as well as the residual displacements. The output are real measures of safety and failure.

The kinematics formulas are the same as those in the forward analysis, but the physical meaning is somewhat different. The coefficient matrices of the backward DDA are from the least square method which is positive definite and symmetric.

1.1 Backward Analysis of Excavated Rock of the Test Pit

This computation is based on the six measured distances only. Since only the rocks of test pit are considered and there is no boundary constrain.

However the results of this computation are still close to the results of Figure 2, even the mesh of Figure 2 is totally different. Since Figure 2 has boundary constrain and two more displacement measurements, the results of Figure 2 should be more reliable. The joint opening of Figure 2 is smaller.

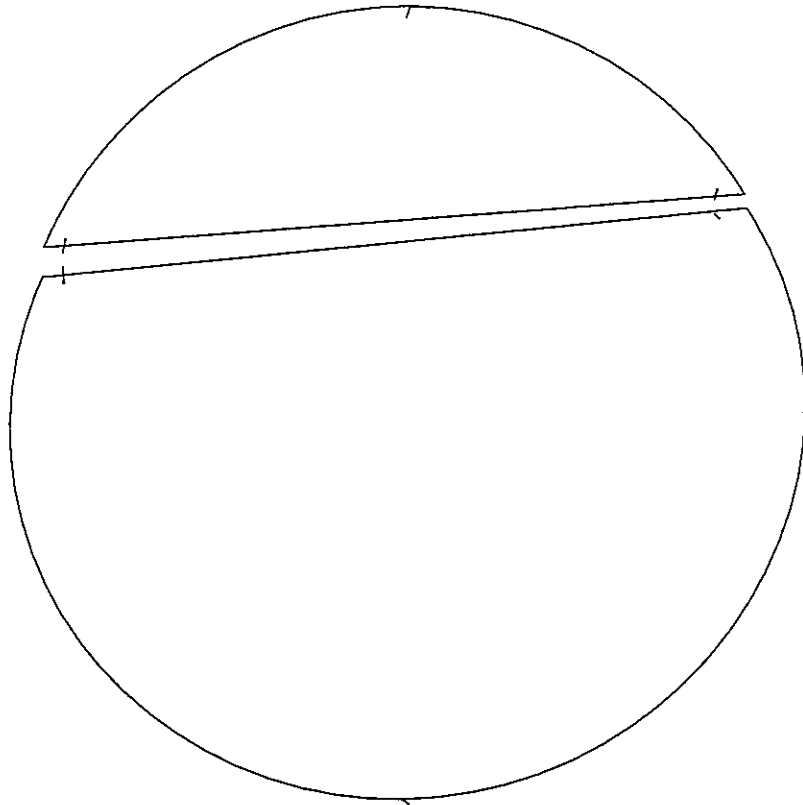


Figure 1. Backward analysis of the excavated rock of the test pit

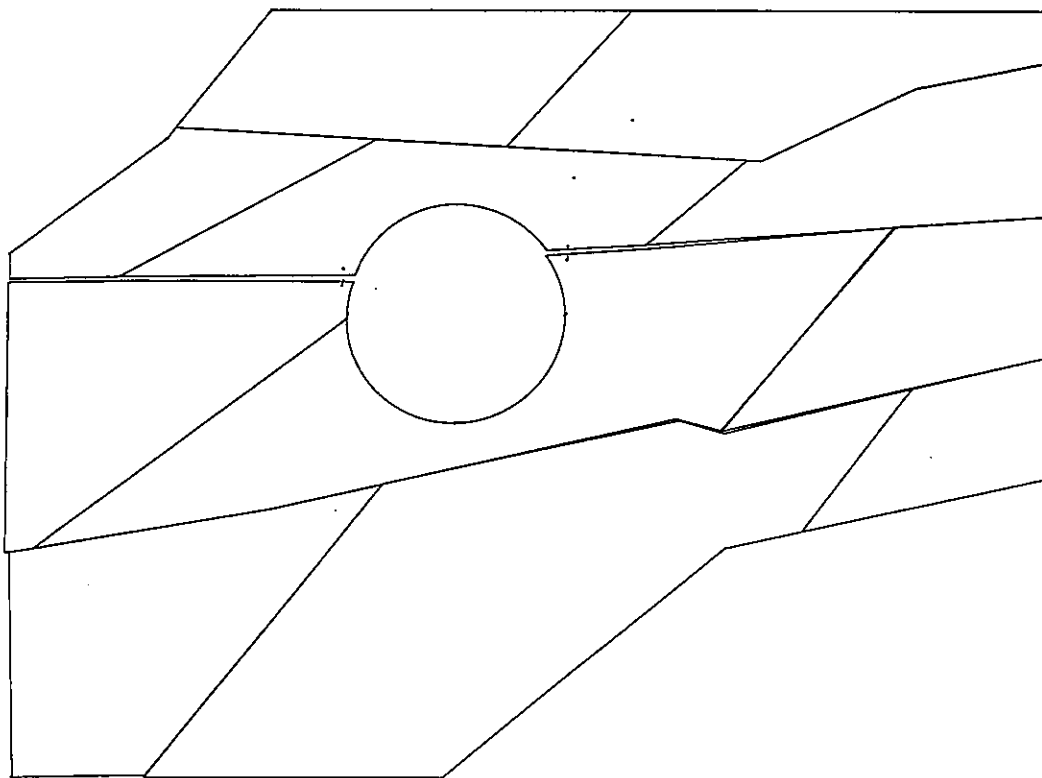


Figure 2. Backward analysis of rock masses outside the test pit

Average fitted error	16.8978 %
Opening distance of fracture at the west side	6.5952 mm
Opening distance of fracture at the east side	3.2386 mm

Figure 1 shows the deformations of excavated test pit rocks. The deformations and the joint opening is ten times of the original scale.

1.2 Backward Analysis of Rock Masses Near the Test Pit

This is the backward analysis of rocks near the test pit. The block kinematics and boundary constrains are considered. The results from this analysis should be more accurate than the previous analysis. The fitted movements and deformations are shown by Figure 2. The deformations and the joint opening is ten times of the original scale.

Average fitted error	16.5767 %
Opening distance of fracture at the west side	5.2435 mm
Opening distance of fracture at the east side	3.8132 mm

1.3 Backward-Forward Analysis of Rock Masses Near the Test Pit

Backward-forward analysis is forward analysis plus all measured displacements, measured distances. The weight of measured displacements and measured distances are high enough to dominant the results. Therefore the results are basically the backward analysis results if the measurements are sufficient to define all of the degrees of freedom. In case the measurements are not sufficient to define all of the degrees of freedom, the normal forward computation will help to define all of the degrees of freedom.

Parameters	
Rock unit weight	0.028 MN/m^3
E of Rock	7000 MPa
ν of Rock	0.25
Rock/rock friction angle = 45°	cohesion = 0.0

The input stresses are $\sigma_x = -13 \text{ MPa}$, $\sigma_y = -13 \text{ MPa}$, $\tau_{xy} = 6.3 \text{ MPa}$	
average fitted error	23.5820 %
Opening distance of fracture at the west side	3.8926 mm
Opening distance of fracture at the east side	2.8710 mm

Here the displacements, the deformations especially the joint opening results are relatively reliable than the results of the previous computations. The result figure of backward-forward DDA is similar to Figure 2.

2 STABILITY ANALYSIS OF DAM FOUNDATIONS USING 2-D DDA

2.1 Stability of Pueblo Dam Buttress #8 - #9

Load	Top of spillway + 26.5
------	------------------------

Condition	with 5 ft high RCC block	
Rcc/rcc	friction angle = 41°	cohesion = 0.0
Up-stream joint	friction angle = 17°	cohesion = 0.0
Down-stream joint	friction angle = 17°	cohesion = 0.0
Sandstone/sandstone	friction angle = 41°	cohesion = 0.0
Concrete/sandstone	friction angle = 45°	cohesion = 100psi
Factor of safety	by DDA = 1.99	

Figure 3 shows the buttress #8 and #9 of Pueblo dam are stabilized by the rear RCC block.

Load	Top of spillway + 26.5	
Condition	without RCC block	
Rcc/rcc	friction angle = 41°	cohesion = 0.0
Up-stream joint	friction angle = 17°	cohesion = 0.0
Down-stream joint	friction angle = 17°	cohesion = 0.0
Sandstone/sandstone	friction angle = 41°	cohesion = 0.0
Concrete/sandstone	friction angle = 45°	cohesion = 100psi
Factor of safety	by DDA 0.51	

DDA program shows the mode of failure. Figure 4 shows the buttress #8 and #9 of Pueblo dam are sliding without rear RCC block.

2.2 Stability of Pueblo Dam Buttress #10

Load	spillway crest	
Condition	with 7ft high RCC block on back of buttress	
Rcc/rcc	friction angle = 45°	cohesion = 0.0
Concrete/sandstone	friction angle = 45°	cohesion = 0.0
Up-stream joint	friction angle = 9.9°	cohesion = 0.0
Down-stream joint	friction angle = 26.39°	cohesion = 0.0
Resistant force	x = 0 kips	y = 0 kips
Factor of safety	by DDA= 0.49	

DDA program shows the mode of failure. Figure 5 shows the buttress #10 of Pueblo dam is sliding without the resistant force.

Load	spillway crest	
Condition	with 7ft high RCC block on back of buttress	
Rcc/rcc	friction angle = 45°	cohesion = 0.0
Concrete/sandstone	friction angle = 45°	cohesion = 0.0
Up-stream joint	friction angle = 9.9°	cohesion = 0.0
Down-stream joint	friction angle = 26.39°	cohesion = 0.0
Resistant force	x = -180 kips	y = -180 kips
Factor of safety	by DDA = 1.12	

Figure 6 shows the buttress #10 of Pueblo dam is stabilized by the resistant force.

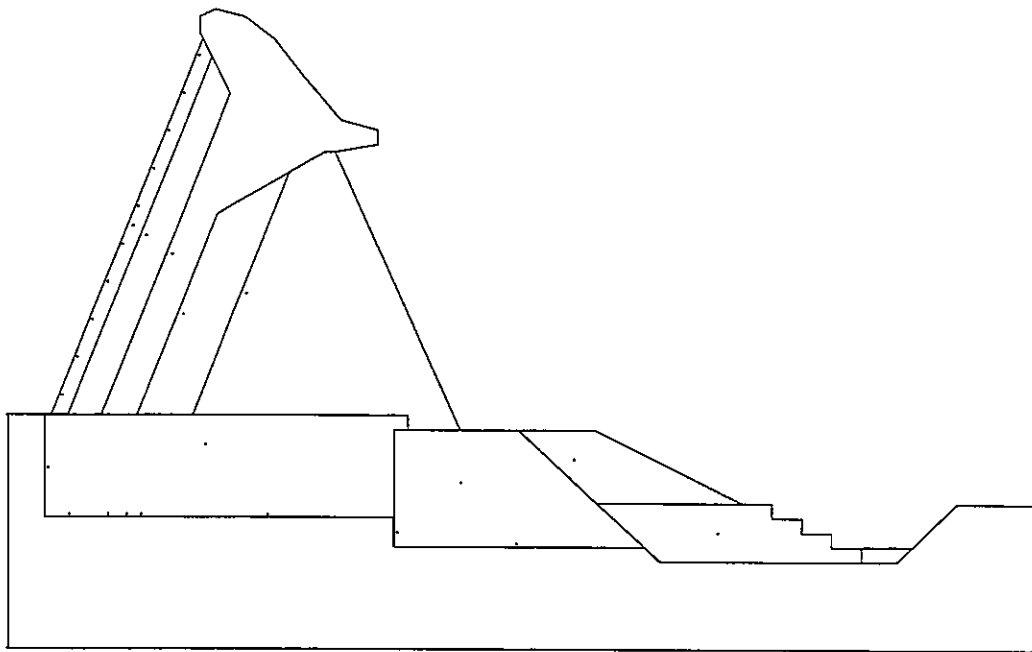


Figure 3. Buttress 8-9 of Pueblo dam are stablized by a rear block

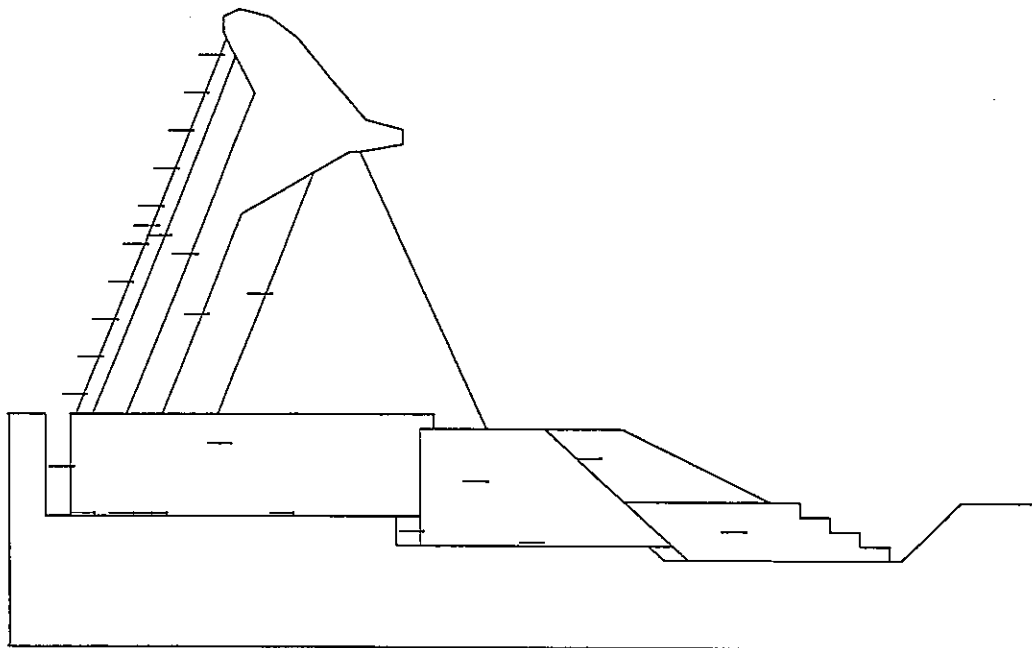


Figure 4. Buttress 8-9 of Pueblo dam are sliding without rear block

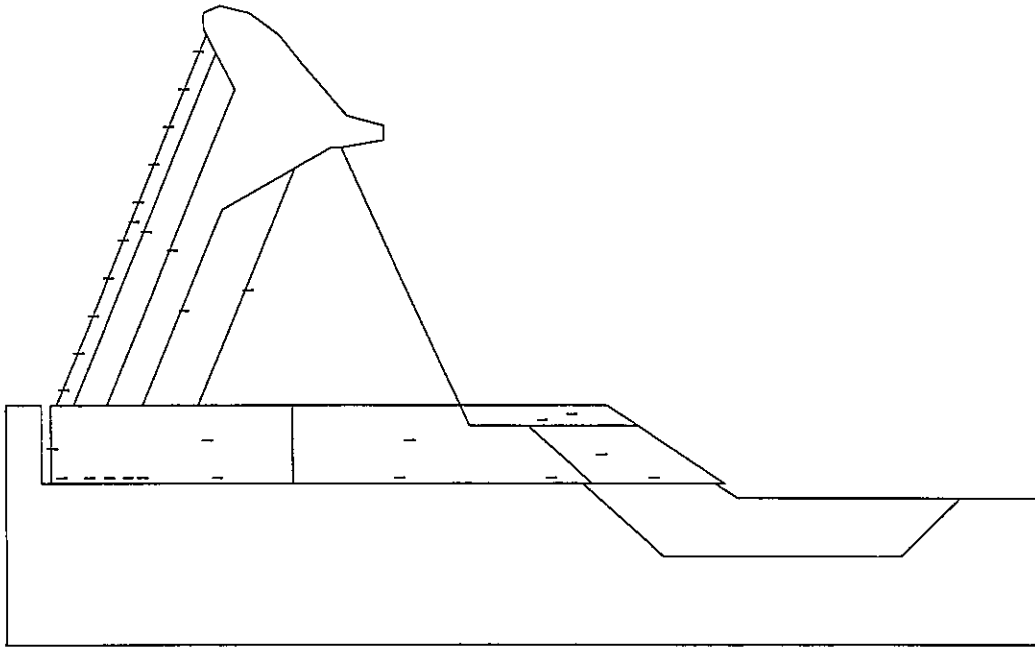


Figure 5. Buttriss 10 of Pueblo dam slides without resistant force

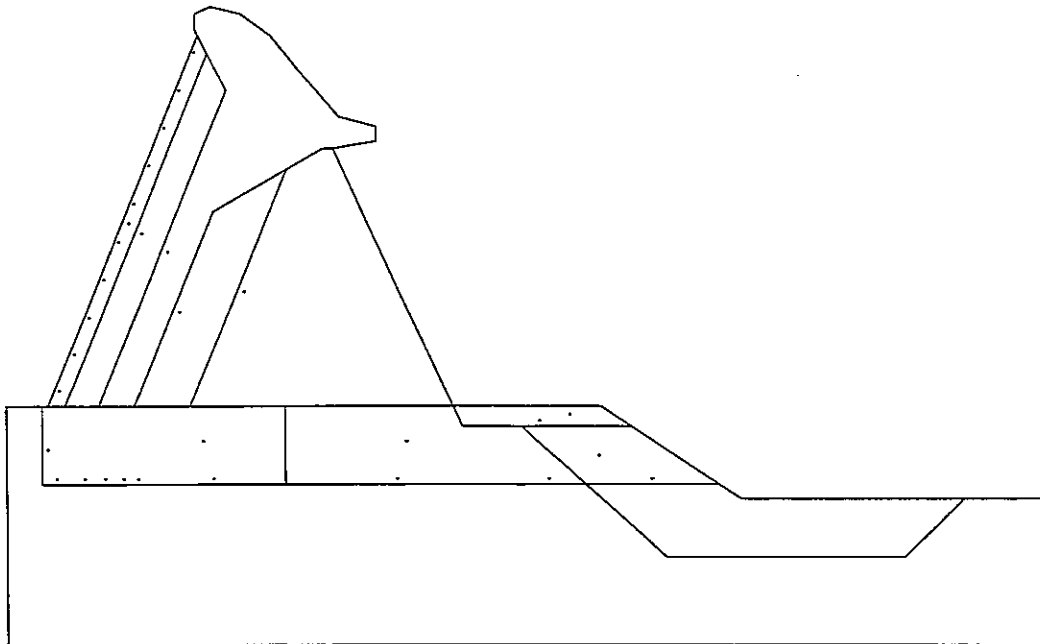


Figure 6. Buttriss 10 of Pueblo dam is stabilized by resistant force

3 EARTH QUAKE STABILITY ANALYSIS OF A PORTAL BY 2-D DDA

The necessary condition for directly input earth quake acceleration is that the computation has no damping. Since the damping can reduce the earth quake dynamic energy. Therefore the earth quake damage would be underestimated. DDA can do the computation without damping.

It is very likely, if the discontinuities are considered, especially the tension stresses would be much lower than continuous computation. It is obvious the opening of the discontinuous interfaces will absorb the tension force. DDA will let us know how much the discontinuous interfaces open and slide.

3.1 *Different Methods of Using Earth Quake Records*

There are three possible ways to input recorded earth quake waves: time depending accelerations, time depending displacements and time depending velocity (only from theory).

Time depending acceleration input is multi-block Newmark method. There are long time experiences of using one-block Newmark method. Here the only difference is to extend to multi-block case which is DDA case. Also if the time depending acceleration is directly measured on the spot, the result would be true.

Two dimensional DDA is capable to input time depending displacements. Also DDA may be able to take time depending velocity. However We can not find any previous cases even for a single block. Therefore in the real engineering practice, these computations only can be considered as reference results.

3.2 *DDA Dynamic Computation of East Portal of Yuba Buna Tunnel*

In this section, the multi-block rotation such as toppling or bucking are examined. Since there is a joint set which made side cut, therefore 2-d computation is close to the real case.

The measured time depending earth quake accelerations are input directly into DDA computation. Figure 7 shows the time depending horizontal accelerations. Figure 8 shows the time depending vertical accelerations.

The input data of DDA computations also include block geometry and mechanical parameters. The following tables listed the actual input data:

unit weight	0.145 kips/ft ³
E of rock mass	80000 kips/ft ³
ν of rock mass	0.25
friction angle	35°
cohesion	0.0
number of time steps	20000
time step	0.0025 seconds

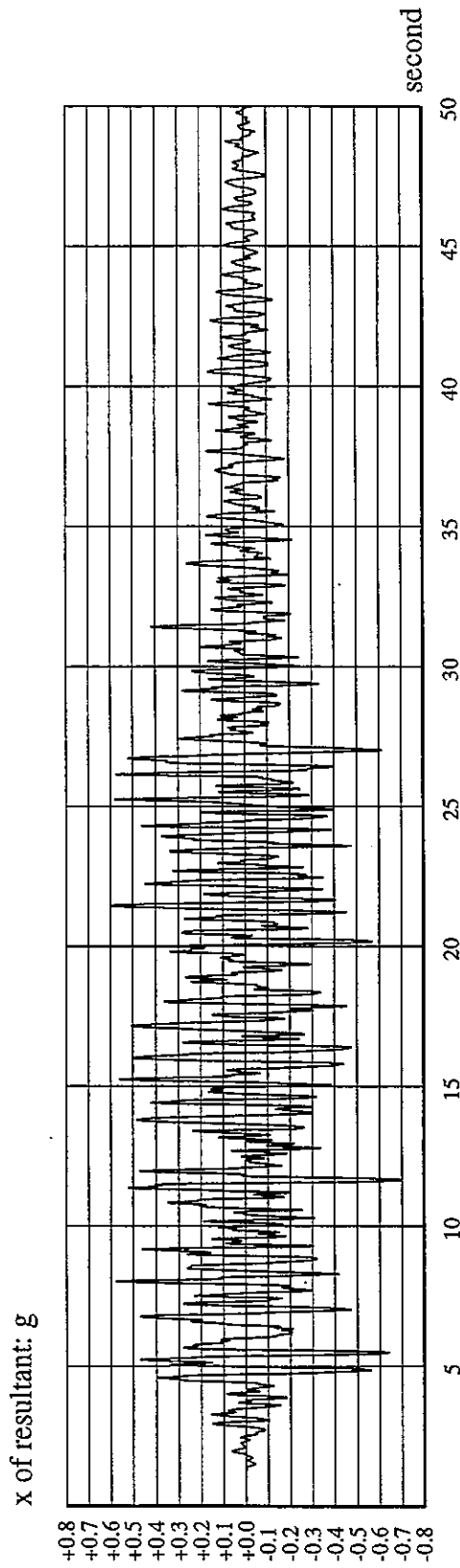


Figure 7. Time depending horizontal accelerations

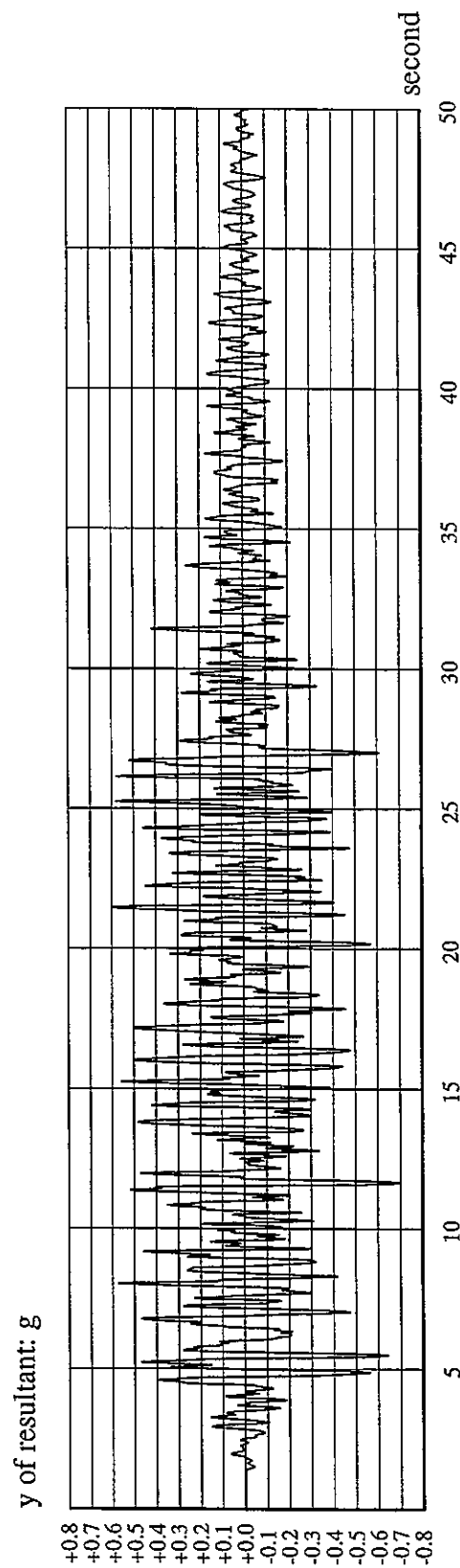


Figure 8. Time depending vertical accelerations

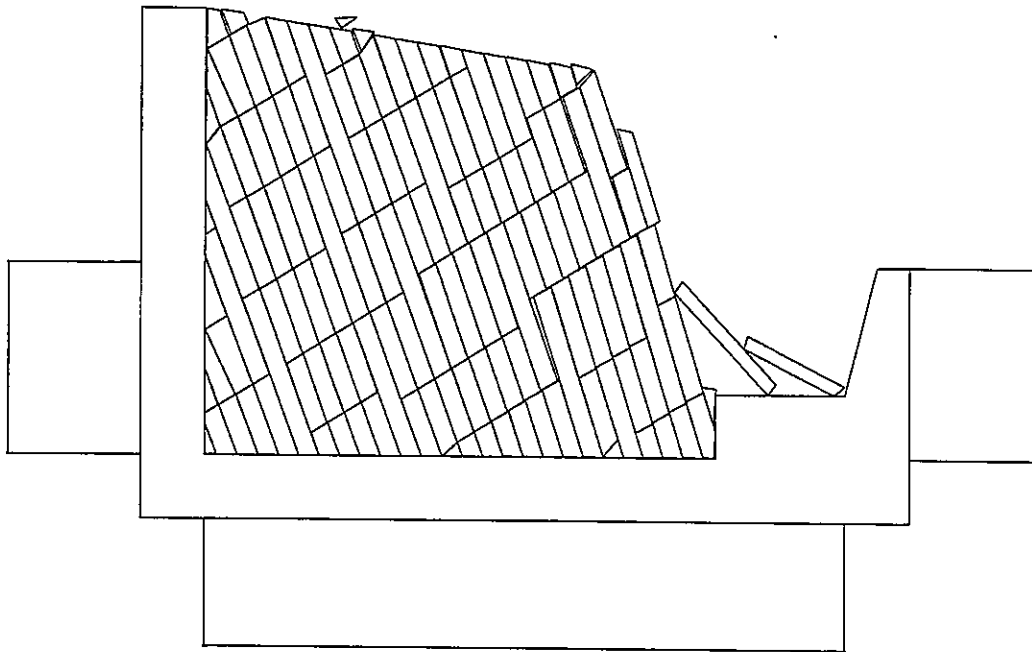


Figure 9. Block movement after 20 seconds

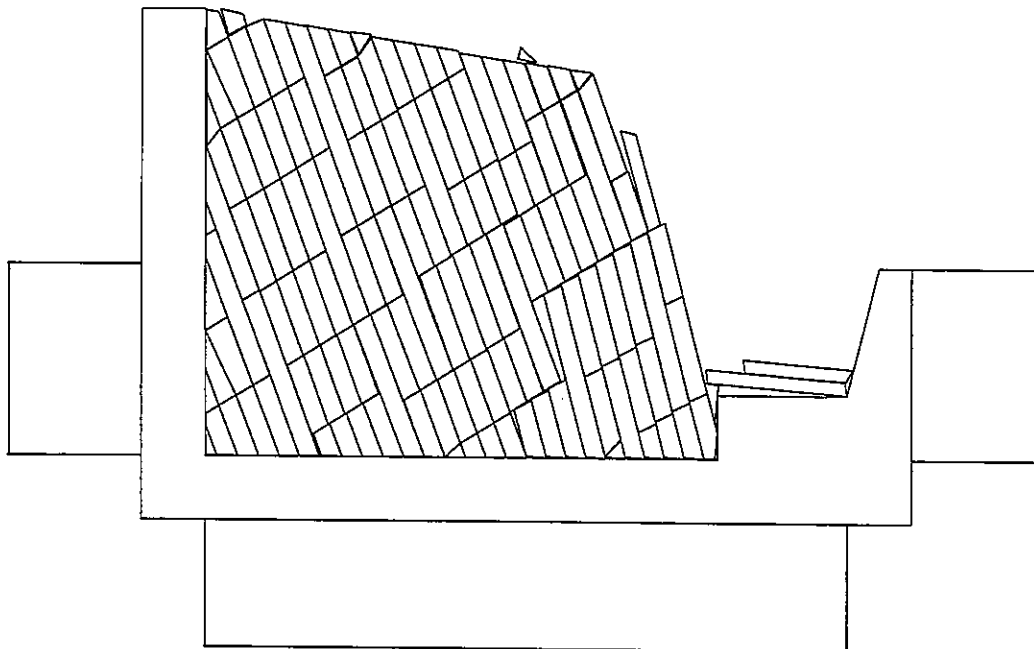


Figure 10. Block movement after 50 seconds

The results of DDA computation can be seen from Figure 9 and 10. Figure 9 is the block movements after 20 seconds. Figure 10 is the block movements after 50 seconds. No blocks will go over the retaining wall under such a strong earth quake. Only up to 6 feet rock layer can fall down.

4 TUNNEL STABILITY ANALYSIS BY 2-D MANIFOLD METHOD

4.1 Comparison of DDA, Manifold Method and FEM

Two dimensional MM has higher accuracy stress distribution and computes both joints and blocks. The variables of MM with FEM mesh are less independent, the convergency of equilibrium equations is substantially slower than DDA.

Compare with FEM, The mesh of manifold method is more flexible than FEM mesh. The boundary of blocks or joints of MM is not defined by nodes of elements. The boundary is used for integration only. The cover function of FEM is constant (0 order), MM can use any high order cover functions to reach high accuracy.

The mass matrices of DDA and MM are analytical solutions, It will makes accurate solution for dynamics, faster and reliable convergency for statics.

4.2 Rock Stability of Yuba Buna Tunnel

The manifold method codes can perform traditional limit equilibrium analysis for whole joint or block systems. In continuous material zones, finite element meshes are applied.

Mechanical parameters for MM computation

unit weight	0.145 kips/ft ³
E of rock mass	80000 kips/ft ³
ν of rock mass	0.25
number of time steps	1000 - 2000
friction angle	33
time step	0.005 seconds

Tunnel rock displacements without lining

Figure	friction angle	deformation
Figure 11	35°	non-converge displacements
Figure 12	45°	small converge displacements

4.3 Stability and Stresses of Concrete Lining

Stresses on frame lining kips/sq ft

location	σ_x	σ_y	τ_{xy}
arch center	-143.409489	-15.653142	-18.735051
arch right end	-96.185288	-109.772609	75.450149
arch left end	-114.362376	-88.652007	-69.511647

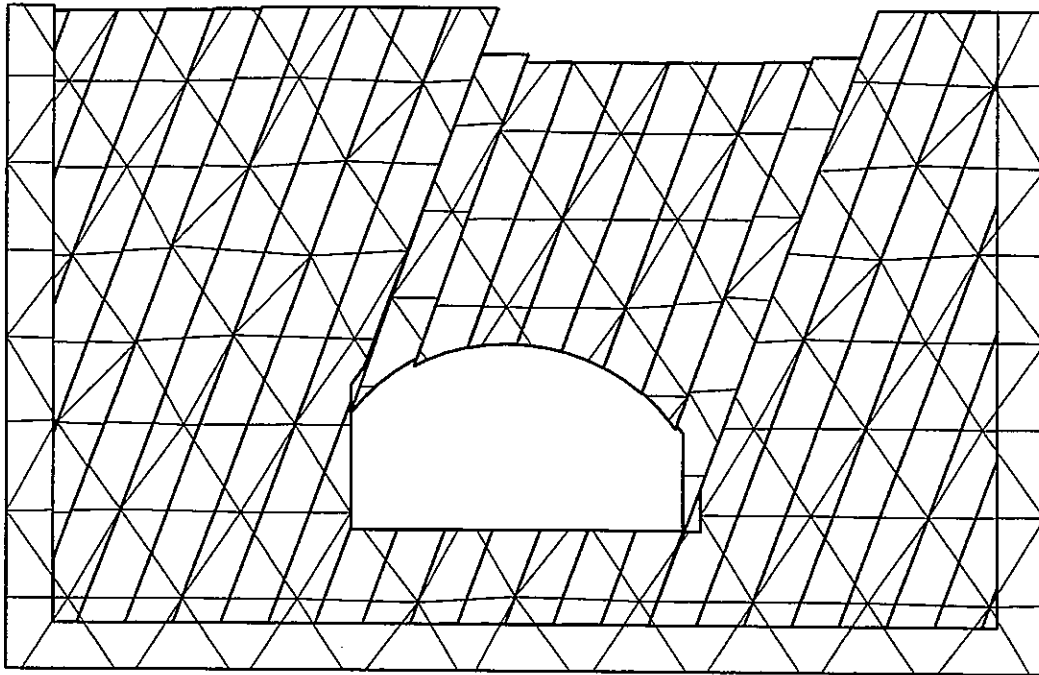


Figure 11. Rock movement of the tunnel with 35 degrees of friction angle

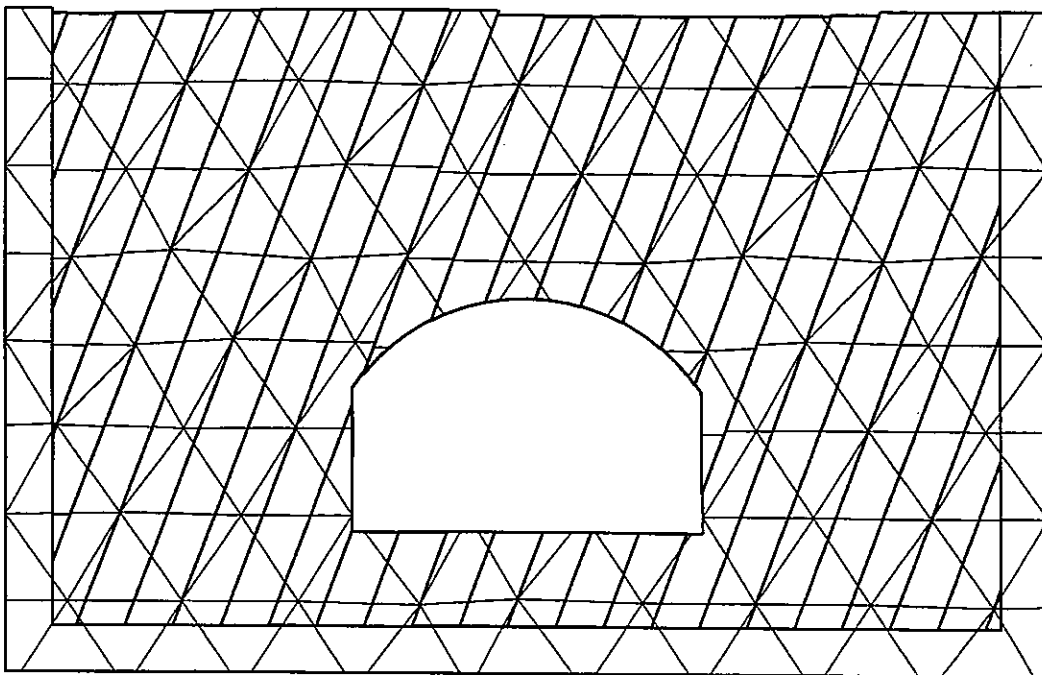


Figure 12. Rock movement of the tunnel with 45 degrees of friction angle

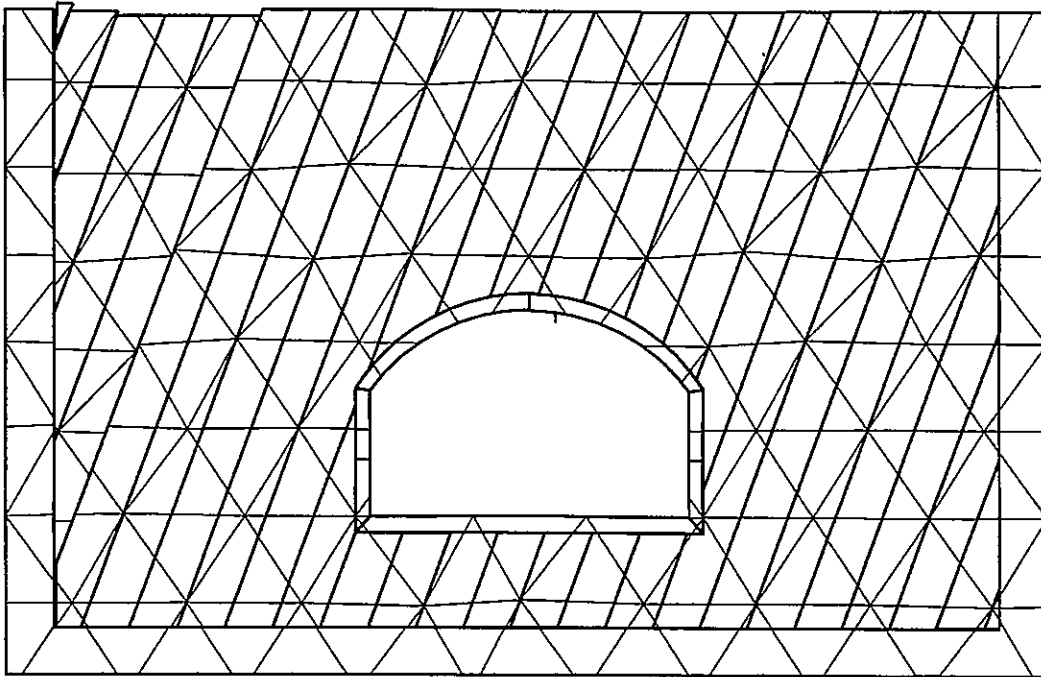


Figure 13. Rock deformation of the tunnel with concrete lining

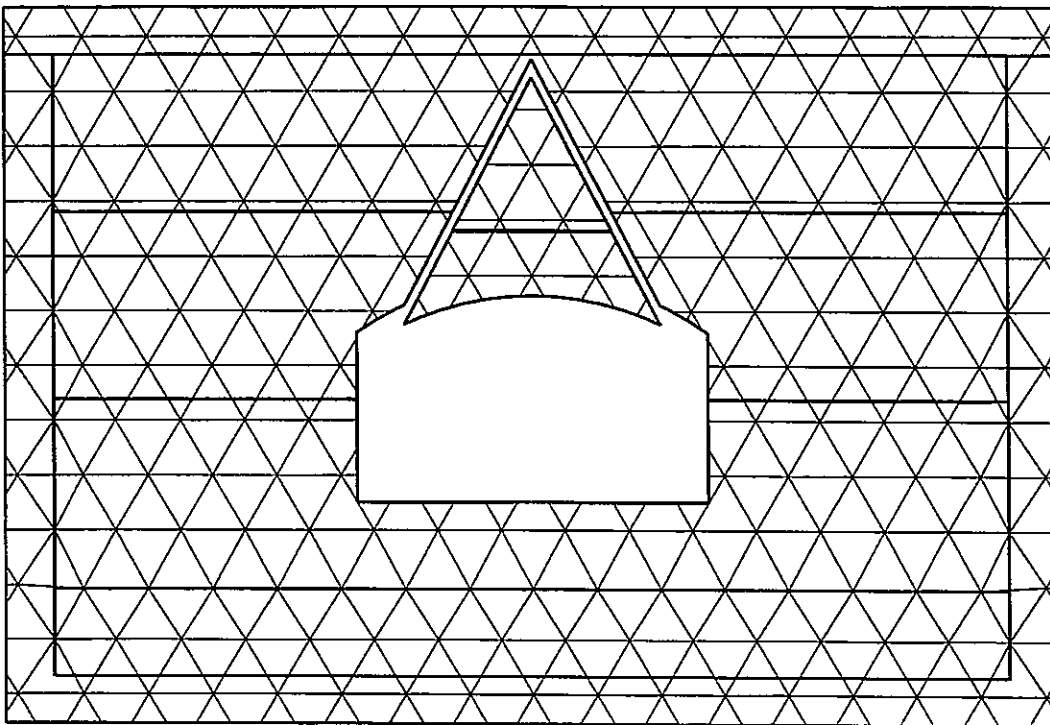


Figure 14. Key block movement of the tunnel with 35 degrees of friction angle

Figure 13 shows the rock deformations with concrete lining. Figure 14 shows the key block movements with 35° of friction angle.

5 DEVELOPMENT OF THREE DIMENSIONAL DDA

Three dimensional block forming code DC of DDA has been finished. It can produce 10000 blocks using less than 32 MB memory. The blocks formed by DC code of DDA can be very complex. The blocks can have any number of polygon faces. There are no differences to form convex and concave blocks. Two intersecting tunnels can be in a single block.

The volumes, the centers of gravity or the integrations of any polynomial over the block are analytical close form solution.

Before the end of this year, the simple three dimensional DDA will be available. This code can handle convex blocks with static and dynamic loading. Same as two dimensional DDA, each block has linear displacement function or constant strains. The number of blocks will be large enough to be able to compute the whole dam and its foundations.

ACKNOWLEDGEMENT

The data of the backward DDA are from Mr. Ryo Yamashita of HAZAMA corporation. Professor Yuzo Ohnishi of Kyoto University helped to choose backward DDA. Mr. Joe Kottenstette of Bureau of Reclamation offered the data of Pueblo dam. The tunnel and slope data are from Dr. Hubert K. Law of Earth Mechanics Inc. The suggestions from Ignatius Po Lam, Principal of Erath Mechanics Inc. and Professor Tor L. Brekke are helpful.

REFERENCES

Gen-hua Shi, 1993. *Block system modeling by discontinuous deformation analysis*. Southampton UK and Boston USA.

Gen-hua Shi, 1996. Manifold Method. *Proceedings of The First International Forum on Discontinuous Deformation Analysis (DDA) and Simulations of Discontinuous Media*. pp. 52-204.

DEVELOPMENT OF DISCONTINUOUS DEFORMATION ANALYSIS THE FIRST TEN YEARS (1986 to 1996)

Max Y. Ma
Golder Associates Inc., 4104 148th Ave. N.E.
Redmond, WA 98052, U.S.A.

ABSTRACT: During the first 10 years (1986-1996) of development of the Discontinuous Deformation Analysis (DDA), considerable progress has been achieved in improving the DDA method and developing its applications. In this paper, a review of DDA computer code development history is presented along with its modifications and improvements. Discussions on contact model (penalty method vs. Lagrange method) block deformability and non-linearity of block material/interface are given. The differences between DDA and the Distinct Element Method (DEM) are summarized. DDA applications in rock, geotechnical and earthquake engineering are reviewed. For future applications, the Numerical Manifold Method (NMM) is recommended over DDA, with the exception of rock fall and masonry structure problems.

1 INTRODUCTION

This paper was initially prepared as an effort to clarify the different versions of the Discontinuous Deformation Analysis (DDA) code originally developed by Dr. Gen-Hua Shi when Shi released DDA '95. In 1996, this paper was revised to provide a complete overview of the development and applications of DDA.

The material presented in this paper has been obtained through years (1989-1998) of active participation and discussion with DDA researchers and frequent conversation with Shi on issues regarding DDA. On countless occasions, the potential and unique capabilities of DDA were presented to engineers and managers in industry to convince them to use DDA in their projects. This paper will summarize the discussions and industrial expectation on the development and application of DDA.

This paper intends to share comments or assessment of DDA with the reader, especially someone who is new to DDA. Most developments presented in this paper were made by other DDA researchers during its first 10 years. Due to limited space, some contents are not presented in this version of the paper. The full version will be posted in the future Web site: www.keyblock.com.

2 DDA, A MODEL OR A THEORY?

First, DDA is not only a computer code based on existing methods or theories unlike UDEC/DEM. In general, DDA is a more realistic physical model based on existing theories (i.e. principle of minimum total potential energy, topology theories) and its own theories. DDA is a set

of theories for mechanical behavior of discontinuous systems including its integration, the best displacement approximations, graph matrix solver and block kinematics (open-close iteration). The major features of DDA are listed as follows:

1. Topological Identification of Block Systems
2. Simultaneous Rigid Body Movement and Deformation
3. The Best Displacement Approximations
4. Block Kinematics: Algebraic Inequalities and Open-Close Iteration.
5. Static and Dynamic Solutions
6. Graph Matrix Solver – Based on Topological Relationships of Matrix
7. Forward and Backward Analysis
8. Implicitly Coupled with FEM, or BEM
9. Integration for multi-body systems.

DDA was initially developed for backward analysis applications (Shi and Goodman, 1985). Up to now, there has been very little attention towards the backward analysis. Only one attempt was made by Prof. M. Pei in 1992 to use the backward analysis on a dam foundation.

To numerically model a discontinuous system, a complete solution has to satisfy both equilibrium and compatibility conditions. The most difficult part is the compatibility condition between blocks. Uniqueness and convergence of the complete solution are associated with the compatibility condition. Though convergence of DDA solution can be theoretically proved, its uniqueness is not clear to most people. DDA uses an open-close iteration criterion to fulfill the compatibility condition between blocks by solving a set of system equilibrium equations and a set of algebraic inequalities during each iteration loop for a time step. Solution of these equations is unique. However, there could be two or more sets of equations satisfying the open-close iteration criterion or compatibility condition. Therefore, there are potentially two or more solutions for each set of equations during iteration at one time step. In theory, DDA has a unique solution for each time step when the time interval is so small that only ONE algebraic inequality is needed to satisfy the compatibility condition. Too small time intervals are not practical and could introduce other numerical errors. More research is needed to select the time interval with consideration of the unique solution. Note that the open-close iteration is not a perfect theory for contact problems. However, the open-close iteration is very practical, straightforward and reliable compared to other existing methods or theories.

One significance of DDA is its integration theory for block bodies and blocky systems, not in two dimensions, or even three dimensions. It is the n th dimensional integration theory. DDA's integration theory (Shi, 1996) extended Newton's integration theory. In Newton's integration theory, all volume objects like the earth traveling around the sun are treated as one point in order to find the path, no deformation and no rotation information. With DDA, such information can be easily obtained. More significantly, using its backward analysis, DDA has the potential to estimate the deformation, rotation and displacement of the earth and its continental blocks millions of years ago.

3 DDA COMPUTER CODES

The first DDA computer code (Shi, 1996) was a PC-based BASIC language program code in 1986 by Dr. Gen-Hua Shi who was, at that time, a Ph.D. student under Prof. Richard Goodman in the Civil Engineering Department at U.C. Berkeley. In 1989, Shi using the NDP C compiler completed a C version DDA. Since then, the DDA C code has been modified and improved four times by Shi. A summary of DDA codes developed by Shi and others is presented in Table 1.

Table 1. Summary of major DDA codes.

Version	Lang.	Developer	Notes
DDA '86	BASIC	Shi	The first DDA code.
DDA '89	C/PC	Shi	The first C DDA code
DDA '92	C /UNIX	Shi	The first X-windows DDA code
DDA '94	C/UNIX	Shi	Cohesion, Tension and Auto Kn
DDA '95	C /UNIX	Shi	Correction of shear lock, and rotation problem
NDDA '92	C/PC	Shyu	The first node-based DDA code
FBA	C/SUN	Gbara&Pan	The first DDA with good interface, limited functions, 1993
DDA/W	C/Win	Berkeley	The first DDA/Win., less mature ,1996
DDA/WT	C/SUN	Ohnishi	Advanced, new functions, great potential, Only on SUN
DDA/IJ '94	FORTTRAN	Ke	Artificial Joint
DDA/SB '95	FORTTRAN	Lin	Sub-Block, breakable block; good validations

Several DDA codes with additional functions or capabilities have been independently developed by a number of individuals during their Ph.D. research. They include NDDA, DDA/AJ and DDA/BK as listed in Table 1. These codes, based on Shi's code at their time of development, potentially inherited the limitations and possible errors rooted in Shi's original code. Users should be aware of this shortcoming and are suggested to conduct their own validations. More discussion of NDDA, DDA/AJ and DDA/SB can be found in the next section.

Zhang et al. (1990) attempted to code a DDA program using an object-oriented method. When compared to other existing theories, very competitive conclusion in term of matrix solver was obtained. The preconditioned bi-conjugate method was also implemented into the DDA code to speed up the matrix solving (Koo and Chern, 1996). However, finding a faster matrix solver is secondary. In order to have a stable solution without sacrificing the accuracy and efficiency of matrix solving process, setting a diagonally predominated matrix is the key to success (Shi, 1996).

The rigid-body rotation term in DDA is separated from other deformation variables. Consequently, DDA does not preserve block area as blocks rotate and the blocks expand with each increment of rotation. This can be problematic when blocks rotate in large amounts. Young and Ke discovered this problem in 1991 and 1993, respectively. Ke (1995) proposed an updating approach whereas MacLaughlin (1997) adopted the Taylor polynomial approximation as the displacement function. Both approaches reportedly have shown satisfactory results. In 1990, inconsistent results were observed when validating the shear resistance at contact governed by Mohr-Coulomb in DDA for a two-block system. Ke mentioned similar observations in 1993. It is the so-called 'shear lock' problem in which the amount of elastic shear displacement at the

contact point is not accumulated in the DDA code. Both rotation and shear lock problems were 'corrected' in DDA '95 by Shi.

Since the early 1990's, DDA researchers started developing user-friendly DDA programs. In 1993, Dr. Gebara and Dr. Pan of Purdue University made the first effort to bring DDA into a user-friendly editing and reporting environment on Sun workstations. Dr. MacLaughlin and Dr. Sitar of U.C. Berkeley developed DDA for Windows Version 1.1 (1995) sponsored by WES, Army Corp. Both have very limited engineering functions. DDAWorkTool, a UNIX version, developed by Prof. Ohnishi's DDA group (Ohnishi et al. 1995 and Chen et al. 1996) in Japan is the most comprehensive version by comparison. However, DDAWorkTool lacks sufficient validation examples.

It is recommended that future commercial DDA codes include the following functions or features:

- Engineer friendly, different from user friendly
- Flexibility of input and reporting (cad, xls, doc, html and xml)
- Statistical/risk analysis tool, easy sensitive analysis
- Database support (easily store, search and retreat DDA project data)
- Individual, specific application (slope, tunnel, topping etc.)
- Cheaper, short learning curve (run first DDA problems within 8 to 12 hours)
- Rich reference of published information (paper, report/thesis and case studies)
- More tutorial, validation and examples, less QA for user.
- COM (COM+, CORBA, Java Bean) and DDA Web server.

4 MAJOR MODIFICATIONS AND IMPROVEMENTS OF DDA

Most modifications and improvements of DDA have been focusing on 1) higher deformable blocks, 2) contact models, 3) non-linearity, and 4) granular mechanics.

4.1 *Higher Deformable Blocks*

Development of higher deformable blocks was divided into two groups: a) sub-block function by imposing a special model on the interface between sub-blocks, b) node-based or high order displacement functions.

Ke (1993) developed Artificial Joints for DDA (DDA/AJ) under the direction of Prof. Goodman. Ke rewrote the DDA portion of the code in FORTRAN. Similar to DDA/AJ, Lin (1995) developed Sub-Blocks for DDA (DDA/SB) under the supervision of Prof. Amadei. Both approaches divide a block into a number of sub-blocks. A strong tension spring was used in DDA/AJ whereas a special compatibility condition was employed in DDA/SB. A similar approach was used in the bonding element proposed by Ohnishi et al. (1995). The benefits of sub-blocks include refining the stress field, the capabilities of crack propagation and block breaking. The sub-block approach has great practical application to rock engineering and potential application in the numerical manifold method (NMM). A number of validations in DDA/AJ and DDA/SB have been well documented.

Shyu (1993) and Chang (1994) developed a node-based DDA (NDDA) using four-node elements based on equations by Shi for his soon-to-be-released NMM. Early attempts for three-node elements have shown some difficulties. More validations are needed for NDDA. The first effort to use higher order Taylor displacement functions (DDA/T) was made by Koo et al. (1995) for the second order (DDA/T2) and followed by Koo and Chen (1996) and Ma et al. (1996) for the third order (DDA/T3). The third order is necessary to locate the maximum stress within a block. Koo and Chen (1997) developed Fra_DDA for fracture modeling based on DDA/T3. However, how to model the contact in two dimensions still remains a challenge for DDA/T. This led Ma (1995) to develop the first DDA/F (high order Fourier displacement function) only in one dimension with n th order. DDA/F has advantages in wave propagation analysis in which spatial discretization errors are 'eliminated'. That is one of two major numerical errors in other numerical methods for wave propagation analysis. DDA/F produced more accurate results in well-known 'two identical beam problem' than FEM. It is interesting to note that in some cases (one dimension) DDA/T is more efficient than DDA/F in terms of number of order depending on impacting or dynamic source. Further research is suggested to elevate DDA/T and DDA/F for wave propagation analysis.

4.2 Contact Models

The DDA contact model is not a perfect solution. Many DDA researchers (Lin 1994, Cai et al. 1996, Chen et al. 1997, Lin and Hynes 1998) adopted the Lagrange type approach. Better than the penalty method results were reported and predicted. Augment to adopt the Lagrange approach is that stiffer springs result in ill-conditioned matrices whereas softer springs cause serious penetration problems (Lin, 1994 and Chen et al. 1977). The Lagrange approach is a mathematical model with little physical meaning.

Contact between blocks that control the block system mechanical behavior has more significant physical meaning. The contact spring method in DDA is a very effective way to represent these physical characteristics on contact interfaces. In a real world, there is a contact stiffness, which is never too soft or too stiff, and always somewhere in between. Moreover, this is non-linear.

It is hard to select the 'correct' or close spring stiffness to represent the physical stiffness. This becomes more complicated when a simplification is made from edge/edge contacts (2D) between blocks in reality to the point /edge contact model in DDA. In the point/point case, instability has also been observed. It was widely reported that the normal contact stiffness is stress dependent; softer at the beginning and becoming much stiffer when deformation at the contact increases. Therefore, non-linear stiffness has been suggested. In DDA '94, the stiffness was selected based on maximum displacement and penetration at each time step. It is not a favorable approach, but it works in some cases, especially for large number block systems.

Improvement of contact modeling should not only focus at the 'CONTACT' points. The deformability of blocks also has strong influence on contact behavior. Ma (1995, 1996) suggested that using high order displacement functions within blocks could improve the contact behavior for penalty string method in a simple impact problem. In case of a point/edge contact, if there is more than two points on one edge, individual point contact force may not be correct. But sum of these contact forces is correct. With high order deformable blocks, this problem goes away, and more desirable contact behavior can be expected. With cover functions and weight functions in NMM,

the negative impact of simplified point/edge in DDA contact model will be further reduced. Better performance of contact model is expected in NMM.

Time interval also has an impact on contact behavior among blocks. Often, small time intervals are needed to increase the inertia term in the global coefficient matrix (Shyu, 1992). The inertia matrix is far more important than the elastic stiffness matrix and, to some extent, more important than the contact matrix. Larger inertia terms in the diagonal of global coefficient matrix increase the stability of computation.

4.3 Non-linearity

Non-linearity of DDA is not a system's non-linearity since a blocky system is a higher non-linear system itself. Beside that, there is non-linearity within blocks and between blocks. Chang (1994) implemented a material non-linearity model to NDDA using strain hardening curves; no constitutive law was applied or needed. On the other hand, the Drucker-Prager failure criterion was incorporated by Ohnishi et al. (1995). In 1992, Huang and Ma developed a non-linear contact model for analysis of slope progressive failure including strain softening using the stress and strain curve. In general, one issue of non-linearity still not accounted for is the contact stiffness non-linearity as discussed above.

4.4 Granular Mechanics

Even before Peter Cundall's DEM, a discontinuous or discrete approach was used in particulate media, especially that of granular flow. From the 80's to the early 90's, Cundall and Strack (1978), Ting et al (1987), Ishibashi et al. (1989) and Ma (1994) extensively conducted DEM simulations of granular materials. One mystery of DEM for the two dimensional circular disk was the excessive rolling, and was 'solved' by increasing the polar moment of inertia in the order of 5 to 7. However, a physical model of 3D disk by Ishibashi et al. (1989) indicated no excessive rolling. Ishibashi's study suggested that excessive rolling was the result of DEM numerical errors or method's limitations.

Ohnishi's group in Japan, Wang's group in Taiwan and Bray's group in the U.S. developed the DDA code for rigid disks, known as DDAD. Ohnishi and Miki (1996) and Wang et al. (1997) also developed DDAD for elliptic disks in two and three dimensions, respectively. Thomas (1997) has developed a disk cluster model. Up to now, no validation has been reported on the disk rotation in DDAD; neither other well documented validations of DDAD, regardless of shape (circular or elliptic). There is not enough convincing validation that excessive rolling does not occur in DDAD. Developing elliptic or disk cluster does obtain reasonable results, but did not fully address its formulation questions.

Normally, over thousands disks or elements are needed for the simulation of granular media. The original DDA solver is not suitable for large numbers of elements. Thomas (1997) incorporated the PBCG equation solver and reported reasonable performance. Wang et al. (1997) discussed selection of the contact spring stiffness value in DDAD which is similar to those suggested by Ting (Ting et al. 1987) for DEM. Ishijawa et al. (1997) and Huang et al. (1995) presented their studies of mechanical behavior of particulate assembly of the polygon shape. Reasonable results were found.

5 DDA APPLICATIONS

During the past 10 years, DDA has been applied to several real world projects at different stages of design and investigation. It was never intended to be used as a primary or main tool for design or investigation. DDA applications, unfortunately, are still at early stage for real world problems. A good engineering solution normally comes from three approaches: observational, empirical and analytical. In the last 10 years, most of the effort has been focused on developing DDA as a useful analytical tool. DDA could also be a very powerful tool to improve existing empirical/analytical equations/methods (Yeung 1993, Shinji 1997, and Ma and Yeung, 1994).

5.1 *Rock Engineering*

A great amount of progress has been made in validating DDA for rock engineering problems. Yeung (1993), the first DDA Ph.D., conducted a series of DDA validations. His contributions not only include DDA's validation, but also suggestions of improvement over existing widely used methods such as Goodman & Bray Chart, G&B limit equilibrium analysis of toppling and three hinged beam. In a sense, its contribution is beyond the DDA application itself. Ohnishi et al. (1995) and Sasaki et al. (1996) compared DDA results with FEM and experiment results in the areas of stress distribution, displacement and toppling. These comparisons are the most valuable information for future DDA development and application. Inconsistency in displacement between DDA and measured values in tests still remains unknown. It is speculated that this due to contact stiffness values used in DDA and actual values in test.

There is quite a distance to go before DDA can be used in rock engineering as a practical tool. Unfortunately, the key elements, which are essential in rock engineering practices, have not been well developed. The key elements include the structural elements, groundwater and residual strength.

A simple model of rock bolt (Yeung et al. 1994; Ohnishi et al. 1995 and Ke 1997) and concrete lining was developed and implemented. However, these models do not model more practical structural elements and construction sequences. Structural elements consist of reinforcement (cables, bolts) and surface support (concrete lining, steel sets and shotcrete). Non-linearity of the structural elements and interface between the elements and the rock should be implemented with consideration of construction sequences in future development.

Most rock slope slides or failures are triggered by increased hydrologic pressure. Directly coupling rock and flow interactions is extremely challenging with the uncertainties in existing coupling methods and concepts. A simple algorithm using pressure load presenting water pressure or changing unit weight may simply do the job.

Even in structural failure of a rock mass, the residual strength along joints is a key controlling factor for design or evaluating rock mass stability. Shear strength including roughness is described in terms of a friction angle, cohesion and tension, and contact is modeled using normal and shear springs in DDA. With such a simple contact model, residual values of these parameters are necessary to be considered in future DDA models to account for complicate contact/shear mechanism between rocks. Implementation of those structural elements and residual strength is relatively easy and more effective in NMM. Therefore, NMM is recommended for future development.

Key elements mentioned in this section are not critical for simulating rock fall problems. Rock fall problems involve block impact, rotation, traveling and breaking. DDA provides an ideal application for this problem. MacLaughlin (1997) presented a well-documented validation of block traveling. Most DDA rock fall related developments can be found in Ohnishi et al. (1996), Shinji et al (1997), and Cheng and Tsui (1997).

5.2 Geotechnical Engineering

In 1990, Dr. W.F. Chen and Dr. Austin P. Pan (1990, 1991) pointed out the potential for using DDA to analyze bearing capacity (limit equilibrium) problems in geotechnical engineering. DDA does not have the limitations of the limit analysis (LA), limit equilibrium method (LEM), and FEM. Their work was published in 1990, which was the first DDA publication except that by Shi and Goodman. In their study, DDA was validated and 'corner effect' or 'corner cutting' was mentioned for the first time, which later was adopted in many studies and was carefully examined by Gebara (1994).

Even though Dr. Chen and Dr. Pan's claim that DDA is a type of limit analysis is debatable, DDA's ability to yield more accurate solutions in bearing capacity problems was demonstrated by comparison with the limit analysis solutions in their report. The bearing capacity solutions from limit analysis or limit equilibrium method are not complete solutions (Fang 1991), since they do not satisfy all the requirements for the solution of a boundary-value problem. The solutions (LA or LEM) usually satisfy either equilibrium in a limited form or kinematics compatibility. The solutions do not satisfy the constitutive relations and, therefore no information on deformations. LA or LEM does not consider the effect of geometry and boundary condition changes during loading, load direction. Empirical reduction factors have been applied in determining bearing capacity by limit analysis for problems with less complicated geometries and loading conditions such as: eccentric and inclined loads, tilt footing base, footing adjacent to or on a slope, and non-homogeneous/layered foundation.

DDA offers a simple and straightforward solution without a need for empirical reduction factors. Moreover, the foundation settlements due to the deformation or sliding along shear planes can be estimated by DDA since the shear stress vs. displacement relations can be implemented into DDA (Ma et al. 1995). Therefore, a block or slice system is not necessary to be assumed in the limit equilibrium status as in the limit equilibrium analysis or in one extreme condition (low bound or upper bound case) by the limit analysis. DDA can simulate the entire failure process starting from the initial condition with consideration of changing boundary conditions and more realistic constitutive relations at assumed failure planes. A validation case of retaining wall was presented by Ma et al. (1995). Active pressure from DDA and classical solutions is within 5% difference. Huang (1995) demonstrated a unique DDA approach to handle 'H' Block retaining walls with a number of log-spiral failure planes in the backfill soil. Consistent results from DDA and field verification were reported.

In slope stability problems, with exception of circular failure in cohesive soils, an "exact" or "true" factor of safety (F.S.) of a slope based on limit equilibrium theory cannot be obtained. An average factor of safety computed from different rigorous methods may provide a good estimate of the degree of stability for a slope. Duncan (1992) concluded in his state-of-the-art paper that methods satisfying all conditions of equilibrium are accurate for any conditions. The F.S.'s computed from conventional methods differ by no more than about 12 percent from those

calculated by other more complicated methods that satisfy all conditions of equilibrium, and no more than about 6 percent from what can fairly be considered to be the correct answer. Such conclusion was supported by Espinoza et al. (1994), in their five examples studies. However, an average value may not necessarily represent the "most accurate" value of a slope factor of safety (Sharam, 1996). In addition, all of these methods have numerical problems under some conditions. For example, the friction angle between inter-block in the Spencer Method for non-circular failure planes is usually over estimated in general practices. That was the case in Kettleman Hill Landfill failure (Ma and Yeung, 1994) where overestimation of the friction angle between slices results in too higher F.S. This DDA study confirmed the previous finding of potential overestimation of F.S. using conventional methods (Huang and Ma, 1992).

Like limit equilibrium analysis or limit analysis, the failure plane or surface has to be pre-defined in DDA. However, one major difference between DDA and LA or LEM is that besides simulation of deformation or displacement at different loading stages, DDA can also implement more realistic soil behavior such as strain softening. In LA or LEM, only perfect elastic and plastic behavior of soil can be considered. Huang and Ma (1992) demonstrated the capability of DDA to handle the progressive failure problem of the Carsington Embankment Dam. Progressive failure analysis normally involves the complex deformation or displacement and strain softening, which is far beyond the LA or LEM's capability, even though several attempts have been made in the past (Baker and Frydman, 1983). Chen (1993) also demonstrated the potential of DDA in soil slope stability problems.

LEM provides solutions for practical use in almost every soil stability problems (foundation bearing capacity, slope and retaining structure stability), and DDA has a great opportunity in these areas. A chance of DDA becoming a popular engineering tool for these problems is extremely low. Furthermore, DDA for soil stability problems requires the accurate computation of contact forces. With the simplified point/edge contact in DDA, it likely produces incorrect contact forces when more than two points are on one edge. Therefore, NMM, instead of DDA is recommended. Moreover, NMM has the flexibility to implement non-linear material properties, which is essential in geotechnical engineering. More progress should be made to improve existing method and empirical equations based on DDA study.

5.3 Earthquake Engineering

DDA is a dynamic model that can be used in earthquake engineering applications in rock engineering (Ma and Yeung, 1992), geotechnical engineering (Ma et al. 1992 and Ma 1995) and masonry structures (Ma et al. 1997). Tsai and Wang (1995) made a good effort to apply DDA for sliding structures under seismic excitation. Lin and Hynes (1998) modified the DDA with Lagrange multiplier in contact model for a few sliding blocks system, but did not provide conclusive results. A common problem in DDA seismic analysis may have an unrealistic or excessive displacement or rebound mainly in normal contact direction (Ma and Yeung, 1992). A constant spring stiffness value was believed to be the fact. In reality, the spring stiffness is non-linear, stress dependent. It is relatively small with small contact forces at the beginning. Using constant spring stiffness values, normally 100 to 1,000 times the Young's modulus, leads to large and unrealistic reaction forces. It becomes worse for blocks on free surfaces. Moreover, as discussed in the previous section, the deformability of blocks also is a major fact in contact models especially for seismic analysis. In addition, the time interval has a major influence on the

dynamic contact model as well. The scheme to select the time interval proposed in Wang et al. (1995) is very similar to a simply approach presented by Ting et al. (1987) and Ma (1994) for the DEM model.

Back in 1991, Prof. R. Seed of U.C. Berkeley suggested a DDA seismic analysis validation test using a two-block system (Figure 1). Dr. Seed indicated that to his knowledge, no one was able to validate existing numerical methods with analysis solution for this case.

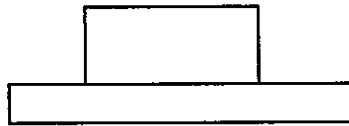


Figure 1. Two-block system.

A successful validation for this two-block system was presented in Ma et al. (1992) and confirmed by Tsai and Wang (1995). However, in 1997, it was found that the seismic induced displacement of the top block varied with the time interval when the time interval was reduced to below a certain limit. In theory, this should not happen. No explanation has been found for this phenomenon.

As a physical model, DDA is a powerful tool to simulate the seismic response of a complex structure such as a slender tall masonry tower (Ma et al. 1996). It was found that a discrete system could sustain a strong earthquake without total collapse. As mentioned before, NMM would give better contact modeling than DDA in two aspects; higher deformability within blocks and cover/weight function instead of point/edge contact.

5.4 Masonry Structures and Other Applications

Similar to rock fall problems, masonry structure problems are ideal candidates to use DDA applications. Masonry structures have a strong non-linear effect and dominate the strength and deformation structural behavior. The assessment of the load carrying capacity of masonry structures like bridges is of particular interest when these structures are still in service and have to sustain service loads higher than in the past. When Lin (1995), Chiou et al. (1995) and Amadei et al. (1995) more focused on the shears stress within blocks, Shyu (1993), Gebara (1994), and Ma et al. (1995,1996) were interested in masonry structural stability and seismic deformation. A case study of seismic response of a slender tall tower (Ma et al., 1996) suggested that discontinuities or joints between blocks inherently reduce the integrity and strength of masonry structures, but sliding along these joints consumes the seismic energy during earthquake. Therefore, while local failure occurs due to sliding or separating, the probability of overall structural collapse is low. DDA could provide some insight to why actual seismic displacements along failure surfaces are always lower than predicted by other analytical or empirical methods in rock or geotechnical engineering.

DDA has been applied to others areas such as seismic fault slips (Chen, 1996) and seabed excavation (Chien and Oh, 1997). Gebara (1994) conducted an outstanding DDA research on rock-rubble/boulder overlay penetration problems under the supervision of Prof. Austin Pan.

6 DDA AND DEM

The discrete (distinct) element method (DEM) as proposed by Cundall and Strack (1978) is conceptually simple. DEM employs the explicit central finite difference scheme to solve the equations of motion of block system to obtain dynamic relaxation solution. However, it is extremely difficult to achieve the static equilibrium of a discrete system with a large number of elements, especially in a loose packing state (Ishibashi et al. 1989 and Ma 1994). Even Cundall and Strack (1978) stated in their 1978 report that the static equilibrium of a discrete system can be reached '*when the inertia force is significantly smaller than the contact forces*'. The inertial force normally has the same magnitude as the contact force at the initial stage. Only in dense packing configurations, the inertia force would relatively quickly be reduced to far below the contact force after many time steps.

In contrast to DEM, DDA does not have such complex and uncertain static solutions. Kinetic damping is applied in DDA, which effectively filters out the motions with higher modes to unconditionally bring the system to a static equilibrium (Chang and Acheampong 1993, and Wang et al. 1995). The time interval determined by users prior to computation is 100 to 1,000 time larger or more than that used in DEM. Consequently, DDA could be faster than DEM for static problems as predicted in 1992 (Chang, 1992). The time interval can be relatively large as long as the small displacement assumption in DDA is not violated.

The time interval should be kept very small in dynamic analysis for both DDA and DEM. It also depends on contact stiffness, especially for problems involving wave propagation. No damping is used in current DDA. There are two types of damping that are used in DEM: mass-proportional damping and stiffness-proportional damping. The mass proportional damping is effective in reducing low frequency oscillatory motion of a given system whereas the stiffness proportional damping is more effective in removing the high frequency oscillation of individual block against each other. DEM permits "inadmissible" or "excess" penetration, which further leads to extra energy. Two types of damping are utilized to consume such extra energy. In DEM, these damping phenomena are inevitable, even for damping free block systems in loose packing configuration with a considerable number of blocks, and viewed as the "artificial" or "numerical" damping. DEM cannot simulate the real time dynamic response of given block systems, because there is no real time 'artificial' damping. These two types of damping can be easily implemented into a DDA code to 'truly' represent physical energy absorption. DDA should not have problems with modeling damping free block systems.

Table 2 shows a comparison of DDA and DEM equilibrium and compatibility conditions, which must be fulfilled in order to obtain a complete solution.

Table 2. DDA and DEM.

Within Blocks	Equilibrium	Compatibility
DDA	Guaranteed	Displacement function
DEM	Dynamic equilibrium	Rigid body
Between Blocks	Equilibrium	Compatibility
DDA	Stable	No penetration & tension
DEM	Unstable	Inadmissible penetration

7 CLOSING REMARKS

For future DDA applications, more effort is needed to improve and modify the methods or empirical equations used in current accepted practices.

Non-linear spring stiffness should be considered along with higher deformable blocks for a better contact model. The Lagrange method for contact model is not recommended, especially in seismic analysis.

Validation of seismic induced displacement of two-block system for DDA and rotation for DDAD are recommended. Published or unpublished validations are needed to confirm, independently checked and documented results.

Except for rock fall and masonry structure problems, DDA is not recommended. Instead, the numerical manifold method should be considered as the first choice.

ACKNOWLEDGEMENTS

I started DDA in 1989. All my DDA work has been done after my daily job without any funding in the past years. I am indebted to my wife, Lin, for her support and understanding. She refers to DDA as my lover.

I would like to thank Dr. C.S. Cheng of U. Mass. for his valuable discussion, Mr. Brian Dorwart of Shannon and Wilson Inc., for helping me understand the concept of engineer-friendly program. I specially thank Prof. Neville Cook for his interest and encouragement. Finally, thank Gen-Hua for all the stories he has told me during the past 10 years (1989-1999).

REFERENCES

- Baker, R., and Frydman, S. 1983. Upper bound limit analysis of soil with nonlinear failure criterion. *Soil and Foundation* 23(4): 34-42.
- Cai, Y., Liang, G.P., Shi, G. and Cook, N.G.W. 1996. Studying an impact problem by using LDDA method. *Proceedings of the First International Forum on Discontinuous Deformation Analysis and Simulations of Discontinuous Media, Berkeley, CA*: 288-294.
- Chang, C. S. 1991. Discrete element method for slope stability analysis. *J. of Geotech. Eng. ASCE*, 118(12): 1189-1905.
- Chang, C. S. 1992 Personal communication on speed and memory requirement of DDA and DEM computations, July.
- Chang, C. S. and Acheampong, K. B. 1993. Accuracy and stability for static analysis using dynamic formulation in discrete element methods. *Proceedings of the 2nd International Conference on Discrete Element Methods, MIT, Cambridge*: 379-389.
- Chang, C. S. 1994. Nonlinear dynamic discontinuous deformation analysis with finite element meshed block system. *Ph.D. dissertation, Civil Eng., U.C. Berkeley*.
- Chen, S. 1993. Slope stability assessment based upon discontinuous deformation analysis. *Ph.D. dissertation, School of Engineering, University of Pittsburgh*.
- Chen, W.F. and Pan, A.D.E. 1990. Finite element and finite block methods in geomechanics.

Structural Engineering Report: CE-STR-90-20, School of Civil Engineering, Purdue University.

- Chen, W.F. and Pan, A.D.E. 1991. Finite element and finite block methods in geomechanics. *Proceedings of the Third International Conference on Constitutive Laws for Engineering Materials: Theory and Application, Tuscon, Arizona*: 669-675.
- Chen, G., Miki, S. and Ohnishi, Y. 1996. Practical improvements on DDA. *Proceedings of the First International Forum on Discontinuous Deformation Analysis and Simulations of Discontinuous Media, Berkeley, CA*: 302-309.
- Chen, M.H., Wang, C.Y. and Sheng, J. 1997. Static contact problems of discrete systems solved by the diffuse element method. *Proceedings of the second international Conference on Analysis of Discontinuous Deformation, Tokyo*: 323-342.
- Cheng, Y.M. and Tsui, Y. 1997. Advancements in discontinuous deformation analysis. *Proceedings of Computer Methods and Advances in Geomechanics, Wuhan, China*: 479-482.
- Chien, L.K. and Oh, Y.N. 1997. A preliminary study of excavated seabed assessment based on discontinuous deformation analysis. *Proceedings of Computer Methods and Advances in Geomechanics, Wuhan, China*: 489-494.
- Chiou, Y.J., Tzeng J.C. and Lin, M.J. 1995 Discontinuous deformation analysis for masonry structures. *Proceedings of the First International Conference on Analysis of Discontinuous Deformation, Chungli, Taiwan*: 288-297.
- Cundall, P.A. and Strack, O.D. 1978. The distinct element method as a tool for research in granular media, part I&II. *Report to the NSF*.
- Duncan, J.M. 1992. State-of-the-art: static stability and deformation analysis. *Proceedings of Stability and Performance of Slopes and Embankments - II, ASCE Geotechnical Special Publication 31*: 222-266.
- Espinoza, R.D., Bourdeau, P.L. and Muhunthan, B. 1994. Unified formulation for analysis of slopes with general slip surface. *ASCE J. Geotech. Eng.* 120(7): 1185-1203
- Fang, H.Y. 1991. Foundation engineering handbook, 2nd Edition. *Van Nostran Reinhold, New York*.
- Gebara, J.M. 1994. The Finite block method: an analysis tool for structural engineers. *Ph.D. Dissertation, School of Civil Engineering, Purdue University*.
- Huang, A. B. and Ma, M. Y. 1992. Discontinuous deformation slope stability analysis. *Proceedings of Stability and Performance of Slopes and Embankments - II, ASCE Geotechnical Special Publication 31*: 479-492.
- Huang, A. B., Hsiao, M., and Lu, Y. 1995. DDA simulations of a graded particulate assembly under shear. *Proceedings of the First International Conference on Analysis of Discontinuous Deformation, Chungli, Taiwan*: 360-372.
- Huang, T. K. 1995. The discontinuous deformation analysis of 'H' block retaining wall. *Proceedings of the First International Conference on Analysis of Discontinuous Deformation, Chungli, Taiwan*: 274-287.
- Ishibashi, I., Agarwal, T. and Ashraf, S. A. 1989. Anisotropic behaviors of glass spheres by a discrete element model and laboratory experiments. *Proceedings of the First U.S. DEM Conference, Golden, Colorado*: 77-89
- Ishikawa, T., Ohnishi, Y. and Namura, A. 1997. DDA applied to deformation analysis of coarse granular materials (ballast). *Proceedings of the second international Conference on Analysis of Discontinuous Deformation, Tokyo* : 253-262.

- Koo, C.Y., Chern, C.Y. and Chen, S. 1995. Development of second order displacement function for DDA. *Proceedings of the First International Conference on Analysis of Discontinuous Deformation, Chungli, Taiwan*: 91-108.
- Koo, C.Y. and Chern, J.C. 1996. The development of DDA with third order displacement function. *Proceedings of the First International Forum on Discontinuous Deformation Analysis and Simulations of Discontinuous Media, Berkeley, CA*: 342-349.
- Koo, C.Y. and Chern, J.C. 1997. Modeling of progressive fracture in jointed rock by DDA method. *Proceedings of the second international Conference on Analysis of Discontinuous Deformation, Tokyo*: 186-200.
- Ke, T.C. 1993. Simulated testing of two dimensional heterogeneous and discontinuous rock masses using discontinuous deformation analysis. *Ph.D. dissertation, Civil Eng., U.C. Berkeley*.
- Ke, T.C. 1995. Modification of DDA with respect of rigid-body rotation. *Proceedings of the First International Conference on Analysis of Discontinuous Deformation, Chungli, Taiwan*: 260-273.
- Ke, T.C. 1997. Improved modeling of rock bolting in DDA. *Proceedings of Computer Methods and Advances in Geomechanics Wuhan, China*: 483-488.
- Lin, C.T. 1995. Extensions to the discontinuous deformation analysis for jointed rock masses and other blocky systems. *Ph.D. dissertation, Dept. of Civil Eng. and Arch. Eng., University of Colorado*.
- Lin, J.S. and Hynes, M. 1998. Seismic discontinuous deformation analysis. *Geotechnical Earthquake Engineering and Soil Dynamics III, Geo. Special Publication 75*: 790-799.
- Liu, L. 1996. Modeling a seismic fault slips and block deformation in northern China by DDA. *Proceedings of the First International Forum on Discontinuous Deformation Analysis and Simulations of Discontinuous Media, Berkeley, CA*: 373 -382.
- Ohnishi, Y., Chen, G. and Miki, S. 1995. Recent development of DDA in rock mechanics. *Proceedings of the First International Conference on Analysis of Discontinuous Deformation, Chungli, Taiwan*: 26 -47.
- Ohnishi, Y., Yamamukai, K and Chen, G. 1996. Application of DDA in rockfall analysis. *Proceedings of the 2nd north american rock mechanics symposium: NARMS '96, Montreal*: 2031-2037.
- MacLaughlin, M. M. 1997. Discontinuous deformation analysis of the kinematics of landslides. *Ph.D. dissertation, U.C. Berkeley*.
- Ma, Y. M., Yeung, A. T. and Huang, A. B. 1992. Seismic stability of landfill, *ASCE Ninth Eng. Conf., Texas*: 721-724.
- Ma, Y. M., Yeung, A. T. and Huang, A. B. 1993. Seismic response of a waste repository by discontinuous deformation analysis. *Second International Conference on Discrete Element Methods, MIT, Cambridge*: 499-509.
- Ma, Y. M. and Yeung, M. R. 1993. Toppling and sliding of blocks under dynamic loading, *First Canadian Symposium on Numerical Modeling Applications in Mining and Geomechanics, Montreal*: 198-206.
- Ma, Y. M. 1994. A numerical study of cone penetration tests in granular assemblies *Ph.D. dissertation, Clarkson University*
- Ma, Y. M. and Yeung, A. T. 1994. DDA study for Kettleman Hill landfill failure, *unpublished*.
- Ma, Y. M., Barbeau, P. and Penumadu, D. 1995. Evaluation of active thrust on retaining walls

- using DDA. *Proceeding of the 2nd Congress of Computing Methods in Civil Engineering in Conjunction with AEC*: 104-111,
- Ma, Y. M., Pan, A. D., Luan, M. and Gebara, J. M. 1995. Stone arch bridge analysis by the DDA method. *First International Conference on Arch Bridges, Bolton, UK*: 211-221.
- Ma, Y. M. 1995. Single field manifold method using Fourier Function for Wave Propagation Analysis. *WES, Working Forum on the Manifold Method of Material Analysis*: 24-45.
- Ma, Y. M., Zaman, M. and Zhu, J. H. 1996. Discontinuous deformation analysis using the third order displacement function. *Proceeding of Discontinuous Deformation Analysis and Simulations of Discontinuous Media, Berkeley, CA*: 383-394.
- Ma, Y. M., Pan, A. D., Luan, M. and Gebara, J. M. 1996. Seismic analysis of stone arch bridges using discontinuous deformation analysis. *CD proceedings of Eleventh World Conference of Earthquake Engineering, Acapulco, Mexico, Paper No. 1353*.
- Sasakai, T., Morikawa, S., Ishii, D., Ohnishi, Y. and Yoshinaka, R. 1996. Comparison with DDA and FEM by jointed rock foundation models. *Proceeding of Discontinuous Deformation Analysis and Simulations of Discontinuous Media, Berkeley, CA*: 432-439.
- Sharam, S. 1996. Discussion of unified formulation for analysis of slopes with general slip surface. *ASCE J. Geotech. Eng.* 122(2): 160.
- Shi, G. and Goodman, R.E. 1985. Two dimensional discontinuous deformation analysis. *Intl J. for Numerical and analytical Methods in Geomechanics* 9: 541-556.
- Shi, G. 1992. Personal Communication on DEM & DDA simulations of a damping free system.
- Shi, G. 1996. Personal Communication on fast matrix solving in DDA. September.
- Shinji, M., Ohno, H., Otsuka, Y. and Ma, G. 1997. Viscosity coefficient of the rockfall simulation. *Proceedings of the second international Conference on Analysis of Discontinuous Deformation, Tokyo*: 201-210.
- Shyu, K. 1992. Personal Communication on selection of time interval, August.
- Shyu, K. 1993. Nodal-based discontinuous deformation analysis. *Ph.D. dissertation, Civil Eng., U.C. Berkeley*.
- Tsai, F.C. 1993. Dynamic interaction of discrete continua-the theory of non-overlapping continua. *Ph.D. dissertation, Material Science and Mineral Eng., U.C. Berkeley*.
- Tsai, J. and Wang, W. 1995. Dynamic responses of sliding structure subjected to seismic excitation. *Proceedings of the First International Conference on Analysis of Discontinuous Deformation, Chungli, Taiwan*: 420-432.
- Thomas, P.A. 1997. Discontinuous deformation analysis for particular media. *Ph.D. Dissertation Civil Eng., U.C. Berkeley*.
- Ting, J.M., Corkum, B.T., Kauffman C.R. and Greco, C. 1987. Discrete numerical modeling of soil: validation and application", *Publication No.87-3, Civil Engineering, University of Toronto*
- Wang, C.Y. Sheng, J. and Chen, M.H. 1995. Dynamic-contact analysis scheme applied in the DDA method. *Proceedings of the First International Conference on Analysis of Discontinuous Deformation, Chungli, Taiwan*: 433-459
- Wang, C.Y. Chuang, C.C. and Sheng, J. 1996. Time integration theories for the DDA method with finite element meshes. *Proceeding of Discontinuous Deformation Analysis and Simulations of Discontinuous Media, Berkeley, CA*: 263-287.
- Wang, C.P., Sheng J., Wang, C.Y. Lee, C.L. 1997. Selection of contact spring stiffness values in the numerical analysis for the system rigid disks. *Proceedings of the second International Conference on Analysis of Discontinuous Deformation, Kyoto, Japan*: 451-458

- Yeung, M.R. 1991. Application of Shi's discontinuous deformation analysis to the study of rock behavior. *Ph.D. dissertation, Civil Eng., U.C.Berkeley.*
- Yeung, M.R., Klein, S.J. and Ma, Y. M.. 1994. Application of discontinuous deformation analysis to the evaluation of rock reinforcement for tunnel stabilization. *First North American Rock Mechanics Symposium, Austin*: 607-614.
- Zhen, H., White, D. W. and Chen, W.F. 1990. An object-oriented matrix manipulating library. *Structural Engineering Report, CE-STR-90-11, Purdue University*

COMPARISON BETWEEN PHYSICAL AND MANIFOLD METHOD MODELS OF DISCONTINUOUS ROCK MASSES

Yuzo OHNISHI, Guangqi CHEN and Masahiro OGAWA

Kyoto University, School of Civil Engineering, Kyoto 606-8501, Japan

Takahiro ITOH

Mitsubishi Heavy Industry CO., Kobe 662, Japan

Takumi NAKAI

Earth-tech Toyo CO., Kyoto 606, Japan

ABSTRACT: The original Manifold Method has been modified on the two aspects. One is the modification on mesh generating program by adding two functions: 1). one piece of regular meshes with any density can be generated for one physical block; 2). sub-meshes can be generated in some important local areas within a large block. This modification is of special usefulness for processing stress-concentrated problems. The other modification is that a non-linear mechanical model for discontinuities is adopted instead of the criteria of no tension and no penetration in original MM so that the deformation of a discontinuous zone can be modeled by MM.

Two laboratory experiments have been made. One is for the kinematic behavior of a block on the slope with a sharp step. The other is a model test for discontinuous rock mass. Comparisons between physical tests and MM computations are made in order to evaluate the ability and inability of the method in practical applications.

1 INTRODUCTION

The Manifold Method of material analysis (MM) is a very flexible numerical method which attracts more and more engineers in rock engineering because it contains and combines widely used Finite Element Method (FEM) and joint or block oriented Discontinuous Deformation Analysis (DDA) method in a unified form (Shi, 1991).

Among MM advantages, the following two are of practical usefulness: 1). regular meshes are always available in MM no matter how complicated the shapes of physical blocks are, 2). it can easily deal with discontinuities involved in rock masses. The method has already been put into many practical applications in rock engineering problems.

In order to promote MM to more widely practical applications, in this paper, we make two modifications on the original MM program. One is the modification on the mesh generating program by adding two functions to it so that the generated meshes are flexible enough to processing stress-concentrated problems. The other is adoption of a non-linear mechanical model for discontinuities instead of the criteria of no tension and no penetration in contact

processing. Thus, the deformation from a discontinuous zone can be modeled by the method.

In addition, in order to evaluate the affectivity of MM, two laboratory experiments are made and modeled by using the method. One is for the kinematic behavior of a block on the slope with a sharp step. The other is a model test for discontinuous rock mass. By comparing the results from laboratory tests and MM computations, we can clearly find both ability and inability of the present MM, which is helpful to both current practical applications and future studies on the method.

2 MODIFICATIONS ON ORIGINAL MM

2.1 Modification On Mesh Generating Program

One of MM advantages is that uniform meshes are always available no matter how complicated the shapes of material blocks are. In original MM, one piece of uniform triangular meshes can be automatically generated over the whole range of the physical material. This makes the MM calculation very easy and one can save much time in making calculation models.

However, it is found that one piece of uniform meshes over the whole material is not always good. As we know, the accuracy of numeric analysis method is affected by element sizes. The smaller the elements are, the better the accuracy is. On the other hand, using small elements needs more elements and more computing time. Therefore, considering both the accuracy and computing time, it is more effective to make much denser meshes only over part of physical blocks or some local areas rather than the whole material.

For this reason, we make the following modifications on the original MM program.

2.1.1 One Piece of Uniform Meshes for One Individual Physical Block

We add a function to original MM mesh generating program that one piece of uniform triangular meshes can be generated over one individual physical block. Thus, some blocks may have much denser meshes than others. For the modified MM program, users can choose either the original way "one sheet for whole" or the new way "one sheet for individual". When the new way is chosen, a division number can be designated to an individual block. Then, different blocks may have different densities of meshes. It is also possible to let a small block be completely covered by a single triangle in the new program.

2.1.2 Sub-Meshes In An Element

For a large block, stress concentration may occur in a local area. Therefore, much denser meshes are required in this area. Generating sub-meshes is an effective measure and usually used in FEM. We also add the function in MM.

Since MM is based on cover theory, sub-meshes can not be drawn as arbitrarily as in FEM. In original MM, a cover, represented by a node, is defined by all the triangles around the node which is also called a star. A triangular element is right the common part of the three covers which take the three nodes of the element as their stars.

According to this definition, we present a way of generating sub-meshes based on the

original ones, which is shown in Figure 1. In the figure, thick lines and five-angle stars are original meshes and nodes, thin lines are sub-meshes, dot lines are meshes for connecting the element with sub-meshes to its surrounding elements, four-angle stars are the new nodes because of sub-meshes. Figure 1(a) shows one division in an edge of the element and (b) for two divisions.

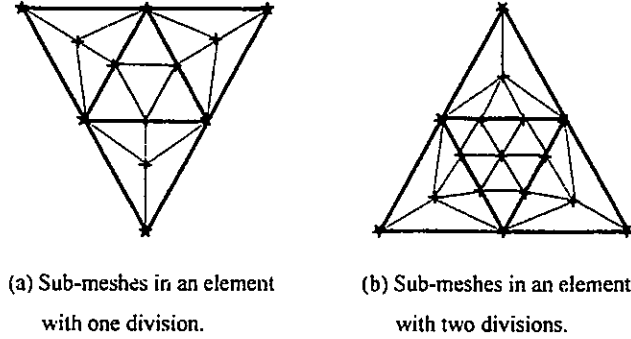


Figure 1: Sub-Meshes based on the original ones.

2.2 A Non-Linear Model For Discontinuities

In original MM, penalty method is used to connect the individual discontinuous boundaries into a system. For the movements of discontinuous boundaries, no tension and no penetration are allowed between contact sides. With this way, the method is successfully used to simulate the coupling state, separating and sliding movements between contact blocks.

However, original MM is only suitable for ideal blocks, i.e., for the case that blocks are completely divided by discontinuous lines. In practice, a discontinuity such as a joint or a fault is not a dimensionless line but a zone.

In general, the rigidity of a discontinuous zone is much weaker than the surrounding blocks, large deformation may happen in the zone when it is compressed or sheared. On the other hand, when a discontinuous zone is pulled apart, it still has tension resistance before completely being broken although the resistance may be small.

In order to model the deformation of a discontinuous zone, we adopt a non-linear mechanical model for discontinuities shown in Figure 2, which is presented and discussed in DDA (Chen et al, 1999). f_n , f_t are contact spring forces and δ_n , δ_t are spring strains in normal and tangential directions.

For the case of compression, the behavior of a discontinuous zone can be divided into three stages.

It is of elastic behavior on the first stage, which is represented by OB in Figure 2(a).

Once the strain of the discontinuous zone gets larger than the allowed maximum elastic strain ϵ_m , the zone becomes failure. Then, it enters the second plasticity stage shown by BC in the figure.

It should be noted that the second stage is just an instantaneous one, the zone gets

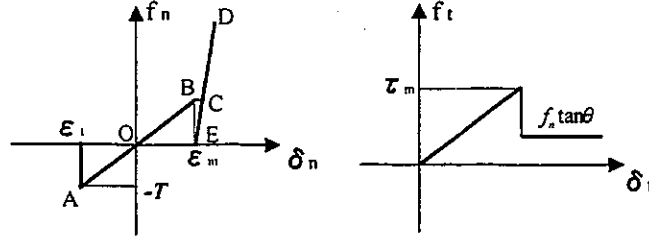


Figure 2: Non-linear mechanical model for discontinuities.

hardening very quickly and ϵ_m is remained as the permanent deformation. Then, the zone enters the third stage shown by CD immediately after yielding, and it is of elastic behavior again but with very strong rigidity.

We can make above assumption because we believe that the soft zone of a discontinuity may be vanished by the large compressing deformation, and blocks are contacted each other by their essential parts. Therefore, very little deformation will be produced from the discontinuity, and the zone is small enough to be treated as a dimensionless line.

It should be noted that the third stage just corresponds to the model of original MM and deformation will not recover to O but to E even if compressing force becomes zero in the discontinuity.

In the case of tension, at first, the discontinuous zone is of elastic behavior shown by OA in the figure. Once tension force gets larger than the tension strength T of the zone, the discontinuous zone will be broken completely. Then, the two contacted blocks can be moved apart freely and there should be no longer normal contact force acting on the discontinuity. After broken, criterion of no tension is adopted just the same as original MM.

In the case of shearing, the new model uses shearing rigidity of the discontinuous zone instead of penalty spring used in original MM. Therefore, shearing deformation from the zone can be simulated before shearing failure.

Mohr-Coulomb's law is used for shearing failure of two coupled blocks. If the shearing force calculated from the tangential spring gets larger than shearing strength τ_m of the discontinuity, the tangential spring will be removed, and then, friction force takes the place of the spring. τ_m is calculated by the following formula

$$\tau_m = C + f_n \tan \theta \quad (1)$$

where C and θ are cohesion and friction angle of the discontinuity and f_n is the compressing force from the normal spring.

3 PHYSICAL MODEL TESTS AND MM COMPUTATIONS

In order to verify the effectiveness of MM, we make two physical model tests. One is for investigating kinematic behavior of a block on the slope with a sharp step. The other is for

investigating large deformation behavior of discontinuous rock mass under bi-axial loading. Then we model the two laboratory experiments by using Manifold Method and compare the results from MM computations and those from experiments in this section.

3.1 Kinematic Behavior Of A Block On The Slope With A Sharp Step

In order to apply MM to rock fall analysis more effectively, we make an experiment for investigating kinematic behavior of a block on the slope with a sharp step shown in Figure 3(a).

The slope is formed by the two blocks with points A , B and C . They are fixed on a vertical base plate. The other block with point D is the sliding one on the slope.

The dimensions are shown in Figure 4(b) where $\alpha_1 = 30^\circ$ and $\alpha_2 = 10^\circ$, the sliding block is $100mm \times 48mm$ with a thickness of $48mm$. The blocks for the slope has the thickness of $60mm$.

Since only two-dimensional MM is available at present, the movements of the sliding block should be carried out in a vertical plan. In order to make the sliding block move without the displacement component vertical to the base plate, we let the base plate have an angle 70° to the horizontal rather than 90° . Thus, the sliding block gets friction resistance from both the slope and the base plate.

The slope blocks are made of aluminum material and the sliding block is made of wood. The surfaces of the slope are covered by two kinds of papers for obtaining two different frictions, called case 1 and case 2 here. Ten times of experiments are made for each friction case.

A digital video camera is used for recording the movements of the sliding block on the slope. The pictures have been taken with a speed of 30 pictures per second. The block moves without initial velocity by sliding on the above part and falls down to the lower part of the slope in each experiment.

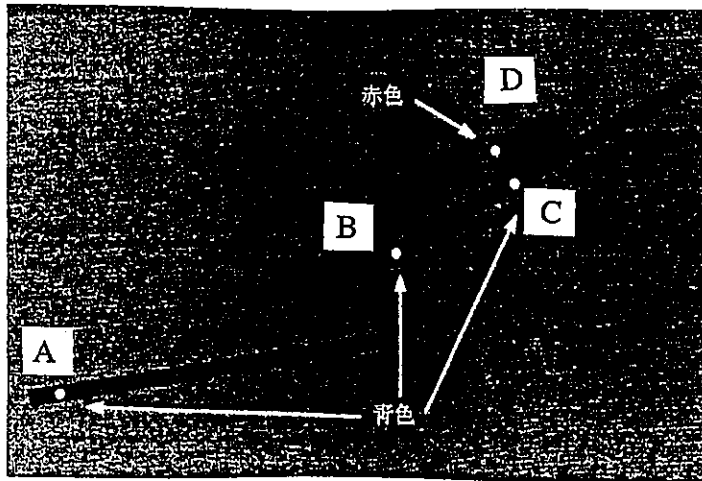
The scale of a picture can be determined based on the coordinates of points A , B and C . The movements are obtained from the coordinates of point D . Therefore, the graphic of displacements with time can be easily made for each experiment.

The experiments are modeled by using Manifold Method. The model is shown in Figure 3(c). There are 44 and 80 elements in sliding block and slope blocks respectively. The lower boundaries of the slope blocks are fixed at each nodes.

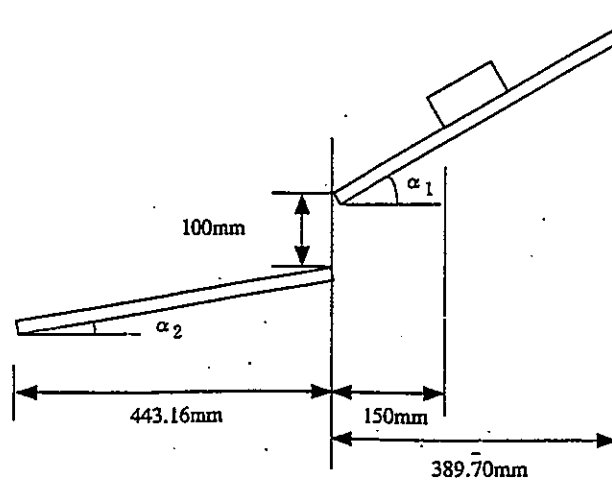
The parameters used in MM are listed in Table 1, where, Δt and D_{max} are the designated time interval and the designated allowed maximum displacement for one step respectively, ρ , E and ν are mass per unit volume, Young's modulus and Poisson's ratio respectively.

The parameters for discontinuities are taken as follows: $C = 0$, $\theta = 18^\circ, 19^\circ, \dots, 24^\circ$, $T = 0$, $k_n = 10E_1$ and $k_t = E_1$

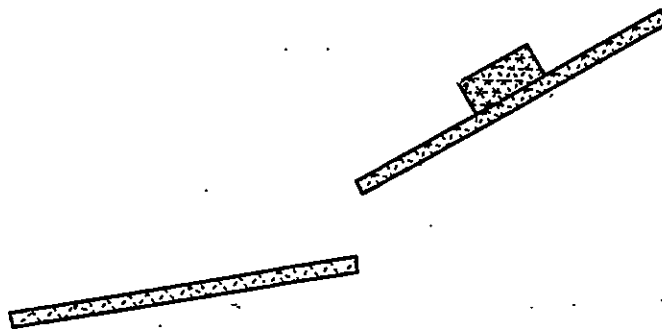
It should be mentioned that since it is difficult to obtain the friction angle directly, the values in Table 1 are determined based on theoretical inverse calculations from the movements of the sliding block on the upper part of the slope. The theoretical results are shown



(a) The physical model for the experiment



(b) The dimensions of the model



(c) The mathematical model for MM

Figure 3: The physical model for the experiment and mathematic model for MM

Table 1: The parameters used in Manifold Method

Controlling Parameters		Aluminum	Wood
Δt	0.01 sec	ρ_1 2700 kg/m ³	ρ_2 720 kg/m ³
steps	3000	E_1 7000 MN/m ²	E_2 1000 MN/m ²
D_{max}	0.001	ν_1 0.34	ν_2 0.24

by curves in Figure 4(a). In this figure, since 10 times of the experiment have been carried out for each case, the displacements in one experiment are shown by empty circles for case 1 and empty squares for case 2, the solid circles and solid squares are corresponding averages.

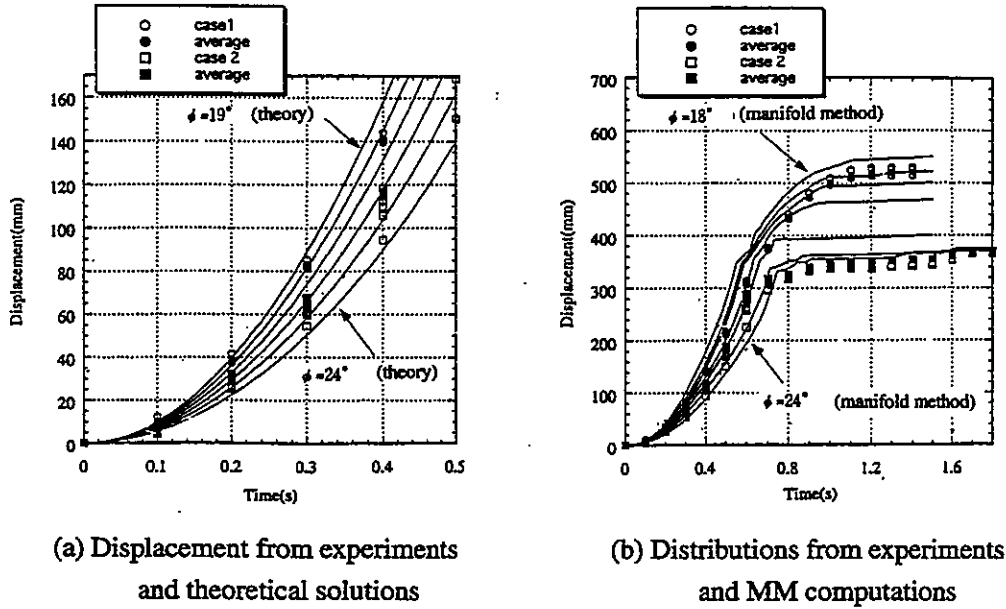


Figure 4: The displacements from experiments, theoretical solutions and MM computations.

The MM computations have been carried out corresponding to each friction angle from 18° to 24° . The calculated displacements for whole slope are shown by curves in Figure 4(b), where one curve corresponds to one friction angle with 1° increasing from top to bottom.

Comparing the movement behavior on the lower part of the slope, we can see that the experiment and MM modeling have the same displacement patterns, and it seems that the results calculated with the friction angles 19° for case 1 and 24° for case 2 are in good agreement with that from the experiments.

When the block moves on the slope, it has a jumping movement from the upper part to the lower part of the slope. We are mainly interested in whether MM can be used to model the jumping behavior such as the starting and stopping time, the maximum jumping distance, height and rotation pattern.

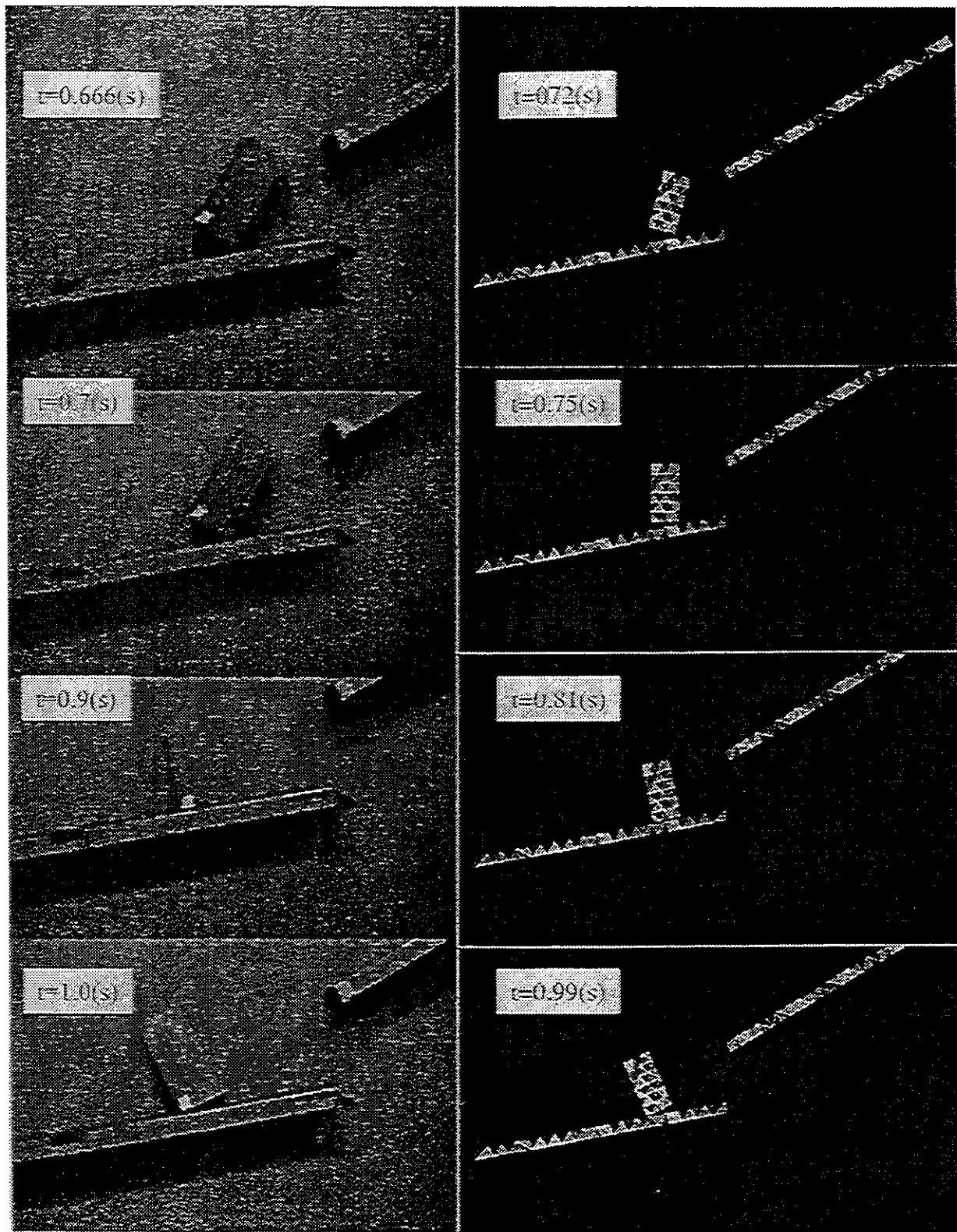


Figure 5: The rotation patterns from the experiment and MM modeling.

In case 1, the jumping starting time is about 0.6sec, the stopping time is about 1.1sec in both experiment and MM modeling. The jumping distances are about 330mm from the experiment and about 350mm from MM modeling. These are in agreement with each other. However, it is found a rebounding of about 15mm at the back part of the sliding block while there is not any rebounding obtained from MM simulation after the block reached on the lower part of the slope. This is because rebounding is related to many parameters such as the designated step time interval, the elastic parameters and the strengths of penalty springs in MM modeling. It is a problem in MM application that should be studied carefully in future.

In case 2, since the friction is different from case 1, there are rotating movements involved in the jumping by experiment. The rotating movements are also obtained by MM modeling. The pictures from both the experiment and MM modeling are shown in Figure 5, where the left side is for the experiment and the right side for MM modeling. It can be seen that the rotation patterns are in good agreement with each other.

3.2 Model Test For Discontinuous Rock Mass

Laboratory model tests for discontinuous rock masses are made. The discontinuous models are loaded in uniaxial and bi-axial loading conditions.

One of the models is shown in Figure 6(a). The sample rock is made of mortar with silica of 6/11, cement 3/11 and water 2/11. It is divided into 8 blocks by 4 discontinuities which are made of cement paste without sands.

The parameters of the sample rock are estimated as $\rho = 2.56kg/m^3$, $E = 13000MN/m^2$ and $\nu = 0.18$ by other experiments.

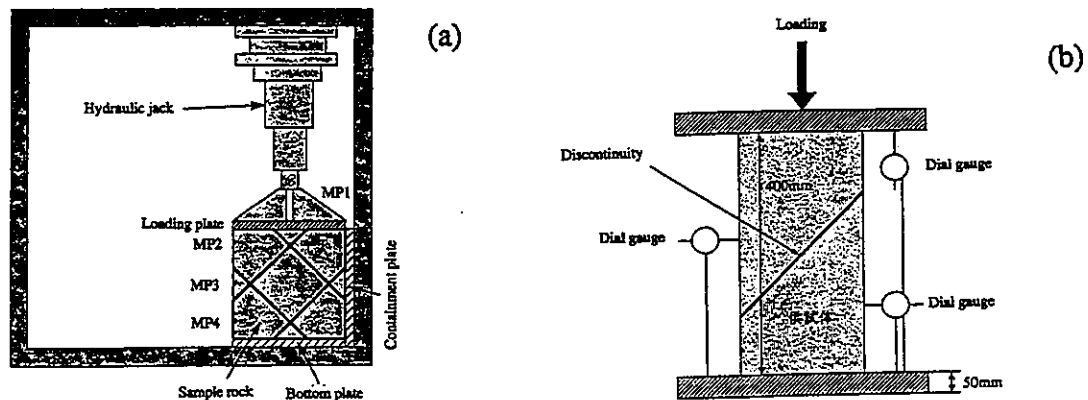


Figure 6: Laboratory model tests for discontinuous rock mass.

The rock mass is loaded step by step on the top of the sample rock by a hydraulic jack with an increment of $0.2MN/m^2$ in each step. When the loading got to $5.4MN/m^2$, the rock failure happened.

The vertical displacements of the point indicated by MP1 and the horizontal displacements of the points indicated by MP2, MP3 and MP4 are measured by using dial gauges. It has

been found that the deformation from discontinuities is much larger than elastic deformation of rock itself from the measured displacements.

Another kind of tests as shown in Figure 6(b) are also made for estimating the parameters of the discontinuities such as cohesion C and friction angle ϕ . The sample rock is divided into two blocks by a discontinuity with an angle θ to the horizontal direction.

Since the sample rock and the discontinuity are made by the same way for both model tests, they are believed to have the same behavior of discontinuity.

In the second test, the stress components σ_n and τ for normal and tangential directions of the discontinuity can be obtained from the loading stress σ_v as follows

$$\begin{cases} \sigma_n = \sigma_v \cos^2 \theta \\ \tau = \sigma_v \sin \theta \cos \theta . \end{cases} \quad (2)$$

As we know, the sample will get failure right after the maximum loading value σ_{max} . Then, according to Mohr-Coulomb's law, we have

$$\tau^* = C + \sigma_n^* \tan \phi , \quad (3)$$

where (σ_n^*, τ^*) correspond to the maximum loading, that is

$$\begin{cases} \sigma_n^* = \sigma_{max} \cos^2 \theta \\ \tau^* = \sigma_{max} \sin \theta \cos \theta . \end{cases} \quad (4)$$

Therefore, C and ϕ can be estimated based on (3) if two more sets of (σ_n^*, τ^*) are obtained by changing the angle θ of the discontinuity in each test.

We have made three times of the tests by taking different angles: $\theta = 45^\circ, 50^\circ, 55^\circ$. Then, the cohesion C and friction angle ϕ are estimated as follows by using the least square method

$$\begin{cases} C = 0.17MN/m^2 \\ \phi = 39^\circ . \end{cases} \quad (5)$$

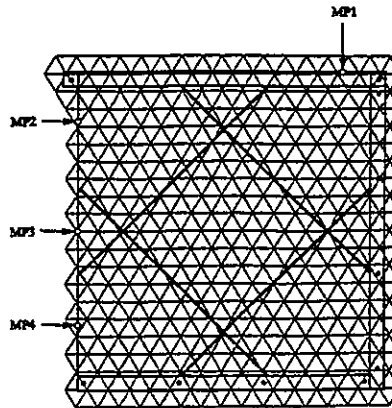


Figure 7: MM model for the laboratory test.

Manifold Method is used to model the laboratory test shown in Figure 6(a). The mathematical model is shown in Figure 7 where the solid circles are fixed points.

The displacements of measured points from both laboratory test and MM computations are shown in Figure 8, where we have results from three cases of MM computations with different C and ϕ :

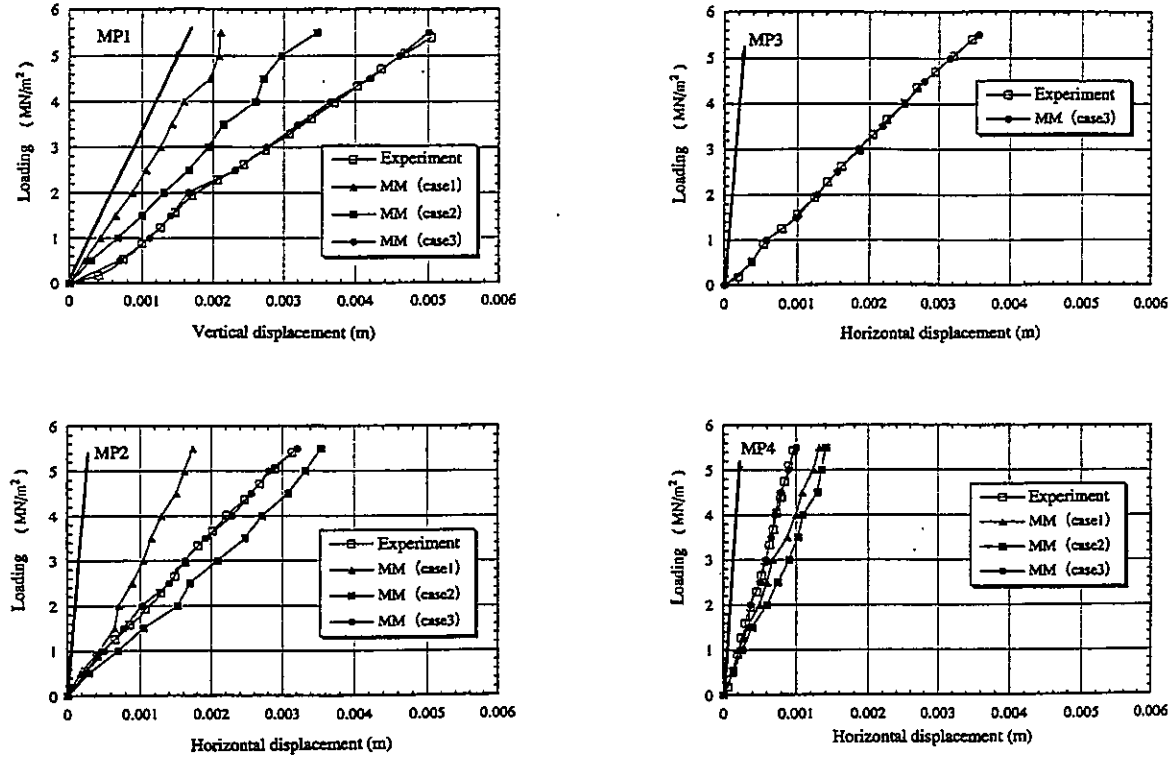


Figure 8: Displacements of measured points from physical test and MM computations.

Case 1: All the discontinuities have the same values of $C = 0.17MN/m^2$ and $\phi = 39^\circ$.

Case 2: Only the discontinuities of the sample rock have above values but the other discontinuities have values of $C = 0$ and $\phi = 0$.

Case 3: The discontinuities of the sample rock have modified values of $C = 0.13MN/m^2$ and $\phi = 41^\circ$ and the other discontinuities have values of $C = 0$ and $\phi = 5.5^\circ$.

The elastic displacements from the same size of the same rock without discontinuities are also shown by solid lines in the figures. It can be seen that large deformations come from discontinuities.

It should be mentioned that the modeling work presented here was done before the modification on MM with a non-linear mechanical model. In this work, we just used $k_n = 6200MN/m$ and $k_s = 4870MN/m$ as the coefficients of contacting springs instead of much stronger penalty springs in order to obtain deformations of discontinuities from

penetrations. However, when weak contacting springs are used, penetrations will get larger and larger if they are not limited. In order to prevent this, the calculation was stopped at the point when the displacements of MP3 got the same level as that from the experiment. Therefore, it can not be said that the test is successfully modeled by MM here although the displacements calculated in case 3 are in good agreement with the test.

We show this example in this paper only because we want to point out the following facts: 1). the deformations from discontinuities may be larger than elastic deformation of the rock itself, 2). the original MM should be modified with the non-linear mechanical model for discontinuities.

For this reason, we are going to make MM modeling of this physical test again by using the modified MM with the non-linear model of discontinuities.

4 CONCLUSIONS

In order to promote Manifold Method in widely applications, we have made the following modifications on the original MM program:

1. Modification on the mesh generating program by adding two functions to it. One function is that generating one piece of regular meshes on one physical blocks so that different dense meshes are available. The other is that sub-meshes can be generated in some important areas for a large physical block. This modification makes MM much flexible for processing stress-concentrated problems.

2. Use a non-linear mechanical model for discontinuities instead of the criteria of no tension and no penetration in contact processing so that the deformation from a discontinuous zone can be modeled by MM.

The kinematic behavior of a block on the slope with a sharp step has been investigated by both the laboratory model tests and MM computations. It has been found that the displacement, the velocity, the jumping distance, height and rotation pattern can be simulated very well by MM. But, it is difficult to reshow the rebound movement by using present program. We should pay attention to this problem in future study.

Model tests for discontinuous rock mass have been made. It has been found that large deformation may come from the discontinuities rather than elastic deformation of rock itself. Although the deformation pattern can be modeled, the real deformation can not be obtained for this case by original MM program. It is expected that this kind of problems may be well modeled by the modified MM with the non-linear mechanical model of discontinuities.

REFERENCES

- Chen, G and Ohnishi, Y. 1999. A Non-Linear Model for Discontinuities in DDA. *Proceedings of ICADD-3*.
- Shi, G. 1991. Manifold Method of Material Analysis. *Transactions of the 9th Army Conference on Applied Mathematics and Computing, Report No. 92-1*.

Discontinuous Deformation Analysis (DDA) – Methodology

AN EFFICIENT ADAPTIVE SKYLINE SOLVER FOR CONTACT DYNAMICS IN DISCRETE BODY SYSTEMS

Chung-Yue Wang ; Ching-Chiang Chuang and Jopan Sheng

Department of Civil Engineering
National Central University
Chungli, Taiwan 32054, ROC

ABSTRACT: In this paper a new simultaneous algebraic equation solver named the "adaptive skyline solver" is proposed for use with the implicit type of numerical simulations of dynamic contact behaviors in flexible discrete multibody systems. In the numerical analysis of dynamic contact problem, the bandwidth of the system coefficient matrix may vary due to contact or separation among bodies during motion. Therefore, neither computation time nor storage space can be effectively managed in conventional direct or iterative solvers and data storage methods. In this paper, the skyline solver method commonly used in finite element theory is modified by combining it with a contact detection technique to develop a new solver for the dynamic contact analysis of discrete body system. Results from numerical examples demonstrate that both the computation time and the storage capacity are much reduced by this new technique compared with a direct solver using the upper triangle storage method.

1 INTRODUCTION

Due to mechanical loading, chemical reactions and thermal treatment during the manufacturing process, or from damage during service, discontinuities in the physical field of an engineering system might exist on different scope levels. Complicated behaviors due to these discontinuities may lead to difficulties in interpretation and analysis. In the past few years, topics concerning such discontinuities in the behavior of jointed rock masses, ice plates or granular materials, the delamination of a layered medium, blasting fragmentation, the damage/fracture progression of a material etc., have been worked on by a number of researchers and engineers.

Some researchers have applied Shi's DDA method to the study of some fundamental problems in solid mechanics (Jing 1993; Ke 1993). Through these studies, it has been found that the DDA method, with its effective contact detection and numerical simulation algorithms, can quantitatively model the dynamic interaction behaviors of deformable bodies. However, in the original DDA formulation (Shi 1988), a constant strain field in each block is assumed which leads to some computational inaccuracy when dealing with problems where blocks have complicated strain fields. Due to this disadvantage, it becomes natural to attach a finite element mesh to the block to give a better deformation description (Shyu 1993, Chang 1994). This concept motivated Shi's development of his newly proposed manifold method (Shi 1991, 1996). From the manifold method theory, one realizes the potential for solving various challenging mechanical problems in an effective and straightforward manner. Some researchers (Shyu 1993; Wang et al. 1998) call the DDA method with a finite element mesh, the "Nodal Based Discontinuous Deformation Analysis

Method”, according to the Manifold method or the Meshless/ Element Free method point of view (Belytschko 1991).

It is well recognized that the main objective for developing the DEM, DDA or any other such method is to simulate nonlinear interaction behaviors in a multibody system. For an implicit time integration scheme, a large, sparse coefficient matrix of the discretized system is usually obtained. For example, the required storage space and the computation time is proportional to NM and NM^2 , respectively, when applying a constant bandwidth solver in a system with N unknowns and a bandwidth M . However, the bandwidth of this system coefficient matrix may vary due to the contact or separation among bodies during motion. Hence, the computation time and storage space can not be effectively utilized in conventional direct or iterative solvers and data storage methods. Therefore, a more efficient storage and solving scheme for simulated dynamic behaviors of a discrete flexible blocky system has been developed and is presented in this paper.

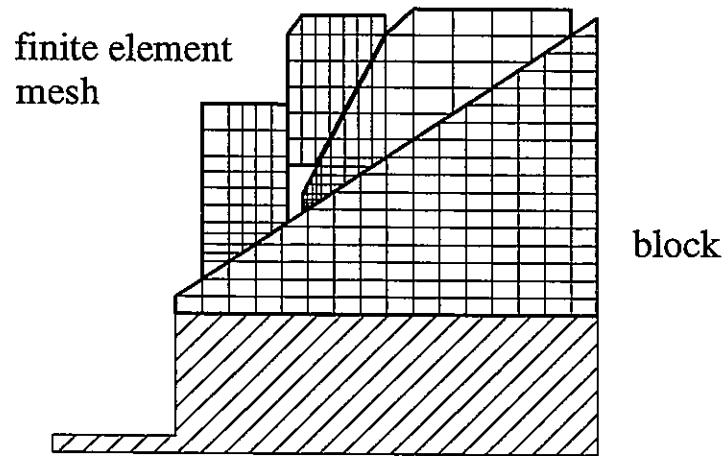


Figure 1. Discrete blocks patched with finite element meshes.

2 NODAL BASED DDA METHOD

In order to enhance the deformation field modeling capability within the blocks, the approximation functions for the displacement field are constructed using the finite element theory. As shown in Fig.1, a finite element mesh is patched to each block in order to construct the global approximation displacement functions. The calculation of virtual work in a discrete system is calculated in an element-by-element manner. For each element, the strain energy, the work due to the external load, and the inertial effect are all evaluated by the FEM constructed displacement functions. Through the use of the time integration theory, the acceleration (inertial) term can be approximated in terms of a time increment and the associated displacement increment, velocity and initial acceleration data. The penalty method is used to handle the in-penetrability condition required for contact analysis. The virtual work due to the contact mechanism is calculated by the deformation of the penalty spring. From the virtual work principle, the deformation, the external load, and the inertia contributed to the coefficient matrix $[K]$ and to the load vector $\{F\}$ of the discrete system

can be derived in the following form (Shyu 1993; Wang et al. 1998).

$$[K]\{d\} = \{F\} \quad (1)$$

3 CONTACT DETECTION BETWEEN BLOCKS

Contact detection is the core step for any motion analysis of a discrete system. As a discrete system consists of finite blocks patched with finite element meshes as shown in Fig. 1, the basic contact detection units can only be identified as vertex-to-edge, and vertex-to-vertex two types (see Fig. 2). In the nodal based DDA method, the vertex is defined by the nodal points located on the boundary of the blocks, while the edge is defined by the boundary between two neighboring nodes. The vertex-to-vertex type contact can be further decomposed into four possible vertex-to-edge type contacts. According to the angles of the four edges (Shi 1988, 1996), the penetration time, and the distance criterion, one can determine which one of the four possible cases is occurred first. Figure 3 shows four possible contact conditions between two vertices of convex polygons. The contact evaluation of the vertex-to-edge type becomes the basis of the multibody contact analysis.

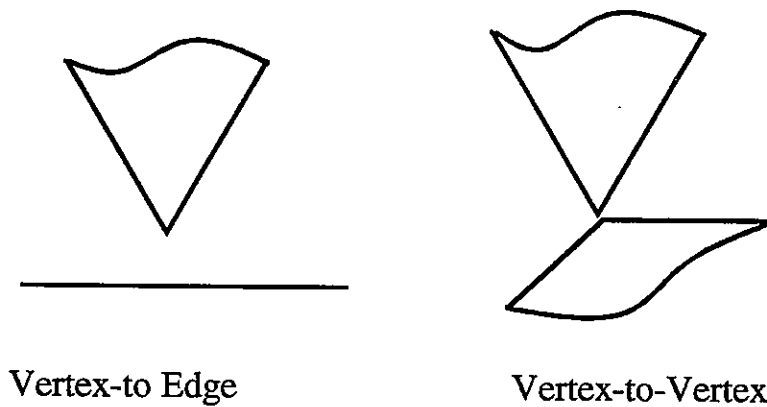


Figure 2. Basic contact detection units for the motion analysis of multibody system.

4 MATRICES FROM NORMAL CONTACT, SHEAR CONTACT AND FRICTIONAL EFFECTS

Once the contact condition has been detected after the first iteration step of a time increment, the penalty springs have to be applied to satisfy the in-penetrability constraint between material points. These penalty springs will provide the resistance force in the system. Since the contact location and types vary during the motion of a discrete system, this leads to the so-called "moving boundary value problems" in solid mechanics. For any vertex-to-edge contact, there are three types of contact effect, namely normal, shear and frictional, have to be considered in the system equations. To maintain the in-penetrability constraint condition during contact, normal and shear penalty springs are introduced into the system at locations where bodies come into contact. Through

virtual work principle, the corresponding normal and shear stiffness matrices of dimensions (6 x 6) and the normal, shear resistance force vectors of dimensions (6 x 1) can be derived.

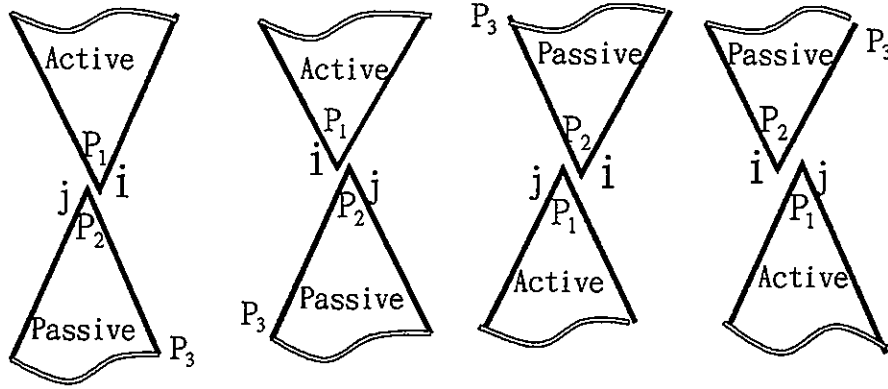


Figure 3. Four possible contact conditions between two vertices.

5 ADAPTIVE SKYLINE SOLVER FOR DYNAMIC CONTACT PROBLEMS

5.1 Algorithm for Solving Equation System with Varying Coefficient Matrix Bandwidth

Many physical problems can be modeled in linear equation system as shown by Eq. (1). The Gaussian elimination method, which can decompose the $[K]$ matrix into a lower triangle matrix, $[L]$ and an upper triangle matrix $[U]$ is often used to solve this type of simultaneous equation. If the $[K]$ matrix is symmetric, the Cholesky method can decompose it into $[K]=[L][U]$ making $[L]^T = [U]$. Then, a solution can be obtained by forward and backward substitution processes. In the Cholesky method, only elements above and on the $[K]$ diagonal are used, while the calculated element data \bar{u}_{ij} can replace the one for the original element k_{ij} during the solution process.

$$\begin{bmatrix} k_{11} & k_{12} & k_{13} & & & & & & & \\ . & k_{22} & k_{23} & k_{24} & k_{25} & & & & & \\ . & . & k_{33} & k_{34} & k_{35} & k_{37} & & & & \\ & . & . & k_{44} & k_{45} & 0 & & & & \\ & . & . & . & k_{55} & k_{56} & k_{57} & k_{58} & k_{510} & \\ & & . & . & k_{66} & k_{67} & k_{68} & 0 & & \\ & & . & . & . & k_{77} & k_{78} & k_{79} & 0 & \\ & & & . & . & . & k_{88} & k_{89} & k_{810} & \\ & & & & . & . & k_{99} & k_{910} & & \\ & & & & . & . & . & k_{1010} & & \end{bmatrix} \quad (2)$$

For the symmetric matrix $[K]$ shown by the Eq. (2), only the elements in the upper half bandwidth of each column, as $k_{11}, k_{12}, k_{22}, k_{13}, k_{23}, k_{33}, k_{24}, k_{34}, k_{44}, k_{25}, k_{35}, k_{45}, k_{55}, k_{56}, k_{66}, k_{37}, 0, k_{57}, k_{67}, k_{77}, k_{58}, k_{68}, k_{78}, k_{88}, k_{79}, k_{89}, k_{99}, k_{510}, 0, 0, k_{810}, k_{910}, k_{1010}$ need to be stored.

5.2 Skyline Method

In order to identify the location of the storage element, position indices $LL(j)$, $j = 1, 2, 3, \dots, N$ are introduced, where N is the total number of columns in the matrix. The value of $LL(j)$ is equal to the value of $LL(j-1)$ plus the half bandwidth from column j . Here, the position index for the first column, $LL(1)$ is set to be one. If the dimension announcement of the stiffness matrix in the subroutine is $A(1, 1)$, then according to the dynamic array storage technique, the correspondence address of element K_{ij} in the array is $K(i, LL(j))$. Therefore, the total number for the required storage space is $LL(N) + N - 1$. Based on this definition, we can recognize that the position indices $LL(1)$ to $LL(10)$ for the matrix shown in Eq. (2) are 1, 2, 4, 6, 9, 10, 14, 17, 19, 24, respectively.

The half bandwidth for each column is defined as the row number of the first nonzero element counted from the top of the column subtracting its row number. Since the global stiffness matrix $[K]$ is obtained from the superimposition of all the augmented element stiffness matrices, the determination of the row number for the first nonzero element is conducted by scanning all the conventional finite elements and special elements used in the system. The smallest global row number for each newly superimposed augmented element stiffness matrix is recorded and will be compared separately with the previously recorded first nonzero row number for columns to which the augmented element stiffness matrix correspond. The smaller row number from each column is saved and waits for the next comparison.

This skyline method (Burnett 1987) can much reduce the storage space leading to the saving of computation time. Thus, it has been adopted and modified for the analyses of the dynamic contact behaviors in multibody systems.

5.3 Adaptive Skyline Solver

For a multibody system patched with finite element meshes, the element stiffness matrices and the sub-matrices due to contact among blocks construct the global stiffness matrix. But, the contents of this global stiffness matrix varies during motion due to the contact or separation of discrete bodies. To solve the linear system of equations with this symmetric, sparse global stiffness matrix, the skyline method introduced above can be effective.

Here, we proposed a new concept which treats the vertex-to-edge unit as a special kind of triangular element, introducing it into the skyline method mentioned above. This special element provides a normal contact stiffness matrix (6×6) and/or a shear contact stiffness matrix (6×6) to the global system, if two degrees of freedom are specified on each finite element node. The exact forms of the normal contact stiffness matrix and the shear contact stiffness matrix can be found in References (Shi, 1988, 1996). When applying the skyline method to the arrangement of storage space and the location of the global stiffness matrix, all these contact elements are scanned over together, with the conventional finite elements patched to blocks. For the vertex-to-vertex type

of contact, four special vertex-to-edge elements are used. Therefore, the storage space required for the corresponding contact stiffness matrices for these four possible vertex-to-vertex cases is spared. Although a little bit is wasted, it is conservative, since one correct vertex-to-edge case is not previously known, unless some evaluation and calculation has been conducted in the analysis

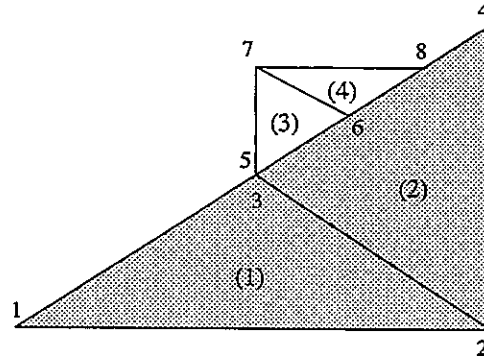


Figure 5. A triangular block slides down on other triangular block.

Table 1. Contact elements formed at one instant during the simulation of the relative sliding between two triangular blocks.

Element No.	Vertex Node	Edge Nodes	Element Nodal No.
5	6	3,4	6,3,4
6	8	3,4	8,3,4
7	3	5,6	3,6,5
8	3	5,7	3,5,7
9	5	1,3	5,1,3
10	5	3,4	5,3,4

In the following section, an example is given to illustrate one way to calculate the half bandwidth, position index, and the row number of the first non zero element, and the required storage space for the system stiffness matrix. As shown in Fig. 5, a triangular block slides down from the top of an inclined surface of another triangular block. Two triangular finite elements are patched onto each block; each node has two degrees of freedom. At the instant shown in Fig. 5, there are two vertex-to edge contact conditions, node 6 to edge $\overline{34}$, node 8 to edge $\overline{34}$ and one vertex-to-vertex contact condition between node 3 and node 5.

Therefore, 6 special contact elements formed at this instant are listed in Table 1. These six special elements together with the original four conventional finite elements, model the dynamic contact behavior at this instant. Table 2 demonstrates the correspondence among elements in a 16×16 full stiffness matrix and these ten finite elements. Each number shown in Table 2 represents the code number of a finite element.

From Table 2, one finds that the row number of the first none zero element in the stiffness matrix of each column is (1, 1, 1, 1, 1, 1, 3, 3, 1, 1, 5, 5, 5, 5, 5, 5), while the associated half

bandwidth of each column is (0, 1, 2, 3, 4, 5, 4, 5, 8, 9, 6, 7, 8, 9, 10, 11), respectively. According to the theory discussed previously, the position index for each column is (1, 2, 4, 7, 11, 16, 10, 25, 33, 42, 48, 55, 63, 72, 82, 93) and the number of the required storage size for applying the skyline method is $93+16-1 = 108$. Using this adaptive skyline method other than the upper triangular storage method when the total degrees of freedom of the system are increased can tremendously reduce the memory size and the computation time.

Table 2. Correspondence among elements in the global matrix and finite elements at one instant of the motion analysis.

	1	2	3	4	5	6	7	8	9	10	11	12	13	14	15	16
1	1,9	1,9	1	1	1,9	1,9			9	9						
2	1,9	1,9	1	1	1,9	1,9			9	9						
3	1	1	1,2	1,2	1,2	1,2	2	2								
4	1	1	1,2	1,2	1,2	1,2	2	2								
5	1,9	1,9	1,2	1,2	1,2,5, 6,7,8, 9,10	1,2,5, 6,7,8, 9,10	2,5 .6, 10	2,5 .6, 10	7,8, 9,10	7,8, 9,10	5,7	5,7	8	8	6	6
6	1,9	1,9	1,2	1,2	1,2,5, 6,7,8, 9,10	1,2,5, 6,7,8, 9,10	2,5 .6, 10	2,5 .6, 10	7,8, 9,10	7,8, 9,10	5,7	5,7	8	8	6	6
7			2	2	2,5,6, 10	2,5,6, 10	2,5 .6, 10	2,5 .6, 10	10	10	5	5			6	6
8			2	2	2,5,6, 10	2,5,6, 10	2,5 .6, 10	2,5 .6, 10	10	10	5	5			6	6
9	9	9			7,8,9, 10	7,8,9, 10	10	10	3,7, 8,9, 10	3,7, 8,9, 10	3,7	3,7	3,8	3,8		
10	9	9			7,8,9, 10	7,8,9, 10	10	10	3,7, 8,9, 10	3,7, 8,9, 10	3,7	3,7	3,8	3,8		
11					5,7	5,7	5	5	3,7	3,7	3,4, 5,7	3,4, 5,7	3,4	3,4	4	4
12					5,7	5,7	5	5	3,7	3,7	3,4, 5,7	3,4, 5,7	3,4	3,4	4	4
13					8	8			3,8	3,8	3,4	3,4	3,4,8	3,4,8	4	4
14					8	8			3,8	3,8	3,4	3,4	3,4,8	3,4,8	4	4
15					6	6	6	6			4	4	4	4	4,6	4,6
16					6	6	6	6			4	4	4	4	4,6	4,6

6 NUMERICAL EXAMPLES

To verify the accuracy and the efficiency of the newly proposed adaptive skyline solver, a dynamic contact problem is simulated. A simulation code has been developed based on the Nodal Based Discontinuous Deformation Method theory, which has such features as: the discretization of blocks by finite element meshes, contact detection among blocks, a collocation time integration scheme and the adaptive skyline solver presented in this paper. As shown in Fig. 6, a 2 m by 2 m triangular block slides down the surface of a 8 m by 8 m triangular block due to the force of gravity. The frictional coefficient between these contact surfaces is zero. To simulate rigid bodies, for both blocks, the Young's modulus is set to $E = 10^9 \text{ Pa}$, the Poisson's ratio is $\nu = 0$ and the density is $\rho = 100 \text{ kg/m}^3$. The parameters for the collocation time integration scheme (Wang et al. 1998) used in the simulation are $\theta = 1$, $\beta = 0.5625$, $\delta = 1$, with a time step size $\Delta t = 10^{-4} \text{ sec}$.

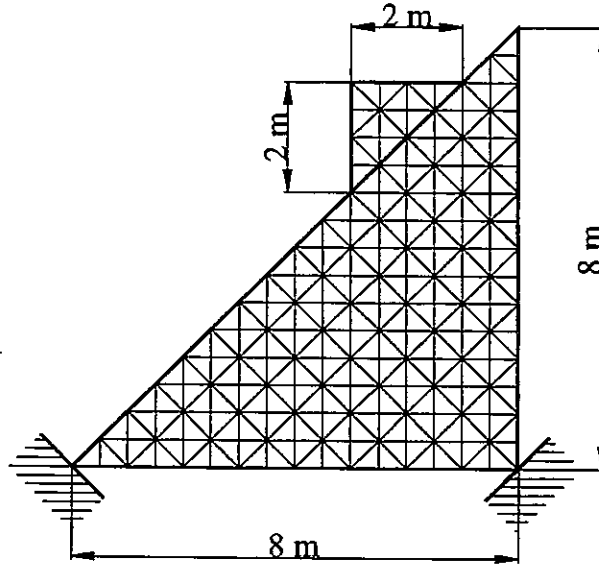


Figure 6. Simulation of a triangular block sliding down another triangular block by the nodal based DDA method with an adaptive skyline solver.

6.1 Accuracy:

According to rigid body dynamics, the sliding distance, d and the velocity, v of an initially resting block when slides down a surface with an incline angle α at time t are

$$d = \frac{1}{2}(g \sin \alpha)t^2 \quad (3)$$

and

$$v = (g \sin \alpha)t \quad (4).$$

From comparisons of the simulation results and the analytical solutions, it was proved that the computation code could accurately model the dynamic contact behaviors of a multibody system.

6.2 Efficiency

To evaluate the influence of the total degrees of freedom in a discretized system on the required storage size and the total computation time, the sliding problem shown in Fig. 6 was studied using the code in a Pentium 200MMX personal computer. In total 15000 time steps were conducted. Table 3 shows the data and performance results for the various cases, patched with different finite element meshes, using both the upper triangle and the adaptive skyline solver schemes. It may be seen that both the computation time and the storage are much reduced and effectively saved by this new adaptive skyline solving technique, compared to the direct solver using the upper triangle storage method, especially when the total number of degrees of freedom are increased.

Table 3. Discretization data for a block system and the associated performance results using different methods.

Block I		Block II		Computation Method, Time and Memory Size			
Number of elements	Number of total nodes	Number of elements	Number of total nodes	Upper Triangle Method		Adaptive Skyline Method	
				Computation Time	Storage Size (8 bytes)	Computation Time	Storage Size (8 bytes)
2	4	2	4	46.19 sec.	136	45.04 sec.	132
4	6	4	6	1 min. 14.81 sec.	300	1 min. 7.67 sec.	248
8	9	8	9	2 min. 18.52 sec.	666	1 min. 16.93 sec.	490
16	15	8	9	3 min. 38.17 sec.	1176	2 min. 48.84 sec.	840
32	25	8	9	7 min. 12.92 sec.	2346	4 min. 32.49 sec.	1226
64	45	8	9	21 min. 6.59 sec.	5886	8 min. 10.65 sec.	2370
128	81	8	9	1 hr. 14 min. 38.4 sec.	16290	16 min. 13.89 sec.	4930
192	117	8	9	3 hr. 3 min. 46.13 sec.	36878	23 min. 20.82 sec.	7290
256	153	16	15	6 hr. 53 min. 20.5 sec.	56616	34 min. 20.04 sec.	12852

7 CONCLUSIONS

For the analysis of dynamic contact problems in a multibody system, the uncertainty and variation of contact locations and conditions in time usually cause some difficulties in the construction of the stiffness matrix and in the solving of the system equations. To overcome these difficulties, a full matrix or upper-triangle type storage method can be used. The obtained system equations can then be solved either by the Gaussian direct elimination method or by iterative methods, such as the SOR and conjugated gradient method.

The direct method is an accurate and stable method, but, the usage of the upper triangle part of the full matrix during its operation leads to an unacceptable storage size and computation time when the total degrees of freedom are increased. The iterative method however is an approximation method, which is fast in solving large-scale problems but its computation time is case dependent and can sometime not reach to the correct solution. Therefore, the iterative solver has constraints in application to multibody dynamics.

In the present paper, the newly proposed adaptive skyline solver combining the conventional skyline method with a contact detection scheme can efficiently and accurately simulate the dynamic contact behaviors of a flexible multibody system.

REFERENCES

- Belytschko, T., Lu, Y. Y. and Gu, L. 1994. Element-free Galerkin methods. *International Journal for Numerical Methods in Engineering* Vol. 37: 229-256.
- Chang, Chiao-Tung 1994. *Nonlinear Dynamic Discontinuous Deformation Analysis with Finite Element Meshed Block System*. Ph. D. Dissertation, University of Calif., Berkeley.
- Jing, L. 1993. Contact formulations by energy minimization in DDA. *Proceedings of the 2nd International Conference on Discrete Element Methods (DEM)*, edited by Williams, J. R., and Mustoe, G. G. W., IESL Publication: 15-26.
- Ke, Te-chih 1993. *Simulated Testing of Two Dimensional Heterogeneous and Discontinuous Rock Masses Using Discontinuous Deformation analysis*. Ph. D. Dissertation, University of Calif., Berkeley, USA.
- Shi, Gen-hau 1988. *Discontinuous Deformation Analysis: A new numerical model for the statics and dynamics of block system*. Ph. D. Dissertation, University of Calif., Berkeley, CA.
- Shi, Gen-hau 1991. Manifold method of material analysis. *Proceedings of the Ninth Army conference on Applied Mathematics and Computing*, June 18-21, Minneapolis, Minnesota, USA.
- Shi, Gen-Hua 1996. Manifold Method. *Proceeding of the first international forum on discontinuous deformation analysis (DDA) and simulations of discontinuous media*, edited by M. Reza Salami and Don Banks, Berkeley California, USA, June 12-14, 1996: 52-204. TSI Press.
- Shyu, Kuokai 1993. *Nodal-based Discontinuous Deformation Analysis*. Ph. D. Dissertation, University of Calif., Berkeley, CA, USA.
- Wang, Chung-Yue, Chuang, Chiang-Chiang and Sheng, Jopan 1998. Nodal Based Discontinuous Deformation Method with Collocation Time Integration Schemes. To be appeared in the *Journal of the Chinese Institute of Civil and Hydraulic Engineering*.

A NON-LINEAR MODEL FOR DISCONTINUITIES IN DDA

Guangqi CHEN and Yuzo OHNISHI

Kyoto University, School of Civil Engineering

Kyoto 606-01, Japan

ABSTRACT: A non-linear model for discontinuities is presented to Discontinuous Deformation Analysis so that the tension, compression and shearing deformations of a discontinuity can be modeled by the method. The formulas for the new model are given, and the computing program is introduced. The determination of new parameters in the new model is also discussed in this paper.

1 INTRODUCTION

Discontinuous Deformation Analysis (DDA) is a very useful numerical method which can be used not only for stress-strain analysis like Finite Element Method (FEM) but also for large deformation modeling such as simulation of rigid body movements. Since it was developed by Shi in 1984, the method has been put into widely practical applications such as tunnel and slope stability analysis, rock fall analysis and other rock mechanical analysis.

DDA uses the displacements of an individual block as unknowns and solves the equilibrium equations in the same manner as that in FEM. One of its advantages is that discontinuities can be easily handled. Penalty method is used for connecting individual blocks into a block system. That is, two springs are set at each contact point in normal and tangential directions of the boundary when two blocks gather together.

In original DDA, criteria of no tension and no penetration are adopted. If the normal spring has tension deformation, it will be removed so that no tension force exists between the two pulled blocks. As a result, the normal spring is set only for compression between two blocks. Since zero penetration is not realizable in the calculation of spring force, a very small value δ_m is allowed in practical computation program.

Mohr-Coulomb's law is used for shearing failure of two coupled blocks. If the shearing force calculated from the tangential spring gets larger than shearing strength τ_m of the discontinuity, the tangential spring will be removed, and then, friction force takes the place of the spring. τ_m is calculated by the following formula

$$\tau_m = C + f_n \tan \theta \quad (1)$$

where C and θ are cohesion and friction angle of the discontinuity and f_n is the compressing force from the normal spring.

With this way, DDA is successfully used to simulate the coupling state, separating and sliding movements between contact blocks.

However, original DDA is only suitable for ideal discontinuities, i.e., for the case that

blocks are completely divided by discontinuous lines. In practice, a discontinuity such as a joint or a fault is not a dimensionless line but a zone as shown in Figure 1(a).

In general, the rigidity of a discontinuous zone is much weaker than the surrounding blocks, large deformation may happen in the zone when it is compressed or sheared as shown in Figure 1(b) and (c). On the other hand, when a discontinuous zone is pulled apart, it still has tension resistance before completely being broken although the resistance may be small.

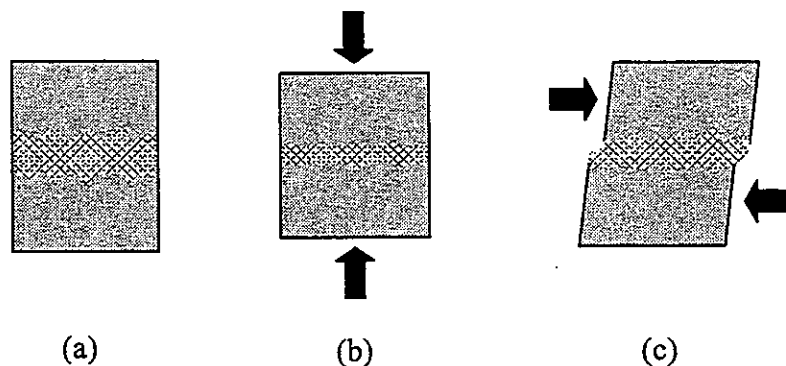


Figure 1: A discontinuous zone and its deformations.

In order to model the deformation of a discontinuous zone, we present a new non-linear mechanical model for discontinuities. We also show how to code the model in computation program and discuss how to choose the parameters in this paper.

2 THE NON-LINEAR MODEL FOR DISCONTINUITIES

We present a non-linear mechanical model for practical discontinuities in order to simulate deformations of a discontinuous zone. Figure 2(a) is for the normal direction corresponding to compression and tension and Figure 2(b) is for the tangential direction corresponding to the case of shearing in the discontinuity.

For the case of compression, the behavior of a discontinuous zone can be divided into three stages.

It is of elastic behavior on the first stage, which is represented by OB in Figure 2(a).

Once the strain of the discontinuous zone gets larger than the allowed maximum elastic strain ϵ_m , the zone becomes failure. Then, it enters the second plasticity stage shown by BC in the figure.

It should be noted that the second stage is just an instantaneous one. The zone gets hardening very quickly and ϵ_m is remained as the permanent deformation. Then, it enters the third stage shown by CD immediately after yielding, and it is of elastic behavior again

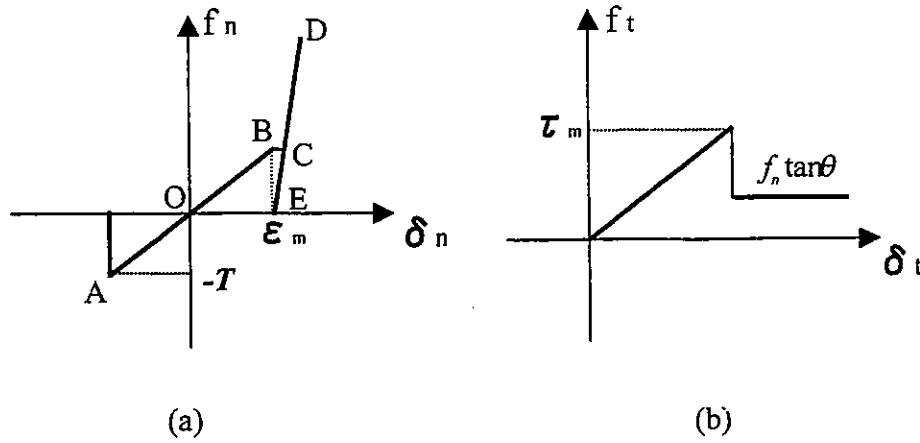


Figure 2: The new non-linear mechanical model for discontinuities

but with very strong rigidity.

We can make above assumption because we believe that the soft zone of a discontinuity may be vanished by the large compressing deformation, and blocks are contacted each other by their essential parts. Therefore, very little deformation will be produced from the discontinuity, and the zone is small enough to be treated as a dimensionless line.

It should be noted that the third stage just corresponds to the model of original DDA and deformation will not recover to O but to E even if compressing force becomes zero in the discontinuity.

In the case of tension, at first, the discontinuous zone is of elastic behavior shown by OA in the figure. Once tension force gets larger than the tension strength T of the zone, the discontinuous zone will be broken completely. Then, the two contacted blocks can be moved apart freely and there should be no longer normal contact force acting on the discontinuity. After broken, criterion of no tension is adopted just the same as original DDA.

In the case of shearing, the new model uses shearing rigidity of the discontinuous zone instead of penalty spring used in original DDA. Therefore, shearing deformation from the zone can be simulated before shearing failure.

Also, when the shearing force calculated from the tangential spring gets larger than shearing strength τ_m of the discontinuity, the tangential spring will be removed, and then, friction force takes the place of the spring.

The new non-linear mechanical model can be also expressed by the following formulas

$$f_n = \begin{cases} k_n \delta_n & -\frac{T}{k_n} \leq \delta_n \leq \epsilon_m \\ P_n(\delta_n - \epsilon_m) & \delta_n > \epsilon_m \\ 0 & \delta_n < -\frac{T}{k_n} \end{cases} \quad (2)$$

and

$$f_t = \begin{cases} k_t \delta_t & |\delta_n| \leq \frac{T_m}{k_t} \cap -\frac{T}{k_n} \leq \delta_n \leq \varepsilon_m \\ f_n \tan \theta & |\delta_n| > \frac{T_m}{k_t} \cap f_n > 0 \\ 0 & |\delta_n| > \frac{T_m}{k_t} \cap f_n \leq 0 \end{cases}, \quad (3)$$

where

- f_n, f_t = stresses in the discontinuity,
- δ_n, δ_t = strains in the discontinuity,
- k_n, k_t = rigidity coefficients of the discontinuity,
- n, t = referring to normal and shear components,
- P_n = penalty spring rigidity coefficient,
- ε_m = allowed maximum deformation from the discontinuity,
- T = tension strength of the discontinuity,
- θ = friction angle of the discontinuity,
- τ_m = shear strength of the discontinuity.

3 DISCUSSION

3.1 New Model in Computation Program

In practical programming, a discontinuous zone is not treated as an individual block since its real shape is hardly determined. The deformations of a discontinuity are obtained from the deformations of contacting springs. Thus, tension and penetration are allowed before failure of the discontinuity.

For the cases of tension and shearing, it is not necessary to add new code to the original program. At first, the rigidity coefficients k_n and k_t of a discontinuity are used for the rigidities of contacting springs. Penalty coefficients P_n and P_t will take the place of k_n and k_t after failure.

The modifications are needed for the case of compression. At first, the rigidity coefficients k_n a discontinuity is used for the rigidity of normal contacting spring. And penetration is allowed for modeling the large compressing deformation of a discontinuous zone. After yielding, the plastic deformation is obtained by modifying the boundaries of two penetrated blocks. By changing the strength of the normal contact spring from k_n to P_n , the third stage can be modeled.

The approach is shown in Figure 3 and can be described as follows.

1. The middle line of a discontinuous zone is used as the boundary of the two contacting blocks as shown in Figure 3(a).

2. At first, the rigidity coefficients k_n and k_t are used instead of penalty springs P_n and P_t in the original DDA. Tension and penetration are allowed and taken as the deformation of the discontinuity. For example, Figure 3(b) shows the compressing deformation of the discontinuity obtained from the penetration.

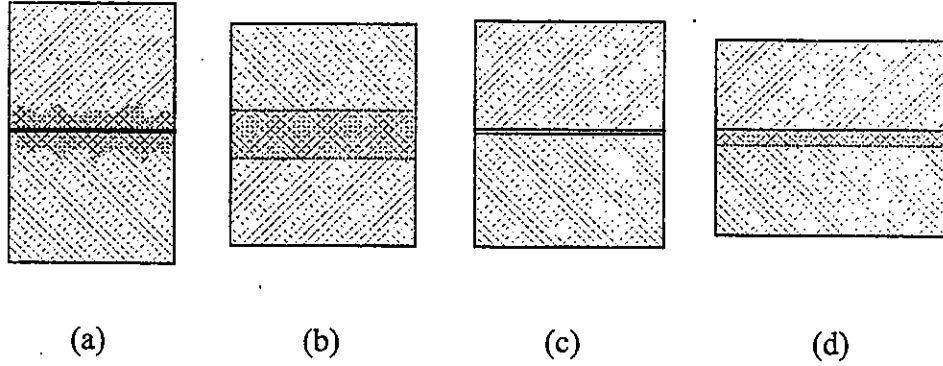


Figure 3: Modeling deformation of a discontinuous zone.

3. In the case of tension, once tension force from the normal spring gets larger than the tension strength T of the discontinuous zone, the normal spring is removed and T is set to zero. Then, no tension is allowed and the same approach in the original DDA is used.

4. In the case of compression, once the penetration gets larger than δ_m , the contacting vertices are modified so that each edge moves backward $\delta_m/2$ as shown in Figure 3(c) for obtaining permanent plastic deformation δ_m . The formulas for the modification of contact vertices will be given in the next sub-section.

5). After the modification of contacted edges, penalty P_n is used instead of k_n and δ_m is set as zero so that from now on no penetration is allowed and the same approach in the original DDA can be used.

6). For tangential contact spring, the real rigidity of a discontinuous zone k_t is used instead of tangential penalty P_t so that large shearing deformation may be obtained from the strain of the tangential spring. Once the shearing force $k_t \delta_t$ gets larger than the shearing strength τ_m , the tangential spring is removed and not used from now on. Friction force takes the place of the spring.

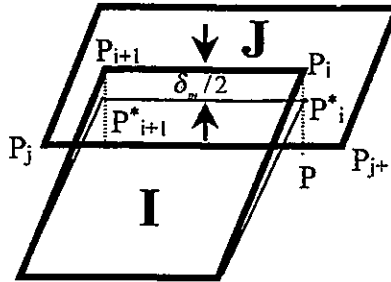


Figure 4: Modification of the edge for obtaining permanent plastic deformation.

3.2 Modification of Contacting Vertices

Supposing that the penetration of block I and block J gets larger than δ_m between edge $P_i P_{i+1}$ and edge $P_j P_{j+1}$ (Fig. 4), two edges should be modified for obtaining permanent plastic deformation. The distance from edge $P_i P_{i+1}$ to its new position $P_i^* P_{i+1}^*$ is $\delta_m/2$.

It should be noted that although each new edge is moved $\delta_m/2$ from its position, there should be no change on the tangential distance between the contacted points because we do not want that the modification affects the length of shearing spring.

We give the formula for modifying P_i as an example. The vertex P_i should be moved to P_i^* by $\delta_m/2$ along the line $P_i P$, where P is the projective point of P_i in the edge $P_j P_{j+1}$, and its coordinates (x_p, y_p) can be calculated by the following formulas

$$\begin{cases} x_p = x_j + k_p(x_{j+1} - x_j) \\ y_p = y_j + k_p(y_{j+1} - y_j) \end{cases} \quad (4)$$

where

$$k_p = \frac{\overrightarrow{P_j P_i} \cdot \overrightarrow{P_j P_{j+1}}}{|\overrightarrow{P_j P_{j+1}}|^2} \quad (5)$$

By using the coordinates of P , we can obtain the coordinates (x_i^*, y_i^*) of P_i^* as follows

$$\begin{cases} x_i^* = x_i + k(x_p - x_i) \\ y_i^* = y_i + k(y_p - y_i) \end{cases} \quad (6)$$

where

$$k = \frac{\delta_m}{2|\overrightarrow{P_i P}|} \quad (7)$$

3.3 Parameters

In the original DDA, the strengths of penalty springs are initially taken as follows

$$\begin{cases} P_n = 500E_{max} \\ P_t = 0.4P_n \end{cases} \quad (8)$$

where E_{max} is the maximum Young's modulus among all the material blocks. And then, they will be adjusted after a step calculation as follows

$$P_n = \max\{r_1, r_2, 1/3\}P_n \quad (9)$$

where

$$r_1 = \frac{t_m}{2d_m} \quad (10)$$

$$r_2 = \frac{p_m}{p_a} \quad (11)$$

t_m and p_m are the maximum tension and maximum penetration among all the contacts, d_m is the allowed maximum displacement among all the blocks, and p_c is the allowed maximum penetration among all the contacts.

P_n and P_t always change from step to step for the following two purposes: 1) their values get as small as possible; 2) no penetration exceeds the allowed maximum penetration value. As a result, the deformation from a discontinuity is unknown and also changed from step to step.

Therefore, it is a noticeable problem that how to consider the deformations from discontinuities in the use of original DDA.

In the use of new model, three more parameters k_n , k_t and δ_m are needed. They can be determined by experiment. Especially, k_n and k_t can be estimated from Young's modulus E and Poisson's ratio ν of a discontinuous zone as follows

$$\begin{cases} k_n = \frac{l}{2}E \\ k_t = \frac{l}{2}G \end{cases} \quad (12)$$

where l is the length between two adjacent contacting point and G is shearing strength

$$G = \frac{E}{2(1 + \nu)} \quad (13)$$

It should be noted that the tension strength T should be also taken into account in the determination of k_n . This is because that the maximum tension may gets too large before tension broken if k_n is not large enough corresponding to the tension strength T .

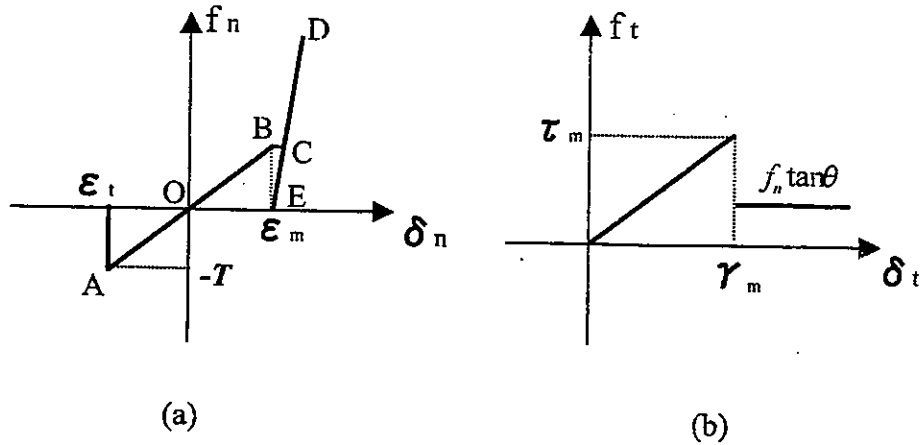


Figure 5: Allowed maximum tension and maximum shearing strains.

Therefore, it is better to designate an allowed maximum tension $|\epsilon_t|$ so that the tension broken happens within the allowed tension range (Fig 5(a)). It is obvious that there is the following relationship

$$k_n |\epsilon_t| \geq T \quad (14)$$

In our program, if k_n calculated from (12) can not make (14) true, it will be modified by the value of $T/|\varepsilon_t|$ automatically.

The shearing strength τ_m should be also taken into account in the determination of k_t . In order to prevent too large shearing deformation happens, it is better to designate an allowed maximum shearing dislocation γ_m for the control(Fig 5(b)). It is obvious that there is the following relationship

$$k_t \gamma_m \geq \tau_m \quad (15)$$

In our program, if k_t calculated from (12) can not make (15) true, it will modified by the value of τ_m/γ_m automatically.

4 CONCLUSION

Original DDA is only suitable for ideal discontinuities, i.e., for the case that blocks are completely divided by discontinuous lines. In practice, a discontinuity such as a joint or a fault is not a dimensionless line but a zone. Large deformation may come from discontinuities.

For this reason, we have presented a non-linear model for discontinuities. The tension, compression and shearing deformations of a discontinuity can be obtained from contacting spring deformations.

The formulas for the new model have been given, and how to code the model in computing program is introduced. The determination of new parameters in the new model is also discussed in this paper.

References

- Shi, G. 1984. Modeling dynamic rock failure by Discontinuous Deformation Analysis with simplex integrations. *Proceedings of the 1st North American Rock Mechanics Symposium*. 591-598.
- Shi, G. 1995. Simplex integration for Manifold Method and Discontinuous Deformation Analysis. *Proceedings of Working Forum on the Manifold Method of Material Analysis*. 129-164.

A Gravity Turn-On Routine for DDA

Mary M. MacLaughlin

Montana Tech of the University of Montana, Department of Geological Engineering
Butte MT 59701, USA

Nicholas Sitar

University of California at Berkeley, Department of Civil and Environmental Engineering
Berkeley CA 94720, USA

ABSTRACT: Discontinuous deformation analysis, DDA, is a numerical method developed to model the behavior of discontinuous media. It is a fully dynamic method that uses inertia forces to determine the motion of a system of blocks. The inertia forces are updated after each time step, and are dependent on the block displacements in the previous step. Consequently, sudden loading of the block system at the beginning of an analysis, whether by gravity or any other applied load, produces unwanted artificial accelerations and displacements of the blocks that propagate throughout the first few critical time steps of the analysis. In order to minimize this problem, an approach is proposed that involves conducting a static "gravity turn-on" phase prior to the dynamic analysis. Additionally, two extra iterations are conducted within each time step in order to guarantee accurate determination of the contact forces between the blocks. Although this does involve some additional computational effort, the proposed approach is effective. As an example, the simple case of a block on an inclined plane is investigated, and the DDA analyses show definitively that the results produced by the enhanced gravity turn-on routine are more accurate than those calculated without the enhanced routine.

1 INTRODUCTION

1.1 Discontinuous Deformation Analysis

Discontinuous deformation analysis, DDA, is a numerical method developed to model the behavior of discontinuous media (Shi, 1988, 1993). DDA models a discontinuous material as a system of individual deformable blocks, which move independently and interact without penetrating one another. Its formulation is based on a dynamic equilibrium and it considers the kinematics of individual blocks as well as friction along the block interfaces. The displacements and deformations of the blocks are the result of the accumulation of a number of small increments, corresponding to small time steps. The transient formulation of the problem, which is based on minimization of potential energy, makes it possible to investigate the progression of block movements with time. A complete description of the formulation of the equations can be found in Shi and Goodman (1984, 1985) and Shi (1988, 1990, 1993).

The formulation is both transient and fully dynamic. Large displacements are the result of accumulation of displacements over a number of small time steps. The kinematical constraints of the system of blocks are imposed using the penalty method, described as follows. Contact detection is performed in order to determine which block vertices are in contact with edges and vertices of other blocks. Numerical penalties analogous to stiff springs are applied at the contacts to prevent interpenetration of the blocks. Tension or penetration at the contacts results in expansion or contraction of these "springs," which adds energy to the block system; the minimum energy solution is one with no tension or penetration. Technically, however, the forces on each block are in equilibrium, so the energy of the contact force between the blocks is balanced by the penetration energy. When the system converges to an equilibrium state, there are very small penetrations at each contact. The contact forces can be determined from the penetration values. Solution of the system of equations is an iterative procedure in which contact springs are repeatedly added and subtracted until each of the contacts converges to a constant state.

1.2 The "Gravity Turn-On" Problem

One typical problem encountered when performing dynamic analysis on block systems with realistic material parameters is commonly referred to as the "gravity turn-on" problem (Desai and Abel, 1972). There are several issues involved with this problem. First, the geometry of the rock mass must be modeled in such a way that the in situ stress state is representative of the actual field conditions, or the displacements will not be correct. The classic example of this is excavation of an open pit. In reality, removal of the overburden will result in upward displacement of the floor of the pit. However, if the post-excavation geometry is modeled without regard to the initial stress conditions, the floor of the pit will displace downward as the material deforms elastically when gravity load is introduced. This issue has been identified and widely addressed with regard to both analytical (Goodman and Brown, 1963) and finite element methods (Clough and Woodward, 1967, Coates, 1970, Dunlop et al. 1970, Pariseau et al. 1970). Other researchers are currently devising methods to implement into DDA which correctly model the sequence of excavation or construction of rock mass geometries to match in situ stress conditions.

Another issue exists in dynamic analyses. The sudden turn-on of gravity at the beginning of the first time step produces displacements due to elastic deformation of the blocks and "seating" of the contacts. Although these displacements are very small, they result in propagation of initial block velocities and accelerations that should be dissipated prior to analysis.

DDA is a fully dynamic method that uses inertia forces to model the motion of the blocks. For two-dimensional DDA analysis and assuming constant velocity and acceleration within a time step, the x- and y-components of the force of inertia per unit area of a block are (Shi, 1993):

$$\begin{bmatrix} i_x \\ i_y \end{bmatrix} = -M \cdot \begin{bmatrix} \partial^2 u(t)/\partial t^2 \\ \partial^2 v(t)/\partial t^2 \end{bmatrix} = -M \cdot \left(\frac{2}{\Delta t^2} \cdot \begin{bmatrix} u \\ v \end{bmatrix} - \frac{2}{\Delta t} \cdot \begin{bmatrix} \partial u/\partial t \\ \partial v/\partial t \end{bmatrix} \right) \quad (1)$$

where M is the mass per unit area, t represents time, and u and v are the x- and y-components of the displacement vector. (See the Appendix for the derivation of this equation.) Inertia forces are used for both dynamic and static analyses; the difference is that the initial velocities are set to zero for each time step during the static analysis. For the dynamic analysis, the velocities are updated after each time step, according to the following scheme:

$$\begin{aligned}
\begin{bmatrix} \partial u / \partial t \\ \partial v / \partial t \end{bmatrix}_{new} &= \begin{bmatrix} \partial u / \partial t \\ \partial v / \partial t \end{bmatrix}_{old} + \begin{bmatrix} \partial^2 u(t) / \partial t^2 \\ \partial^2 v(t) / \partial t^2 \end{bmatrix} \Delta t \\
&= \begin{bmatrix} \partial u / \partial t \\ \partial v / \partial t \end{bmatrix}_{old} + \left(\frac{2}{\Delta t^2} \cdot \begin{bmatrix} u \\ v \end{bmatrix} - \frac{2}{\Delta t} \cdot \begin{bmatrix} \partial u / \partial t \\ \partial v / \partial t \end{bmatrix}_{old} \right) \Delta t \\
&= \frac{2}{\Delta t} \cdot \begin{bmatrix} u \\ v \end{bmatrix} - \begin{bmatrix} \partial u / \partial t \\ \partial v / \partial t \end{bmatrix}_{old}
\end{aligned} \tag{2}$$

Consequently, for dynamic analysis, any displacement at all, regardless of cause and/or magnitude, will result in velocity terms, which in turn create inertia forces that propagate throughout the analysis. (Technically, the displacements may be caused by initial stresses or any type of applied loads, so the term "gravity turn-on" may not be entirely appropriate.)

2 PROPOSED SOLUTION

In order to minimize this effect, an optional routine has been implemented in DDA which consists of a gravity turn-on phase prior to the first time step. A pseudo-static analysis is conducted, in which the velocities are reset to zero at the beginning of each step, and artificially high joint strength parameters are used to inhibit motion of the blocks aside from that due to development of internal strain and small penetrations at the contacts. The gravity turn-on stage continues until the normal and shear contact forces and the block displacements and strains have converged to a specified tolerance. After the gravity turn-on phase is complete, the geometry of the system is slightly different than originally specified. In most situations this deformed geometry is sufficiently close to the initial state as to be of no consequence. However, analysis of a highly deformable system may require development of a more sophisticated approach.

Since the completion of the gravity turn-on phase is dependent on the values of the contact forces, it is of utmost importance that the force calculations be as accurate as possible. DDA's open/close iteration convergence criteria guarantee that the state of the contacts has converged to the point where none of the contacts have changed from open to closed (or closed to open) during the current iteration, but does not address any changes between closed and sliding states. Although these changes are addressed by adding/subtracting shear contact springs in subsequent time steps, the shear forces calculated during the current step may not be accurate. Yeung (1991) proposed that for any time step during which the contact forces need to be explicitly calculated, two additional iterations be conducted after open/close convergence in order to ensure that the closed and sliding contacts are modeled correctly. Alternative contact force convergence approaches were investigated, but Yeung's proved to be the most efficient. A similar routine has been implemented as part of the proposed gravity turn-on scheme; it requires the completion of two extra iterations after open/close convergence, during every time step. Although the extra iterations do require more CPU time, the improved accuracy is worth the additional effort, as demonstrated in the next section.

3 EXAMPLE: BLOCK ON AN INCLINE

The importance of using the gravity turn-on routine may be illustrated through analysis of the simple problem of a rectangular block on an incline as depicted in Figure 1. This problem was examined quite extensively by Yeung (1991). DDA does not directly model edge/edge contacts between blocks. Rather, an edge/edge contact is modeled as two point contacts where the block vertices intersect the edge. According to this two-point model for the block on the incline, there are two slightly different analytical solutions for the normal and shear contact forces at the vertices, depending on the relative values of the friction angle ϕ and the slope angle α .

When $\phi < \alpha$:

$$\begin{aligned} N_L &= W \cos \alpha \left(\frac{1}{2} + \frac{h}{2b} \tan \phi \right) \\ N_U &= W \cos \alpha \left(\frac{1}{2} - \frac{h}{2b} \tan \phi \right) \\ S_L &= N_L \tan \phi \\ S_U &= N_U \tan \phi \end{aligned} \quad (3)$$

When $\phi \geq \alpha$:

$$\begin{aligned} N_L &= W \cos \alpha \left(\frac{1}{2} + \frac{h}{2b} \tan \alpha \right) \\ N_U &= W \cos \alpha \left(\frac{1}{2} - \frac{h}{2b} \tan \alpha \right) \\ S_L &= N_L \tan \alpha \\ S_U &= N_U \tan \alpha \end{aligned} \quad (4)$$

where (N_L, S_L) and (N_U, S_U) are the normal and shear forces at the lower and upper contact points, and b , h , and W and the base, height, and weight of the block. The derivation may be found in Yeung (1991).

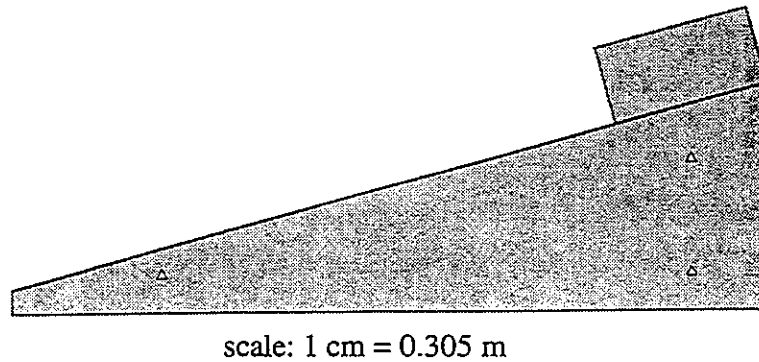


Figure 1. Geometry of example problem involving a single block on an inclined plane. The base and height of the block are 0.631 m and 0.315 m; the width in the third dimension is 0.305 m.

A comparison of the analytical solution and the DDA results is shown in Figures 2 and 3. Figure 2 displays the results computed with and without the contact force routine, and Figure 3 displays the results with the combined contact force and gravity turn-on routines. In each figure, part (a) shows the results for the situation with $\phi < \alpha$, and part (b) corresponds to the case with $\phi \geq \alpha$. The specific data considered in the two examples, as well as the analytical solutions for the contact forces, are listed in Table 1.

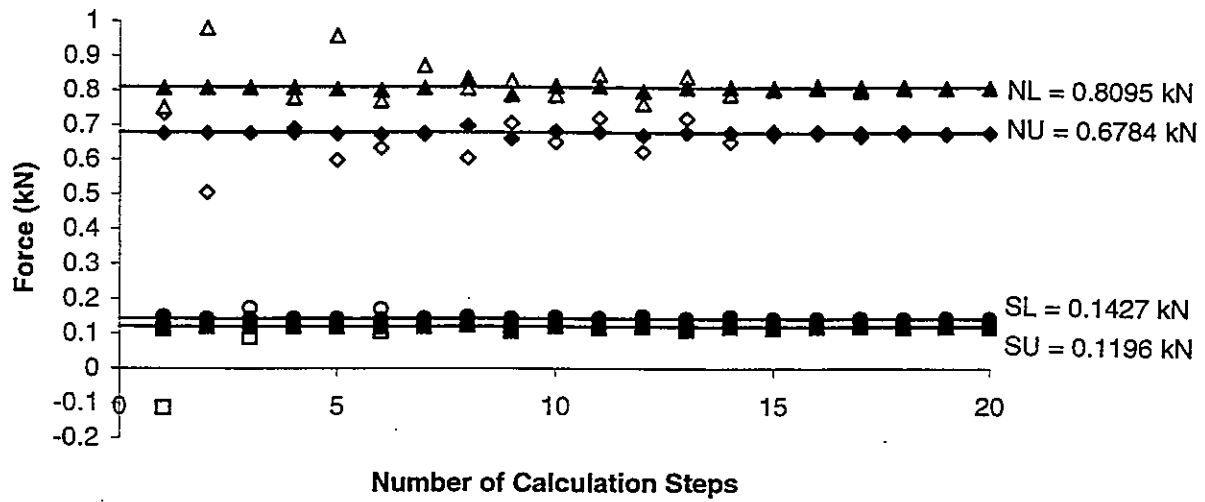
Figure 2 shows that the DDA solution with the improved contact force routine (solid symbols) matches the analytical solution (solid line) much better than without it (open symbols). For the case with $\phi < \alpha$, the normal forces continue to fluctuate by as much as 10% after more than ten calculation steps. This compares well with the results of Yeung (1991). He conducted dynamic analysis of several cases with $\phi < \alpha$ and found that the majority of contact forces calculated using DDA were in the 15-25% error range after 100 steps of 0.01s (although with 1000 steps of 0.001s the maximum error was less than 6%). With the improved contact force routine proposed in this paper, the error is reduced to 5% or less, beginning with the very first step, and has reduced to 1% or less after ten steps. Overall, the contact force calculations during the first ten steps or so are basically an order of magnitude better when the enhanced contact force calculation routine is used. For the case with $\phi \geq \alpha$, the improved routine allows the shear forces to monotonically converge to within 10% of the analytical solution; without it the shear forces display large oscillations.

The results shown in Figure 3 indicate that the gravity turn-on phase took 17 calculation steps to reach the desired convergence tolerance level (1% change in normal and shear forces, as well as block displacements and strains, between successive time steps). The plots for both cases also show that the contact forces, both normal and shear, match the analytical solution almost exactly (within 0.5%), from the first calculation step of the analysis phase forward. The exception is the shear force determination for the case with $\phi \geq \alpha$; the shear force at the upper contact calculated using DDA is slightly higher than the analytical solution, and at the lower contact is slightly lower. The reasons for this are discussed in the following section. The plots also show that when $\phi < \alpha$, the forces are different during the gravity turn-on phase because of the artificially high strength parameters used to prevent motion. This problem may be eliminated by using excessively high cohesion only, rather than excessively high values for both cohesion and friction angle.

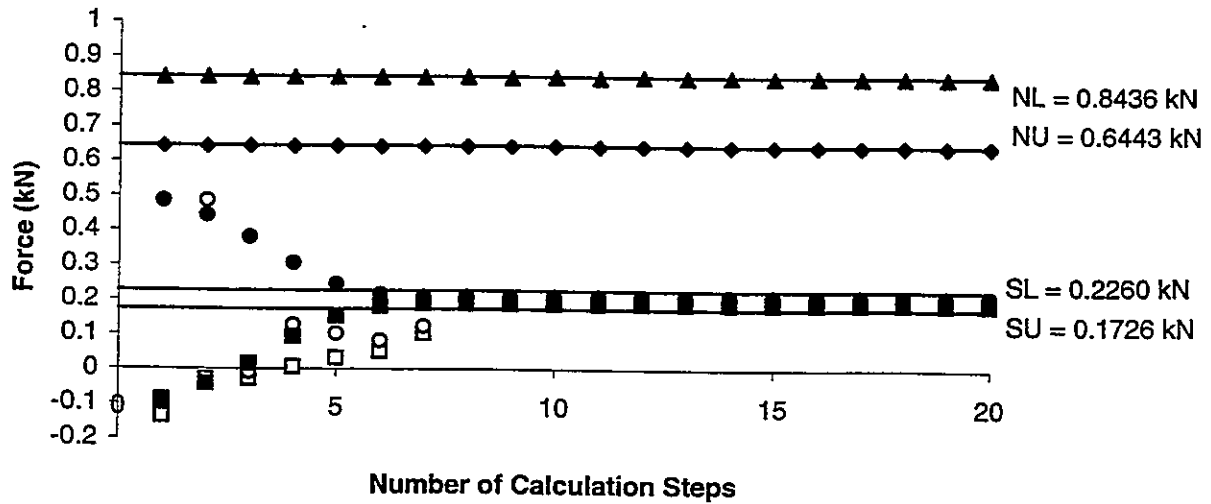
The figures indicate that the gravity turn-on routine produces results that are slightly better than those using the contact force routine alone, and significantly more accurate than without either one. For these simple validation problems, the major gain in accuracy corresponds to the first few time steps; however, this first time step is particularly critical, since correct modeling of the shear forces at the beginning of the analysis is absolutely essential for almost any type of problem.

Table 1. Analytical solution for the normal (N_L and N_U) and shear (S_L and S_U) forces at the lower and upper vertices of a block on an incline. The angle of the incline is α and the friction angle between the block and the incline is ϕ . The weight of the block in both cases is 1.54 kN.

Case	α	ϕ	N_L (kN)	S_L (kN)	N_U (kN)	S_U (kN)
1	15°	10°	0.8095	0.1427	0.6784	0.1196
2	15°	30°	0.8436	0.2260	0.6443	0.1726

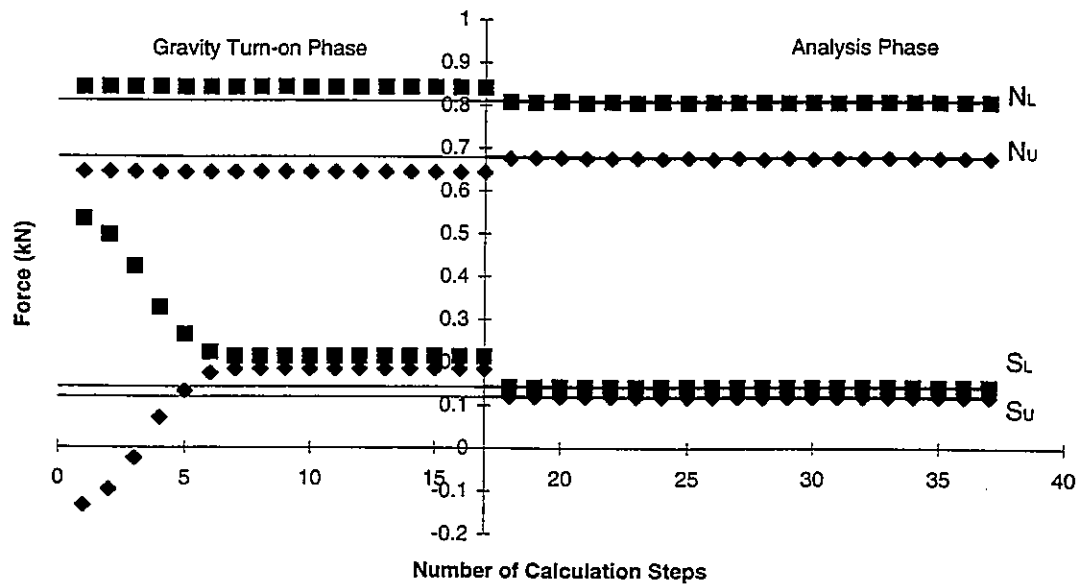


(a)

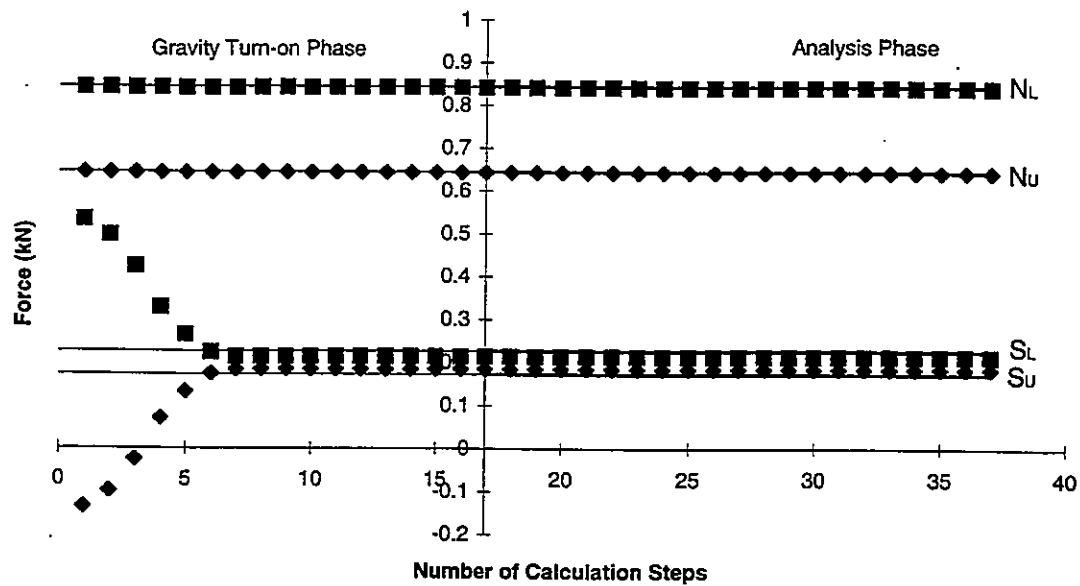


(b)

Figure 2. Comparison of analytical solution and DDA results, for calculation of contact forces at the vertices of a block on an incline with slope $\alpha = 15^\circ$. The solid lines are the analytical solution; the open symbols correspond to the data from the original DDA program, and the solid symbols represent data from the enhanced version with the improved contact force routine. (a) Friction angle $\phi = 10^\circ$. (b) Friction angle $\phi = 30^\circ$.



(a)



(b)

Figure 3. Comparison of analytical solution and DDA results, for calculation of contact forces at the vertices of a block on an incline with slope $\alpha = 15^\circ$, using the enhanced version with the combined contact force and gravity turn-on routines. (a) Friction angle $\phi = 10^\circ$. (b) Friction angle $\phi = 30^\circ$.

4 DISCUSSION

The proposed gravity turn-on approach follows parallel approaches used in finite element (Yu and Coates, 1979), finite difference (Coetzee et al. 1995), and discrete element applications (Itasca Consulting Group, Inc., 1996), but it is by no means perfect. As discussed in the previous section, the contact forces corresponding to the artificially high joint strength used to inhibit motion are not exactly the same as those corresponding to the actual strength values. Therefore, when the gravity turn-on phase is complete and the strength is lowered to the actual value to begin the analysis phase, some readjustments will occur as the system reaches equilibrium under the new conditions, again producing unwanted displacements. However, the magnitude of these displacements is now much smaller and the gravity turn-on effect, while not totally eliminated, is significantly reduced.

Another minor imperfection was mentioned in Section 2. After the gravity turn-on phase is complete, the geometry is slightly different than originally specified. Although in most situations this deformed geometry is sufficiently close to the initial state as to be of no consequence, a more sophisticated approach may be required for analysis of highly deformable systems, for example, an impact problem with one block entirely separated from the main rock mass. The gravity turn-on routine proposed in this paper would fail because of the displacement tolerance criterion. A simple solution would be to develop a system that would allow the user to choose which criteria are to be satisfied during the gravity turn-on phase of any particular problem.

During the gravity turn-on phase, the normal forces at the contacts converge very quickly. However, the enforcement of the additional criteria of convergence of shear forces and block displacements and strains has ramifications that are not at all obvious. As discussed previously, DDA models an edge/edge contact as two vertex/edge contacts located at the block vertices. Therefore, any load transferred between the blocks is actually modeled as a point load rather than a distributed load. The shear forces initially correspond to the individual normal forces (i.e., $N \tan \phi + c$), but with subsequent iterations to reach shear and displacement convergence under conditions where motion does not take place, the shear forces readjust to reach equal values, with the sum of the two remaining constant. In the example discussed in the previous section with $\phi \geq \alpha$, this caused the shear force at the upper contact as calculated using DDA with the enhanced gravity turn-on routine to be 7% higher than the analytical solution, and the shear force at the lower contact to be 6% lower. Several of the characteristics of the DDA method combine to produce this result.

First, DDA uses the "penalty method" to prevent interpenetration of the blocks. The normal force N at a contact is equal to the product of the penetration distance and the penetration penalty stiffness. The shear force S is equal to the product of shear penalty stiffness and the component of the relative vertex/edge displacement parallel to the reference line. If the shear force $S < N \tan \phi + c$ (where ϕ and c are the friction angle and cohesion of the material), the contact is "closed" or "locked" because the resisting shear force according to the Mohr-Coulomb model of joint strength will balance the shear force. Although technically there should be no displacement of a locked contact, the penalty method requires a slight "compression" of the shear contact penalty "spring" to balance the shear force, which results in a small displacement of the vertex. The manifestation of this is numerical "creep" of the blocks, a small but finite downslope movement with a constant value that is directly proportional to the magnitude of the shear penalty stiffness.

Second, DDA blocks are "simply deformable," which means that the strain components are constant everywhere within each block. Therefore, different shear displacements at adjacent vertices due to "compression" of the shear penetration "springs" cannot be accommodated within the block and iteration will proceed until the shear displacements reach equal values. Thus, enforcing shear and displacement convergence results in shear forces at the contacts that do not necessarily correspond to the normal forces. However, since the two point load model is itself just an approximation to a distributed load, it is not clear representation which is more accurate. Preliminary tests indicate that the benefits of enforcing the shear and displacement criteria outweigh the disadvantages.

5 CONCLUSIONS

"Gravity turn-on," or sudden loading of a block system at the beginning of a dynamic DDA analysis leads to propagation of artificial block accelerations and displacements throughout the system. These artificial accelerations should be dissipated prior to the onset of the actual analysis phase. The proposed approach to minimizing this problem is effective, although it does involve some additional computational effort. The results of the analysis of the simple example of a block on an inclined plane show that the DDA analysis with the enhanced gravity turn-on routine is more accurate, particularly during the first several time steps, the most critical part of the analysis. However, the benefit of increased accuracy should be weighed against the disadvantage of increased computational effort. Two extra iterations are required during each time step to guarantee accuracy of the contact force calculations, and a gravity turn-on phase is required to dissipate the transient accelerations prior to analysis. The number of blocks and the specified tolerance will directly influence the computation time. Further analysis is required in order to fine-tune this approach.

REFERENCES

- Coates, D.F. 1970. *Rock mechanics principles, 3rd edition*. Mines Branch Monograph 874. Ottawa: Department of Energy, Mines, and Resources.
- Clough, R.W., and Woodward, R.J. 1967. Analysis of embankment stresses and deformations. *Journal of the Soil Mechanics and Foundations Division, ASCE* 93: 529-549.
- Coetzee, M.J., Hart, R.D., Varona, P.M., and Cundall, P.A. 1995. *FLAC basics*. Minneapolis: Advanced Duplicating and Printing, Inc.
- Desai, C.S. and Abel, J.F. 1972. *Introduction to the finite element method*. New York Van Nostrand-Reinhold.
- Dunlop, P., Duncan, J.M., and Seed, H.B. 1970. Finite element analysis of slopes in soils. *Journal of the Soil Mechanics and Foundations Division, ASCE* 96: 471-493.
- Goodman, R.E., and Brown, C.B. 1963. Dead load stresses and the instability of slopes. *Journal of the Soil Mechanics and Foundations Division, ASCE* 89: 103-134.
- Itasca Consulting Group, Inc. 1996. *Universal Distinct Element Code user's manual*. Minneapolis: Itasca Consulting Group, Inc.

- Pariseau, W.G., B. Voight, and Dahl, H.D. 1970. Finite element analysis of elastic-plastic problems in the mechanics of geologic media: an overview. *Proceedings of the Second International Congress on Rock Mechanics*. Belgrade, Yugoslavia: 311-323.
- Shi, G.-h. and Goodman, R.E. 1984. Discontinuous deformation analysis. *Proceedings of the 25th U.S. Symposium on Rock Mechanics*. Evanston, Illinois: 269-277.
- Shi, G.-h. and Goodman, R.E. 1985. Two dimensional discontinuous deformation analysis. *International Journal for Numerical and Analytical Methods in Geomechanics* 9: 541-556.
- Shi, G.-h. 1988. *Discontinuous deformation analysis: a new numerical model for the statics and dynamics of block systems*. Ph.D. Thesis, Department of Civil Engineering, University of California, Berkeley.
- Shi, G.-h. 1990. Forward and backward discontinuous deformation analyses of rock systems. *Proceedings of the International Conference on Rock Joints*. Loen, Norway: 731-743.
- Shi, G.-h. 1993. *Block system modeling by discontinuous deformation analysis*. London Computational Mechanics Publications.
- Yeung, M. R. 1991. *Application of Shi's discontinuous deformation analysis to the study of rock behavior*. Ph.D. Thesis, Department of Civil Engineering, University of California, Berkeley.
- Yu, Y.S. and Coates, D.F. 1979. Chapter 22: Canadian Experience in Simulating Pit Slopes by the Finite Element Method. *Rockslides and Avalanches*, B. Voight, editor. Amsterdam: Elsevier.

APPENDIX

The displacement of the center of gravity of a block during a particular time step, assuming constant velocity and acceleration over a time step of length Δt , can be described by:

$$\begin{bmatrix} u \\ v \end{bmatrix} = \frac{1}{2} \cdot \frac{\partial}{\partial t^2} \begin{bmatrix} u(t) \\ v(t) \end{bmatrix} \cdot \Delta t^2 + \frac{\partial}{\partial t} \begin{bmatrix} u(t) \\ v(t) \end{bmatrix} \cdot \Delta t = \frac{\Delta t^2}{2} \cdot \begin{bmatrix} \partial^2 u(t) / \partial t^2 \\ \partial^2 v(t) / \partial t^2 \end{bmatrix} + \Delta t \cdot \begin{bmatrix} \partial u / \partial t \\ \partial v / \partial t \end{bmatrix} \quad (A1)$$

Solving for the acceleration:

$$\begin{bmatrix} \partial^2 u(t) / \partial t^2 \\ \partial^2 v(t) / \partial t^2 \end{bmatrix} = \frac{2}{\Delta t^2} \cdot \left(\begin{bmatrix} u \\ v \end{bmatrix} - \Delta t \cdot \begin{bmatrix} \partial u / \partial t \\ \partial v / \partial t \end{bmatrix} \right) = \frac{2}{\Delta t^2} \cdot \begin{bmatrix} u \\ v \end{bmatrix} - \frac{2}{\Delta t} \cdot \begin{bmatrix} \partial u / \partial t \\ \partial v / \partial t \end{bmatrix} \quad (A2)$$

The force of inertia per unit area of the block is then:

$$\begin{bmatrix} i_x \\ i_y \end{bmatrix} = -M \cdot \begin{bmatrix} \partial^2 u(t) / \partial t^2 \\ \partial^2 v(t) / \partial t^2 \end{bmatrix} = -M \cdot \left(\frac{2}{\Delta t^2} \cdot \begin{bmatrix} u \\ v \end{bmatrix} - \frac{2}{\Delta t} \cdot \begin{bmatrix} \partial u / \partial t \\ \partial v / \partial t \end{bmatrix} \right) \quad (A3)$$

where M is the mass per unit area and t represents time.

Practical Computing Formulas of Simplex Integration

Guangqi CHEN and Yuzo OHNISHI

Kyoto University, School of Civil Engineering

Kyoto 606-01, Japan

ABSTRACT: We have derived the solutions for the integration of a polynomial function in a polygon area or in a polyhedral volume based on the ordinary integral calculus. For easy computing, we have given practical general formulas and attached C-code source functions to this paper. By many practical calculations and comparison with the results from Gaussian Quadrature method, the advantages of the new method have been summarized. It can be expected that simplex method will be used more widely.

1 Introduction

In many numerical analysis methods such as Finite Element Method (FEM), Manifold Method (MM) and Discontinuous Deformation Analysis (DDA), it is necessary to calculate the integration of a polynomial function in a general polygon area B

$$\int \int_B x^{n_1} y^{n_2} dx dy \quad (1)$$

or in a general polyhedral volume V

$$\int \int \int_V x^{n_1} y^{n_2} z^{n_3} dx dy dz, \quad (2)$$

where, n_1 , n_2 , and n_3 are non-negative integers.

Although Gaussian Quadrature (Stroud et al 1966) is a method widely used in the past, it is only suitable for the integration in triangles, rectangles and rectangular hexahedral. Furthermore, since it is only an approximate numerical method, large error may be involved especially for high order polynomial functions.

Shi (1984) presented the analytical solutions of (1) and (2) in his simplex integration, which have already been used in his numerical analysis methods: DDA and MM. However, Shi only gave concrete formulas for second order polynomial function. He coded the individual formula one by one in his DDA and MM programs. Up to now, there is no practical explicit general formula available for computation. One should follow Shi's theory to derive new formulas for the given high orders in the development of high order DDA and MM or in other applications. As a result, the practical application of simplex integration may be limited very much because of the following reasons: 1). It is not easy for an engineer to derive new formulas based on Shi's complicated simplex theory; 2). It is difficult to deal with concrete formulas for higher orders. For example, there are more than one thousand of items for the function $x^{10}y^{10}z^{10}$, so that, it is difficult to obtain such large amount of

coefficients and code them in program without error. Also, the program will get too long if thousands of formulas are coded in it.

For this reason, in this paper, we also derive analytical solutions of (1) and (2) just based on the ordinary integral calculus without using any concept of simplex theory. For easily programming, we present practical general formulas for two- and three-dimensional integration of any order polynomial function. C-language functions for calculating the integration are developed and attached to the paper. By comparing with analytical solutions and results from Gaussian Quadrature, the advantages of the new method are summarized.

2 Formulas of Simplex Integration

Simplex integration is only referred to (1) and (2) in this paper, i.e., the integration of a polynomial function in a general polygon area or in a general polyhedral volume.

In this section, we derive general formulas for simplex integration just based on the ordinary integration theory. At first, we show the solution for the integration of a polynomial function in a regular triangle. And then, by coordinate transformation, we show that integration in a general triangle can be converted to that in the regular one, which is usually carried out in FEM. Finally, based on Shi's idea, we show that integration in a general polygon with n vertices can be converted to the algebraical sum of integration in each of n triangles;

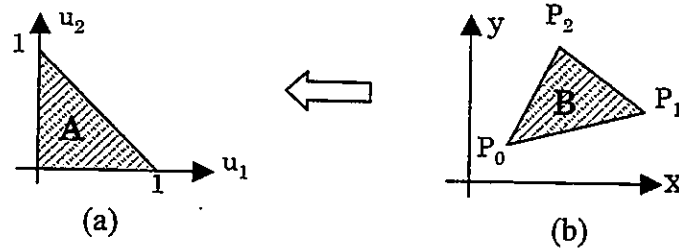


Figure 1: The regular triangle and a general triangle

2.1 Integration in a regular triangle

The analytical solution for the integration of a polynomial function in a regular triangle A (Fig. 1(a)) has been obtained by many researchers (Hammer et al 1956, Brebbia et al 1984, Shi 1995)

$$\iint_A u_0^{i_0} u_1^{i_1} u_2^{i_2} du_1 du_2 = \frac{i_0! i_1! i_2!}{(i_0 + i_1 + i_2 + 2)!}, \quad (3)$$

where i_0 , i_1 and i_2 are non-negative integers, u_0 , u_1 and u_2 are homogeneous coordinates, i.e.,

$$u_0 + u_1 + u_2 = 1. \quad (4)$$

Please refer to Shi(1995) for detail derivation.

If $i_0 = 0$, we have

$$\int \int_A u_1^{i_1} u_2^{i_2} du_1 du_2 = \frac{i_1! i_2!}{(i_1 + i_2 + 2)!} . \quad (5)$$

2.2 Integration in a general triangle

When the integration (1) is carried out in a general triangle B as shown in Figure 1(b), by coordinate transformation

$$\begin{cases} x = x_0 u_0 + x_1 u_1 + x_2 u_2 \\ y = y_0 u_0 + y_1 u_1 + y_2 u_2 \end{cases} , \quad (6)$$

it can be converted to the integration in the regular triangle A (Fig. 1(a)) as follows

$$\int \int_B x^{n_1} y^{n_2} dx dy = \int \int_A \left(\sum_{i=0}^2 x_i u_i \right)^{n_1} \left(\sum_{i=0}^2 y_i u_i \right)^{n_2} |J| du_1 du_2 , \quad (7)$$

where (x_i, y_i) are the coordinates of triangular vertex P_i , and $|J|$ is the absolute value of the Jacobi determinant, i.e.,

$$J = \begin{vmatrix} x_1 - x_0 & x_2 - x_0 \\ y_1 - y_0 & y_2 - y_0 \end{vmatrix} \quad (8)$$

For the following case

$$\begin{cases} x_0 = 0 \\ y_0 = 0 \end{cases} , \quad (9)$$

$x^{n_1} y^{n_2}$ can be easily expanded as

$$(x_1 u_1 + x_2 u_2)^{n_1} = \sum_{k_1=0}^{n_1} \frac{n_1!}{k_1! (n_1 - k_1)!} x_1^{n_1 - k_1} x_2^{k_1} u_1^{n_1 - k_1} u_2^{k_1} \quad (10)$$

$$(y_1 u_1 + y_2 u_2)^{n_2} = \sum_{k_2=0}^{n_2} \frac{n_2!}{k_2! (n_2 - k_2)!} y_1^{n_2 - k_2} y_2^{k_2} u_1^{n_2 - k_2} u_2^{k_2} \quad (11)$$

Then, we have

$$x^{n_1} y^{n_2} = \sum_{k_1=0}^{n_1} \sum_{k_2=0}^{n_2} \frac{n_1!}{k_1! (n_1 - k_1)!} \frac{n_2!}{k_2! (n_2 - k_2)!} x_1^{n_1 - k_1} x_2^{k_1} y_1^{n_2 - k_2} y_2^{k_2} u_1^{n_1 + n_2 - k_1 - k_2} u_2^{k_1 + k_2} \quad (12)$$

Substituting (12) into (7) and using (5), we can obtain the analytical solution of (??) as follows

$$\int \int_B x^{n_1} y^{n_2} dx dy = |J| \sum_{k_1=0}^{n_1} \sum_{k_2=0}^{n_2} a(n_1, n_2, k_1, k_2) x_1^{n_1 - k_1} x_2^{k_1} y_1^{n_2 - k_2} y_2^{k_2} \quad (13)$$

where

$$a(n_1, n_2, k_1, k_2) = \frac{n_1! n_2!}{(n_1 + n_2 + 2)!} \frac{(n_1 + n_2 - k_1 - k_2)! (k_1 + k_2)!}{k_1! k_2! (n_1 - k_1)! (n_2 - k_2)!} \quad (14)$$

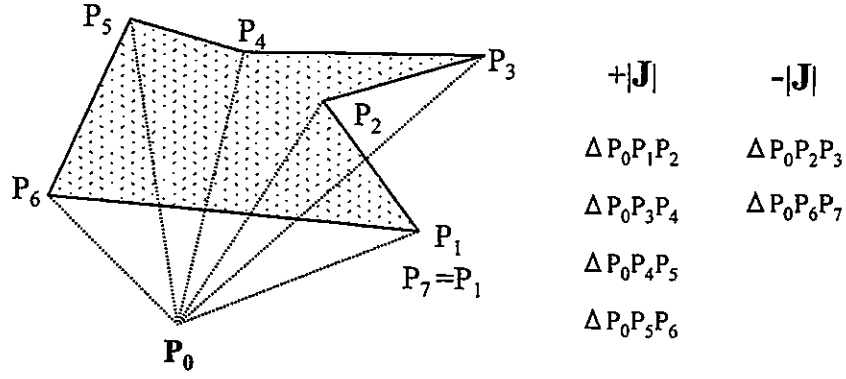


Figure 2: 6 triangles formed from the polygon with 6 vertices

2.3 Integration in a general polygon

When the integration (1) is carried out in a general polygon with n vertices, the integration can be converted to the algebraical sum of the integration in each of n triangles (Shi, 1993).

Numbering the n vertices of the polygon counterclockwise from P_1 to P_n with $P_{n+1} = P_1$, and taking an arbitrary point P_0 inside or outside of the polygon, we can get the n triangles ($\Delta P_0P_iP_{i+1}$, $i = 1, 2, \dots, n$). It is easy to show that the Jacobi determinant of a triangle $\Delta P_0P_iP_{i+1}$ will have positive value if it runs counterclockwise from $\overrightarrow{P_0P_i}$ to $\overrightarrow{P_0P_{i+1}}$, otherwise, the value will be negative. For example, 6 triangles are formed from the polygon with 6 vertices in Figure 2. Two of them ($\Delta P_0P_2P_3$ and $\Delta P_0P_6P_7$) have negative values of their Jacobi determinants while others are positive. Therefore, if the absolute sign of $|J|$ in the formula (13) is taken away, the sum of the integration in each of n triangles is right equal to the integration in the polygon. Then, we have

$$\iint_C x^{n_1} y^{n_2} dx dy = \sum_{i=1}^n (J_i \sum_{k_1=0}^{n_1} \sum_{k_2=0}^{n_2} a(n_1, n_2, k_1, k_2) x_i^{n_1-k_1} x_{i+1}^{k_1} y_i^{n_2-k_2} y_{i+1}^{k_2}) \quad (15)$$

and

$$J_i = x_i y_{i+1} - y_i x_{i+1} \quad (16)$$

It should be noted that since P_0 can be arbitrarily taken, it has been taken at $(0, 0)$ here for the most convenience.

2.4 Integration in a general polyhedral volume

Using the same approach as shown in above two-dimensional integration, we can get the formulas for calculating the integration of a polynomial function in general polyhedral volume as follows

$$\begin{aligned} & \iiint_V x^{n_1} y^{n_2} z^{n_3} dx dy dz \\ &= \sum_{i=1}^N \sum_{j=1}^{m_i} (J_{ij} \sum_{k_1=0}^{n_1} \sum_{k_2=0}^{n_2} \sum_{k_3=0}^{n_3} \sum_{j_1=0}^{k_1} \sum_{j_2=0}^{k_2} \sum_{j_3=0}^{k_3} a(n_1, n_2, n_3, k_1, k_2, k_3, j_1, j_2, j_3) f(P_{ij}, P_{ij+1}, P_{ij+2}) \end{aligned} \quad (17)$$

where

$$\begin{aligned}
a(n_1, n_2, n_3, k_1, k_2, k_3, j_1, j_2, j_3) &= \frac{n_1! n_2! n_3! (n_1 + n_2 + n_3 - k_1 - k_2 - k_3)!}{j_1! j_2! j_3! (n_1 + n_2 + n_3 + 3)!} \\
&\times \frac{(k_1 + k_2 + k_3 - j_1 - j_2 - j_3)! (j_1 + j_2 + j_3)!}{(n_1 - k_1)! (k_1 - j_1)! (n_2 - k_2)! (k_2 - j_2)! (n_3 - k_3)! (k_3 - j_3)!}
\end{aligned} \quad (18)$$

$$J_{ij} = \begin{vmatrix} x_{ij} & x_{ij+1} & x_{ij+2} \\ y_{ij} & y_{ij+1} & y_{ij+2} \\ z_{ij} & z_{ij+1} & z_{ij+2} \end{vmatrix} \quad (19)$$

and

$$f(P_{ij}, P_{ij+1}, P_{ij+2}) = x_{ij}^{n_1-k_1} x_{ij+1}^{k_1-j_1} x_{ij+2}^{j_1} y_{ij}^{n_2-k_2} y_{ij+1}^{k_2-j_2} y_{ij+2}^{j_2} z_{ij}^{n_3-k_3} z_{ij+1}^{k_3-j_3} z_{ij+2}^{j_3}, \quad (20)$$

N is the total number of the surfaces on the polyhedral volume; m_i ($i = 1, 2, \dots, N$) is the number of vertices on i th surface; P_{ij} ($j = 1, 2, \dots, m_i + 2$) are vertices with coordinates (x_{ij}, y_{ij}) on i th surface. The vertices on a surface are also numbered counterclockwise and there are $P_{im_i+1} = P_{i1}$, $P_{im_i+2} = P_{i2}$.

3 Practical Computing Formulas of Coefficients

The calculation of the coefficients given by (14) or (18) is the major task in the use of general simplex integration formulas.

In the special case of $n_1 = 0$ or $n_2 = 0$, the coefficient formula (14) can be simplified very much and the integration (15) can be easily calculated by the following formulas

$$\int \int_B x^{n_1} dx dy = \sum_{i=1}^n \left(\frac{J_i}{(n_1 + 1)(n_1 + 2)} \sum_{k_1=0}^{n_1} x_i^{n_1-k_1} x_{i+1}^{k_1} \right) \quad (21)$$

or

$$\int \int_B y^{n_2} dx dy = \sum_{i=1}^n \left(\frac{J_i}{(n_2 + 1)(n_2 + 2)} \sum_{k_2=0}^{n_2} y_i^{n_2-k_2} y_{i+1}^{k_2} \right) \quad (22)$$

In general, it is not a good idea to compute directly each factorial of (14) or (17). This is not only because it will take a lot of computing time, but also the order will be limited. We found that the computing error: Float Overflow (A value is larger than 1.0×10^{308}) would happen if the orders are higher than $x^{90}y^{90}$. Therefore, (14) and (17) need to be simplified further. As an example, we show how to simplify (14).

The coefficient given by (14) can be divided into three parts

$$a(n_1, n_2, k_1, k_2) = A_1 A_2 A_3. \quad (23)$$

Each part can be simplified as follows

$$A_1 = \frac{n_1!}{(n_1 - k_1)!k_1!} = \begin{cases} \prod_{i=n_1-k_1+1}^{n_1} i / \prod_{i=1}^{k_1} i & k_1 < n_1 - k_1 \\ \prod_{i=k_1+1}^{n_1} i / \prod_{i=1}^{n_1-k_1} i & k_1 \geq n_1 - k_1 \end{cases} \quad (24)$$

$$A_2 = \frac{n_2!}{(n_2 - k_2)!k_2!} = \begin{cases} \prod_{i=n_2-k_2+1}^{n_2} i / \prod_{i=1}^{k_2} i & k_2 < n_2 - k_2 \\ \prod_{i=k_2+1}^{n_2} i / \prod_{i=1}^{n_2-k_2} i & k_2 \geq n_2 - k_2 \end{cases} \quad (25)$$

$$A_3 = \frac{(n_{12} - k_{12})!k_{12}!}{(n_{12} + 2)!} = \begin{cases} \prod_{i=1}^{k_{12}} i / \prod_{i=n_{12}-k_{12}+1}^{n_{12}+2} i & k_{12} < n_{12} - k_{12} \\ \prod_{i=1}^{n_{12}-k_{12}} i / \prod_{i=k_{12}+1}^{n_{12}+2} i & k_{12} \geq n_{12} - k_{12} \end{cases} \quad (26)$$

where

$$\begin{cases} n_{12} = n_1 + n_2 \\ k_{12} = k_1 + k_2 \end{cases} \quad (27)$$

Furthermore, the following formula is used in the programming

$$\prod_{i=n_1}^{n_2} i / \prod_{j=k_1}^{k_2} j = \prod_{i=n_1}^{n_2} (i/w_i) \quad (28)$$

where

$$w_i = \begin{cases} i - n_1 + k_1 & i - n_1 \leq k_2 - k_1 \\ 1.0 & i - n_1 > k_2 - k_1 \end{cases} \quad (29)$$

It should be noted that (28) is based on the condition of $n_2 - n_1 \geq k_2 - k_1$. If $n_2 - n_1 < k_2 - k_1$, numerator and denominator should be reversed.

The C-language codes for calculating two-dimensional simplex integration are listed in Appendix B. By practical calculations, it has been found that the computing time becomes much shorter after simplification. The order as high as $x^{500}y^{500}$ can be still calculated.

4 Discussions

In order to verify the accuracy of the formulas and the program, practical calculations are made based on the polygon shown in Figure 3. We choose the quadrangle just because we can easily get analytical solution

$$\int \int_B x^m y^n dx dy = \int_0^b \int_{-a_1}^{\frac{a_2}{b}x} x^m y^n dx dy = \frac{a_2^{n+1} b^{m+1}}{(n+1)(m+n+2)} - \frac{(-a_1)^{n+1} b^{m+1}}{(n+1)(m+1)}. \quad (30)$$

Also, for comparison, all examples have been calculated by Gaussian Quadrature method, which is briefly described in Appendix A.

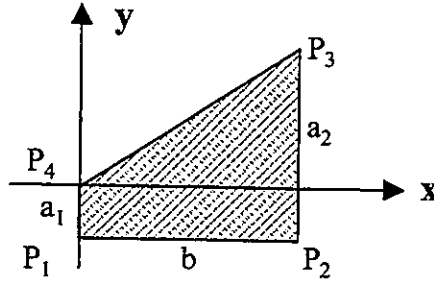


Figure 3: The polygon used in integral calculations

4.1 Accuracy with order

The integration for $m = 0, 1, \dots, 500$ and $n = 0, 1, \dots, 500$ has been calculated one by one when $a_1 = 0.5$, $a_2 = 1.5$ and $b = 2.0$. Some results are listed in Table 1. The first column is the order for both m and n ; the second and third columns are the relative errors of simplex integration method and Guassian method to the analytical solution respectively.

Table 1: The results of integration with different orders from different methods

order $m \ n$	Relative Error		Analytical S	Result	
	$(S - S_s)/S$	$(S - S_g)/S$		Simplex S_s	Guassian S_g
10	0.000000e+000	2.018989e-015	1.464029e+003	1.464029e+003	1.464029e+003
15	3.461625e-016	1.038488e-015	-1.681513e+005	-1.681513e+005	-1.681513e+005
20	-3.141104e-016	0.000000e+000	2.371962e+007	2.371962e+007	2.371962e+007
25	0.000000e+000	1.296528e-009	-3.760157e+009	-3.760157e+009	-3.760157e+009
30	-3.798434e-016	3.919172e-007	6.427403e+011	6.427403e+011	6.427400e+011
50	1.108063e-015	7.823796e-004	8.280254e+020	8.280254e+020	8.273775e+020
100	-1.306820e-016	8.306050e-002	1.515668e+044	1.515668e+044	1.389776e+044
500	-2.030690e-016	9.962157e-001	4.345834e+233	4.345834e+233	1.644580e+231

It can be seen that the relative errors of simplex method are quite small and the accuracy does not change even if the order gets as high as $x^{500}y^{500}$. However, the relative errors of Guassian method are small only when the orders are lower than $x^{20}y^{20}$ and the accuracy gets poorer and poorer when the order gets higher and higher.

Table 2: The results of integration in different shapes

b/a_2	Relative Error		Analytical S	Result	
	$(S - S_s)/S$	$(S - S_g)/S$		Simplex S_s	Guassian S_g
10^0	0.000000e+000	2.028316e-006	1.133787e-003	1.133787e-003	1.133785e-003
10^4	0.000000e+000	2.028316e-006	1.133787e+081	1.133787e+081	1.133785e+081
10^8	0.000000e+000	2.028316e-006	1.133787e+165	1.133787e+165	1.133785e+165

4.2 Accuracy with shape

In order to investigate whether the accuracy varies with the shape of the polygon, we take $a_1 = 0.0$, $a_2 = 1.0$ and change the ratio of b/a_2 from 1 to 10^8 . Then, we calculate the integration of $x^{20}y^{20}$ for each shape of the quadrangle. Some results are listed in Table 2.

It can be seen that the accuracy of simplex method does not change even if the shape is changed so much. However, the relative errors of Guassian method become much larger than the results in Table 1. For the shape of $a_1 = 0.0$, $a_2 = 1.0$ and $b = 1.0$, the relative errors of Guassian method with different orders are listed in Table 3. It can be seen that the accuracy gets poor when the orders are higher than $x^{15}y^{15}$.

Table 3: The results of integration with different orders

order $m\ n$	Relative Error		Result		
	$(S - S_s)/S$	$(S - S_g)/S$	Analytical S	Simplex S_s	Guassian S_g
5	0.000000e+000	2.248202e-015	1.388889e-002	1.388889e-002	1.388889e-002
10	0.000000e+000	1.469311e-015	4.132231e-003	4.132231e-003	4.132231e-003
15	0.000000e+000	5.182344e-009	1.953125e-003	1.953125e-003	1.953125e-003
50	0.000000e+000	1.777038e-002	1.922338e-004	1.922338e-004	1.888177e-004

5 Conclusions

We have derived the analytical solutions for the integration of a polynomial function in a general polygon area or in a polyhedral volume just based on the ordinary integral calculus. The practical general formulas have also been presented for computing programming. C-language functions have been developed and attached to the paper.

The following points can be summarized from this work: 1). Because of the presented practical general formulas, it is no longer necessary to derive new individual formula for a given order, which is very helpful in the development of high order DDA and MM or in other applications. 2). By practical calculations, it has been found that a maximum order of $x^{500}y^{500}$ can be still calculated by using a PC computer. Therefore, it is possible to deal with complicated function by series expansion. 3). It has been shown that the accuracy of the presented method is not affected by the order of a polynomial function while the accuracy of Gaussian Quadrature method gets poorer and poorer when the order gets higher and higher. Therefore, the new method is of importance for high order integration. 4). The accuracy of the presented method is not affected by shapes of polygons. Therefore, it can work well for any shape of meshes.

References

- Brebbia C., Telles J. and Wrobel L. 1984. *Boundary Element Techniques*. Berlin Heidelberg New York Tokyo: Springer-Verlag. (pp134)

- Shi, G. 1984. Modeling dynamic rock failure by Discontinuous Deformation Analysis with simplex integrations. *Proceedings of the 1st North American Rock Mechanics Symposium*. 591-598.
- Shi, G. 1995. Simplex integration for Manifold Method and Discontinuous Deformation Analysis. *Proceedings of Working Forum on the Manifold Method of Material Analysis*. 129-164.
- Stroud, A.H. and Secrest, D. 1966. *Gaussian Quadrature Formulas*. New York Tokyo: Prentice-Hall.

Appendix A: Gaussian Quadrature for Quadrangles

The standard Gaussian quadrature formula is based on a regular rectangle in the form

$$\int_{-1}^1 \int_{-1}^1 f(\xi, \eta) d\xi d\eta \cong \sum_{j=1}^n \sum_{i=1}^n f(\xi_i, \eta_j) w_i w_j \quad (31)$$

where the integration point coordinates $((\xi_i, \eta_j), i, j = 1, 2, \dots, n)$ and weighting factors $(w_i, i = 1, 2, \dots, n)$ are listed in Table 1 for $n = 12$. For a general quadrangle, the following coordinate transformation can be made

$$\begin{cases} x = \sum_{i=1}^4 \varphi_i x_i \\ y = \sum_{i=1}^4 \varphi_i y_i \end{cases}, \quad (32)$$

where

$$\begin{cases} \varphi_1 = \frac{1}{4}(1 - \xi)(1 - \eta) \\ \varphi_2 = \frac{1}{4}(1 + \xi)(1 - \eta) \\ \varphi_3 = \frac{1}{4}(1 + \xi)(1 + \eta) \\ \varphi_4 = \frac{1}{4}(1 - \xi)(1 + \eta) \end{cases}, \quad (33)$$

where $((x_i, y_i), i = 1, 2, 3, 4)$ are the vertex coordinates of the quadrangle. Then, the integration in a general quadrangle becomes

$$\int \int_B x^{n_1} y^{n_2} dx dy = \int_{-1}^1 \int_{-1}^1 x^{n_1} y^{n_2} |J| d\xi d\eta \quad (34)$$

which can be calculated by using (31) with

$$f(\xi, \eta) = x^{n_1} y^{n_2} |J| \quad (35)$$

and

$$J = \begin{vmatrix} \frac{\partial x}{\partial \xi} & \frac{\partial x}{\partial \eta} \\ \frac{\partial y}{\partial \xi} & \frac{\partial y}{\partial \eta} \end{vmatrix} \quad (36)$$

Table 4: The integration point coordinates and weighting factors

$\pm \xi_i$	$\pm \eta_i$	w_i	$\pm \xi_i$	$\pm \eta_i$	w_i
0.125233408511469	0.249147045813403	0.769902674194305	0.160078328543346		
0.367831498998180	0.233492536538355	0.904117256370475	0.106939325995318		
0.587317954286617	0.203167426723066	0.981560634246719	0.047175336386512		

Appendix B: Functions for Two-Dimensional Simplex Integration

```

double djiechen(int k1, int k2, int n1, int n2)
{
    int i, nk;
    double s, k;
    nk = n1 - k1;
    s = 1.0;
    for (i = n1; i <= n2; i++){
        k = i - nk;
        if (k > k2) k = 1.0;
        s = s * i / k;
    }
    return(s);
}

double coefficient(int n1, int n2, int k1, int k2)
{
    int N12, K12, NK;
    double a;
    a = 1.0;
    NK = n1 - k1;
    if (k1 < NK)    a *= djiechen(1, k1, NK+1, n1);
    else            a *= djiechen(1, NK, k1+1, n1);
    NK = n2 - k2;
    if (k2 < NK)    a *= djiechen(1, k2, NK+1, n2);
    else            a *= djiechen(1, NK, k2+1, n2);
    N12 = n1 + n2;
    K12 = k1 + k2;
    NK = N12 - K12;
    if (K12 < NK)    a /= djiechen(1, K12, NK+1, N12+2);
    else            a /= djiechen(1, NK, K12+1, N12+2);
    return(a);
}

void Allcoefficient(int n1, int n2, double **a)
{
    int k1, k2;
    for (k1 = 0; k1 <= n1; k1++)
        for (k2 = 0; k2 <= n2; k2++)
            a[k1][k2] = coefficient(n1, n2, k1, k2);
}

double Sint(int n1, int n2, double x[], double y[], int N, double **a)
{
    double s, J, s1;
    int i, k1, k2;
    s = 0.0;
    for (i = 0; i < N; i++){
        J = x[i] * y[i+1] - x[i+1] * y[i];
        s1 = 0.0;
        for (k1 = 0; k1 <= n1; k1++)
            for (k2 = 0; k2 <= n2; k2++)
                s1 = s1 + a[k1][k2] * pow(x[i], n1-k1) * pow(x[i+1], k1) * pow(y[i], n2-k2) * pow(y[i+1], k2);
        s = s + s1 * J;
    }
    return(s);
}

```

A METHOD OF SUB-MESHING IN DISCONTINUOUS DEFORMATION ANALYSIS (DDA)

Dave Clatworthy and Friedrich Scheele
University of Cape Town, Department of Civil Engineering
Rondebosch 7701, RSA

ABSTRACT: A sub-meshing method is described which allows mixed formulation analyses, with DDA blocks and FE meshes interacting within a single system. Blocks of particular interest can thus be subdivided into Finite Element (FE) meshes in order to obtain a more accurate description of their deformation.

The method takes advantage of the fact that both DDA and FE analyses use the principle of total potential energy minimisation to obtain the solution equations for system equilibrium. Both DDA blocks and sub-block triangular elements can therefore be treated initially as DDA blocks, using the standard DDA formulation. Before solution, however, the equilibrium equations for the sub-block elements are converted into FE format by a simple transformation procedure, thereby allowing sub-block elements to be meshed together into FE analysis format. The solution equations for standard DDA blocks are not affected, and are solved in their original form.

The method is efficient, and because it uses the DDA formulation to obtain the initial solution equations for the FE meshes, it remains reasonably simple to incorporate into existing DDA program codes. First and second order DDA blocks are considered in this paper, along with their FE equivalents, the C^0 -linear and C^0 -quadratic triangular elements.

1 INTRODUCTION

Discontinuous Deformation Analysis is a tool for modelling blocky rock masses. It is an assumption of this method that the rockmass deforms and fails primarily by sliding or separation of the blocks relative to one another. Because of this, strains within individual blocks are given only a cursory treatment in the analysis, and fracture of intact rock material is not considered.

While this approach is often valid, there are occasions where it introduces serious limitations into the method. This is particularly the case where engineering components interact with the rockmass. Examples of such components are retaining walls, mining support structures and tunnel linings. At present, these structures are generally modelled as a single DDA block, with the assumption that stresses and strains are constant throughout the structure. This approach has two drawbacks. The deformed shape of the structure is not accurately modelled, and this may affect the course of the simulation. Further, it is not possible to obtain a model of the stresses in the structure for design purposes.

2 METHODS FOR IMPROVING STRAIN DETERMINATION

Three broad solutions to this problem have been considered in the past by researchers.

One approach is to use higher order blocks. By allowing a block more degrees of freedom, strains may vary in a linear or quadratic form across the block. Second- and third-order blocks have been incorporated into the DDA code by Chern et al. (1995) and by Koo and Chern (1996). Alternatively, Ke and Goodman (1994) developed the 'artificial joint concept'. This method builds a block out of a number of triangular DDA sub-blocks, with neighbouring sub-blocks connected together by penalty functions to ensure that they remain locked together. The penalty functions have the same formulations as the normal or shear springs used in the modelling of contacts in the DDA method.

Finally, Chang (1994) developed a mixed formulation code, where a Finite Element code is used to model individual blocks as meshes, while interactions between blocks are controlled by the DDA method. The FE and DDA solution equations are solved simultaneously, to arrive at an overall system equilibrium.

The advantage of a meshing method such as that used by Ke and Goodman (1994) and Chang (1994) is that the degree of mesh refinement, and hence the quality of the strain determination, can be chosen by the user, and increased in areas of particular interest.

A disadvantage of the method used by Ke and Goodman (1994) is that the system has the same number of solution unknowns as if the individual sub-blocks were separate blocks. In fact, because elements in a mesh are restrained by their neighbours, the number of degrees of freedom of a mesh is as much as six times lower than the sum of the degrees of freedom of the individual elements. The extra element degrees of freedom do not contribute to the accuracy of the solution, as they are restrained by the penalty functions. This is discussed further in Section 5.

A fourth approach is introduced in the remainder of this paper. The method has similarities to the methods of Ke and Goodman (1994) and of Chang (1994). As with the 'artificial joint concept', blocks are built up of a number of smaller DDA sub-blocks. However, the blocks are transformed into FE format before solution. This eliminates the superfluous degrees of freedom described above, and results in a solution system similar to that arrived at by the mixed formulation of Chang (1994). However, because the sub-blocks, or elements, are treated as standard DDA blocks for the purposes of developing the equilibrium equations, the method is much simpler to incorporate into existing DDA codes.

3 DISPLACEMENT VARIABLES

The DDA method is based on the assumption that individual blocks are able to move independently to one another, and therefore the displacement variables which describe the displacement and deformation of the block are chosen to represent the individual blocks. The displacement variables are the rigid body displacements and rotation of the centroid of the block, u_0 , v_0 and r_0 , and the strains in the block, ε_x , ε_y and γ_{xy} , which are assumed to be constant over the area of the block.

The displacement (u , v) of any point (x , y) in the block can be found from these variables by

$$\begin{pmatrix} u \\ v \end{pmatrix} = \begin{bmatrix} 1 & 0 & -\bar{y} & \bar{x} & 0 & \bar{y}/2 \\ 0 & 1 & \bar{x} & 0 & \bar{y} & \bar{x}/2 \end{bmatrix} \begin{pmatrix} u_0 \\ v_0 \\ r_0 \\ \varepsilon_x \\ \varepsilon_y \\ \gamma_{xy} \end{pmatrix} \quad \text{or} \quad \begin{pmatrix} u(x, y) \\ v(x, y) \end{pmatrix} = \underline{T}^i(x, y) \underline{d}^i \quad (1)$$

where $\bar{x} = x - x_0$

$\bar{y} = y - y_0$

and (x_0, y_0) is the undisplaced position of the centroid of the block.

In the FE method, the displacement variables chosen are generally the displacements of nodes at the corners and edges of elements. Because the elements are locked together corner-to-corner and edge-to-edge, these values usually apply to more than one element.

In the case of a simple, 3-noded triangular element, it is assumed that the edges of this element will remain straight if the element is deformed. A complete description of the element's displaced position can therefore be obtained if the displaced positions of the corners are known. The displacement variables chosen are therefore u_1, v_1, u_2, v_2, u_3 and v_3 , the displacements of the three corner nodes in the global axis system.

The above descriptions of the displacement of a triangular block or element are equivalent, both being complete first order displacement functions. It is also possible to convert between the two sets of displacement variables. Using Equation 1,

$$\begin{pmatrix} u_1 \\ v_1 \\ u_2 \\ v_2 \\ u_3 \\ v_3 \end{pmatrix} = \begin{bmatrix} \underline{T}^i(x_1, y_1) \\ \text{-----} \\ \underline{T}^i(x_2, y_2) \\ \text{-----} \\ \underline{T}^i(x_3, y_3) \end{bmatrix} \begin{pmatrix} u_0 \\ v_0 \\ r_0 \\ \varepsilon_x \\ \varepsilon_y \\ \gamma_{xy} \end{pmatrix} \quad \text{or} \quad \underline{u}^i = \underline{S}^i \underline{d}^i \quad (2)$$

The 6×6 matrix \underline{S}^i is invertible, unless the block has zero area. Defining the inverse of \underline{S}^i as \underline{Q}^i , it follows that

$$\underline{d}^i = \underline{Q}^i \underline{u}^i \quad \text{and} \quad \underline{d}^{iT} = \underline{u}^{iT} \underline{Q}^{iT} \quad (3)$$

4 THE DDA SOLUTION METHOD

The DDA method is based on the principle of potential energy minimisation. The Total Potential Energy (TPE) of the system, Π , is defined as the sum of the internal strain energy of the system and the external work done by applied loads. The system is in equilibrium if the TPE remains unchanged for a small perturbation of any of its degrees of freedom.

In a DDA system of n blocks, the potential energy equations are built up in the general form

$$\Pi = d_r K_{rs} d_s - d_t f_t, \quad (4)$$

where $r, s, t = 1, \dots, 6n$

Minimisation of the TPE yields

$$\frac{\partial \Pi}{\partial d_r} = K_{rs} d_s - f_r = 0 \quad (5)$$

For a system of n blocks, the equilibrium equations are rearranged into the form

$$\begin{bmatrix} \underline{\underline{K}}^{11} & \underline{\underline{K}}^{12} & \underline{\underline{K}}^{13} & \dots & \underline{\underline{K}}^{1n} \\ \underline{\underline{K}}^{21} & \underline{\underline{K}}^{22} & \underline{\underline{K}}^{23} & \dots & \underline{\underline{K}}^{2n} \\ \underline{\underline{K}}^{31} & \underline{\underline{K}}^{32} & \underline{\underline{K}}^{33} & \dots & \underline{\underline{K}}^{3n} \\ \vdots & \vdots & \vdots & \ddots & \vdots \\ \underline{\underline{K}}^{n1} & \underline{\underline{K}}^{n2} & \underline{\underline{K}}^{n3} & \dots & \underline{\underline{K}}^{nn} \end{bmatrix} \begin{pmatrix} \underline{d}^1 \\ \underline{d}^2 \\ \underline{d}^3 \\ \vdots \\ \underline{d}^n \end{pmatrix} = \begin{pmatrix} \underline{f}^1 \\ \underline{f}^2 \\ \underline{f}^3 \\ \vdots \\ \underline{f}^n \end{pmatrix} \quad \text{or} \quad \underline{\underline{K}} \underline{d} = \underline{f} \quad (6)$$

In the above equation, each element $\underline{\underline{K}}^{ij}$ is a 6×6 sub-matrix, each element \underline{d}^i is the displacement variables for block i : $(u_0, v_0, r_0, \varepsilon_x, \varepsilon_y, \gamma_{xy})$, and each term \underline{f}^i represents the loading on block i in terms of the displacement variables, a 6×1 array.

The system is solved by inverting the global matrix $\underline{\underline{K}}$ and solving for the displacement variables.

5 INTRODUCING MESHING INTO THE DDA SOLUTION METHOD

Where a mesh is introduced into the DDA method, the individual triangular elements are treated as normal DDA blocks for the purposes of creating the solution equations. No interaction between elements in the same mesh is considered. It is only when the solution equations are in the form of Equation 6 that there is any change in the DDA method.

The global solution equations are transformed so that, for elements that are part of FE meshes, the solution is in terms of the nodal displacements, while for all other blocks in the system, the solution equations remain unaltered.

In the stiffness matrix of Equation 6, the diagonal terms $\underline{\underline{K}}^{ii}$ represent the internal stiffness of individual blocks, while the off-diagonal terms, $\underline{\underline{K}}^{ij}$ are produced by interaction between blocks due to contact, or rock bolt connection. These off-diagonal terms are null matrices, unless blocks i and j are directly interacting.

Considering a pair of interacting blocks, blocks p and q , within the system, the potential energy of the pair can be written as

$$\Pi = \Pi^p + \Pi^q = \frac{1}{2} \underline{d}^{pT} \underline{\underline{K}}^{pp} \underline{d}^p + \frac{1}{2} \underline{d}^{qT} \underline{\underline{K}}^{qq} \underline{d}^q + \underline{d}^{pT} \underline{\underline{K}}^{pq} \underline{d}^q + \underline{d}^{qT} \underline{\underline{K}}^{qp} \underline{d}^p - \underline{d}^{pT} \underline{f}^p - \underline{d}^{qT} \underline{f}^q \quad (7)$$

Minimisation yields

$$\begin{aligned}\frac{\partial \Pi}{\partial \underline{d}^p} &= \underline{\underline{K}}^{pp} \underline{d}^p + \underline{\underline{K}}^{pq} \underline{d}^q - \underline{f}^p = \underline{0} \\ \frac{\partial \Pi}{\partial \underline{d}^q} &= \underline{\underline{K}}^{qq} \underline{d}^q + \underline{\underline{K}}^{qp} \underline{d}^p - \underline{f}^q = \underline{0}\end{aligned}\quad (8)$$

If one of these blocks, e.g. block p , is a sub-block element, then Equation 3 can be substituted into Equation 7, to obtain

$$\begin{aligned}\Pi &= \frac{1}{2} \underline{u}^{pT} \underline{\underline{Q}}^{pT} \underline{\underline{K}}^{pp} \underline{\underline{Q}}^p \underline{u}^p + \frac{1}{2} \underline{d}^{qT} \underline{\underline{K}}^{qq} \underline{d}^q + \underline{u}^{pT} \underline{\underline{Q}}^{pT} \underline{\underline{K}}^{pq} \underline{d}^q + \underline{d}^{qT} \underline{\underline{K}}^{qp} \underline{\underline{Q}}^q \underline{u}^q - \underline{u}^{pT} \underline{\underline{Q}}^{pT} \underline{f}^p - \underline{d}^{qT} \underline{f}^q \\ \frac{\partial \Pi}{\partial \underline{u}^p} &= \underline{\underline{Q}}^{pT} \underline{\underline{K}}^{pp} \underline{\underline{Q}}^p \underline{u}^p + \underline{\underline{Q}}^{pT} \underline{\underline{K}}^{pq} \underline{d}^q - \underline{\underline{Q}}^{pT} \underline{f}^p = \underline{0} \\ \frac{\partial \Pi}{\partial \underline{d}^q} &= \underline{\underline{K}}^{qq} \underline{d}^q + \underline{\underline{K}}^{qp} \underline{\underline{Q}}^p \underline{u}^p - \underline{f}^q = \underline{0}\end{aligned}\quad (9)$$

Alternatively, if both blocks are sub-block elements, then

$$\begin{aligned}\Pi &= \frac{1}{2} \underline{u}^{pT} \underline{\underline{Q}}^{pT} \underline{\underline{K}}^{pp} \underline{\underline{Q}}^p \underline{u}^p + \frac{1}{2} \underline{u}^{qT} \underline{\underline{Q}}^{qT} \underline{\underline{K}}^{qq} \underline{\underline{Q}}^q \underline{u}^q + \underline{u}^{pT} \underline{\underline{Q}}^{pT} \underline{\underline{K}}^{pq} \underline{\underline{Q}}^q \underline{u}^q + \underline{u}^{qT} \underline{\underline{Q}}^{qT} \underline{\underline{K}}^{qp} \underline{\underline{Q}}^p \underline{u}^p \\ &\quad - \underline{u}^{pT} \underline{\underline{Q}}^{pT} \underline{f}^p - \underline{u}^{qT} \underline{\underline{Q}}^{qT} \underline{f}^q \\ \frac{\partial \Pi}{\partial \underline{u}^p} &= \underline{\underline{Q}}^{pT} \underline{\underline{K}}^{pp} \underline{\underline{Q}}^p \underline{u}^p + \underline{\underline{Q}}^{pT} \underline{\underline{K}}^{pq} \underline{\underline{Q}}^q \underline{u}^q - \underline{\underline{Q}}^{pT} \underline{f}^p = \underline{0} \\ \frac{\partial \Pi}{\partial \underline{u}^q} &= \underline{\underline{Q}}^{qT} \underline{\underline{K}}^{qq} \underline{\underline{Q}}^q \underline{u}^q + \underline{\underline{Q}}^{qT} \underline{\underline{K}}^{qp} \underline{\underline{Q}}^p \underline{u}^p - \underline{\underline{Q}}^{qT} \underline{f}^q = \underline{0}\end{aligned}\quad (10)$$

However, if both blocks are sub-block elements within the same mesh, then in general no interaction matrices are required between them, so that $\underline{\underline{K}}^{pq} = \underline{\underline{K}}^{qp} = 0$.

Inspection of the above equations reveals a simple procedure for the transformation of sub-block elements into FE format. For each sub-block element, m , the following process is implemented:

- The transformation matrix $\underline{\underline{Q}}^m$ is determined.
- All block stiffness matrices $\underline{\underline{K}}^{im}$ are post-multiplied by $\underline{\underline{Q}}^m$.
- All block stiffness matrices $\underline{\underline{K}}^{mj}$ are pre-multiplied by $\underline{\underline{Q}}^{mT}$.
- The force vector \underline{f}^m is pre-multiplied by $\underline{\underline{Q}}^{mT}$.

This procedure is carried out in turn for all sub-block elements.

The displacement vector is now partially in terms of the block variables of standard DDA blocks, and partially in terms of the nodal displacements of sub-block elements. Because neighbouring elements share the same nodes, the element stiffness matrix and displacement and force array terms are distributed to the global nodal degrees of freedom, as is done in the Finite Element method. This reduces the size of the global stiffness matrix relative to the DDA method, but the stiffness matrix remains symmetric and invertible.

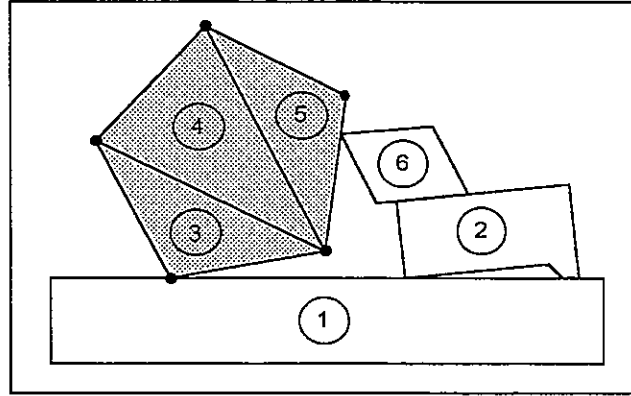


Figure 1. A simple DDA problem.

Figure 1 shows a simple illustrative example. Sub-blocks 3, 4 and 5 are elements of a single block, while the other blocks are typical DDA elements. The solution equations are determined by the DDA method, as shown in Figure 2a. The blank terms in the stiffness matrix are null sub-matrices, as the blocks in question are not directly interacting. To mesh blocks 3, 4 and 5 together, the stiffness sub-matrices and load arrays in the shaded portions of Figure 2a are pre- or post-multiplied by transformation matrices. The final solution equations are illustrated in Figure 2b. It should be noted that the arrays \underline{d}^3 , \underline{d}^4 and \underline{d}^5 of Figure 2a have been replaced by in Figure 2b by the single array \underline{u}^b , the 10 translational degrees of freedom of the corner nodes of the meshed polygon. Similarly, the three stiffness sub-matrices, \underline{K}^{33} , \underline{K}^{44} and \underline{K}^{55} have been transformed by both pre- and post multiplication, and then merged into the single 10 x 10 sub-matrix \underline{K}^{bb} .

The terms in the unshaded regions of Figures 2a and 2b remain unaffected throughout.

$$\begin{array}{ccc}
 \left[\begin{array}{cccc|ccc} \underline{K}^{11} & \underline{K}^{12} & \underline{K}^{13} & & & & & \\ \underline{K}^{21} & \underline{K}^{22} & & & & & & \underline{K}^{26} \\ \underline{K}^{31} & & \underline{K}^{33} & & & & & \\ & & & \underline{K}^{44} & & & & \\ & & & & \underline{K}^{55} & \underline{K}^{56} & & \\ & & & & & \underline{K}^{65} & \underline{K}^{66} & \\ & & & & & & & \end{array} \right] \begin{pmatrix} \underline{d}^1 \\ \underline{d}^2 \\ \underline{d}^3 \\ \underline{d}^4 \\ \underline{d}^5 \\ \underline{d}^6 \end{pmatrix} = \begin{pmatrix} \underline{f}^1 \\ \underline{f}^2 \\ \underline{f}^3 \\ \underline{f}^4 \\ \underline{f}^5 \\ \underline{f}^6 \end{pmatrix} & \Rightarrow & \left[\begin{array}{cccc|ccc} \underline{K}^{11} & \underline{K}^{12} & \underline{K}^{1b} & & & & & \\ \underline{K}^{21} & \underline{K}^{22} & & & & & & \underline{K}^{26} \\ & & \underline{K}^{bb} & & & & & \\ & & & \underline{K}^{66} & & & & \\ & & & & \underline{K}^{6b} & & & \\ & & & & & \underline{K}^{66} & & \end{array} \right] \begin{pmatrix} \underline{d}^1 \\ \underline{d}^2 \\ \underline{u}^b \\ \underline{d}^6 \end{pmatrix} = \begin{pmatrix} \underline{f}^1 \\ \underline{f}^2 \\ \underline{f}^b \\ \underline{f}^6 \end{pmatrix} \\
 \text{(a)} & & \text{(b)}
 \end{array}$$

Figure 2. The global solution equations (a) before and (b) after transformation.

After solution of the global equations, the displacements and strains in the sub-block elements may be recovered by pre-multiplying the element nodal displacements by the transformation matrix Q^m .

6 HIGHER ORDER BLOCKS AND ELEMENTS

The triangular three-noded element is the simplest element available for two-dimensional meshing in the FE method. Alternatively, meshing can be based on the second-order DDA block devised by Chern et al. (1995). The displacement function for this block is a complete quadratic series in x and y . The block's equivalent in the FE method is a six-noded triangular element, with nodes at the corners and the mid-side points. Both have 12 degrees of freedom. The method of transformation between the two is similar to that described for first-order elements, with the matrix $T^i(x,y)$ of Equation 1 now a 2×12 matrix.

The various quadrilateral elements commonly used in Finite Element analysis cannot be formulated as DDA blocks by this method. This is because the displacement functions of these elements are not complete to any particular order, containing some terms from higher orders. Hence, the deformation of the element will be dependent on its orientation to the global axis system, and the method described above will not produce consistent results.

7 PERFORMANCE OF MESHES IN THE DDA METHOD

In order to guarantee that a particular element, if used in a mesh, will converge to a correct solution with increasing refinement of the mesh, two conditions must be met.

The continuity condition requires that the displacement solution should be continuous at element boundaries. In effect, this means that neighbouring elements may not separate or overlap along their common edges. The completeness condition states that the element's displacement function and its first derivatives should be able to assume any constant value. The classic test of this condition is the patch test (see e.g. de Arantes and Oliveira 1977).

Both the first and second order elements meet these convergence requirements. It is therefore guaranteed that both will yield a correct solution to a problem as mesh refinement approaches infinity. However, the convergence conditions do not give any indication of the performance of elements in coarse meshes, and further tests are required to evaluate this.

7.1 The Cook Cantilever Test

Cook et al.(1989) describes a common test for two-dimensional elements subjected to bending. This consists of a short, tapered cantilever which is subjected to a uniformly distributed load at its free end. The geometry of the problem is shown in Figure 3. Also shown is the displaced shape, as modelled by a 32 element mesh. The displacements are exaggerated for clarity. The results of this test are tabulated in Table 1. No closed form solution exists for this problem, and the results are compared to a 'best known value', v_{B0} , which is the result obtained from a FE analysis, using 100 8-noded reduced integration elements.

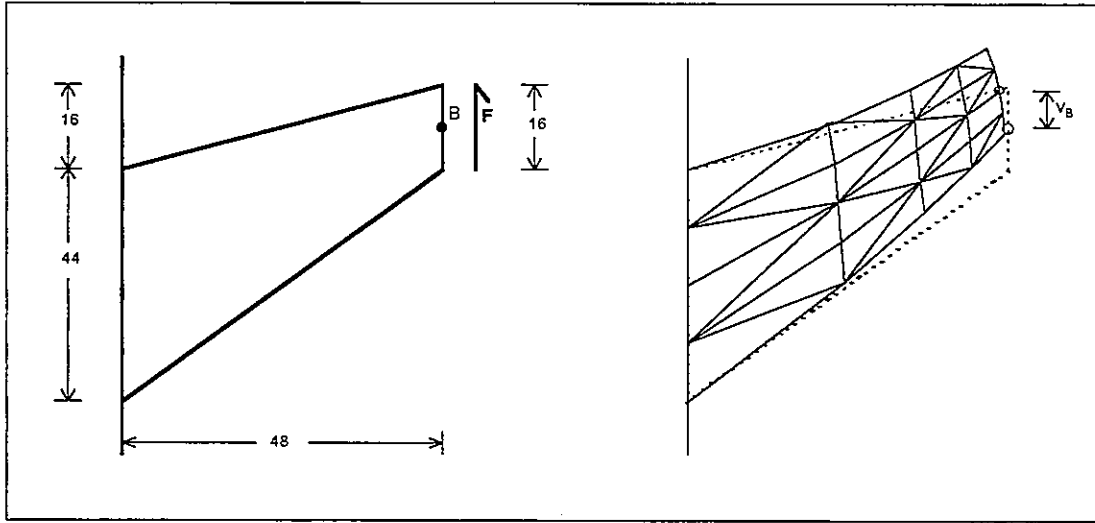


Figure 3. The geometry and meshing of the Cook cantilever test (Cook et al. 1989)

Mesh	No. of Elements	1 st Order Elements			2 nd Order Elements		
		No. of Nodes	No. of d.o.f.	v_B / v_{B0}	No. of Nodes	No. of d.o.f.	v_B / v_{B0}
(a)	2	4	8	0.251	9	18	0.768
(b)	4	5	10	0.262	13	26	0.794
(c)	8	9	18	0.302	25	50	0.898
(d)	18	16	32	0.456	49	98	0.946
(e)	32	25	50	0.529	81	162	0.973
(f)	50	36	72	0.650	144	288	0.983
(g)	72	49	98	0.693	169	338	0.989

Table 1. Results of the Cook cantilever test.

It can be seen from Table 1 that the 1st order elements perform poorly in the test. First order DDA elements are equivalent to the three-noded linear elements used in FE applications, commonly known as the Constant Strain Triangle (CST). These elements are noted for their poor performance in bending. The 2nd order element performs considerably better in the test. This element is identical to the six-noded C^0 -quadratic triangular element found in the FE method. The same tests were carried out using the commercial FE package ABAQUS (1996). The results obtained using the equivalent elements are identical, within the range of rounding errors. This confirms that the DDA meshing method does yield a FE solution within blocks.

7.2 Uniaxial Compression Test

Figure 4 depicts a model of a uniaxial compression test, using 2nd order elements. Due to symmetry, only a quarter of the block is modelled, and the upper edge is restrained horizontally,

and displaced vertically downward, by 1%. The problem is modelled twice, using 1st and 2nd order elements.

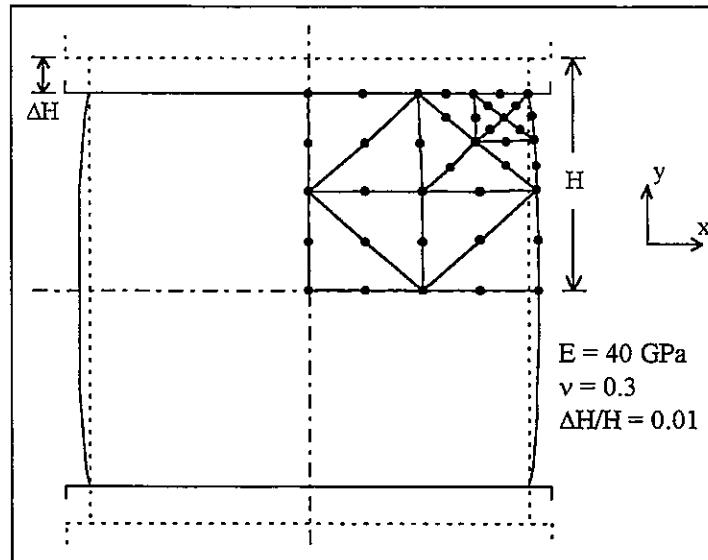


Figure 4. Geometry of the uniaial compression test

The two meshes each have 38 nodes, and therefore 76 degrees of freedom, and are composed of 54 1st order blocks, and 14 2nd order blocks, respectively. The original number of block deformation variables for the sub-block elements is therefore 324 for the 1st order mesh, and 168 for the 2nd order mesh. It can be seen that there is a considerable reduction in the number of degrees of freedom of the system during the meshing method.

In Figure 5, the vertical stress, σ_{yy} is plotted. Both meshes show a similar distribution of stresses across the sample, with a stress concentration at the corner of the sample, where it is restrained by the loading platen. Stress distributions obtained using the FE program ABAQUS (1996) are identical to these plots.

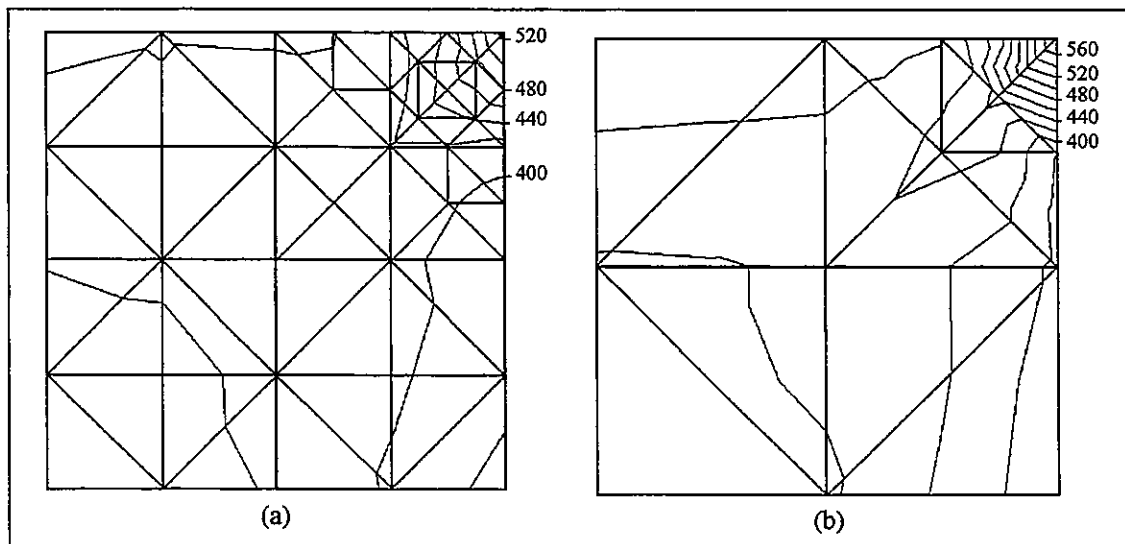


Figure 5. Contour plots of σ_{yy} (MPa) for (a) 1st order and (b) 2nd order elements.

8 CONCLUSIONS

Incorporating a meshing method into DDA extends the scope of the method in modelling engineering problems. The sub-blocking method of Ke and Goodman (1994) is the most common meshing method used at present. The primary disadvantage of this method is that all of the sub-blocks retain their six degrees of freedom. As shown above, using the nodal displacements as the block degrees of freedom can considerably reduce the number of solution equations, with no loss of accuracy.

The meshing formulation described above achieves this, while taking advantage of the numerical similarities of the two methods to incorporate FE meshing into the DDA method in a manner which is relatively simple to undertake, and computationally inexpensive.

The 1st order elements do not perform well in bending, but do provide satisfactory results in situations where bending is not the primary mode of deformation. 2nd order elements perform well in general, but are more expensive to use, as they have a greater number of degrees of freedom.

It should be noted that elements must display geometric isotropy, and therefore quadrilateral elements cannot be formulated. However, non-linear material behaviour could be incorporated, and the introduction of a fracture mechanism would further extend the usefulness of this analytical tool.

REFERENCES

- ABAQUS Version 5.6. 1996. © Hibbitt, Karlsson and Sorensen, Inc.
- Chang, C.-T. 1994. Nonlinear dynamic Discontinuous Deformation Analysis with Finite Element meshed block system. *Ph.D. Dissertation*, University of California, Berkeley.
- Chern, J.C., Koo, C.Y. and Chen, S. 1995. Development of second order displacement function for DDA and manifold method. *Working forum on the Manifold Method of Material Analysis*, Vicksburg. 183-202.
- Cook, R.D., Malkus, D.S. and Plesha, M.E. 1989. Concepts and Applications of Finite Element Analysis. 3rd Edition. John Wiley and Sons, New York.
- de Arantes, E.R. and Oliveira, E. 1977. The patch test and the general convergence criteria of the Finite Element method. *International Journal of Solids and Structures*, Vol. 13: 159-178.
- Ke, T.C. and Goodman, R.E. 1994. Discontinuous Deformation Analysis and the artificial joint concept. *Proceedings, 1st North American Rock Mechanics Symposium*, Austin. Balkema, Rotterdam. 607-614.
- Koo, C.Y. and Chern, J.C. 1996. The development of DDA with third order displacement function. *Discontinuous Deformation Analysis (DDA) and Simulations of Discontinuous Media*, Salami, M.R. and Banks, D. (eds). TSI Press, Albuquerque. 342-349.

Discontinuous Deformation Analysis (DDA) - Applications

METHOD OF STABILITY ANALYSIS OF A DAM-FOUNDATION-PLANT SYSTEM

Jue-Min Pei

Department of Hydraulic Engineering, Tsinghua University
Beijing 100084, PRC

ABSTRACT: DDA is a strong tool for stability analysis of dam foundation. This paper introduces the application of DDA on a complex foundation of a typical gravity dam. This dam consists of tens of dam blocks. Several blocks of the dam have a high foundation, which is cut down deeply behind the dam for setting the power plant. Because of the existence of large joints in dam foundation, the stability analysis of the dam-foundation-plant system is an important problem. DDA is used to compare with the traditional method called limit equilibrium of rigid bodies.

1 METHOD OF STABILITY ANALYSIS

1.1 *Method of Limit Equilibrium of Rigid Bodies*

A large gravity dam introduced here consists of tens of dam blocks. Of them several dam blocks are located on the left bank. These dam blocks have a high rock foundation, which is cut down deeply to the power plant behind the dam. It makes dam, foundation and plant to work as a combined system for bearing the loads of gravity and water pressure. The total height of dam and foundation is about 180 meters. The geological condition is complicated. There are large joints of multi-layers which cut across the foundation with an angle of near 25 degrees inclined to down stream. The stability analysis of the dam-foundation-plant system is a very complex problem.

The standard method of stability analysis used in China is the limit equilibrium method of rigid bodies. It is an experimental method of material mechanics, that is easy to use for engineers, but is too simple for important large projects. Satisfying the demand of simplifying calculation, we have to conceptualize the real distribution of joints to a simple plane and have to isolate the foundation to blocks arbitrarily, as shown in Figure1. In the calculation, the moment on contact plane is ignored and the strength parameters on isolated contact face is assumed, so the equilibrium formulas can be written as following:

$$K_1 = [f_1(W_1 - U_1 + \tau_{12}) + c_1 l_1] / (P - F_{12}) \quad (1)$$

$$K_2 = \{f_2[(W_2 + \tau_{23} - \tau_{21}) \cos \theta_2 - (F_{21} - F_{23}) \sin \theta_2 - U_2] + c_2 l_2\} / [(W_2 + \tau_{23} - \tau_{21}) \sin \theta_2 - (F_{21} - F_{23}) \cos \theta_2] \quad (2)$$

$$K_3 = \{f_3 [(W_3 - \tau_{32}) \cos \theta_3 - F_{32} \sin \theta_3 - U_3] + c_3 l_3\} / [(W_3 - \tau_{32}) \sin \theta_3 + F_{32} \cos \theta_3] \quad (3)$$

$$\text{and} \quad K_1 = K_2 = K_3 = K_c \quad (4)$$

here, K_i is the stability safety factor of block i , f_i is the friction coefficient and c_i is the cohesion, l_i is the length and θ_i is the angle of sliding plane i , W_i is the self weight force, U_i is the buoyancy force, P is the water pressure, F_{ij} is the thrust force and τ_{ij} is the shear force on contact plane between blocks i and j , K_c is the demanded stability factor, i and $j = 1, 2, 3$ is the number of block. Supposing $\tau_{ij} = 0$, K_c and F_{ij} can be found.

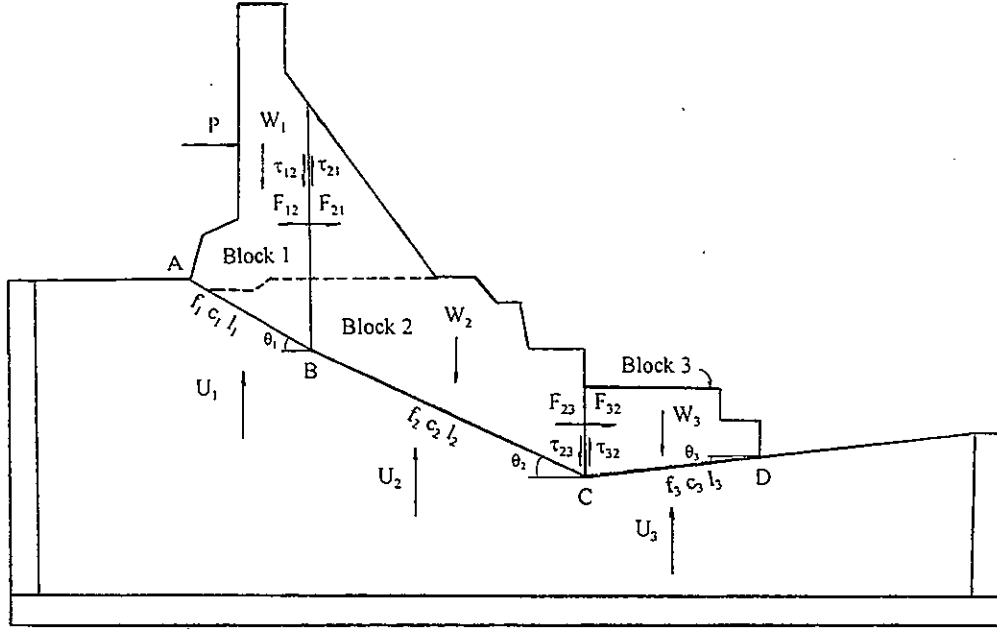


Figure 1. Limit equilibrium of rigid bodies

Obviously the reasonableness of above method is doubtful. The problems are those as followings. τ_{ij} should not be equal to zero, the moment on contact plane also can not be ignored, K_i of each segment of the sliding plane is impossible to be the same, the sliding planes of multi-layers work interactively and do not work only on a plane of single layer, and most importantly the joints exist naturally and could not be isolated arbitrarily.

1.2 Method of DDA

Based on the DDA, above problems are easy to be overcome. The DDA method of stability analysis does not need to assume any joints and blocks. The joints and blocks all are real and natural, shown in Figure 2. It shows that there are about 50 large joints in foundation. Their dip angles all incline to downstream. It is very disadvantageous to the stability of dam and foundation. The power plant is used to increase some resistant force to the dam and foundation.

It forms a combined action system of dam-foundation-plant. Due to the existence of joints of multi-layers, the combination of sliding planes is very complex. There are two single sliding planes, ac and ag, which are possible to slide independently, and five combined sliding planes, AE, AI, AGSOWY, JI and MPNIE, which are possible to slide interactively as a dam-foundation-plant system. Their dominant combination will be the planes AE, JI and MPNIE.

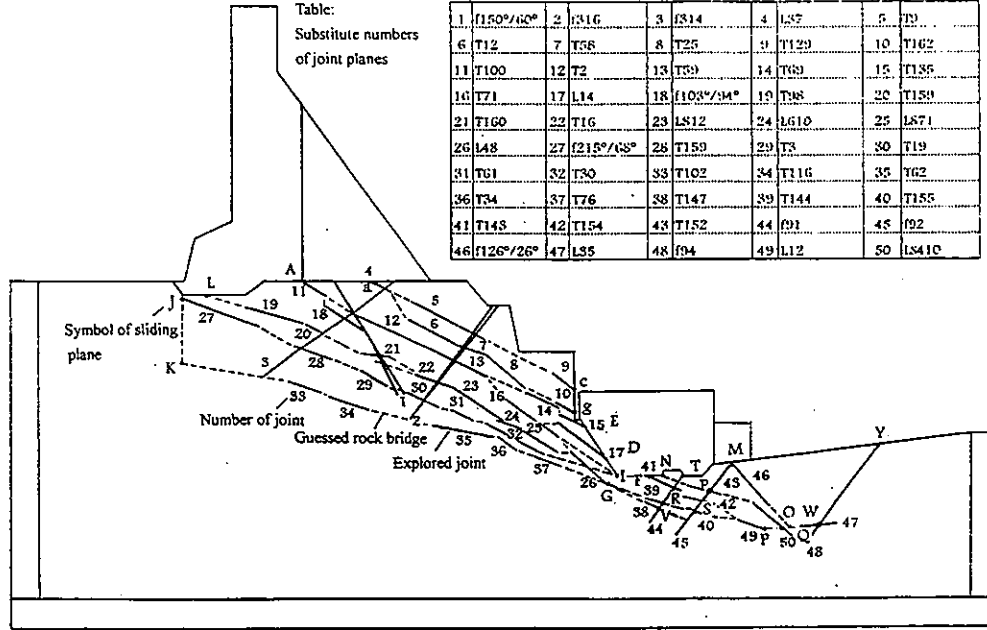


Figure 2. Distribution of joints in DDA

The coefficient of strength reserve, K , is used as the stability safety factor. As taking $K=1,2,3,4$ and 5 , we can obtain a relationship curve of K (the stability safety factor) versus S (the slid displacement of joints) of each connected sliding joint planes. From that the limit value of K_s can be found. This limit K_s is determined by the limit displacement on sliding plane. It can be used to check the stability factor of the force equilibrium, K_e . They are completely identical in both situations and are coupled in calculation.

From the relationship curve of $K \sim S$, we can find the suddenly increasing point on the displacement curve. Corresponding to this point, the safety factor of limit displacement, K_s , can be found. Beyond this limit point the sliding will occur. At same time, the safety factor of limit equilibrium, K_e , can be calculated as below. Assume $\sigma_{x(i)}, \sigma_{y(i)}, \tau_{xy(i)}$ is the stress on i th segment of sliding plane, $\theta_{(i)}$ is the angle of inclination of i th segment, then the normal stress $\sigma_{y(i)}$ and the shear stress $\tau_{\theta(i)}$ on i th segment will be written as:

$$\begin{aligned}\sigma_{\theta(i)} &= \sigma_{x(i)} \cdot \cos^2(90-\theta_{(i)}) + \sigma_{y(i)} \cdot \sin^2(90-\theta_{(i)}) + 2\tau_{xy(i)} \cdot \sin(90-\theta_{(i)}) \cdot \cos(90-\theta_{(i)}) \\ \tau_{\theta(i)} &= (\sigma_{x(i)} - \sigma_{y(i)}) \cdot \sin(90-\theta_{(i)}) \cdot \cos(90-\theta_{(i)}) + \tau_{xy(i)} \cdot [\sin^2(90-\theta_{(i)}) - \cos^2(90-\theta_{(i)})]\end{aligned}\quad (5)$$

If φ is the friction angle and c is the cohesion, then the unit resistant force $S_{(i)}$ and the unit sliding force $T_{(i)}$ of segment i will be:

$$\begin{aligned} S_{(i)} &= \sigma_{\theta(i)} \cdot \tan \varphi_{(i)} + c_{(i)} \\ T_{(i)} &= \tau_{\theta(i)} \end{aligned} \quad (6)$$

The unit resistant force S_L and the unit sliding force T_L on whole sliding plane will be:

$$\begin{aligned} S_L &= \sum_{i=1}^n S_{(i)} \cdot W_{(i)} \\ T_L &= \sum_{i=1}^n T_{(i)} \cdot W_{(i)} \\ W_{(i)} &= L_{(i)} / \sum_{i=1}^n L_{(i)} \end{aligned} \quad (7)$$

Here, $L_{(i)}$ is the length of i th segment of sliding plane, $\sum_{i=1}^n L_{(i)}$ is the full length of n segments, $W_{(i)}$ is the weighting function and $\sum_{i=1}^n W_{(i)}$ is equal to 1. From formula (7), the limit stability safety factor of force equilibrium on whole sliding plane can be written as:

$$K_e = S_L / T_L \quad (8)$$

Comparing K_e with K_s , both values ought to be identical. If it is not, K_s will be reselected until both identical.

2 STABILITY TENDENCY OF DAM-FOUNDATION-PLANT SYSTEM

The method of limit equilibrium of rigid bodies supposes that the blocks can only slide in a static state on a certain sliding plane. Therefore the sliding on a single plane is considered to take place instantly and there is no interaction among the sliding planes of multi-layers. It means that the strength on the sliding planes has to reach the limit value in same time and no stress transfer between planes occurs in sliding process.

Based on DDA, the dynamic process analysis of the stability of sliding planes of multi-layers shows that above hypothesis of limit equilibrium method is not true. It proves that in the dynamic sliding process the slid displacements on joint planes are developed gradually, and with the displacement developing the stress redistributes correspondingly among the sliding planes of multi-layers. The interaction of sliding planes is evidently and they do not work singly.

Figure 3 shows the sliding states of sliding planes of multi-layers when $K \rightarrow \infty$. It gives a displacement tendency of dam-foundation-plant system. The sliding process indicates that the different sliding planes have various slid displacements. The shallow layers ac and ag are possible to slide individually and to cause large displacement first, because they are separated from the plant block at beginning. Once planes ac and ag move slightly, the stress in dam toe will be redistributed to upper part of plane AE, that will make the deformation of longitudinal seam of dam and the thrust force on AE enlarged. Because the stability of plane AE is not enough, the

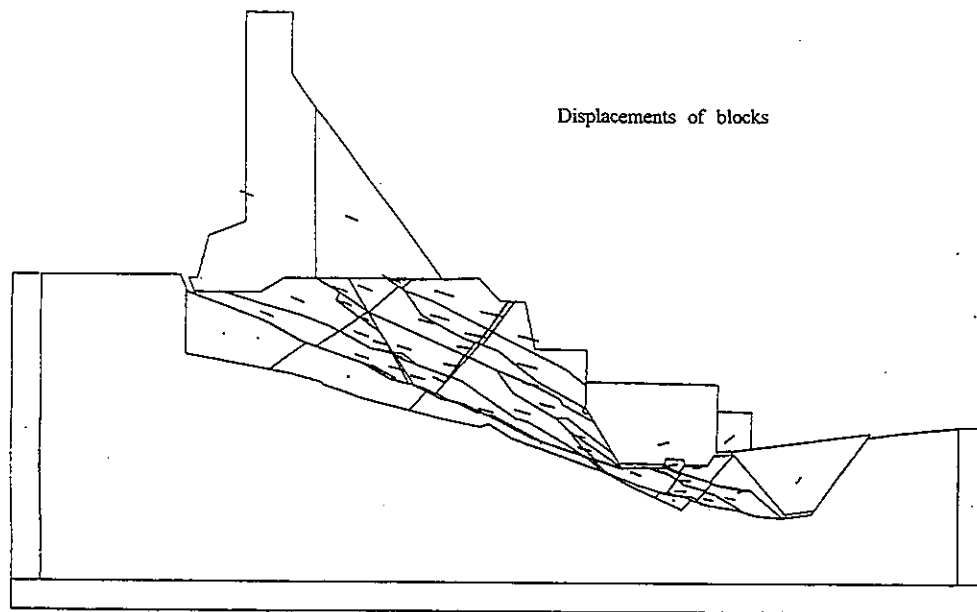


Figure 3. Slid displacement tendency on joint planes

plant block has to suffer a part of sliding force. The stability of sliding planes will be supported by dam-foundation-plant system. Its dominant sliding plane is combined with planes of AE, JI and MPNIE according to calculation. The combined system of dam-foundation-plant will act on planes AE-JI-WPNIE commonly in the sliding process. Figure 4 shows the sliding tendency of dam-foundation-plant system. The dam block tends to move down stream, and its half part behind

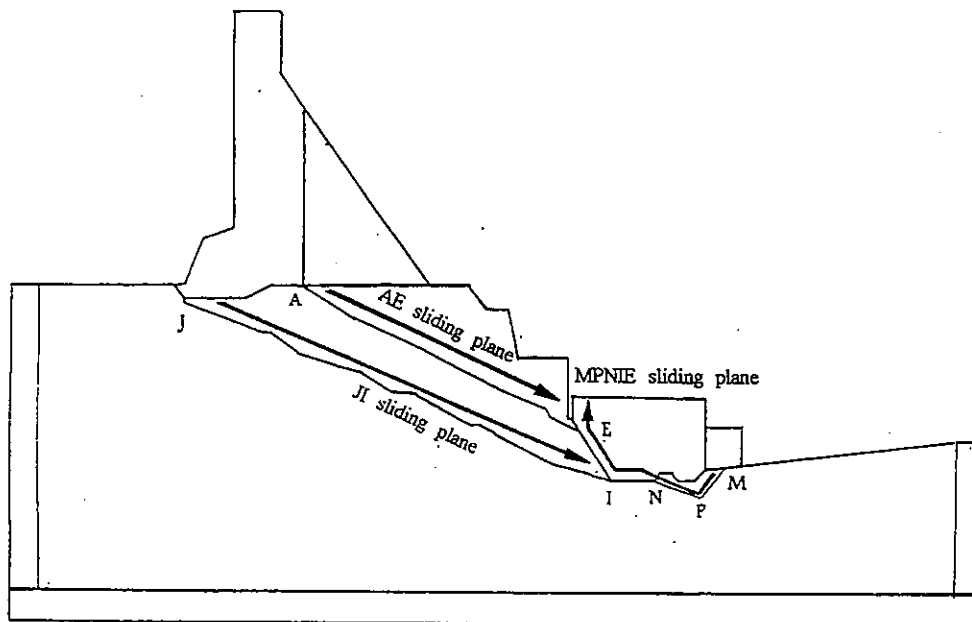


Figure 4. Combined sliding planes

the longitudinal seam will sink along the plane AE. Planes AE and JI tend to slide down stream and the plant block tends to rotate clockwise on plane WPNIE around the point M of tooth trench. This situation will be kept till the bearing capacity on plane WPNIE is lost. Only as plane WPNIE already slid, the sliding force can transfer to the lower plane of AGSOWY and cause it sliding in deep foundation. Therefore the sliding control planes of the system will be combined with AE-JI-WPNIE, which gives a minimal stability factor of the combined system.

3 COUPLED ANALYSIS OF DEFORMATION AND STABILITY

3.1 Contact Modes

The contact modes of joints include three kinds of M_{fc} —before block slides, the parameters of the strength, f (friction coefficient) and c (cohesion), are existent, M_{fp} —as block slides, only f exists and M_{00} —as joint plane bears tensile force, then $f=0$ and $c=0$. Because the slid displacements and bearing forces of joints and rock bridges are different, the strength parameters of contact planes

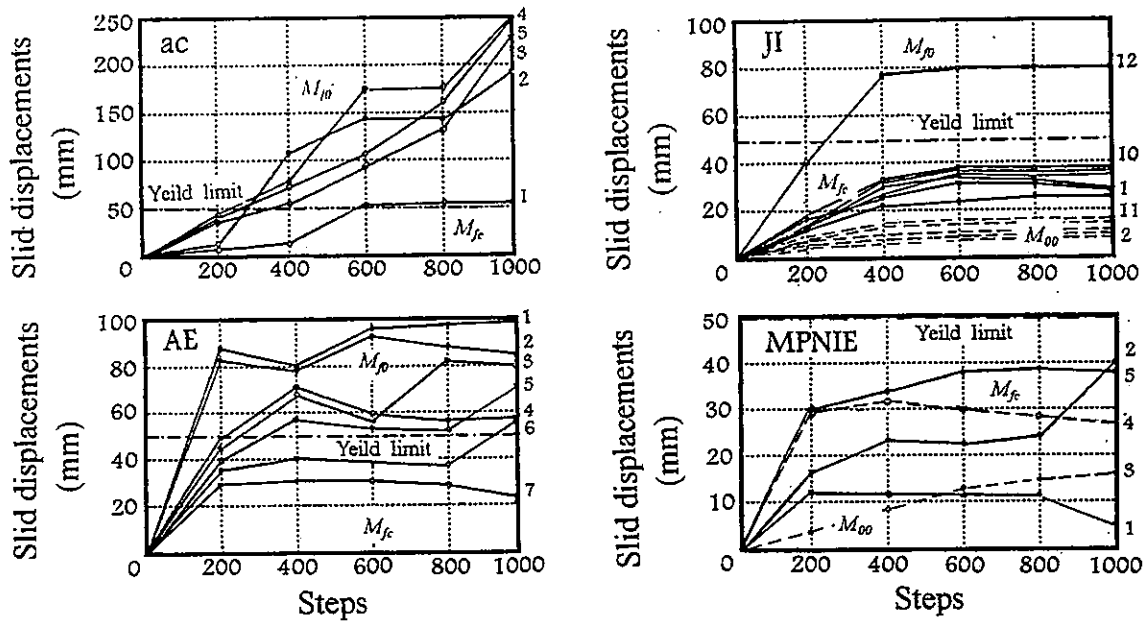


Figure 5. Contact modes of sliding planes

also are variable. Only the relative displacement on the contact plane reaches to a yield limit value, the sliding will occur. Figure 5 shows the fracture process of several segments of sliding planes. The number 1,2,3,... is the segment order that is numbered from the top of sliding plane. If the displacement is less than the yield limit value, the contact mode is M_{fc} , otherwise it is M_{fp} , and if the joint opens it is M_{00} . Figure 5 shows that on the segments of sliding planes, the contact modes are not as the same. If all the blocks on the whole sliding plane slide, it can be said that the sliding plane is really sliding. At this time the contact modes of all blocks are M_{fp} .

3.2 Limit Displacements

The block sliding is gradually developed. With the coefficient of strength reserve, K , increasing, the slid displacement S on sliding plane will increase too. As S suddenly increases to a large value, all the blocks on whole sliding plane are sure to slide. We can consider K at this turn point as a limit K_s , which can be seen as the stability factor of whole sliding plane. In the foundation, there is a certain plane of the sliding planes of multi-layers which will reach to the limit K_s first, and others may be not. Figure 6 shows the relationship curves of $K \sim S$ of different sliding planes. The most instability plane is ag, whose yield limit S is about 50 mm. Its corresponding $K_s = 1.4$. We can use this yield limit value of 50 mm to judge if other sliding planes to be stable, shown in Table1.

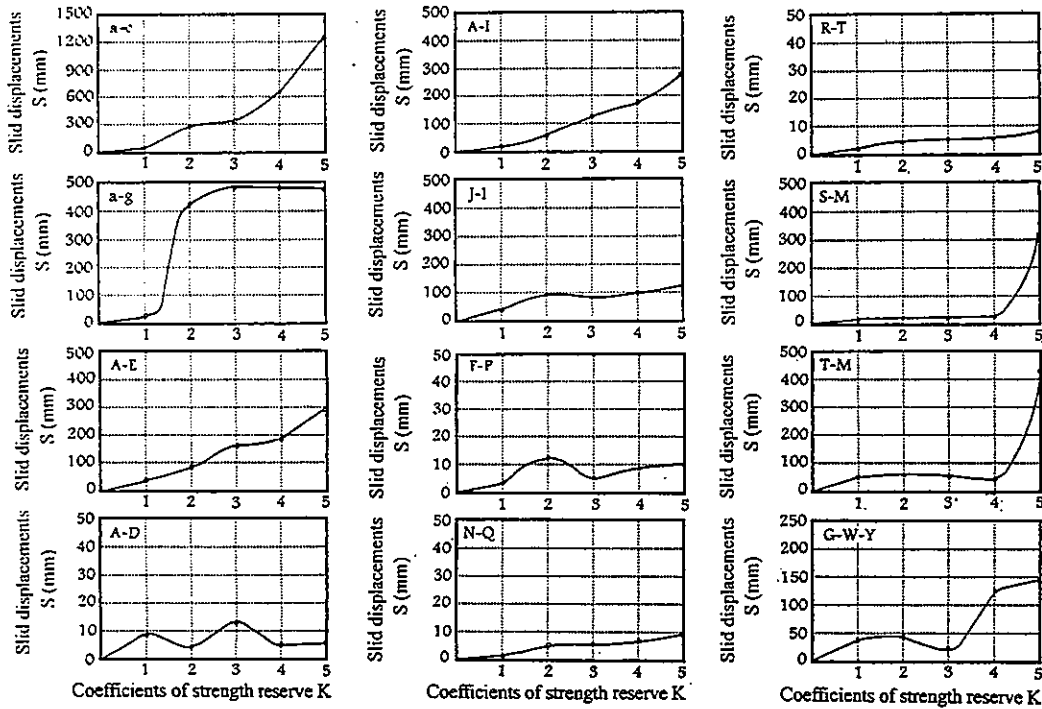


Figure 6. Slid displacements on sliding planes

3.3 Limit Equilibrium

Above K_s is found from curves of $K \sim S$. It has to identify with K_e , which is the stability factor obtained by the equilibrium of contact forces. In the calculation of K_e , the contact forces and contact modes of different sliding planes are considered. According to the formulas 5 to 8, we can obtain K_e of various planes. Table1 shows the percentages of M_{fc} , M_{f0} and M_{00} , sliding and resistant forces and the safety factors of all the sliding planes in interaction. The calculated K_e is compared with K_s . It indicates that they fit close. The limit displacement and limit equilibrium are coupled each other. If the difference between them is too large, the limit S should be

reselected until both closed. The stability factor of pure friction, K_f , is used for checking, which is assumed the complete sliding occurring on whole sliding plane and considered the friction strength to be reduced to eighty percent.

Table 1. Sliding plane, contact modes, unit resistance and sliding force, and K_s , K_e , K_f

Slide plane	Contact mode(%)			Unit force(t/m)		K_s	K_e	K_f
	M_{fc}	M_{θ}	$M_{\theta\theta}$	R	T			
Ac	0	100	0	29.37	18.10	1.60	1.62	1.30
ag	0	100	0	30.52	21.68	1.40	1.41	1.13
AE	13	87	0	36.64	27.37	1.30	1.34	1.00
AI	0	100	0	24.63	13.68	1.90	1.80	1.44
AGSOWY	20	80	0	54.57	14.92	3.50	3.65	2.70
JI	60	0	40	114.37	67.53	1.60	1.69	1.13
MPNIE	75	0	25	88.56	29.76	3.00	2.97	1.49
AE-JI-MPNIE	48	28	24	76.33	47.68	1.74	1.76	1.07

In Table1 the situations of stability of different sliding planes can be seen. The single sliding plane ac and ag has lower stability factors K_f of 1.30 and 1.13. The lowest stability factor K_f is of plane AE, it is 1.00. Although as so, plane AE is not a single sliding plane as ac or ag, it acts in combination with the plant block and others. Its stability ought to be evaluated in the combined action.

3.4 Combined Action

In certain degree, the stability of foundation is dependent upon the combined action of dam and plant. If there is no support of plant, the stability factor of AE can not be satisfied the condition of $K_f > 1.0$. Table 1 shows that K_e of the plant is 2.97 and K_e of the foundation is 1.34~1.69. Under the combined action of dam and plant, the whole stability factor K_e of dam-foundation-plant system can raise to a higher value of 1.76. Its corresponding value of K_s is 1.74 and that of K_f is 1.07. These results show the effects of combined action. The stability factor K_f of plane AE will be enlarged from 1.0 to 1.07 together with the dam-foundation-plant system. But the stability factor of totality is still not high enough in value. Even considering the assumption of DDA method being more actual and detailed and its trusty of calculation more than any other methods, the reinforcements such as anchorage and grouting are still necessary.

3.5 Structure Safety

Under the combined condition, the dam and plant still need to take care to the problem of structure. The longitudinal structure seam of dam is possible to be opened by tension and the plant block is possible to be inclined with rotation, which may effect on the safety of pressure

pipe and turbine generator. According to the calculation, the longitudinal structure seam of dam will open with a horizontal span of 47 to 120 mm and will sink vertically with a differential settlement of 48 to 84 mm at its bottom as K changing from 1 to 5. The acting force loaded on power plant changes from 1500 t/m to 5000 t/m on thrusting and from 0 to 2000 t/m on shearing as K changing from 1 to 5. The safety of deformation and stress of the pressure pipe, which is across the dam and power plant, should be checked later in this situation.

4 CONCLUSION

Using DDA to analyze the stability can thoroughly overcome the shortcomings of limit equilibrium method of rigid bodies. This method of stability analysis of discontinuous deformed blocks can couple the deformation and stability into a whole. In here the results of stability analysis and deformation calculation are identical, that enhances the stability analysis method to a new level.

The new method has many advantages. (1) There is no any hypothesis, the joints can be modeled as nature. (2) The contact forces include the shear force, normal force and the moment. (3) Three kinds of contact modes are used on sliding planes. (4) The stability factor can be calculated by limit displacement and limit equilibrium, they are identical. (5) It can calculate the combined action of sliding planes of multi-layers in dynamical state.

Because this new method considered more actual situation, which is ignored in other methods, the calculated stability factor reduces about 40% than that calculated by limit equilibrium method of rigid bodies. It means that using limit equilibrium method of rigid bodies to calculate the stability factor will lead to an over high value.

The limit equilibrium method of rigid bodies was developed in the fifties of this century. In that time the computer and the numerical method were not very developed. Using the experimental method of material mechanics in that time was normal. As the time up to now, the computer and numerical method, including DDA, are used very widely, we ought to change our conception and to use some new method in our works. According to above comparison, we can say that DDA as a strong tool of the stability analysis is doubtless.

REFERENCES

- Pei, Jue-Min, 1997. *The dynamic stability analysis of discontinuous elastic foundation of a certain dam*. Research Report.
- Water Conservancy Committee of Yangtze River of WCM, 1996. *The direction of the method and results of the limit equilibrium of rigid bodies*. Research Report.
- Water Conservancy Committee of Yangtze River of WCM, 1997. *The geological condition of combined action of foundation, dam and plan of a certain dam*. Research report.

ANALYSIS OF CYCLIC PLASTIC DEFORMATION OF RAILROAD BALLAST BY DDA

Tatsuya Ishikawa,
East Japan Railway Company, Technical Development and Research Department,
2-2-2 Yoyogi, Shibuya-ku, Tokyo 151-8578, JAPAN

Yuzo Ohnishi
Kyoto University, Department of Civil Engineering,
Yoshida-honmachi, Sakyo-ku, Kyoto 606-8501, JAPAN

ABSTRACT: This paper presents an analytical study to elucidate the cyclic plastic deformation of railroad ballast in ballasted railway track under train passage, that is "track deterioration". The simulations of full-scale vertical cyclic loading tests of railroad track regarding a ballast particle as a DDA block were performed, and the applicability of DDA to the cyclic plastic deformation of railroad ballast was discussed. It was found that the cyclic plastic deformation of railroad ballast could be defined as the fabric transformation of particle alignment accompanied by sliding between particles. DDA is useful to trace the movement of particles and to unveil the complex deformation mechanics of granular ballast materials.

1 INTRODUCTION

At a ballasted railway track, the phenomenon such that irregularity of rail level under train passage increases, so called "track deterioration", is frequently observed. Since it threatens the safety of train operation, the mechanism of track deterioration is one of major assignments to be elucidated in railway engineering, and the theories to explain track deterioration have been proposed in many countries for several decades. The track deterioration is a concept different from total failure of structures like landslide, because it is an accumulation of deformation due to cyclic loading. In other word, the dominant factor of track deterioration is supposed to be the plastic deformation of "railroad ballast," which is a track component of ballasted railway track composed of crushed stone (ballast), caused by cyclic train passages. But the conventional analysis method, which assumes railroad ballast as a continuous structural body, can't evaluate such a feature. Now it is urgently necessary to develop a reasonable analysis method of track structure in order to rationalize the design method of ballasted railway track.

In order to investigate track deterioration in detail, vertical cyclic loading tests with a full-scale track at special test facilities (Ishikawa et al. 1999) and monotonic and cyclic loading triaxial compression tests of ballast samples (Ishikawa et al. 1997) had been performed by the authors et al. in the past. At the same time, the possibility of application of DDA (Discontinuous Deformation Analysis, Shi and Goodman 1985) to the coarse granular materials was discussed by simulating laboratory triaxial tests of ballast (Ishikawa et al. 1997). We found that the deformation of railroad ballast could be estimated most effectively by regarding

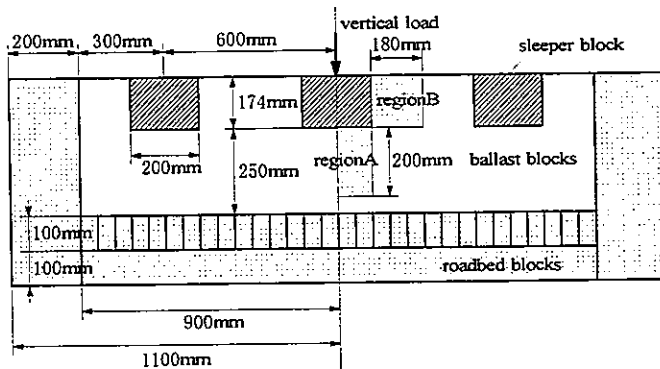


Figure 1. Schematic section of DDA model (line profile)

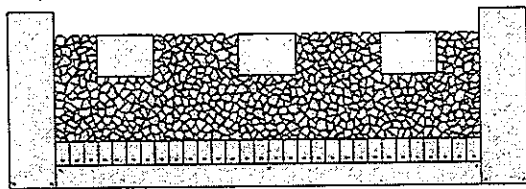


Figure 2a. Element mesh of caseA

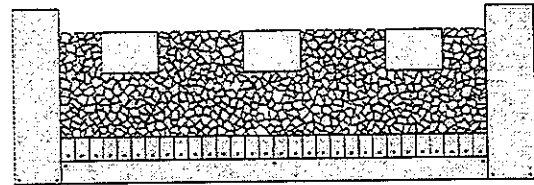


Figure 2b. Element mesh of caseA1

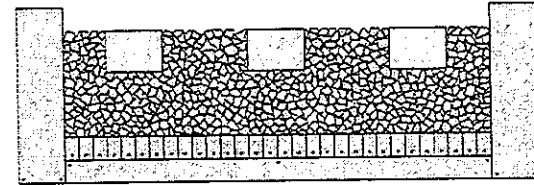


Figure 2c. Element mesh of caseA2

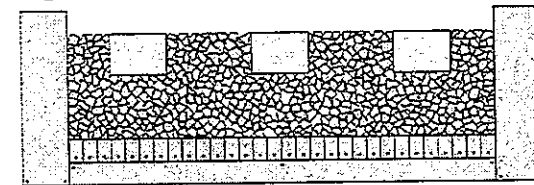


Figure 2d. Element mesh of caseA3

ballast as an assemblage of coarse granular materials. It was shown that DDA is to some extent an effective method to analyze the behavior of ballast. But it was revealed that DDA had some difficulties to handle the deformation of coarse granular materials that had large friction angle between gravel surfaces such as ballast.

Considering the above mentioned results, the simulations of full-scale track tests regarding a ballast particle as a DDA block were performed in this study, and the applicability of DDA to understand the cyclic plastic deformation of railroad ballast was discussed in comparing analytical and experimental results. Also the suitability and limitation of DDA application to track deterioration were discussed considering the mechanics of granular materials. This study is fundamental for establishing the theory of track deterioration that could explain the mechanism of the cyclic plastic deformation of railroad ballast.

2 ANALYTICAL METHOD

2.1 Modeling

Figure 1 shows the size, dimension and boundary condition of analytical model (section profile) for simulating cyclic loading tests of a full-scale track. This profile is normally used for Japanese railway. Detailed testing method and experimental results can be examined in Ishikawa et al. 1999. Figure 2 shows some element meshes of DDA model before loading, which are two-dimensional models using linear elastic elements with plane strain. Each polygon element (block) expressing ballast particle is made by the method of Voronoi tessellation. The gradation curve for the railroad ballast of DDA model is shown with real gradation of ballast in Figure 3, and Table 1 shows the features of DDA model in comparison with test's conditions. CaseA is different from caseB in the block size of ballast blocks because their di-

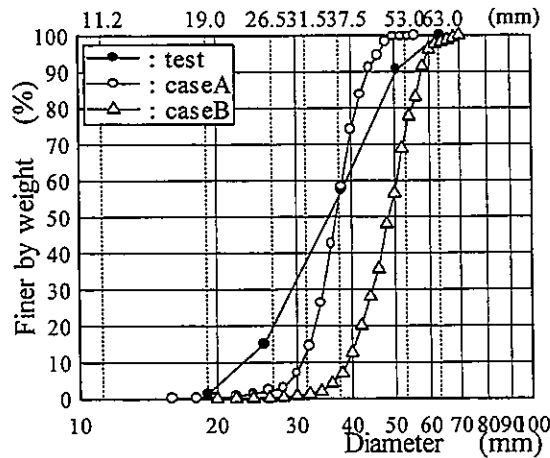


Figure 3. Grain size distribution

Table 1. Features of DDA model

Property	caseA	caseB	test
Number of ballast blocks	571	336	—
Uniformity U_c	1.24	1.29	1.70
Mean grain size D_{50}	37mm	48mm	36mm
Porosity n	15.4%	16.0%	43.2%

Table 2. Material properties of analytical model

Property	tie	ballast	roadbed
Unit mass γ (DDA)	2.38 tm^{-3}	2.77 tm^{-3}	2.20 tm^{-3}
Young's modulus E (DDA)	30 GPa	20 GPa	75 GPa
Poisson's ratio ν (DDA)	0.20	0.10	0.40
Cohesion C_u (DDA)	0	0	0
Friction angle ϕ_u (DDA)	37°	55°	37°
Unit mass γ (FEM)	2.38 tm^{-3}	1.70 tm^{-3}	2.20 tm^{-3}
Young's modulus E (FEM)	30 GPa	150 GPa	75 GPa
Poisson's ratio ν (FEM)	0.20	0.35	0.40

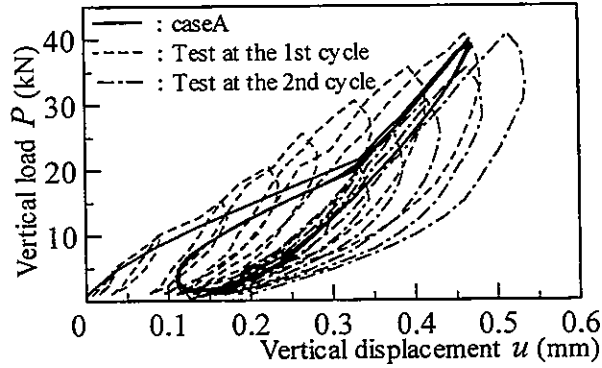
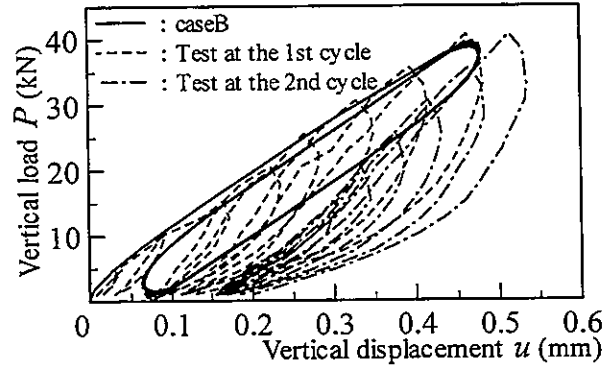
vision number by Voronoi tessellation are different (Table 1). While, four models as shown in Figure 2 are different in the porosity distribution inside railroad ballast. Especially three models of the Cases A1, A2, A3 are ones that remove some DDA blocks from ballast blocks of caseA under sleeper (tie) or between neighboring sleepers at random. Removal of blocks is to simulate the field condition disturbed by an ordinary maintenance operation around sleepers using a hand-held tamper. Here, the actual density distribution of railroad ballast isn't simulated in both caseA and caseB. The actual laminated state of railroad ballast under test conditions is 3-dimensional and shows 40.4%~45.9% range of porosity (Ishikawa et al. 1999). From the past study (Ishikawa et al. 1997), it was known that the porosity of two-dimensional model can be converted into that of three-dimensional model using the reasonable ratio of 2.4. The DDA calculation is two-dimensional and the porosity of their model is probably estimated in the range of 19.1 % from 16.8 %, which is nearly equal to our Voronoi model. DDA simulations were performed as follows; in order to set up a model configuration at the first stage the package of ballast blocks was made by throwing blocks one by one into a form of track profile to express the random particle alignment in a restricted area. Subsequently the form was removed and the stability analysis was done by dead weight. In the case of Figure 1 blocks are randomly thrown in two a rectangular box with invisible sleepers and the initial loading state was made by loading the gravity force. Then the triangular vertical load were applied to the center sleeper (Fig. 1) five times at the load frequency of 2Hz with the amplitude of pulsating compression load.

2.2 Analytical conditions

Table 2 shows the material properties of blocks and the interface properties of block edges. The reason why the block friction angle ϕ_u between ballast blocks was set equal to 55° is that the internal friction angle derived from the DDA analysis results with $\phi_u=55^\circ$ indicated the best fit to the actual triaxial test results of ballast samples (Ishikawa et al. 1997). As for ϕ_u between ballast block and sleeper block, the value was set equal to 37° referring to conventional studies. Furthermore, the parameters except ϕ_u needed for the analysis was derived from the

Table 3. Analytical conditions

Model name	$P_{max}(\text{test})$	$P_{max}(\text{analysis})$	Loading ratio
caseA	40.0kN	1.56kN	3.9%
caseA	30.0kN	0.75kN	2.5%
caseA	20.0kN	0.40kN	2.0%
caseA1	40.0kN	1.08kN	2.7%
caseA2	40.0kN	2.04kN	5.1%
caseA3	40.0kN	1.16kN	2.9%
caseB	40.0kN	1.36kN	3.4%

Figure 4a. P - u relations (caseA)Figure 4b. P - u relations (caseB)

actual triaxial compression test results. Table 3 shows the analytical condition of each simulation briefly. Here, the loading ratio is the value that divided the analytical load by the experimental load when the vertical displacement of analytical results coincide with that of experimental results. According to Table 3, the analytical load is much smaller than the experimental load because the loading ratios are in the range of 2.0 % to 5.0 %. Also it is recognized that the loading ratio increases as the vertical load becomes bigger, and that the loading ratios of each model are different even if comparing them at the same load. So in this paper, the value that divides the analytical load by the loading ratio as shown in Table 3 is regarded as the cyclic vertical load P_{max} of analytical results.

On the other hand, the simulations of full-scale track test were also performed with FEM in order to compare the DDA results with the ones by FEM. The simulations of FEM were done with a three-dimensional element mesh and two two-dimensional element meshes, which sections are similar to the element mesh of DDA model. The element of FEM is the linear elastic body, whose material properties are also shown in Table 2. The analytical parameters for railroad ballast are derived from the triaxial test results of ballast samples under the same stress condition of railroad ballast on train passages (Ishikawa et al. 1997). The parameters except railroad ballast are the same as DDA model. But neither the discontinuity between sleeper and railroad ballast nor the discontinuity between ballast particles is considered in FEM models.

3 CYCLIC PLASTIC DEFORMATION

3.1 Influence of block size

Figure 4 shows the load-displacement relations of $P_{max}=40\text{kN}$ from the 1st cycle to the 5th cy-

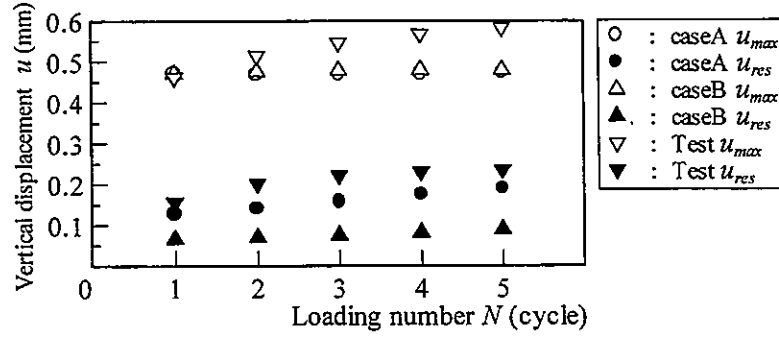


Figure 5. Increment of settlement under cyclic loading

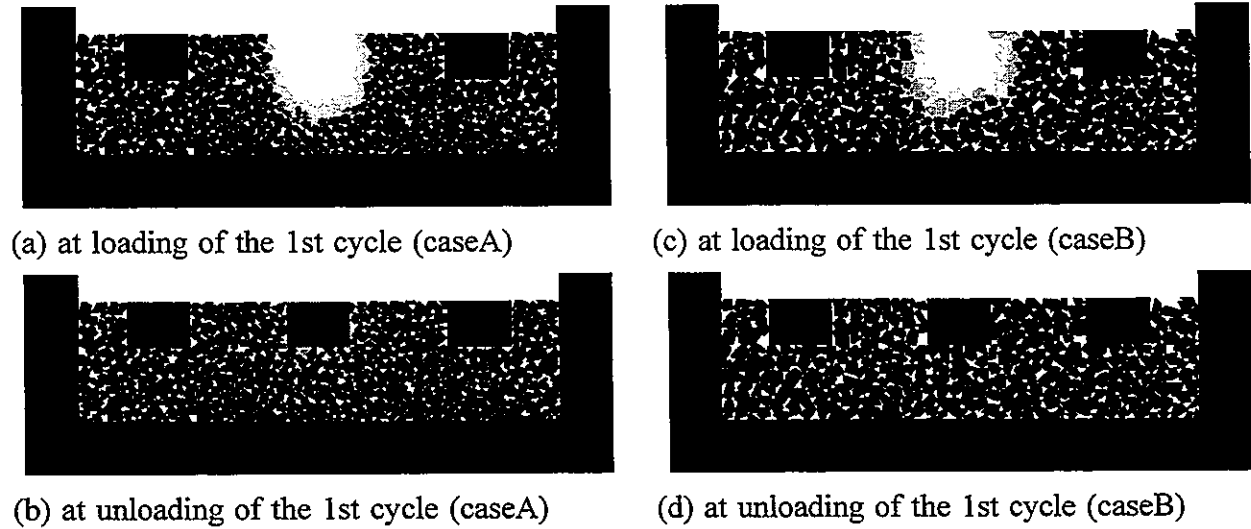


Figure 6. Distribution of vertical displacement

cle comparing analytical results of caseA and caseB with experimental results. Here, the vertical displacement u is the settlement of ballast blocks. Figure 4 shows a big hysteresis-loop in loading curve and unloading curve at the 1st cycle and permanent settlement increases in a great amount. But the area of hysteresis-loop of the 2nd cycle and later decreases and the deformation characteristics of railroad ballast become elastic and constant. Such a tendency of analytical results agrees with experimental results qualitatively. Further comparing the result of caseA with that of caseB in relation to the shape of the loading curve, the latter is nearer to the experimental result than the former because the loading curve of caseA turns in the neighborhood of $u=0.35\text{mm}$. Figure 5 shows the transition of vertical displacement u_{res} at unloading and vertical displacement u_{max} at the maximum load under cyclic loading of $P_{max}=40\text{kN}$ comparing analytical results with experimental results. In particular, u_{res} is used as a measure of cumulative permanent settlement. According to Figure 5, both the permanent settlement generated at the 1st cycle and its increment of the 2nd cycle and later in analytical results of every model are smaller than experimental results, and the result of caseA is closer to the experimental result than that of caseB as to the quantity of plastic displacement. Figure 6 indicates how the vertical component of displacement vector that connects the center of gravity of a block at initial loading state with the one at the designated load is distributed in loading of $P_{max}=40\text{kN}$ at the 1st cycle comparing analytical results of caseA with that of caseB. Here, the

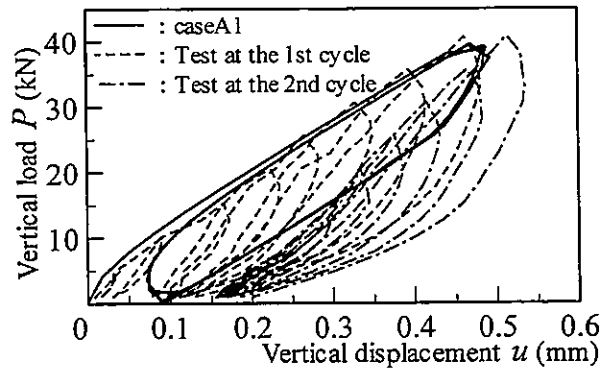


Figure 7a. P - u relations (caseA1)

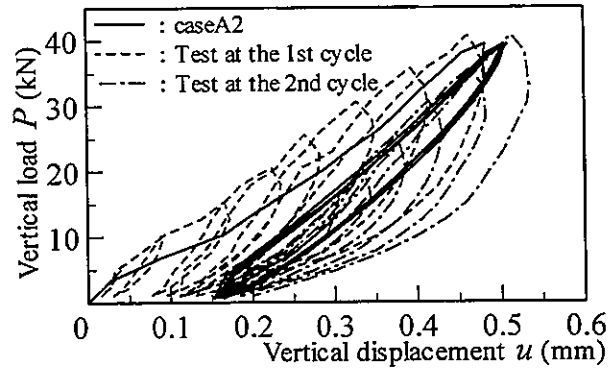


Figure 7b. P - u relations (caseA2)

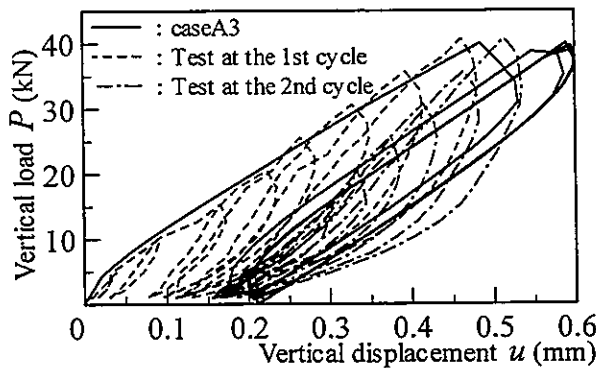


Figure 7c. P - u relations (caseA3)

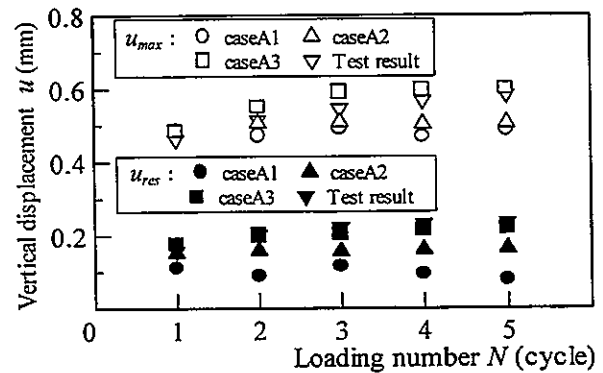


Figure 8. Increment of settlement

more a block moves toward the vertical direction, by the brighter color it is painted. Figure 6 shows that some ballast blocks adjacent to a loading block form the subsidence area, looks like an eggplant shape, where its loading block is the center at loading. And the some blocks don't come back to the original position of initial loading state at unloading. From the preceding results, it is concluded that the cyclic deformation of railroad ballast originates in the movement of ballast particles accompanied by the fabric transformation of particle alignment during cyclic loading. Comparing the result of caseA with that of caseB, the subsidence area of the latter becomes larger than that of the former. And the area of residual subsidence in caseB decreases very much. In general, the movement of individual block in the example analysis with a few blocks influences the deformation of whole model strongly. So it is considered that the analytical results of caseA with many blocks, of which mean grain size D_{50} is almost equal to that of actual tests, became closer to real behavior than that of caseB with a few blocks in case a difference between case A and caseB isn't found in both porosity n and uniformity coefficient U_c as shown in Table 1.

3.2 Influence of porosity distribution

Figure 7 shows the load-displacement relations of $P_{max}=40\text{kN}$ from the 1st cycle to the 5th cycle comparing analytical results of caseA1, caseA2 and caseA3 with experimental results, whereas Figure 8 shows the transition of vertical displacement u_{res} and u_{max} under cyclic loading of $P_{max}=40\text{kN}$. Comparing analytical results of caseA1 that there are some pores at ballast

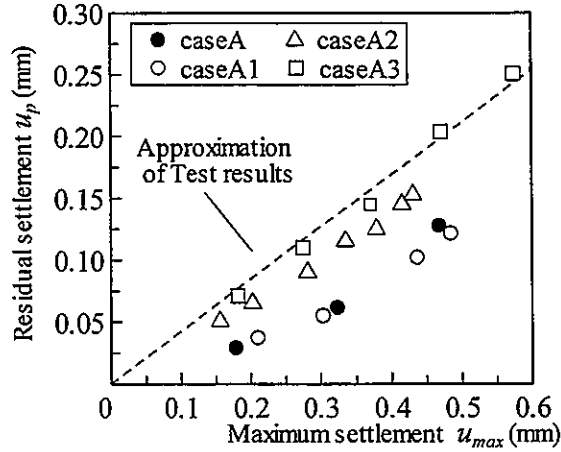


Figure 9. Property of plastic deformation

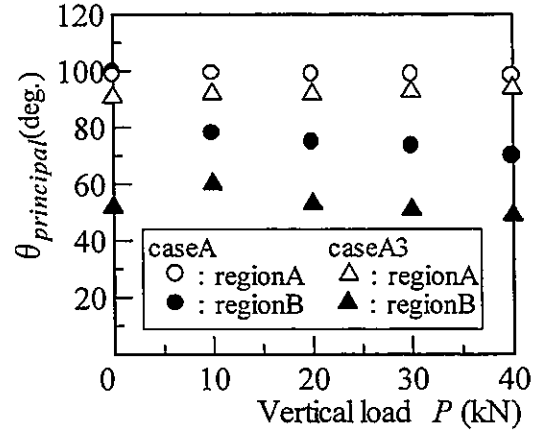


Figure 10. Deformation characteristics

blocks under sleeper with that of caseA2 that there are some pores at ballast blocks between neighboring sleepers, the former is closer to the experimental result as to the shape of the loading curve than the latter, but the latter is nearer to the experimental result as to both the change of hysteresis-loop with the repetition of load and the increasing tendency of plastic displacement than the former. Also the permanent settlement of caseA3 generated at the 1st cycle is nearly as large as that of experimental results and the amount of the plastic displacement generated at the 2nd cycle and later is almost the same as experimental results. Besides, Figure 9 shows the relations between u_{max} and u_{res} at the 1st cycle comparing analytical results of each model with the approximation line derived from experimental results. According to Figure 9, u_{res} of each model increases with the increment of u_{max} as well as experimental results. Also comparing analytical results of each model at the same u_{max} , it is recognized that the plastic displacement by models having some pores only under sleeper is smaller than the one by models having some pores between neighboring sleepers, and that the relation of caseA3 is closest to that of experimental results among all analytical results. From the preceding results, it is considered that the distribution of pores under sleeper has a considerable influence on the rigidity of ballast blocks, and that the distribution of pores between neighboring sleepers has a considerable influence on the cyclic plastic deformation of ballast blocks. The reason why above mentioned consideration was derived from analytical results seems to be that the principal mechanism of cyclic plastic deformation inside railroad ballast changes by the distribution of pores. Figure 10 shows the relations of each model between direction of principal axis $\theta_{principal}$ defined as Equation (1) and vertical load P at each region as shown in Figure 1 in loading of $P_{max}=40\text{kN}$ at the 1st cycle. Here, $\theta_{principal}$ is the prominent direction for the vector of contact force. However the direction θ for the vector of contact force is measured from the horizontal plane counterclockwise.

$$\theta_{principal} = \frac{1}{2} \arctan \frac{\sum \sin 2\theta_k}{\sum \cos 2\theta_k} \quad (0 \leq \theta < 180^\circ) \quad (1)$$

Seeing Figure 10, $\theta_{principal}$ of every model at regionA is almost a constant value of about 90° , whereas at regionB $\theta_{principal}$ of caseA1 is almost a constant value of about 90° but $\theta_{principal}$ of caseA2 and caseA3 is almost a constant value of about 55° . These results indicate that the

stress distribution inside ballast blocks changes by the distribution of pores and the deformation characteristics of ballast blocks at region B change compression into lateral flow in case there are some pores between neighboring sleepers. According to triaxial test results of ballast (Ishikawa et al. 1997), it is revealed that the ballast behaves mainly as an elastic body until the dominant mechanism of deformation changes compression into shear deformation. And the plastic behavior of ballast changes volume shrinkage by compression into volume expansion by shear deformation with the increase of the principal stress ratio. As such experimental results can explain the analytical results mentioned above sufficiently, it seems to be adequate to conclude that DDA model considering the actual density distribution of railroad ballast can simulate the movement of ballast particles under cyclic loading to some extent without setting any particular constitutive relation except the frictional law, which causes the cyclic plastic deformation of railroad ballast.

4 PROBLEMS ON APPLICATION

From the preceding results, it is revealed that DDA is to some extent an effective method to analyze the cyclic plastic deformation of coarse granular materials such as track deterioration. Hence, the application of DDA to track deterioration seems to produce a significant and novel theory to make a geotechnical treatment of railroad ballast in designing ballasted railway track reasonable although the cyclic plastic deformation of railroad ballast had been estimated with an experimental equation in the Japanese conventional theory of track deterioration. But it was also revealed that there were some assignments in applying DDA with two-dimensional elements characterized by plane strain to the design of ballasted railway track. So herein, their assignments are discussed on the basis of analytical results in this paper.

4.1 *Mechanism of stress transmission*

According to Table 3, the analytical load is an unrealistic value because of being 5.0% or less of experimental load. Also it is recognized that the loading condition can't be determined so long as the loading rate isn't set according to each analytical model. These phenomena are similar to the analytical result that the peak stress level in analysis was lower around 60% than the one in the actual test, which was derived in case of simulating the monotonic loading triaxial tests of ballast by DDA (Ishikawa et al. 1997). So it is considered that these phenomena are caused by the reason that the frictional contact mechanism of block surface includes some defects as well as the analytical results of monotonic loading triaxial tests. But it is hard to consider the analytical results in this paper was caused by only the above mentioned reason because the rate of analytical stress to drop for the real value in this paper is much lower than the one in the last paper. Therefore some factors except the above one, for example the difference as to density distribution and grain size distribution or the effectiveness of two-dimensional analysis to three-dimensional problem, seem to influence it, too. It is commonly said that the particle breakage has a considerable influence on the deformation characteristics of coarse granular materials. So a setting method of block friction angle ϕ_u that paid attention to a change in a quantity of particle breakage during cyclic loading is one of assignments that should be examined in future, too.

4.2 Effectiveness of two-dimensional analysis

From the preceding results, it is revealed that the it is recognized that the plastic displacement calculated with an analytical model of line profile not having any pores between neighboring sleepers is smaller than that of experimental results. However in simulating track deterioration with an analytical model of cross section (Ishikawa et al. 1999), it is impossible to express any pores between neighboring sleepers. Further, Table 4 shows the rates of load bearing capacity in each panel of a sleeper in loading of $P_{max}=20\text{kN}$ at the 1st cycle, comparing analytical results by DDA or FEM with experimental results. Here, the rate of load bearing capacity

Table 4. Rate of loading bearing capacity

Model name	Bottom panel	Side panel	End panel
DDA (line profile)	74.2%	25.8%	—
DDA (cross section)	91.9%	—	8.1%
FEM (line profile)	60.7%	39.3%	—
FEM (cross section)	92.6%	—	7.4%
FEM (3-dimension)	56.3%	40.6%	3.1%

is the value that divided the loading bearing capacity in each panel of a sleeper by the total load bearing capacity of a sleeper. Also a panel of 24cm wide \times 17cm height is called "end panel" and a panel of 200cm long \times 17cm height is called "side panel". Seeing Table 4, it is recognized that the discontinuum analysis is more useful for an analytical method of ballasted railway track than the continuum analysis because the evaluation for discontinuity between sleeper and railroad ballast has serious influences on the reliability of analytical results in comparing the analytical results by DDA model of line profile and FEM model with the experimental result. On the other hand, in comparing the analytical results by DDA model of cross section with the experimental result, the former is much larger than the latter. It is considered that this phenomenon was caused by the reason that it is impossible to express the load bearing capacity of side panel sufficiently in case of using DDA model of line profile. These results indicate that to examine the effectiveness of two-dimensional analysis to three-dimensional problems is one of significant assignments controlling the reliability of analytical results.

4.3 Deformation characteristics of blocks

According to the results of FEM models, loading points on sleeper subsided more than peripheral departments and the sleeper was deformed into wavy form toward the longest axial direction. However it is impossible to express such a deformation pattern with DDA model because of using the first order approximations of displacement as the displacement function for each block in this paper. But it is revealed that the movement of ballast particles influences both the generation of local shear stress and the density distribution inside the railroad ballast strongly, and that the deformation characteristics of railroad ballast change with the repetition of load because the movement of a ballast particle changes by the cyclic loading depending on either the contact state between the under-surface of sleeper and ballast particles or the distribution of pores inside railroad ballast. Therefore, in case the deformation characteristics of a block

such as a sleeper in analytical model of cross section have a considerable influence on that of the whole analytical model, the selection of displacement function becomes a factor to let the reliability of analytical results deteriorate.

5 CONCLUSIONS

The following conclusions can be obtained;

1. DDA which takes into account the actual density distribution of railroad ballast with modified porosity can simulate the cyclic plastic deformation of railroad ballast to some extent without setting any particular constitutive relationship except the frictional law between interfaces. The cyclic plastic deformation of railroad ballast is considered to be the movement of ballast particles accompanied by the fabric transformation of particle alignment during cyclic loading in terms of the mechanics of granular materials.

2. The principal mechanism of cyclic plastic deformation inside the railroad ballast, that is compressive or lateral flow, changes by the porosity distribution and the grain size distribution inside railroad ballast because they have a considerable influence on the movement of a ballast particle. Therefore, to bring a DDA model close to the real laminated state of railroad ballast is indispensable to improve the reliability of analytical results.

3. As the evaluation for discontinuity influences the reliability of analytical results strongly in analyzing the deformation of track structure, the discontinuum analysis was more useful than the continuum analysis. However there are some assignments as for the frictional contact mechanism of block surface or the deformation characteristics of block itself in applying DDA to the design of ballasted railway track.

ACKNOWLEDGMENT

The authors would like to thank Prof. Masashi Kamon and Prof. Guanqi Chen of Kyoto University for many invaluable discussions and suggestions.

REFERENCES

- Ishikawa, T., Kamon, M. and Namura, A. 1999. Experimental and analytical studies on the cyclic deformation characteristics of railroad ballast, *Proc. of IS Torino99, Torino*. (in printing).
- Ishikawa, T., Ohnishi, Y. and Namura, A. 1997. DDA applied to deformation analysis of coarse granular materials (ballast), *Proc. of ICADD-2, Kyoto*: 253-262.
- Ishikawa, T., Sunaga, M., Dong, J. and Namura, A. 1997. Cyclic deformation characteristics of railroad ballast in triaxial tests, *Proc. of JSCE*, 575/3-40: 169-178. (in Japanese)
- Shi, G.H. and Goodman, R.E., 1985. Two dimensional discontinuous analysis, *Int. J. Num. Anal. Methods. Geomech*, 9: 541-556.

THE VOUSSOIR BEAM REACTION CURVE

Yossef H. Hatzor

Ben-Gurion University, Department of Geological and Environmental Sciences
Beer-Sheva, Israel, 84105

ABSTRACT: The influence of joint spacing (s) on the stability of a Voussoir beam having a fixed span (B), total thickness (d) and individual bed thickness (t) is studied here using DDA. It is found that: A) The required friction angle ($\phi_{req.}$) for stability against shear sliding along the abutments decreases with increasing spacing down to a minimum value beyond which increasing spacing requires increasing joint strength. The corresponding parabolic function is referred to herein as the "Beam Response Function"; B) The axial compressive stress at the beam (σ_n) increases with increasing spacing up to a maximum value beyond which increasing spacing leads to decreasing level of axial thrust and increasing levels of vertical loads

A new concept: the "Beam Reaction Curve" is proposed in which maximum deflection at mid section vs. time is plotted using DDA. Such numerically developed curves can indicate the expected failure modes: shear sliding along the abutments, onset of stable arching after initial shear deformation, or completely stable arching. With the help of such synthetic diagrams monitoring data from real excavations can be analyzed with respect to the ongoing failure mechanisms in the roof, and conclusions can be drawn concerning imminent failure or stabilization.

1 INTRODUCTION

There is no close form solution for the stability of a horizontally bedded roof with vertical joints, a geometric configuration referred to here as a *Laminated Voussoir Beam*. Classic beam theory can be utilized for the calculation of shear and axial stress distribution, as well as amount of deflection, in the analysis of a bedded roof with beds of varying thickness (Obert and Duvall, 1976) and with given friction angle (Goodman, 1989). In these solutions the beam is assumed to be clamped at the ends and therefore the problem is statically determined. When the beam consists of a single bed with vertical joints, the so called *Voussoir* beam is obtained, and the problem becomes statically indeterminate as the beam is free to displace on either the abutments or across mid joints. Evans (1941) developed a design procedure for Voussoir beam geometry, a method which was later extended by Beer and Meek (1982) and is reviewed in detail by Brady and Brown (1993). However in these solutions only a single layer is modeled, and the influence of spacing and friction between the vertical joints are ignored. Little experimental work has been performed on the mechanical strength of a voussoir beam. Passaris *et al.* (1993) studied the crushing strength of the beam, and the mechanism of shear sliding along side walls has been investigated by Ran *et al.* (1991), both of which have used non liner finite element analysis. In both studies the analysis was extended to the case of multiple mid joints and the spacing between joints was considered, but friction along the discontinuities was not modeled.

In order to truly simulate deformation characteristics of a laminated voussoir beam a numerical method must be used. The selected method should allow rigid body movement and

deformation to occur simultaneously, and convergence in every time step should be achieved after relatively large block displacement and rotation, without block penetration or tension. Furthermore, the vertical load which is typically assigned explicitly, must be evaluated and updated implicitly in every time step, since it varies with vertical location in the beam, as well as with the progress of beam deformation. Finally, the model must incorporate the influence of joint friction on block displacement and on the arching mechanism.

In this paper the failure of a laminated voussoir beam is back analyzed. All geometrical variables including beam span, beam thickness, joint spacing, and bed thickness are determined from careful field mapping and site investigations. All mechanical parameters are determined from expedient rock mechanics testing. The beam geometry and intact rock properties are used as input parameters in both classic Voussoir Beam Analysis (Beer and Meek, 1982) and in Discontinuous Deformation Analysis (Shi, 1993) and the results are compared. Finally using DDA results some new insights regarding the mechanical behavior of a laminated Voussoir beam are proposed.

2 THE FAILURE OF A LAMINATED VOUSSOIR BEAM - A CASE HISTORY

2.1 *A Brief Description of the Failure*

In the archeological site of Tel Beer Sheva, an ancient city dated back to the Iron stage (1,200 - 700 B.C.) an underground water storage reservoir dated back to approximately 1,000 B.C. was explored. The reservoir was excavated in horizontally bedded chalk with vertical joints clustered in three joint sets. The most abundant joint sets (J1 and J2) are orthogonal with mean spacing of 20 to 25 cm; the mean bed thickness is about 50 cm. The intersection of horizontal layers and vertical joint planes creates a dense network of cubic blocks which form the roof of the excavation. The roof collapsed into the shape of a three dimensional dome, probably during time of construction, and the ancient engineers have erected a massive support pillar in the center of the opening in order to support the remaining roof. The collapsed roof is considered here a failed laminated voussoir beam. Hatzor and Benary (1998) provide details of the failure including maps and cross-sections.

2.2 *Rock Mass Properties*

The studied rock mass consists of a horizontally bedded and vertically jointed chalk, covered by 5m. of a well cemented conglomerate, and by about 3m. of soil in which the archeological remains are found. Individual bed thickness in the chalk is between 30 to 80 cm. with an average thickness of 50 cm. The rock mass RQD values determined from core recovery range between 44 - 100% with typical values between 65 - 80%. The unconfined compressive strength of the chalk is 7 MPa, the Elastic module (E) and Poisson ratio (ν) as measured in unconfined compression are 2GPa and 0.1 respectively. A linear Coulomb-Mohr failure envelope fitted to the peak strength values yield a cohesion of 3.1 MPa and internal friction angle of 32° . The porosity of the chalk is between 27 to 30% and the unit weight is between 18.1 to 20.1 kN/m³. The Atterberg limits of the interbedded marl indicate relatively low plasticity and low swelling potential. Estimation of input data for rock mass classification methods yields an estimated Q value between 0.4 to 4.0 and an estimated RMR value of 43. These values indicate a fair to poor

rock with an expected stand up time of one to several days. The estimated rock mass classification values help explain the historic failure: with the given lithological conditions and considering modern experience we do not expect the rock mass to have been able to sustain the loads which were induced by the attempted excavation, for a significant period of time

2.3 Estimated Shear Strength of Joints

Three principal joint sets are defined. The joints are clean and tight with planar surfaces. The roughness of the joint planes is estimated using a profilometer measurements. 10 measured profiles are compared with JRC standards and the mean JRC value is estimated at 9. The residual friction angle of the joints is determined using tilt tests performed on mating saw cut joint planes. The mean residual friction angle is estimated at 35° . In order to assess the peak friction angle which was available at time of deformation the empirical criterion of Barton is used with the following input parameters: $JRC = 9$; $JCS = 7 \text{ MPa}$; $\sigma_n = 0.25 \text{ MPa}$; $\phi_{\text{residual}} = 35^\circ$. The maximum normal stress active on the joints (σ_n) is a function of beam thickness and is determined here from DDA results (see below). Using the criterion of Barton the dilation angle is expected to be about 13° and therefore the peak friction angle is expected to be about 48° .

3. VOUSSOIR BEAM ANALYSIS

The assumed stress distribution in a "classic" voussoir beam (Beer and Meek, 1982, Brady and Brown, 1993) is shown in Figure 1, where the beam consists of a single layer. As the number of intermediate joints is irrelevant, the only relevant geometric parameters in the classic analysis are beam span (B) and beam height (d). The geometry of a *laminated* voussoir beam is shown in Figure 2. The principal geometric parameters are beam span (B), overall beam height (d), individual layer thickness (t), and joint spacing (s). This geometry is used in DDA with fixed point location as marked in Figure 2 by the small triangles.

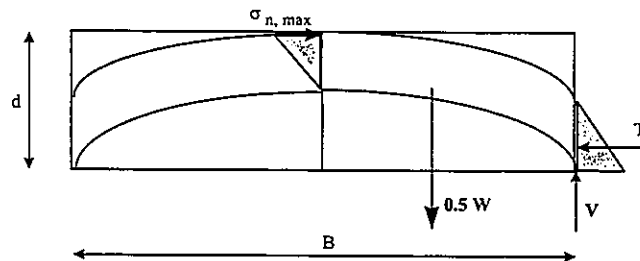


Figure 1a. Assumed stress distribution in classic voussoir beam analysis

The maximum axial stress (σ_n) in the classic voussoir beam analysis is computed for beam spans ranging between 3 to 9 meters and beam thickness between 0.25 to 2.5m. (Figure 3). It can be seen that in general σ_n increases with increasing beam span and decreases with increasing beam thickness. The calculated results however are only valid for a beam consisting of a single layer. The case of Tel Beer Sheva is shown in the heavy line in Figure 3 for a beam span of 7m. The value of σ_n , obtained for an individual layer thickness of 0.25m, is 2.45 MPa.

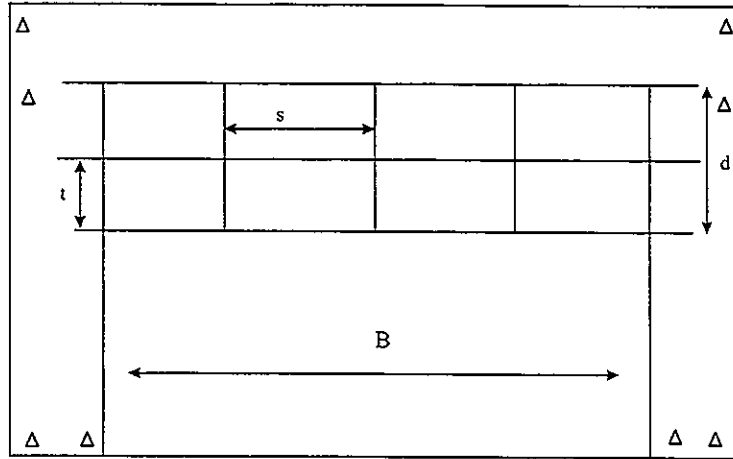


Figure 2. Geometry of a laminated voussoir beam as used in DDA experiments

For a single layer beam with thickness of 2.5m σ_n is 0.244 MPa. At Tel Beer Sheva the average bed thickness is 0.5m. Assuming that each bed transmits the axial thrust independently from the neighboring layers above and below, σ_n within a single layer should be 1.22 MPa. These values are significantly lower than the unconfined compressive strength of the rock which is about 7 MPa, and therefore the beam should be considered safe against failure by local crushing at hinge zones, according to this analysis.

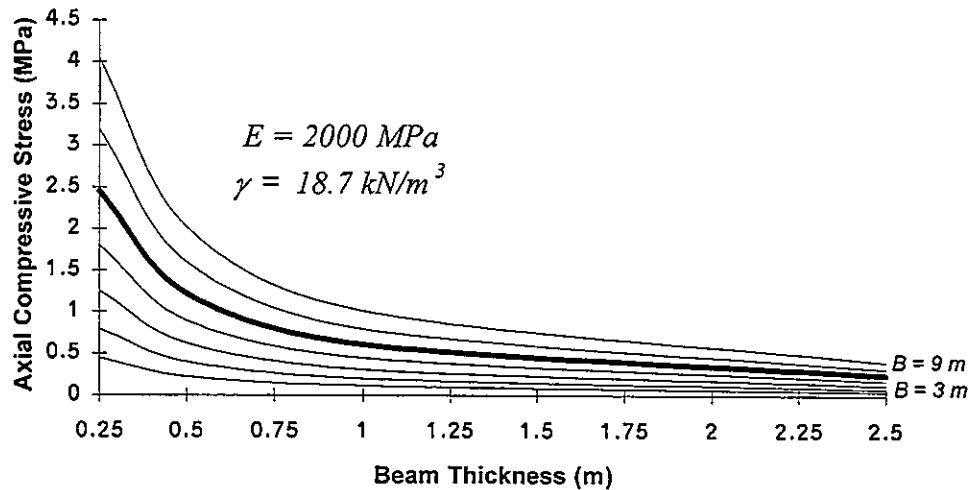


Figure 3. Maximum axial compressive stress (σ_n) as a function of beam thickness according to classic voussoir beam analysis

Brady and Brown (1993) show that for joints and abutments of zero cohesion the factor of safety against failure in shear along the abutments is given by:

$$F.S. = \frac{T \tan \phi}{V} = \frac{0.5 \sigma_n d \tan \phi}{0.5 \gamma B d} = \frac{\sigma_n}{\gamma B} n \tan \phi \quad (1)$$

Where: T = resultant horizontal (normal) force; V = resultant vertical (shear) force; ϕ = available friction angle along abutment wall or vertical joint; n = assumed load/depth ratio (compressive zone thickness is given by $n \times d$); d = beam thickness; B = beam span; γ = unit weight of rock. The factor of safety against shear failure by sliding along the vertical abutments is calculated in Figure 4 for different values of available friction angle and beam thickness using Eqn. 1. It can be seen that the sensitivity of the factor of safety to beam thickness is quite high and a logarithmic scale is used for better resolution.

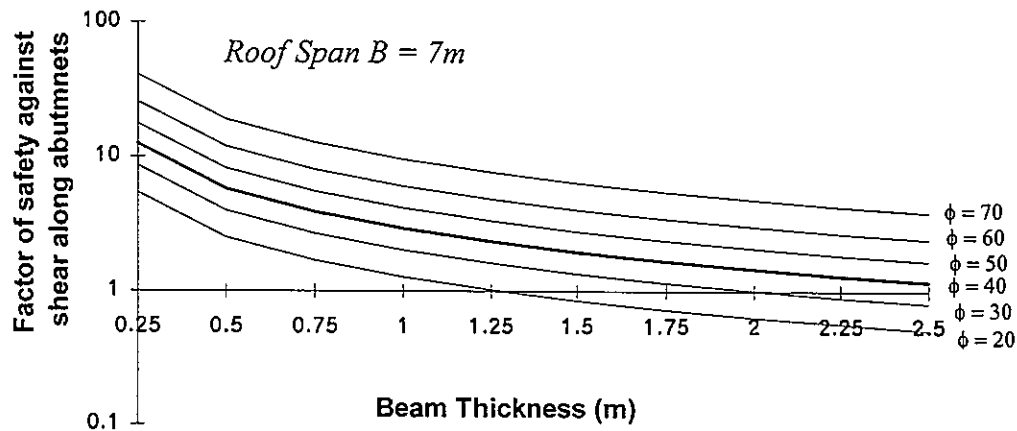


Figure 4. Sensitivity of factor of safety against shear sliding along the abutments to the available friction angle and to the beam thickness according to classic voussoir beam analysis

The available friction angle for Tel Beer Sheva is estimated at 48° ; a heavy line representing available friction angle of 40° is shown in Figure 4 above. With a given friction angle of only 40° the opening should have been safe against shear along the vertical abutments, for any beam thickness between 0.25 to 2.5m. In fact, the required friction angle for stability according to classic voussoir beam analysis is not greater than 36° , for every beam thickness.

The results obtained using classic voussoir beam analysis can not explain the failure. The local compression which develops at the hinge zones is too low comparing to the available compressive strength; the shear stress which develops along the vertical abutments due to beam weight is lower than the shear strength of the abutments, considering a conservative estimate of friction angle. We must conclude therefore that the approach taken by classic voussoir beam analysis, which ignores the influence of joint spacing and the existence of multiple beds, may prove unconservative, and should not be applied in practice for the analysis of a *laminated* voussoir beam.

4 DISCONTINUOUS DEFORMATION ANALYSIS

4.1 Set up of DDA experiments

The carefully documented geometry of the failed roof is used here in back analysis of the failure. The active span is assumed to be 7m as before, but a distinction is made now between overall beam thickness, and individual layer thickness. The overall beam thickness is represented by the

height of the mapped loosened zone, about 2.5m. Individual layer thickness is taken as the average bed thickness, about 50cm. The geometric and mechanical parameters, which are used as variables, are mean joint spacing and joint friction, respectively.

DDA runs are performed for the geometry which is schematically shown in Figure 2, where fixed point location is marked by small triangles. In each analysis a constant mean joint spacing value (s) is used, and the value of friction angle along the boundaries is changed until the system shows stability. The stability of the roof is defined by a specified value of maximum deflection at beam mid section, the magnitude of which would not change regardless of the number of time steps. In this research the roof is considered to arrive at stability when a maximum deflection of up to 5.5cm is detected at mid section, after at least 25 time steps. The maximum allowable displacement ratio, namely the maximum allowable displacement per time step divided by half the vertical dimension of the region, is set to 0.01. In the analyzed case study the maximum allowable displacement per time step is 3.5cm.

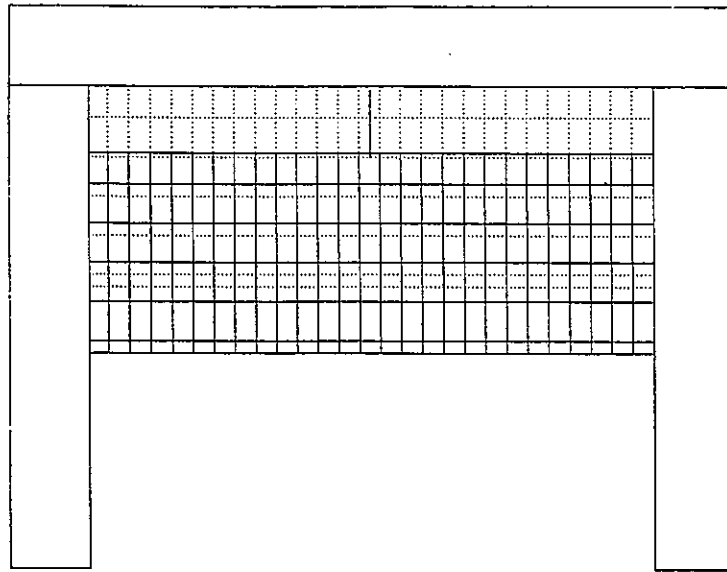
The joints are considered planar and cohesionless with zero tensile strength, an honest representation of the situation in the field. The friction angle of vertical joints and horizontal bedding planes is assumed equal, merely for simplicity; this is by no means a limitation of the method. The input material parameters are: Mass per unit area = 1900 kg/m²; Weight per unit area = 18.7 kN/m²; Young's modulus $E = 2 \cdot 10^6$ kN/m; and Poisson's ratio $\nu = 0.1$. Seven mean joint spacing values are analyzed: $s = 25\text{cm}$, 50cm, 87.5cm, 116cm, 175cm, 350cm, and 700cm. The roof is modeled for friction angle values between 20° and 90°. The maximum deflection at mid section for a given friction angle value is noted in each run. Typically stability and cease of motion is detected after 12 to 16 time steps.

4.2 DDA results

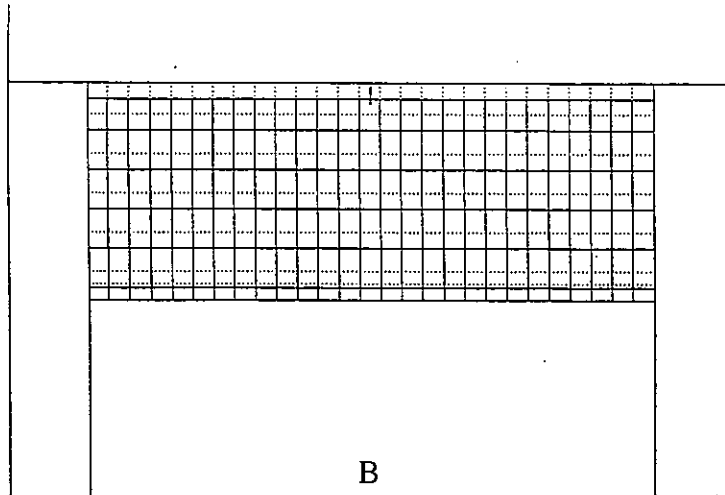
An example of DDA results for a layered beam with $s = 25\text{cm}$. is shown in Figure 5 a, b, c, for available friction angle values of $\phi_{\text{available}} = 20^\circ$, 40°, and 85° respectively. The beam fails in shear along the abutments when the available friction angle is 20° (Figure 5a). An available friction angle of 40° (Figure 5b) is sufficient to induce arching but the roof deflection is excessive, $u_{\text{max}} = 20\text{cm}$. The roof remains completely stable only when the available friction angle is increased to 85° (Figure 5c).

The results of all DDA experiment are graphically demonstrated in Figure 6 for a roof of 7m span and 0.5m horizontal layer thickness. Maximum deflections at mid section (u_{max}), arrived at after up to 25 time steps, are plotted against the value of friction angle which was modeled for all discontinuities. The tests are performed for six different vertical joint spacing values (s).

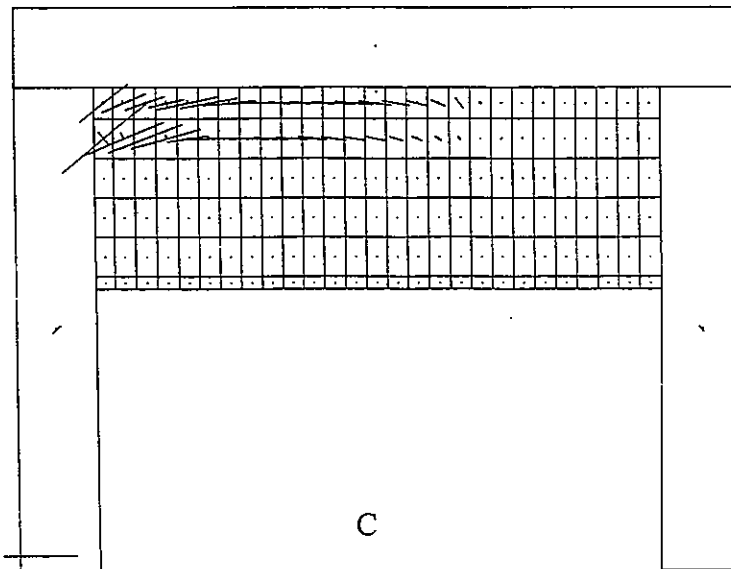
The results of the DDA experiments demonstrate that for the case of Tel Beer Sheva, with mean bed thickness of 0.5m and mean joint spacing of 0.25m, the required friction angle is 80°, a shear strength which was not available at time of construction and thus the failure.



A



B



C

Figure 5. Three DDA experiments for the deformation of a laminated Voussoir beam after 25 time steps (see text for details). Beam geometry: $B=7\text{m}$, $d=2.5\text{m}$, $t=0.5\text{m}$, $s=0.25\text{m}$. A) $\phi_{\text{available}}=20^\circ$, $u_{\text{max}}=0.83\text{m}$; B) $\phi_{\text{available}}=40^\circ$, $u_{\text{max}}=0.2\text{m}$; C) $\phi_{\text{available}}=85^\circ$, $u_{\text{max}}=0\text{m}$.

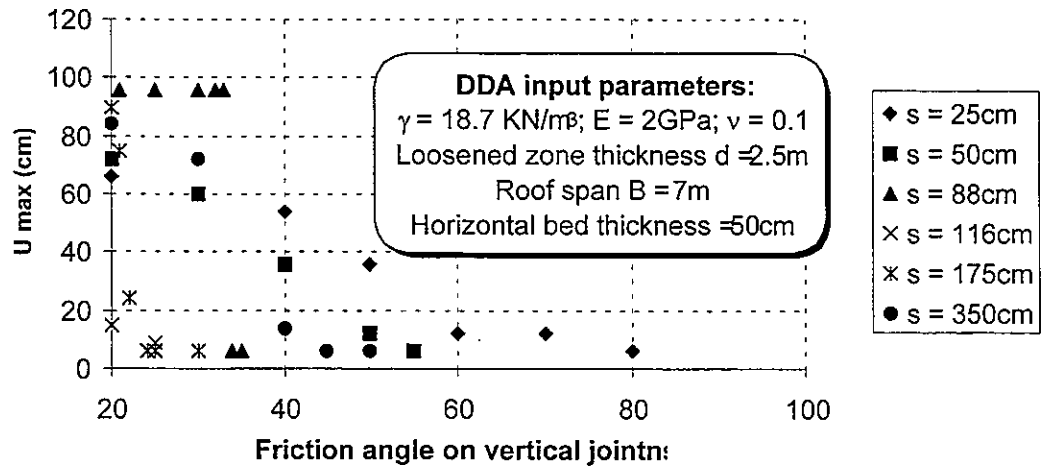


Figure 6. Maximum deflection at beam mid section after up to 25 time steps as predicted by DDA

5 THE VOUSOIR BEAM RESPONSE FUNCTION

The influence of joint spacing, or block length, on the required friction angle for stability is demonstrated in Figure 7 below. The results indicate that the required friction angle for stability decreases with increasing block length, or joint spacing. However, the empirical function is not monotonously decreasing but presents a minimum, when the number of blocks in an individual layer is 4 ($s = 175$). When the number of blocks further decreases (block length or joint spacing increases) the required friction angle for stability increases. Ultimately, when each individual layer consists of a single block the required friction angle is 90° because the abutment walls are vertical with zero cohesion.

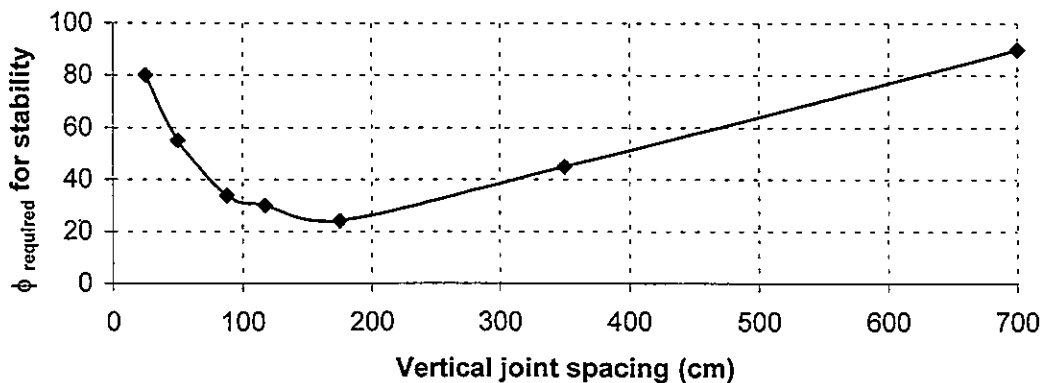


Figure 7. Influence of joint spacing on the stability of a laminated voussoir beam

The empirical function in Figure 7 above is referred to here as the “*Beam Response Function*”. The logic behind this parabolic function may be rationalized as follows: with increasing joint spacing the moment arm length in individual blocks increases, and the arcing mechanism by which axial thrust is transmitted through the blocks to the abutments is enhanced. However,

above a limiting value of block length, the weight of the overlying blocks becomes more dominant. Consequently, the stabilizing effect of greater axial thrust is weakened by the destabilizing effect of dead load transfer from the weight of overlying blocks. This rational may be tested if we investigate the developed axial thrust at beam mid section (upper hinge point) as a function of block length or joint spacing. Results of DDA calculations (Figure 8 below) confirm the stated rational above.

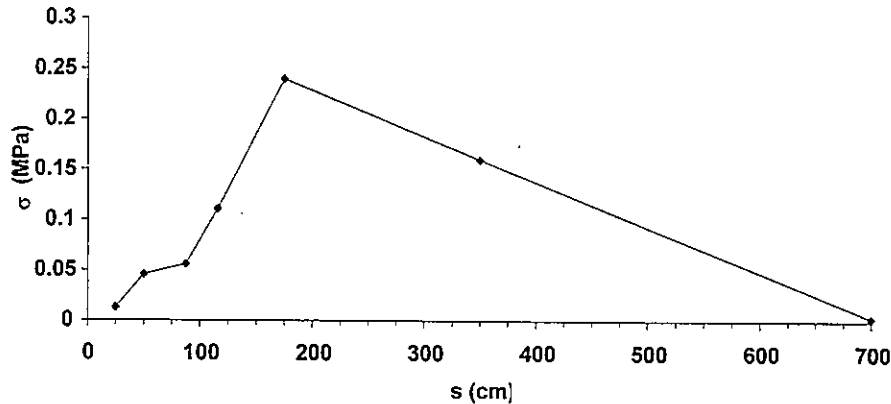


Figure 8. Maximum axial thrust at beam mid section (σ) for a given vertical joint spacing (s) as determined by DDA.

6 THE VOUSSOIR BEAM REACTION CURVE

The dynamic formulation of DDA enables us to gain further insight into the mechanical behaviour of a laminated voussoir beam, in particular its deformation with respect to time. When joint and abutment wall friction is low with respect to the developed vertical shear load continuous sliding deformation along the abutments is expected. With increasing shear resistance onset of arching deformation ensues after initial vertical slip takes place. The beam is completely safe when arching deformation is preceded by minimal vertical slip. The deflection of the beam with time is referred to here as the "*Beam Reaction Curve*". Three different reaction curves are shown in Figure 9 for three different beam configurations. Such developed curves can indicate the expected failure modes: shear sliding along the abutments, onset of arching after initial shear deformation, or completely stable arching. With the help of such synthetic diagrams monitoring data from real excavations can be analyzed with respect to the ongoing failure mode in the roof, and conclusions can be drawn concerning imminent failure or stabilization.

7. CONCLUSIONS

- DDA is more appropriate and more conservative than classic voussoir beam analysis for the analysis of a *laminated* voussoir beam because it can model joint spacing and joint friction, and it can allow for multiple layers in a beam.
- For a laminated beam with a constant layer thickness the resistance to shear along the abutments improves with increasing joint spacing up to a critical value of block length, beyond which the composite beam becomes less stable.

- Using DDA synthetic Beam Reaction Curves which predict vertical beam deflection with time may be generated. With the help of such synthetic diagrams monitoring data from real excavations can be analyzed with respect to the ongoing failure mechanisms in the roof, and conclusions can be drawn concerning imminent failure or stabilization.

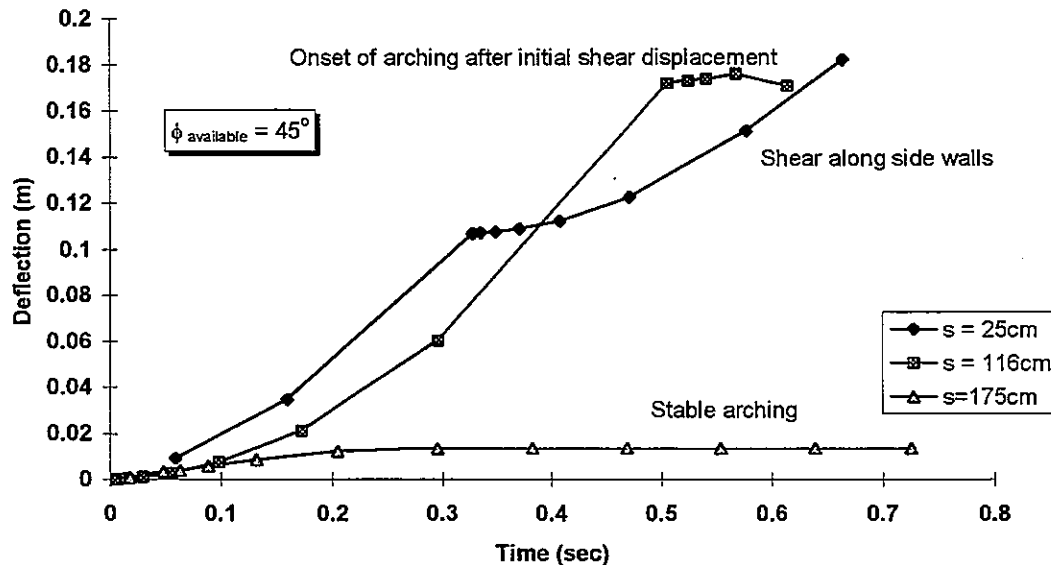


Figure 9. Three different "Beam Reaction Curves" for three different voussoir beam configurations as predicted by DDA.

REFERENCES

- Obert, L. and Duvall, W. I. 1967. *Rock Mechanics and the Design of Structures in Rock*. New York: John Wiley & Sons.
- Goodman, R. E. 1989. *Introduction to Rock Mechanics*. New York: John Wiley & Sons.
- Evans, W. H. 1941. The strength of undermined strata. *Trans. Instn. Min. Metall.*, 50: 475-532.
- Beer, G. and Meek, J. L. 1982. Design curves for roofs and hanging walls in bedded rock based on voussoir beam and plate solutions. *Trans. Instn. Min. Metall.* 91: A18-22.
- Brady, B. H. G. and Brown, E. T. 1993. *Rock Mechanics for Underground Mining* London: Chapman & Hall.
- Passaris, E. K. S., Ran, J. Q. and Mottahed, P. 1993. Stability of the jointed roof in stratified rock. *Int. J. Rock Mech. Min. Sci. & Geomech. Abstr.*, 30 (7): 857-860.
- Ran, J. Q., Passaris, E. K. S. and Mottahed, P. 1991. Shear sliding failure of the jointed roof in laminated rock mass. *Rock Mech. Rock Engng.* 27 (4): 235-251.
- Shi, G.-H. 1993. *Block System Modeling by Discontinuous Deformation Analysis*. Southampton: Computational Mechanics Publications.
- Hatzor, Y. H., Benary, R. 1998. The stability of a laminated Voussoir beam: back analysis of a historic roof collapse using DDA. *Int. J. Rock Mech. Min. Sci. & Geomech. Abstr.* 35(2):165-181.

DDA Analysis of The RCC Modification for Pueblo Dam

Joseph T. Kottenstette
U.S. Bureau of Reclamation,
Denver, CO 80225 USA

ABSTRACT: Pueblo Dam is a massive head buttress structure founded on horizontally bedded sandstone and shale. Prominent shale beds beneath the structure daylight in the spillway stilling basin excavation downstream of the dam. Due to foundation sliding concerns the stilling basin has been filled with roller compacted concrete (RCC). The DDA model was used to check the stability of the modified structure assuming that no cohesion was available along the base of the RCC-plug/stilling basin lining contact. The DDA method is most effective when the structures are below the limit of equilibrium and movement has started, unfortunately at this point the structure is failing. This is not the case at Pueblo Dam.

The potential sliding surface at Pueblo Dam is composed of segments with different available friction coefficients ($\tan \Phi_a$). To evaluate the potential for instability, the friction coefficients for each segment were divided by a constant factor of safety and the resulting values were applied to the DDA model. The reduced friction coefficients which just allow movement to begin are defined as the required friction coefficients ($\tan \Phi_r$). The factor of safety for the system is estimated by the ratio of the shear strengths ($FS = \tan \Phi_a / \tan \Phi_r$).

1. INTRODUCTION

This paper describes Reclamation's Discontinuous Deformation Analysis (DDA) analysis of the spillway section at Pueblo Dam. Pueblo Dam is a composite earth and concrete structure located six miles upstream of Pueblo Colorado on the Arkansas River. The Structural height is approximately 220 feet and crest length is about 11,500 feet. Zoned earthfill embankments flank each end of the concrete section. Bedrock for the concrete dam foundation is the Dakota Sandstone formation and the earth dam sections are founded on Graneros Shale. The concrete portion was constructed with 23 individual massive head and buttress sections. Buttresses 8 through 14 make up the overflow spillway and outlet works part of the concrete dam. A stilling basin was excavated downstream of these buttresses to dissipate energy from the overflow spillway.

In December of 1996 Reclamation performed a risk analysis for the dam based on geologic information provided in the original design and construction related reports. The Dakota Sandstone foundation for the concrete section consists of nearly horizontally bedded sandstone with carbonaceous zones and shale interbeds. The risk analysis indicated a stability concern for the spillway Buttresses 8 through 14 upstream of the stilling basin excavation. The weak shale layers beneath the buttresses daylighted in the stilling basin excavation and created a potentially unstable foundation.

Exploration and excavation performed during the original construction identified and removed portions of weak planes under the downstream portion of the buttresses. This included excavation of a continuous thick shale seam under buttresses 8 and 9. This additional excavation

was backfilled with a concrete block. However, the significance of a thin shale seam at elevation 4715, less than 10 feet below the massive concrete block, was not recognized.

The risk assessment indicated that the lower daylighting shale seam created a continuous weak slide plane and an inordinate risk to the public. A modification was required to reduce this risk. This paper describes the DDA analysis that was used in conjunction with other methods to evaluate the stability of the modification.

2. BUTTRESSES 8 AND 9 POTENTIAL SLIDE PLANE, AND MODIFICATION

The stilling basin excavation at Pueblo Dam daylighted a shale bed creating weak potential slide planes below buttresses 8 and 9 of the spillway section. The foundation model for buttresses 8 and 9 is shown in the geologic section (Fig-2.1); note the lower potential sliding plane daylighting at elevation 4715. The horizontal shale beds shown on this section were mapped in the foundation and identified in numerous core holes. They form a continuous potential stepped foundation slide plane below buttresses 8 and 9.

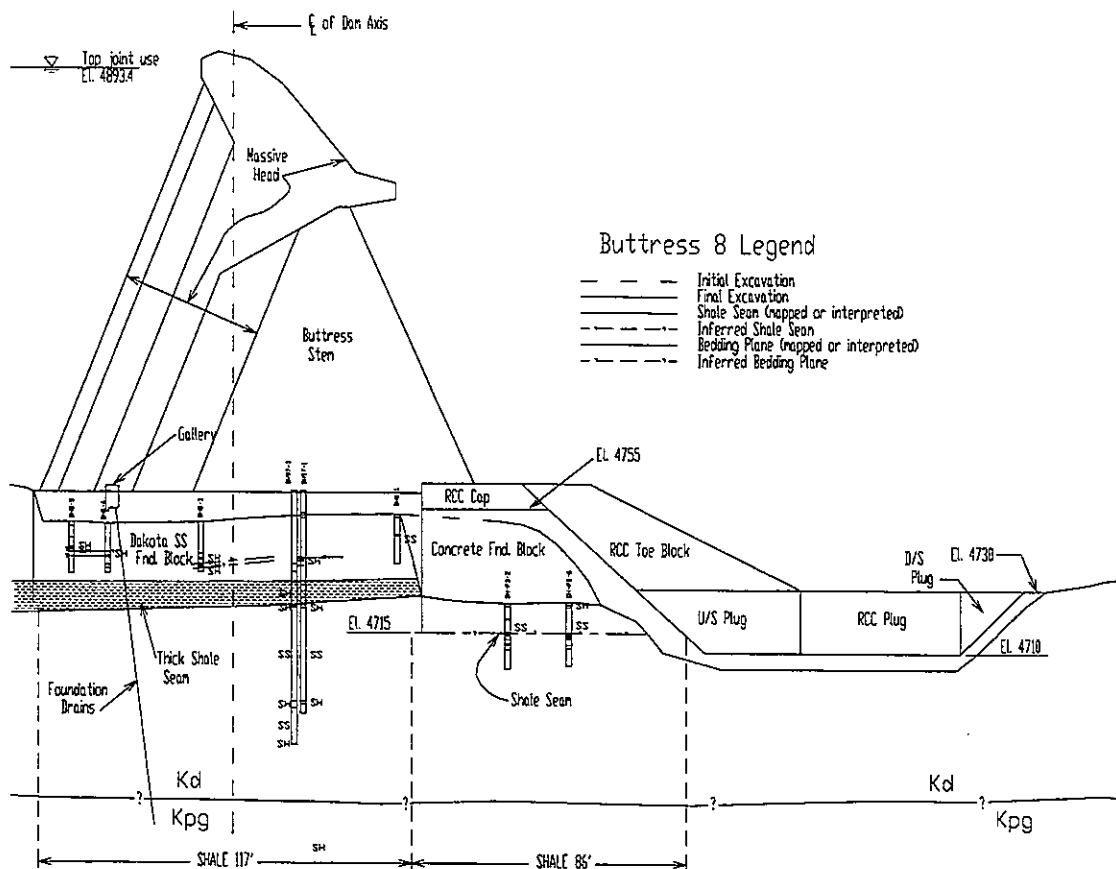


Figure 2.1 Buttresses 8 and 9 Geologic Cross Section and RCC Blocks

The RCC blocks are designed to correct this weakness by blocking the potential sliding plane. The RCC plug fills in the stilling basin preventing the plane from daylighting. Good bond between the RCC and existing basin concrete is anticipated. However, if good bond is not obtained, potential sliding on these surfaces may be possible. This mechanism was evaluated for the buttress 8 and 9 RCC blocks using DDA.

3. DDA MODEL GEOMETRY

The location of the RCC contraction joints, the geometry of the stilling basin, the potential sliding plane geometry, and the design of the RCC blocks, dictated the block geometries for the two-dimensional DDA model. The DDA model for buttresses 8 and 9 consists of five dam blocks, two foundation blocks, and five RCC blocks.

The dam blocks modeled the equivalent stiffness and mass of the structure in a two dimensional section. This was required because the dam is a massive head buttress structure and it does not have a constant upstream-downstream cross section. Figure 2.1 shows the RCC blocks and Figure 3.1 shows potential sliding surfaces.

The two foundation blocks consisted of an upstream Dakota Sandstone block, and the downstream concrete block. Both blocks have horizontal potential sliding planes of shale ($\Phi_a=17\text{deg}$).

The RCC blocks are: the cap, the toe block, the D/S end of the RCC plug, the middle of the RCC plug, and the upstream end of the plug. The plug was divided into three blocks defined by the upstream and downstream contraction joints and the stilling basin contact.

A small corner of the plug was removed from the middle RCC block at the break in slope between the base and down stream end of the stilling basin. This geometry change provided a smooth sliding mode that was controlled by the shear strength of block boundaries and not the change in geometry. The sharp corners create stress concentrations that may crush if movement occurs. Removing them results in a more reliable model of the potential sliding mode.

3.1 Critical Potential Sliding Mode

The DDA model was used to help select the critical potential sliding mode for buttresses 8 and 9. The shale beds below the two foundation blocks and the sloping stilling basin lining/RCC interfaces are the critical potential sliding surfaces. The available friction angle for these surfaces is estimated at 17 degrees for the shale and 45 degrees for the RCC. With these values the model is stable and no movement occurs. However, the margin of safety is unknown. The initial shear strengths for the DDA model were reduced by a safety factor of 1.5 ($1.5 = (\tan \Phi_a) / (\tan \Phi_r)$) with no cohesion. The DDA model with these reduced shear strengths was stable for the reservoir at elevation 4898.7 (spillway crest). The side resistance (see section 5) was then reduced to zero to induce sliding in the RCC block system on the critical surfaces. The critical potential sliding mode in the RCC blocks involved sliding on the upstream and downstream sloping stilling basin walls. Figure 3.1 Shows the potential sliding mode. This potential sliding mode produces tension on the base of the plug, and is considered the critical one for buttresses 8 and 9.

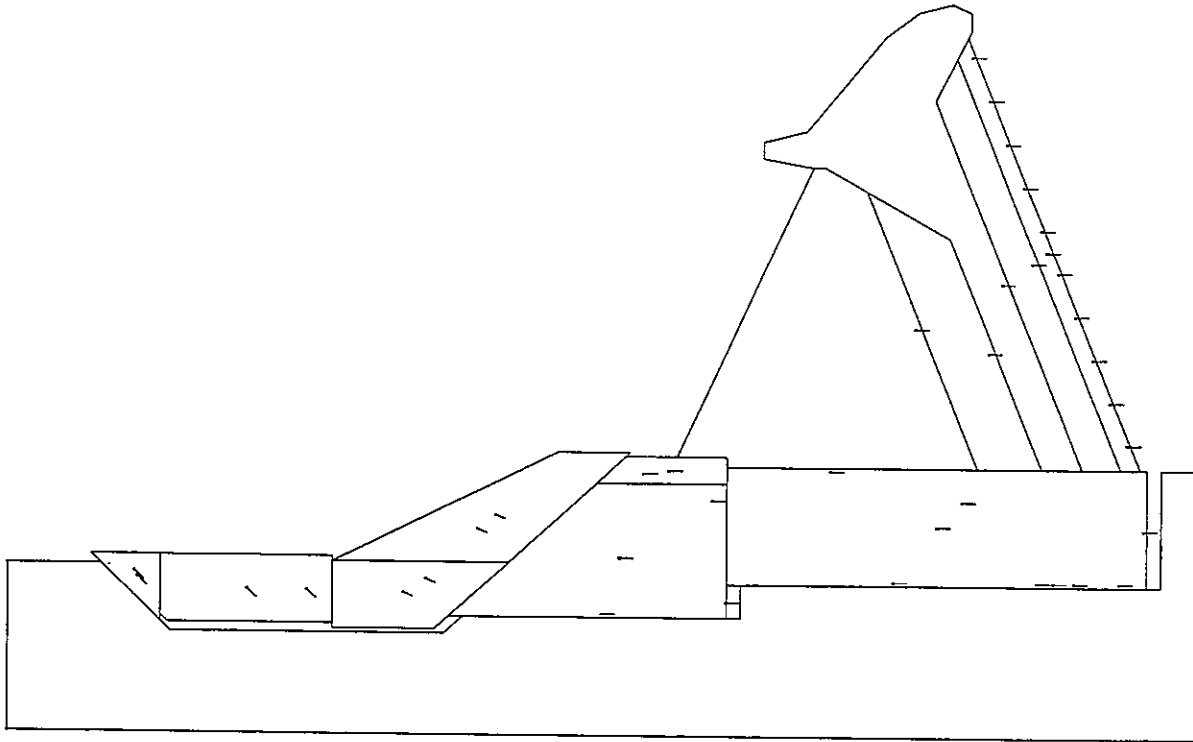


Figure 3.1 Potential Sliding Mode

4. ANALYSIS METHOD

Reclamation has often used a three dimensional limit equilibrium analysis to estimate the safety factor on large individual foundation blocks with daylighting potential sliding planes and simple sliding modes. The blocking mechanism precludes simple limit equilibrium methods. The design deliberately blocks the potential sliding plane and prevents it from daylighting. This forces the system into a multiple block sliding with complex movements, and makes it necessary to use the DDA type of analysis developed by Dr. Shi. The DDA program provides a method for evaluating discontinuous blocky structures with multiple blocks sliding on different surfaces and in the different directions. Reclamation used the DDA program for both static and pseudo static earthquake evaluations of the Pueblo Dam modification.

The DDA computer program models deformations and is effective in detecting the onset of movement. This affects the analysis procedure for stable structures that are designed with safety factors. Structures do not demonstrate significant block movements until they are below the limit of equilibrium. Unfortunately, at this point the structure is sliding. Conventional sliding factors of safety are difficult to apply to a blocky system with potential complex block movements.

The main reason for the DDA modeling is a concern about the reliance on cohesion in the RCC when there is a potential to create tensile stresses along the block boundaries and RCC lift lines. The blocking mechanism of the deeper potential sliding plane and the RCC plug was evaluated with a reduced strength limit equilibrium approach described in the next section. The approach assumed no cohesive strength on the boundary of the RCC modification.

4.1 Reduced Strength Method

After defining the critical potential sliding mode the side resistance (see Section 5) was again included as an external load. The friction angles on the critical surfaces was decreased in small increments by a constant safety factor until sliding occurred on the critical sliding surfaces. The limit equilibrium friction angles (Φ_{required}) and related safety factor ($FS = \tan \Phi_a / \tan \Phi_r$) is defined by this trial and error procedure.

The RCC and shale shear strength values (friction coefficients) were each decreased such that the safety factors for the shale seam and the RCC contact were always equal. The shear strengths required for pseudo static earthquake limit equilibrium were estimated in the DDA model by decreasing them from the measured values on the RCC and the shale until the DDA model became unstable. The new dynamic safety factor was calculated from these results similar to the static case except that dynamic loads were included.

The DDA method for stable structures can make use of a reduction in shear strength on the discontinuities until movement starts. A back calculated safety factor is estimated by the ratio between the available strength and the required strength at movement ($FS = \tan \Phi_a / \tan \Phi_r$). This reduced strength method was used for this analysis and the results are presented for both static and pseudo static earthquake loading conditions.

5. SHEAR STRENGTH

The shale beds have an estimated shear strength of 17 degrees ($\Phi_{\text{available}}$) and no cohesion. This estimated strength indicates sliding at the historic maximum (RWL = 4888.5) loading conditions, a condition known to be stable. In reality, there is side resistance that is not accounted for in a two-dimensional model. An additional resistance of 350 kips per foot was added to correct the model for side resistance.

Side resistance strength for buttresses 8 and 9 was limited to the back calculated value (about 350 kips/ft) for the historic maximum loading conditions ($FS = 1.0$) because of the uncertainty and risk related to potential sliding of this structure. Research and test results indicate an available friction angle along the RCC plug contact of 45 degrees ($\Phi_{\text{available}}$).

6. LOADS

Three types of loads were used in this analysis; 1) reservoir, 2) uplift, and 3) pseudo static earthquake. The preliminary limit equilibrium analysis and the design criteria were used to define the critical combinations of loads and safety factors.

6.1 Reservoir

The reservoir water loads have a downward component and a downstream component because of the slope on the upstream face of the dam. Loads on this surface were based on the water level in the reservoir for the spillway crest (elevation 4898.7), the top of joint use (elevation 4893.7), and historical maximum (elevation 4888.3). Only the results at the spillway crest are presented in this paper.

6.2 Uplift

A line of piezometers under buttress 7 and additional instruments installed in 1997 were used to define the uplift profile based on the reservoir and piezometric levels obtained in 1997. The 1997 piezometers were adjusted to the various reservoir water surfaces as follows:

$$DHR = (PL - TWL) / (RL - TWL) \quad (1)$$

$$PL = DHR (RL - TWL) + TWL \quad (2)$$

Where DHR is the "Differential Head Ratio", PL is Piezometric Level, RL is the Reservoir Level, and TWL is the Tailwater Level. Differential Head Ratios were calculated for the uplift values measured at the historic maximum reservoir levels and uplift values were extrapolated to other reservoir levels using the relationships described above.

6.3 Pseudo Static Earthquake

A three dimensional response history finite element dynamic analysis of the structure was used to calculate dynamic loads at the base of the dam. The time history record from the Oct. 31, 1935 Helena, MT earthquake was used for the dynamic analysis. This earthquake has peak horizontal acceleration components of 0.17g (E-W) and 0.15g (N-S). The dynamic loads result from the time history acceleration acting on the mass of the dam and reservoir. Separate calculations were performed to identify the time step at which the critical dam loading and inertia forces. (the product of mass and acceleration) occurred. Dynamic loads for this time step ($T = 2.69$ sec) and the reduced strength method described above were used to check the pseudo static earthquake safety factor for the RCC modification. Reclamation's version of the DDA program is not designed to accept time history accelerations for direct dynamic evaluation of the full earthquake record.

7. RESULTS

The DDA model was stable for the design friction angle values. The static limit of equilibrium friction angle was 7.20 degrees on the shale and 22.45 on the RCC with the reservoir at the spillway crest. This corresponds to a safety factor on these surfaces of 2.42. The pseudo static earthquake limit of equilibrium friction angle was 14.29 degrees on the shale and 39.81 on the RCC. The corresponding safety factor on these surfaces of 1.2. These values include 350 kips per foot for side resistance.

The RCC design effectively blocks the potential sliding plane. The DDA model shows acceptable safety factors of the RCC block structure assuming the cohesion is lost due to excessive tensile stresses. The blocking mechanism stabilizes these buttresses without cohesion for both the static and pseudo static earthquake loading conditions.

ON THE DDA FRAMEWORK FOR MODELLING CONCRETE FRACTURE

Chris Pearce

Department of Civil Engineering,
University of Glasgow, Glasgow G12 8LT, UK

Nenad Bicanic

Department of Civil Engineering,
University of Glasgow, Glasgow G12 8LT, UK

Appapillai Thavalingam

Department of Civil Engineering,
University of Glasgow, Glasgow G12 8LT, UK

Zhi Hong Liao

Department of Civil Engineering,
University of Glasgow, Glasgow G12 8LT, UK

ABSTRACT: Some possibilities and limitations of the discontinuous deformation analysis in modelling concrete fracture are illustrated on several simple benchmarks, in particular in tracing the entire range of fracture evolution from a continuum to discontinuum. Illustrative examples include a plain concrete beam and the RILEM pull-out benchmark problem. Solution control strategy for monitoring progressive fracture via linearised eigenvalue analysis is considered.

1 INTRODUCTION

Modelling of gradual fracturing of concrete (strain localisation, followed by separation by cracking or shear slip) represents a complex computational modelling task. Continuum based nonlinear material models are usually adopted, which are traditionally based on concepts of damage mechanics, strain softening plasticity or some higher order plasticity theory, where no discontinuities are admitted in the trial displacement field. Further sophistication leads to discontinuous shape function enrichment or internal discontinuity bands on an element level, however the identification of the failure mode again does not consider the actual separation of structural parts.

The discrete crack framework (Ing Raffea 1997) relies on some energy based criterion for crack advancement and extensive remeshing strategies following an introduction of a displacement discontinuity across the introduced crack. Most formulations assume that cracks once open do not close and there is no consideration of a possible re-establishment of contacts between the cracked surfaces. Lattice based modelling approaches have also been very successful, in particular in simulation of the micromechanical behaviour of concrete.

Discontinuous modelling frameworks have become increasingly researched in concrete fracture simulations, including the discrete element method, rigid block spring method and the discontinuous deformation analysis. The DDA method has recently been reformulated as a subset of a more generalised framework, and the procedure is seen as an alternative approach along with a number of approximation procedures suitable for modelling discontinuous media. The most recent generalisation is the Manifold Method (Shi 1997), which advocates very similar ideas as the ones used in the meshless methods (Belytschko et al 1994) and in the method of moving least squares (Nayroles 1992), the development of which can be traced back to early irregular finite difference networks in 1960s. Many common features exist in both approaches, where the meshless methods stem from a continuum side and the manifold method from the discontinuum end of the spectrum, indicating a possibility of a more rigorous treatment in modelling of the development of progressive discontinuities in quasi brittle materials.

Imposition of block contact constraints is established in various algorithmic ways. The initial approach (Shi 1988) adopted the penalty format, where the contact spring with a penalty stiffness is placed between the vertex of one block and the side of another. The convergence process may sometimes be very slow indeed, as both activation and deactivation of contacts during the iteration process is possible. The advantage of the penalty format lies in its simplicity, as the number of system variables does not change and the changes of the secant stiffness matrix are obtained iteratively by augmenting components of the stiffness matrix with components arising from the potential energy of any active contact penalty springs. The convergence of the solution algorithm depends highly on the choice of the penalty term and the process may often lead to ill conditioned matrices, associated with the very large penalty term employed to ensure the contact constraint. The Lagrange multiplier method leads to additional unknowns of the problem, where the system of equations is augmented by the presence of any active contact. The number of unknowns to be solved for at every increment becomes variable as contacts are activated and deactivated. The procedure has a major disadvantage as the resulting system matrix contains a zero sub-matrix associated with λ_i s and it may not be positive definite, requiring the use of a special matrix pseudo inversion procedure.

The most advanced treatment of contact constraints is the Augmented Lagrangian Method, which has been recently advocated in the DDA context (Lin 1995, Amadei et al 1995), where an iterative combination of a Lagrangian multiplier and a contact penalty spring is utilised. The ensuing iterative procedure, to obtain the correct contact forces, proceeds until the penetration distance and the norm of the out of balance forces is not smaller than some specified value. As the number of unknowns does not increase, the method retains the advantage of the penalty method. The rate of convergence of the ensuing iterative procedure to obtain the contact forces is clearly controlled by the penalty stiffness term and the iteration process is ended when the norm of the out of balance forces in between the two iterates is less than a specified tolerance limit.

2 FRACTURING IN DISCONTINUOUS DEFORMATION ANALYSIS

In the context of DDA, concrete fracturing can be modelled by releasing contact constraints along predetermined block interfaces or by the through block fracturing, thereby creating new blocks. The formulation deals naturally with discontinuities along block boundaries, which are created according to the Mohr-Coulomb criterion (with or without the tension cut-off) and this strategy resembles early concrete fracturing FE simulations (Ngo and Scordelis, 1967). The algorithmic argumentation is simple, as the normal and tangential contact springs, which are

added to the system whenever a vertex is in the vicinity of a vertex or a side of another block, are released instantaneously if a pointwise Mohr Coulomb or tension cut off condition (in terms of stress resultants) is violated. Similar possibilities exist within the combined FEM/DEM framework, where the Rankine criterion has been utilised to invoke fracturing and local remeshing (Munjiza et al, 1995), as well with interface elements in concrete mechanics (Rots and Schellekens, 1990)

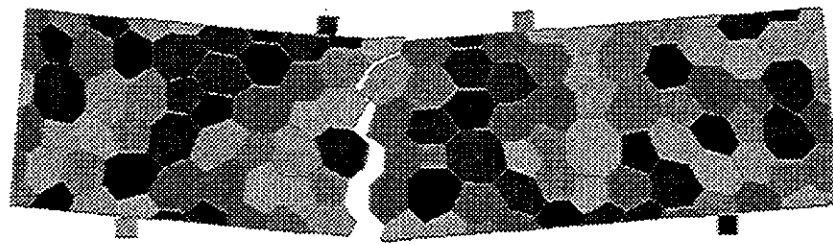
A block fracturing algorithm through block centroids has been proposed recently (Lin 1995), in the context of rock fracture, comprising again the Mohr-Coulomb fracturing criterion with a tension cut-off, where the newly formed discontinuities are introduced and are further treated in the same way as the original discontinuity planes.

It has been increasingly recognised that concrete behaves as a quasi brittle material and the fracture energy control of the reduction of material strength has been frequently adopted in a continuum based softening simulations of localised failure in concrete. Along similar lines, within the discontinuous modelling frameworks it is necessary for contacts to be released gradually and that process should be associated with energy dissipation. Such a control has been recently introduced into the block separation criterion within the RBSM framework (Kitoh et al 1997), by converting the relative displacement between the two rigid blocks into an equivalent cracking strain, which is then related to the reduced interface strength. Similar concept is clearly applicable within the DDA framework, which differs from the RBSM in the manner the medium deformability is accounted for (in RBSM deformability is concentrated on the block interfaces, with DDA within the blocks themselves). Within the DDA framework it is necessary to introduce energy dissipation across block interfaces. In an algorithmic sense, this could be done by converting an equivalent cracking strain across a given boundary into a non zero crack opening, which is then in turn used as a contact constraint (a finite gap, rather than zero) on the same interface. The iterative process would need to satisfy this modified constraint, which is at the same time associated with a reduced interface strength. A full block separation would follow only after the crack opening reaches a critical value, which is controlled by the fracture energy release rate at the interface in question.

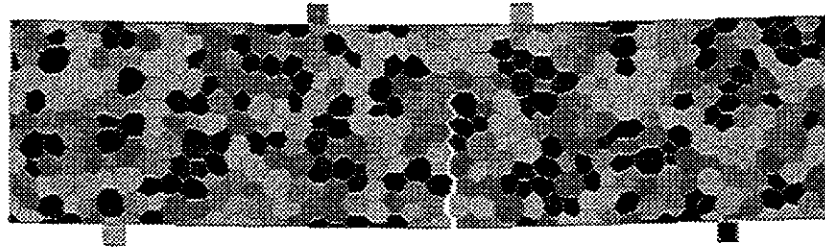
3 BENCHMARK PROBLEMS FOR CONCRETE FRACTURING

Several discontinuous modelling attempts in modelling the fragmentation of concrete structures have been reported. A series of RBSM block size sensitivity tests have been conducted (Kitoh et al 1997), exploring both the geometric size effect on fracture for series of normalised plain concrete beams, as well as the influence of the discretisation effect, resulting from different block sizes.

The Kitoh plain concrete beam four point bending problem ($h=100mm$) is here modelled with two DDA discretisations (Fig 1). The failure load predictions from a coarse discretisation using 130 simply deformable blocks is compared to the failure load prediction from a model comprising 455 simply deformable blocks and both results are set against the failure load prediction reported by Kitoh. The block material characteristics and the interface material law are identical in both cases ($E = 27.5$ MPa, $\nu=0.20$, $c=0.0047$ MPa, $f_t=0.0029$ MPa, $\phi=37^\circ$), the values which correspond to the data adopted in the RBSM analysis. The analysis has been conducted using an enhanced version of the Shi's original code, as a force controlled analysis, with an adaptive load incrementation in approaching failure.



(a)



(b)

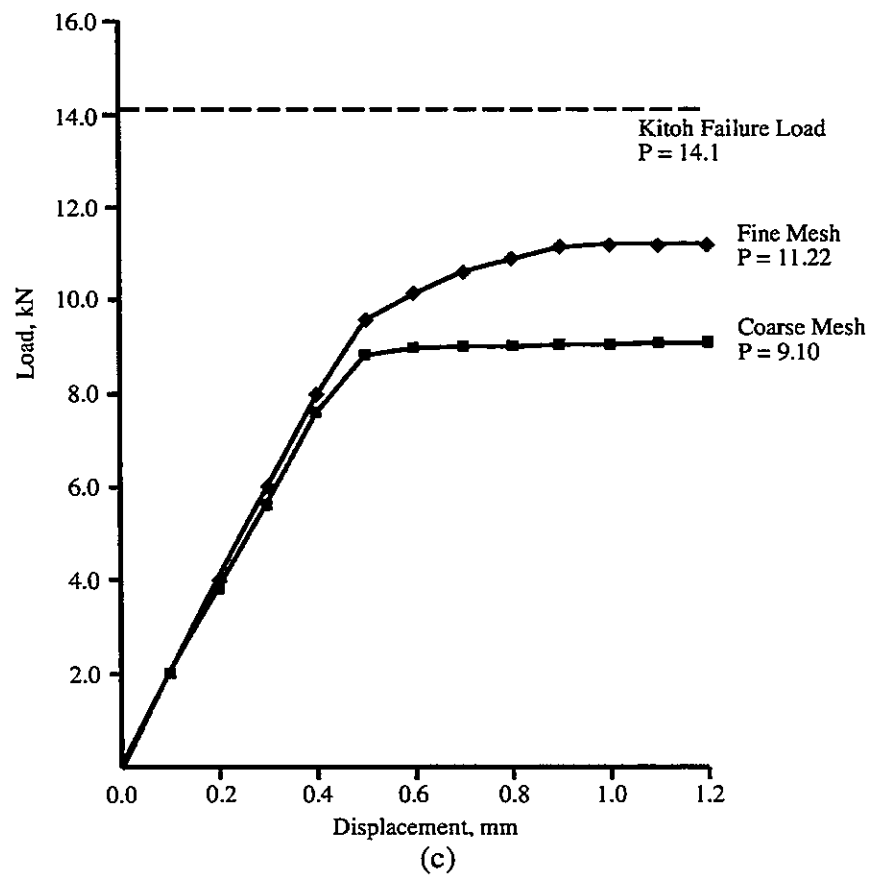


Figure 1. Kitoh Plain Concrete Beam ($h=100\text{mm}$) (a) Failure mode for coarser DDA discretisation (130 blocks), (b) Failure mode finer DDA discretisation (455 blocks), (c) Comparison of $P-\delta$ diagrams for (a) and (b) together with the RSBM failure load.

Another example (Fig 2) illustrates the results of the displacement controlled analysis of a plain concrete pull-out test. The problem geometry, similar to the RILEM Round Robin analysis corresponds to the tests carried out at the Delft University of Technology (Vervuurt et al, 1993). Here, only the bolt head was modelled, utilising the displacement controlled DDA formulation (Pearce et al 1999).

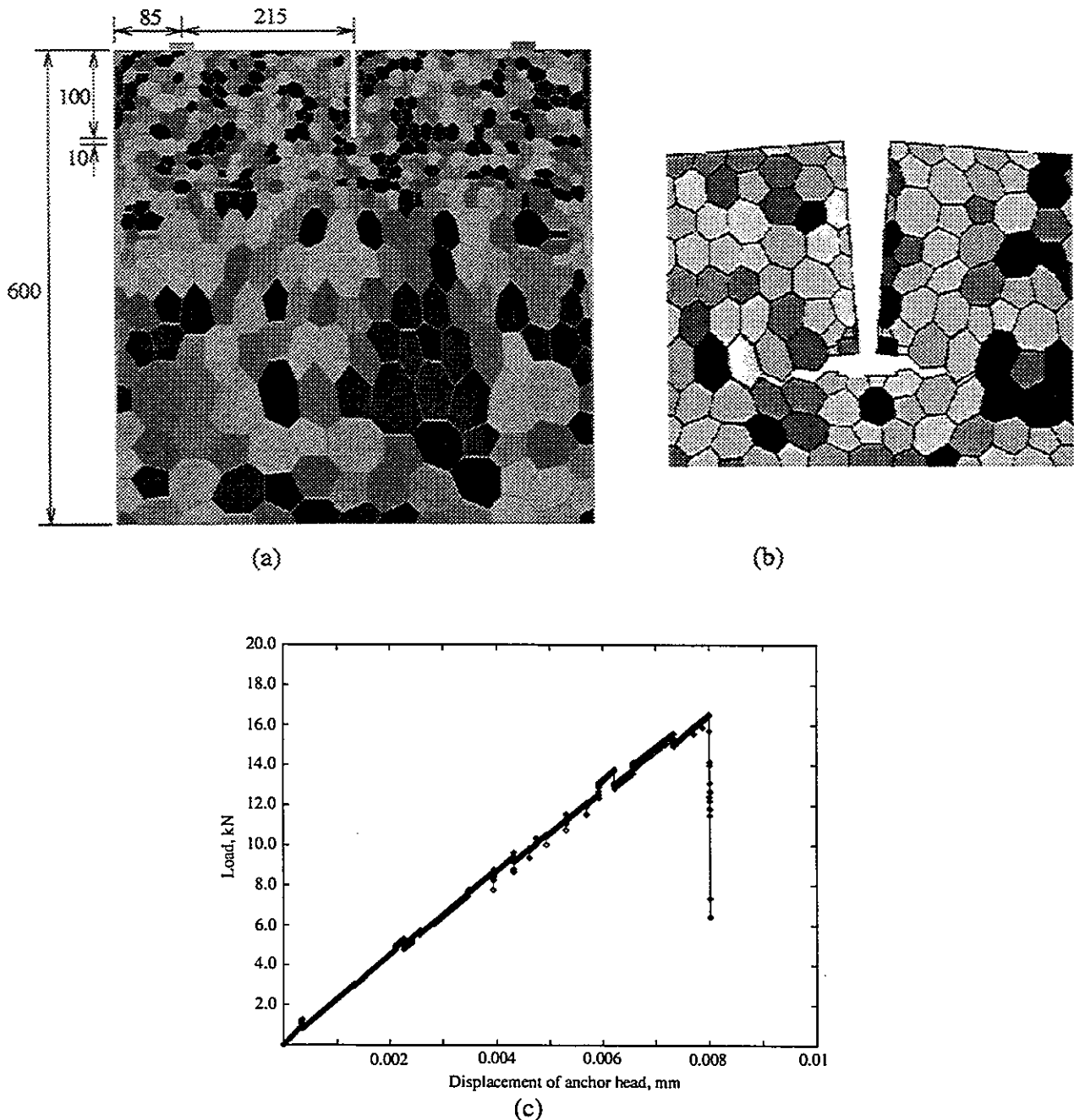


Figure 2. DDA Simulation of the Pull Out Test. (a) DDA discretisation (704 simply deformable blocks) and geometry (dimensions in mm). (b) Close-up of anchor head at end of analysis. (c) Load vs. displacement of anchor head.

The resulting load displacement diagram indicates the peak load which is approximately 70% of the experimentally observed ultimate load. The overly brittle post peak response follows as a direct result of the instantaneous interface release adopted in this analysis, confirming the need for a gradual energy controlled interface fracturing. In addition, there is a clear need for the DDA simulations of such problems to utilise computational strategies associated with overcoming limit points, used successfully in the context of the finite element analysis (e.g. arc length method). Close-up of the anchor bolt head at the end of the analysis is also illustrated.

4 EIGENVALUE ANALYSIS IN MONITORING PROGRESSIVE FAILURE

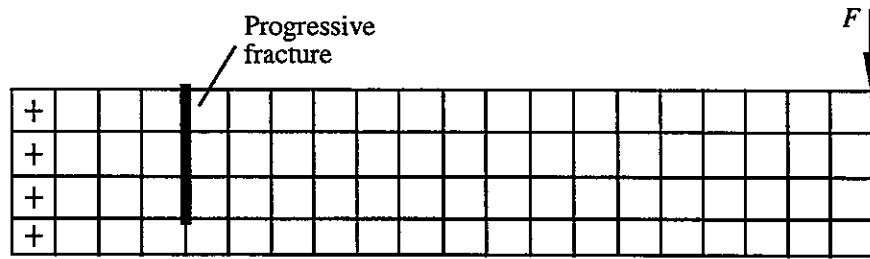
A convenient way of monitoring progressive failure can be established by tracing, as the solution progresses, the evolution of the lowest eigenvalue of the DDA block system, similar to the current stiffness concept used in the finite element context. It was argued that such a monitoring strategy (Pearce et al 1999) can be used to signal a necessary switch in a solution procedure in order to ensure a robust treatment in overcoming limit points.

In light of the above, it is important to distinguish between the algorithmic stiffness matrix and the stiffness matrix to be used to assess the current eigenvalues when using the Augmented Lagrangian format to impose the DDA block contact constraints. The Augmented Lagrangian approach utilises a low penalty term and establishes the correct contact forces in an iterative way. Such an approach is clearly computationally desirable to improve numerical conditioning, however the ensuing algorithmic DDA system stiffness matrix on its own does not reflect the block constraint conditions. Therefore, for the purpose of a current stiffness eigenvalue analysis, the DDA system matrix needs to be modified by replacing the low penalty terms by the high penalty terms, which secures that the block constraints are satisfied in a linearised eigenvalue analysis.

A benchmark problem considering progressive fracturing of a cantilever beam subjected to point load is considered (Fig 3). Evolution of the four lowest eigenvalues of the cantilever beam in various stages of fracturing is indicated, where it is interesting to note that some stiffness eigenmodes are less affected by the presence of discontinuities than others. The current stiffness ratios λ/λ_0 are also given for various stages of fracturing and various deformation modes.

5 CONCLUSIONS

Some aspects associated with the discontinuous deformation analysis framework in modelling concrete fracture have been discussed. The displacement controlled analysis, required for tracing structural response beyond the limit point was illustrated on two illustrative problems. It is noted that - for the purpose of a linearised eigenvalue analysis - the algorithmic DDA system stiffness matrix associated with the Augmented Lagrangian approach needs to be replaced by a stiffness matrix, which correctly reflects the block constraints. It is suggested that the current stiffness ratios can be used as failure indicators in simulations of concrete fracture, in particular to indicate changes in nonlinear solution strategies needed to overcome algorithmic difficulties near limit points.



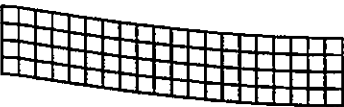





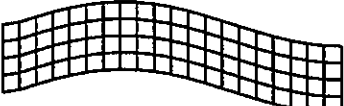
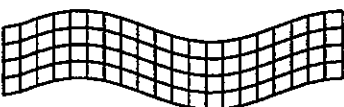
			Stage 0	Stage 1	Stage 2	Stage 3
Mode 1  λ_1						
	λ		22.64	18.22	14.54	4.38
	λ/λ_0		1.00	0.80	0.64	0.19
Mode 2  λ_2						
	λ		66.21	65.00	63.22	58.40
	λ/λ_0		1.00	0.98	0.95	0.88
Mode 3  λ_3						
	λ		105.34	94.46	88.07	78.55
	λ/λ_0		1.00	0.90	0.84	0.75
Mode 4  λ_4						
	λ		148.85	148.85	148.85	148.84
	λ/λ_0		1.00	1.00	1.00	1.00

Figure 3. Progressive fracture of a cantilever subject to end point load. Changes in eigenvalues and eigenmodes corresponding to different stages of fracturing and the evolution of the current stiffness ratio λ/λ_0

REFERENCES

- Amadei, B., Lin C., Dwyer J., 1996. Recent Extension to the DDA Method, in *DDA and Simulations of Discontinuous Media*, TSI Press, Albuquerque 1996, 1-30
- Belytschko T, Y. Lu, L. Gu 1994. Element Free Galerkin Methods, *Intl Journal for Numerical Methods in Engineering* 37: 329-356
- Chen G, Ohnishi Y., Ito T. 1997. Development of High Order Manifold Method, in Y. *Proc ICADD-2 Conf on Analysis of Discont Deformation*, Kyoto University, July 1997: 132-154
- Ghaboussi, J. 1988. Fully deformable Discrete Element Analysis using a Finite Element Approach, *Intl Journl of Comp and Geotech* 5: 175-195
- Goodman, R. E., Taylor R. L., Brekke T. 1968. A model for mechanics of jointed rock, *Jnl of Soil Mech and Found Div Proc ASCE* 94, SM3
- Ingraffea, A. 1997: FE Methods for discrete crack modelling of concrete structure notes, Lecture Notes CISM Course, Udine, Italy
- Ke, T. 1996. Artificial Joint Based DDA, in Salami & Banks (Eds) *DDA and Simulations of Discontinuous Media*, TSI Press, Albuquerque 1996: 326-333
- Kitoh, H. et al 1997. Size Effect Analysis of Plain Concrete Beams by using RSBM, *Proc ICADD-2 Conf on Analysis of Discont Deformation*, Kyoto University, July 1997: 373-382
- Lin, C. 1995. *Extensions to the DDA for Jointed Rock Masses and other Blocky Systems*, PhD Thesis, University of Colorado, Boulder
- Nayroles, B, Touzot B, Villon P. 1992. Generating the finite element method by diffuse approximation and diffuse elements, *Journal of Computational Mechanics* 10: 307-318
- Ngo D., Scordelis A. C., 1967. Finite element analysis of reinforced concrete beams. *ACI Journal*, 64(3): 152-163
- Pearce, C. , Bicanic N., Thavalingam A., Liao Z. H. 1999. Computational aspects of the discontinuous deformation analysis framework for modelling concrete fracture, submitted for publication to *Intl Journal for Fracture Mechanics*
- Rots, J. G. , Schellekens, J. C. J. 1990. Interface elements in concrete mechanics, *Proc SCI-C* 1990 (eds Bicanic/Mang), Pineridge Press, vol 2: 909-918
- Shi, G. H. 1988. *Discontinuous deformation analysis - a new numerical method for the statics and dynamics of block systems*, PhD thesis, Dept Civil Engng, Univ of California, Berkeley
- Shi G. H. 1997. Numerical Manifold Method, in Y. Ohnishi (ed) *Proceedings ICADD-2 Conference on Analysis of Discontinuous Deformation*, Kyoto University, July 1997: 1-35
- Vervuurt A., Schlangen E., van Mier J. G. M, 1993. A numerical and experimental analysis of the pull out behaviour of steel anchors embedded in concrete, Tech Report 25.5-93-1/VFL, Faculty of Civil Engineering, Delft University of Technology

ANALYSIS OF LARGE BLOCK TEST DATA USING THE DDA METHOD

M. Ronald Yeung

San Jose State University, Department of Civil and Environmental Engineering
San Jose, CA 95192-0083, USA

Stephen C. Blair

Lawrence Livermore National Laboratory, Experimental Geophysics Group, L-201
Livermore, CA 94551, USA

ABSTRACT: The Large Block Test (LBT) is one phase of the field-scale thermal testing program of the Yucca Mountain Site Characterization Project (YMP). It is a thermal test on an exposed block of fractured rock. Because the block is a well mapped fractured rock mass, it is a good candidate for analysis using discontinuum models such as the Discontinuous Deformation Analysis (DDA). The approach is to use both DDA back and forward analyses to analyze the temperature and deformation data obtained during the LBT. In the DDA back analyses, local deformations at anchor points of multi-point borehole extensometers (MPBXs) will be used as input to obtain the global deformed configuration of the block. From the computed global deformed configuration, fracture deformation will be calculated and compared with measured fracture monitor data. In the DDA forward analyses, the measured temperature as a function of time will be used as input to predict the global deformed configuration. The computed global deformed configuration will be evaluated to determine if it is consistent with measured MPBX and fracture monitor data. Preliminary results from a DDA back analysis show that while the computed fracture deformation follows a reasonable trend, the magnitude of the fracture deformation computed is in general larger than that measured. Furthermore, in some cases the computed and measured deformation are of opposite sense. These findings point to the need to refine the simplifications and assumptions made in the analysis. To resolve the discrepancy between computed and measured results, additional refined analyses will be performed.

1 INTRODUCTION

The Large Block Test (LBT), conducted at Fran Ridge, near Yucca Mountain, Nevada, comprises one phase of the field-scale thermal testing program of the Yucca Mountain Site Characterization Project (YMP). One of the primary goals of this program is to aid in the understanding and characterization of coupled thermal-hydrologic-mechanical-chemical (THMC) processes in the near field environment of a potential high-level waste repository. The particular objective of the LBT was to monitor and characterize coupled THMC processes in an isolated block of fractured rock subject to a one-dimensional thermal gradient (Wilder et al. 1997).

The deformation of the block during the LBT was simulated using two- and three-dimensional continuum models (Blair et al. 1996), and Blair and Wood (1998) found poor agreement between

the predicted and observed deformations. Because the block is an unconfined, and well mapped fractured rock mass, it is a good candidate for analysis using discontinuum models. One such model is the Discontinuous Deformation Analysis (DDA), which will be used to analyze the thermal-mechanical behavior of the block during the LBT.

In this paper we present a brief discussion of the temperature and deformation data obtained during the LBT, describe the approach we will use to analyze the LBT data using DDA, and present preliminary results of a DDA back analysis of the LBT data.

2 DESCRIPTION OF LARGE BLOCK TEST

The LBT was conducted on a rectangular prism of rock 3 m x 3 m in cross-section and 4.5 m high that was exposed from an outcrop by excavating the surrounding rock (see Figure 1). Detailed geologic mapping showed that two subvertical sets of fractures and one set of subhorizontal fractures intersect the block. The subvertical fracture sets are approximately orthogonal, with spacings of 0.25 to 1 m and are oriented generally in the NE-SW and NW-SE directions. Moreover, a major sub-horizontal fracture is located approximately 0.5 m below the top surface. This fracture is visible in Figure 1.

To create a one-dimensional thermal field within the block heaters were placed in the rock to simulate a plane heat source at a height of 1.75m from the base of the block, and a steel plate fitted with heating/cooling coils was mounted on the top of the block. This plate was connected to a heat exchanger to allow thermal control of the top surface. The block was heated for more than 12 months, from Feb. 27, 1997 until March 10, 1998.

The overall three-dimensional mechanical response of the rock to the heating was monitored using six multi-point borehole extensometers (MPBXs). Three were oriented horizontally in the N-S direction; two were oriented horizontally in the E-W direction, and one was oriented vertically. In addition, deformation of several major fractures that intersect the surface of the block was monitored using three-component fracture monitors. These were installed at 17 locations on the surface of the block. A few of the fracture monitor locations are visible as T-shaped grooves in Figure 1. The fracture monitors measured movement in directions across the trace of the fracture parallel to the face, and along the trace of the fracture both parallel and perpendicular to the face. In addition, temperature, moisture level and electrical resistivity in the block were also monitored.

Preliminary monitoring data have been presented by Wilder et al. (1997). Only temperature and deformation data will be discussed here.

3 SUMMARY OF TEMPERATURE AND DEFORMATION DATA

The temperature measured near the center of the heater plane is plotted against time in Figure 2. This figure shows temperature increased from ambient to 90 °C in the first few hundred hours of heating. A power outage caused a drop in temperature at approximately 600 hours. When power was restored temperatures quickly rose back to pre-outage levels, and near the heater temperature reached approximately 98 °C after 750 hours of heating. The overall temperature profile is consistent with conduction-dominated heat flow in the block, except for the temperature

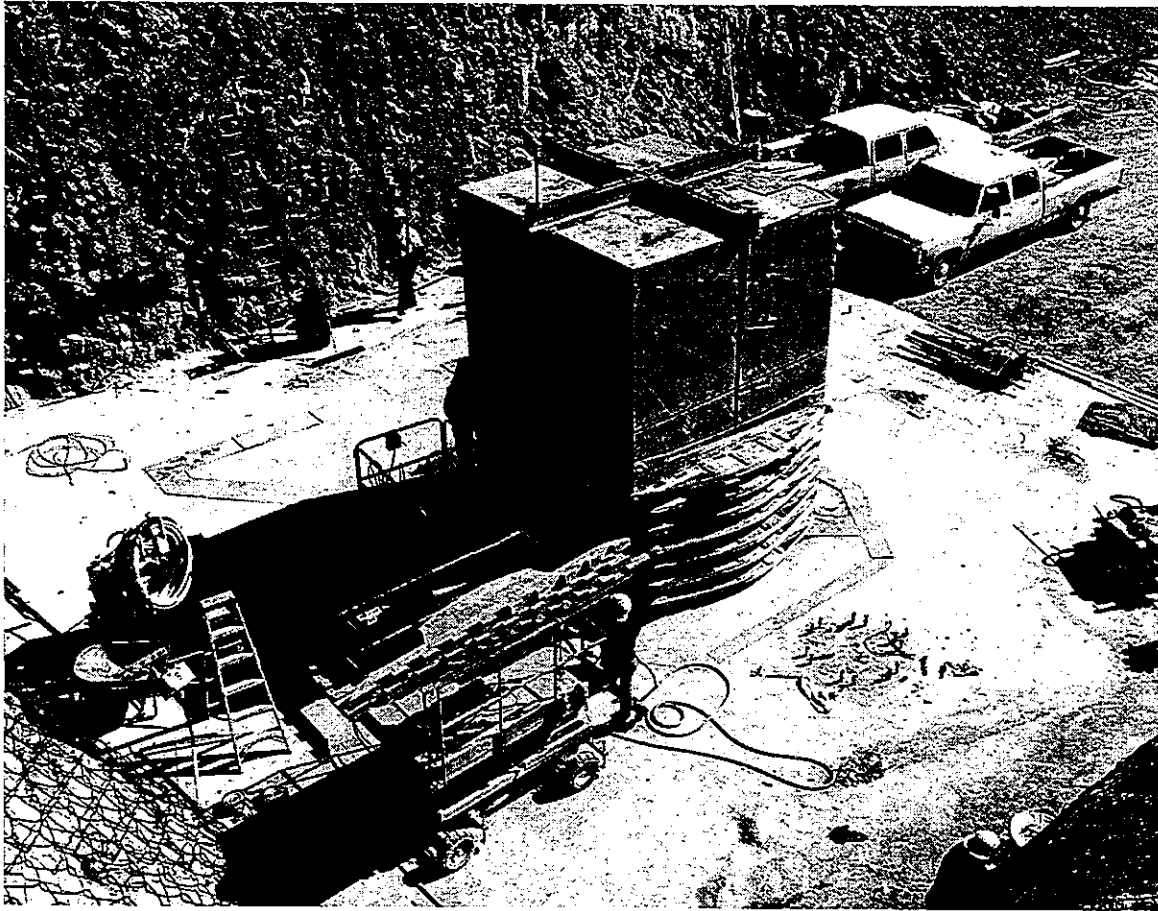


Figure 1. Site of the Large Block Test.

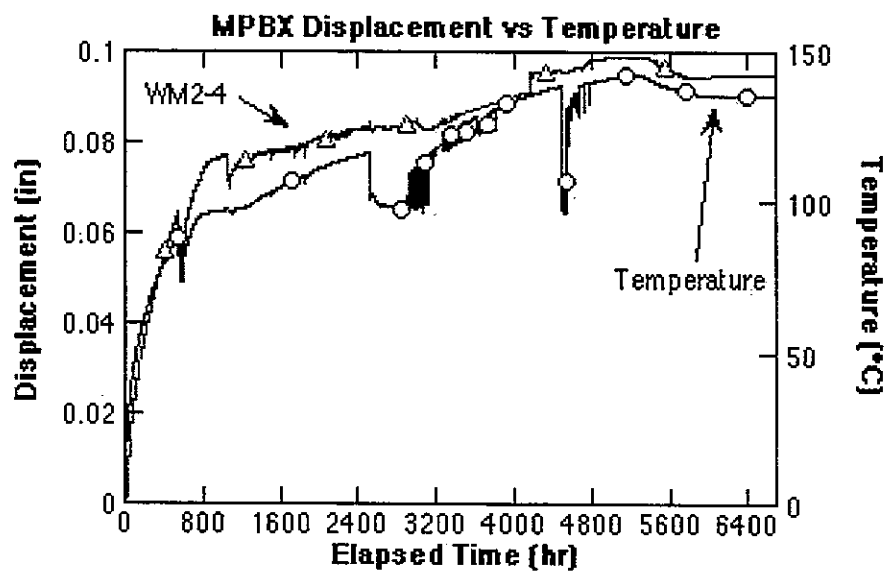


Figure 2. Typical temperature-time history and typical MPBX deformation-time history.

excursions at 2520 and 4475 hours. These excursions are thought to be breakdowns in the metastable hydrothermal regime and formation of transient heat-pipes. Currently the exact mechanism causing this behavior is poorly understood.

Preliminary analysis of data from the MPBX systems shows that within a few hours of the heater start-up the block started expanding. The deformation-time history for a typical MPBX anchor is shown along with the temperature in Figure 2, which shows that the overall deformation is directly correlated with the heating history. Note that the MPBX data do not indicate contraction during the thermal perturbations at 2500 and 4475 hours, indicating that these temperature perturbations are local events within the block.

Overall horizontal deformation of the block after approximately 60 days of heating shows similar amounts of expansion in both the E-W and N-S directions. These data are plotted in Figure 3, which shows that horizontal expansion is a linear function of height above the base. The observed horizontal deformation increases with height and is independent of the thermal profile above the heater plane. Moreover, MPBX data from boreholes in the upper third show that most of the deformation occurs in discrete vertically oriented zones. This may be caused by opening of vertical fractures in this upper region. Data also indicate that strain in the vertical direction is less than that observed in the horizontal direction, and that the region of the block above the heaters is moving upward as a unit.

Results from the fracture monitors are consistent with those from the MPBX in that the fractures are generally opening. Analysis of the fracture monitor data indicates that several of the fractures opened by an amount between 0.13 mm and 0.38 mm (0.005 and 0.015 in), and that closure of some fractures was observed. Moreover, observed shear displacements are generally larger than normal displacements across the fractures, and at three locations 0.51 mm (0.02 in) of shear displacement was observed.

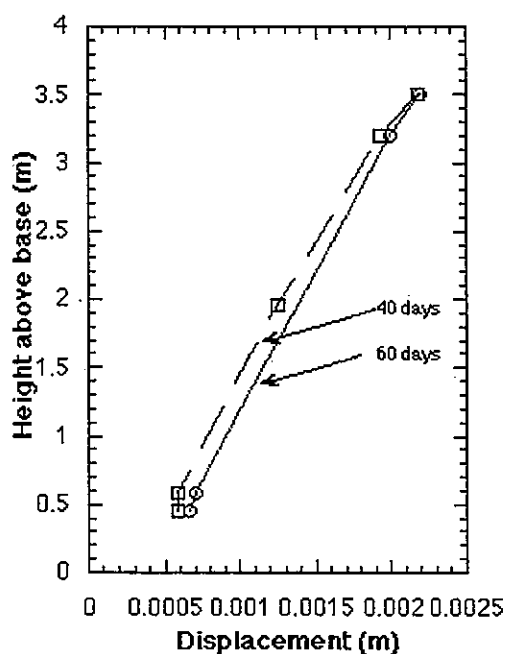


Figure 3. Plot of horizontal expansion against height above base.

4 ANALYSIS OF LBT DATA USING DDA

4.1 *Approach*

The block of fractured rock tested in the LBT will be treated as a discontinuous system of rock blocks bounded by fractures. Sections through the block will be developed to allow two-dimensional analyses using DDA. Two types of analyses using the DDA method, namely the back analysis and the forward analysis, will be performed.

In the DDA back analyses, local deformations at anchor points of the MPBXs will be used as input to obtain the global deformed configuration of the block. From the computed global deformed configuration, fracture deformation will be calculated and compared with measured fracture monitor data. It may be interesting to note that Shi and Goodman (1984) developed the original DDA as a back analysis used to interpret the data obtained from another "large block test."

In the DDA forward analyses, the measured temperature as a function of time at various points in the block will be used as input to predict the global deformed configuration. The computed global deformed configuration will be evaluated to determine if it is consistent with measured MPBX and fracture monitor data.

4.2 *DDA Back Analysis*

Using the fracture maps of the five exposed faces of the block, a three-dimensional physical model of the block was constructed to aid in the selection of sections to be analyzed and fractures to be included in the sections for analysis. Because the fractures in the block are nearly horizontal and vertical, meaningful analysis can be performed on two-dimensional vertical and horizontal sections through the block.

To take advantage of the MPBX data, sections should be developed that cut through planes containing or close to containing MPBXs. One such section is a horizontal section 1 m from the top surface of the block (Section 1), which is near MPBXs designated WM2 and NM3. Using the three-dimensional physical model of the block, all through-going fractures (fractures that cut through the whole block) were identified and included in Section 1. Fractures that terminate inside a rock block and do not form rock blocks were ignored. The fractures are represented by connecting straight line segments in Section 1 as shown in Figure 4.

The MPBX data are used as input in the DDA back analysis. Because the deformation of an MPBX anchor is measured relative to a reference point which is not fixed in space, an assumption must be made on the deformation of the reference point. The assumption used in the analysis is that the block expands outwardly from the center during the test so that the N-S plane of symmetry of the block does not deform in the E-W direction, and the E-W plane of symmetry does not deform in the N-S direction. Based on this assumption, the intersection point between an MPBX and a plane of symmetry does not deform in the direction along the length of the MPBX, given that the MPBX is normal to the plane of symmetry. Therefore, all the anchor deformations in the direction along the length of the MPBX can be referenced against this intersection point. To obtain deformation data in the direction normal to the length of the

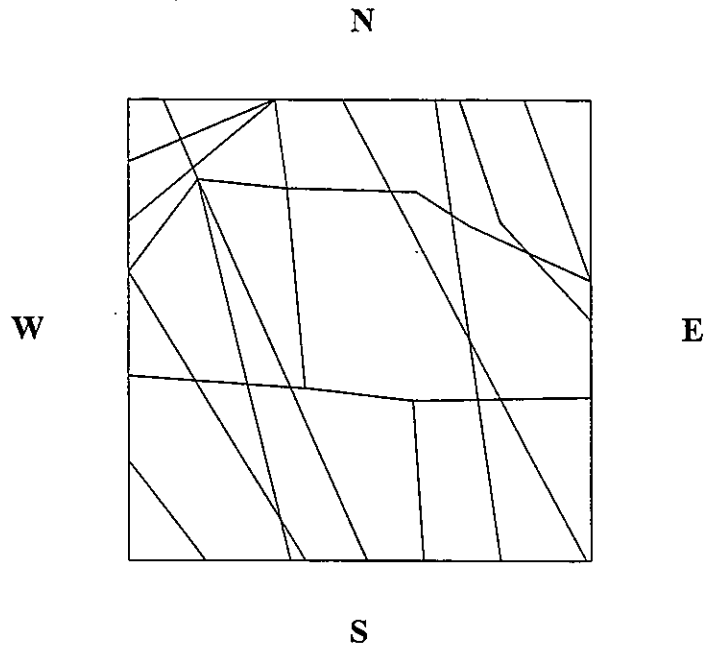


Figure 4. Section 1.

MPBX at the anchor points, an additional assumption made is that all the anchor points of an MPBX have the same deformation normal to the length of the MPBX. Using this assumption, the deformation at an anchor point in the direction normal to the length of an MPBX can be interpolated from deformation data from another MPBX normal to the MPBX. With these assumptions and using the data from the two MPBXs (WM2 and NM3), the deformation-time histories in the N-S and E-W directions for anchor points on Section 1 shown in Figure 5 were computed. In addition, grid points shown on Figure 5 were defined and their deformation-time histories taken from those for the anchor points. For example, for the grid point at the NW corner of the section, its N-S deformation is the same as the N-S deformation for the anchor point on the north boundary of MPBX NM3, and its E-W deformation is the same as the E-W deformation for the anchor point on the west boundary of MPBX WM2.

With the deformation-time histories of the anchor points and additional grid points on Section 1 as input data and additional input data including those on intact rock and fracture properties, a DDA back analysis was performed using DDA programs (Shi, unpubl.) to compute the global deformation of the section with time. Figure 6 shows the deformed configuration of the section at the end of the heating period analyzed (2500 hours of heating). It can be seen from this figure (although not too apparent because of the small deformations) that some fractures in the section have opened (e.g. E-W trending fracture within the southern half of the section) and some fractures have sheared (e.g. see deformed south boundary). These observations are consistent with measured deformation data.

Using the DDA results, the deformations of selected fractures at the boundaries of Section 1 were computed. Four locations on fractures near fracture locations monitored during the LBT by fracture monitors WF4, EF4, NF4, and SF1 were considered, as labeled in Figure 5. For example, fracture location on the north boundary of Section 1 labeled NF4 in Figure 5 is close to fracture monitor NF4; therefore, the computed fracture deformation at this location can be

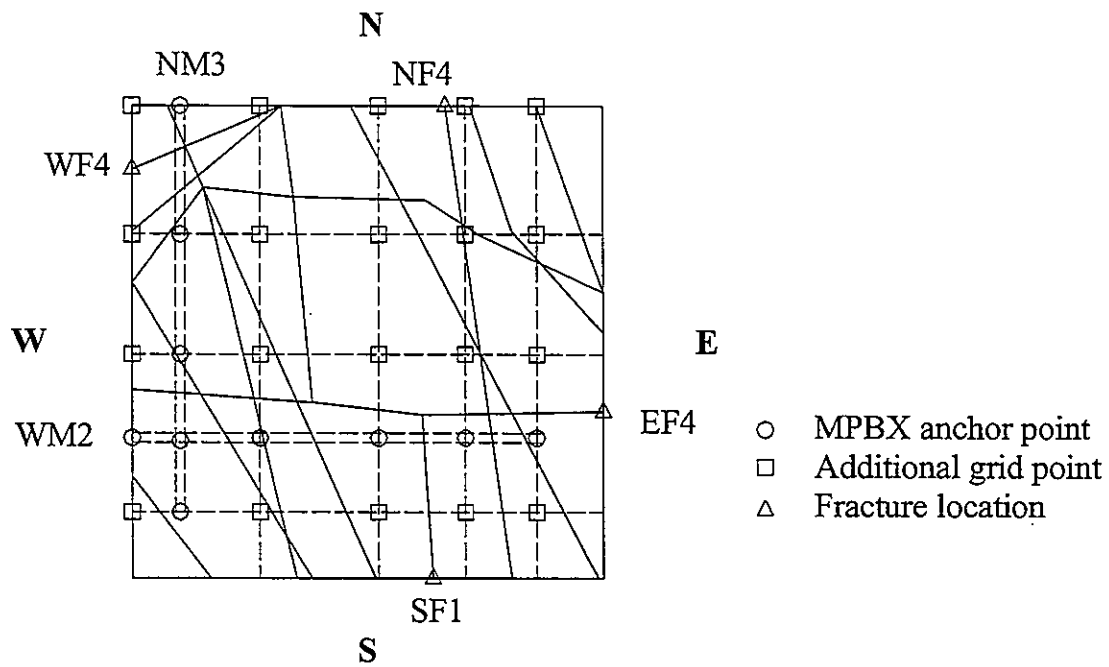


Figure 5. MPBX anchor points, additional grid points and fracture locations on Section 1.

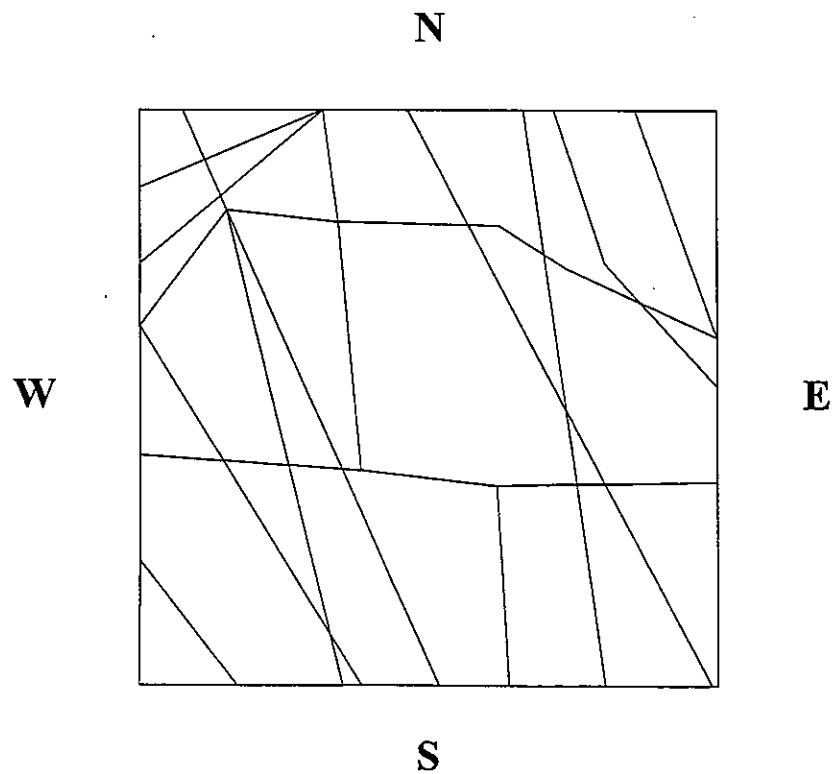


Figure 6. Deformed configuration of Section 1.

compared with that measured by fracture monitor NF4. The deformation has two components, one parallel and one normal to the section boundary. For comparison, the fracture deformation parallel to the section boundary measured and computed by DDA are plotted with elapsed time on the same plot for each of the four fracture locations. A typical plot of this type is shown in Figure 7 for the NF4 location. Similarly, the fracture deformation normal to the section boundary measured and computed by DDA are plotted with elapsed time on the same plot for each of the four fracture locations. A typical plot of this type is shown in Figure 8 for the WF4 location. The sign convention used in these plots is that positive fracture deformation parallel to the section boundary indicates closing of the fracture and that positive fracture deformation normal to the section boundary indicates right-lateral shear.

Some observations can be made from the plots comparing measured and computed fracture deformations. In general, the computed fracture deformation follows a trend consistent with the input deformation-time histories. However, the magnitude of the fracture deformation measured is generally smaller than that computed by DDA, as is the case in Figures 7 and 8. Furthermore, in some cases, the sense of deformation measured is opposite the one indicated by DDA results (see for example Figure 7).

The apparent discrepancy between measured fracture deformation and fracture deformation computed by the DDA back analysis may be explained by the various simplifications and assumptions made in the analysis. First, the section analyzed is a two-dimensional section through a three-dimensional block. The fact that the fractures are not perfectly vertical or horizontal and that a major subhorizontal fracture exists just above the section analyzed may cause discrepancy between computed and measured results. Second, the actual fractured rock mass was simplified and represented by a block system delineated by straight-line segments. The number and locations of the fractures had to be estimated. Often a fracture zone was represented by a single fracture; this may explain the higher fracture deformation computed than measured because the computed fracture deformation is actually for a fracture zone while the measured fracture deformation is for one of many fractures in the fracture zone. Furthermore, because fractured rock mass behavior can be "chaotic" in nature, the computed fracture deformation can conceivably be affected greatly by adding, eliminating or changing a single fracture. Third, assumptions detailed earlier in this section were made to obtain additional deformation data from the limited MPBX data available. It is possible that these assumptions do not reflect the actual conditions. Lastly, DDA assumes constant-strain blocks and therefore may not adequately model blocks with varying strains under a temperature gradient. To evaluate the effects of these simplifications and assumptions and to resolve the discrepancy between measured and computed results, additional analyses will be performed.

5 CONCLUSIONS

The LBT is an in-situ thermal test on an exposed block of fractured rock. Because the block is a well mapped fractured rock mass, it is a good candidate for analysis using discontinuum models such as DDA. The approach is to use both DDA back and forward analyses to analyze the temperature and deformation data obtained during the LBT. In the DDA back analyses, local deformations at anchor points of MPBXs will be used as input to obtain the global deformed configuration of the block. From the computed global deformed configuration, fracture

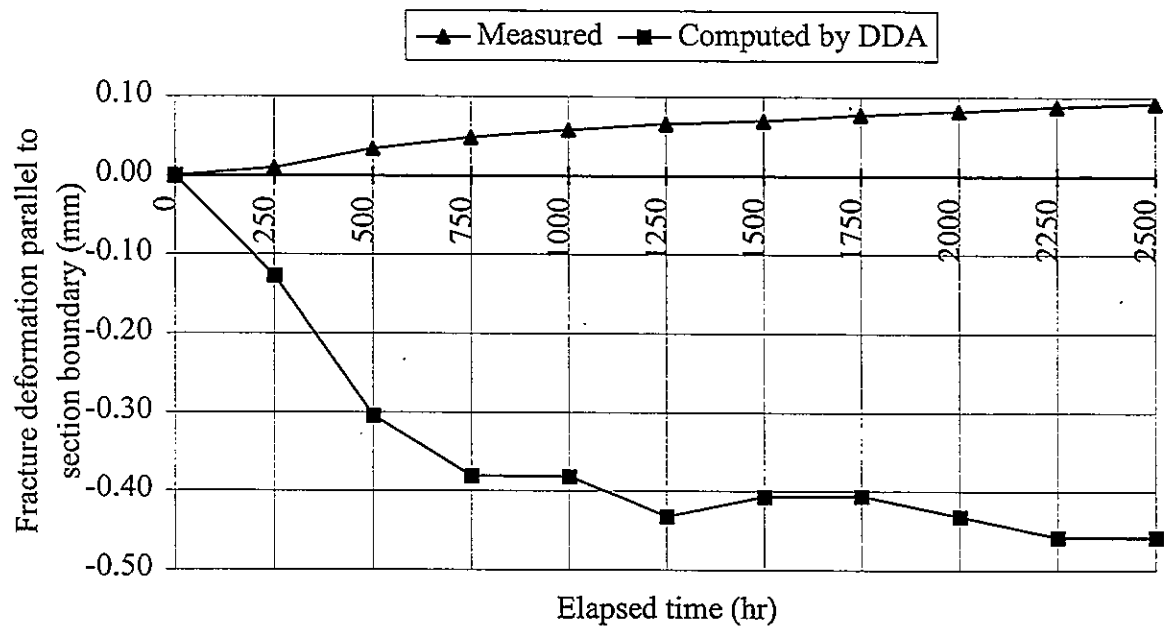


Figure 7. Fracture deformation parallel to section boundary at NF4 location.

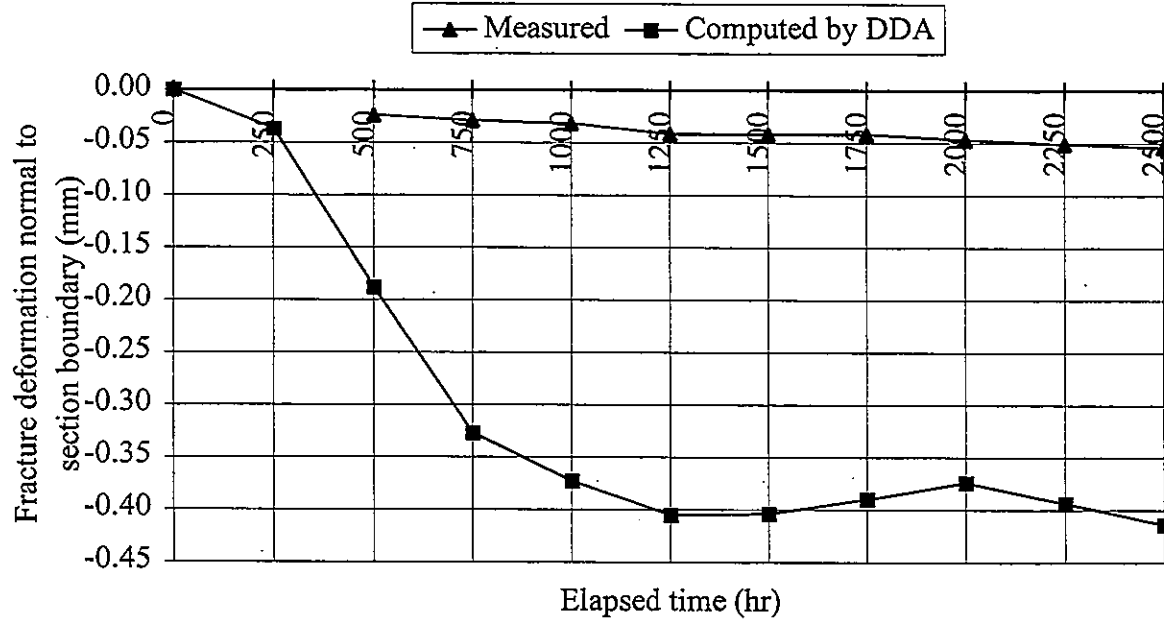


Figure 8. Fracture deformation normal to section boundary at WF4 location.

deformation will be calculated and compared with measured fracture monitor data. In the DDA forward analyses, the measured temperature as a function of time will be used as input to predict the global deformed configuration. The computed global deformed configuration will be evaluated to determine if it is consistent with measured MPBX and fracture monitor data.

Preliminary results from a DDA back analysis show that while the computed fracture deformation follows a reasonable trend, the magnitude of the fracture deformation computed is in general larger than that measured. Furthermore, in some cases the computed and measured deformation are of opposite sense. These findings point to the need to refine the simplifications and assumptions made in the analysis. To resolve the discrepancy between computed and measured results, additional refined analyses will be performed.

REFERENCES

- Blair, S.C. and Wood, S.A. 1998. Geomechanical observations during the large block test. *Proceedings of International High-Level Radioactive Waste Conference*, Las Vegas.
- Blair, S.C., Berge, P.A., and Wang, H.F. 1996. *Geomechanical analysis of the Large Block Test*. UCRL-ID 122898. Lawrence Livermore National Laboratory.
- Shi, G.-H. 1996. Unpublished *User's Manual for Discontinuous Deformation Analysis Programs, Version 96*.
- Shi, G.-H. and Goodman, R. E. 1984. Discontinuous deformation analysis. *Proceedings of the 25th U.S. Symposium on Rock Mechanics*, Evanston, Illinois.
- Wilder, D.G., Lin, W., Blair, S.C., Buscheck, T., Carlson, R.C., Lee, K., Meike, A., Ramirez, A.L., Wagoner, J.L., and Wang, J. 1997. *Large Block Test status report*. UCRL-ID-128776. Lawrence Livermore National Laboratory.

ON THE METHODOLOGY OF NUMERICAL ETCHING

Xinhua Wang
Manifold Engineering
18645 East Gale Avenue, Suite 200, City of Industry, CA 91748-1345, USA

Kuokai Shyu
Manifold Engineering
18645 East Gale Avenue, Suite 200, City of Industry, CA 91748-1345, USA

Chiao-Tung Chang
Manifold Engineering
18645 East Gale Avenue, Suite 200, City of Industry, CA 91748-1345, USA

Dawei Zheng
University of California at Los Angeles, Department of Materials Science and Engineering
Los Angeles, CA 90095, USA

ABSTRACT: The methodology of "numerical etching" used to study the stress distribution of a patterned thin film residing on a silicon wafer was developed. Silicon underlying the pattern was thinned down through etching so that the deformation caused by residual stress in the microstructure could be detected by a Twyman-Green laser interferometer (TGLI). *Successive etching model*, a numerical approach based on discontinuous deformation analysis (DDA), was implemented to simulate the etching process which linked the stress state of the microstructure on a regular wafer to that on a silicon diaphragm. An initial stress field on the pattern was assumed, and its effect on the deformation of the Si diaphragm beneath was calculated and compared with experimental results. The discrepancy between them was used to modify the initially assumed stress field and was repeated until a satisfactory match was achieved. The stress field from numerical analysis accurately predicts the actual stress distribution in and around the patterned structure under investigation. The stress distribution in a titanium pad on a $\text{Si}_3\text{N}_4/\text{SiO}_2/\text{Si}$ composite diaphragm is used as an example.

1 INTRODUCTIONS

For quality control and reliability analysis in semiconductor manufacturing, it is crucial to understand and assess the stress field in semiconductor devices. Such stress may result from process integration in thin film deposition, etching, passivation and thermal treatment. In practice, the residual stress in a blanket thin film can be measured by either using a bending beam method (Tu et al. 1992) or an X-ray diffractometer (Malhotra et al. 1996). Though this gives a good reference to the relative stress level in the materials, device engineers are more concerned with the local stress in and around the patterned microstructure. There have been three key approaches in the industry to measure the localized stress in devices, namely, micro-beam X-ray, micro-indentation, and Raman-microscopy.

During the past decade, the beam-size of X-rays has been reduced to 0.8 μm in diameter with great sensitivity (Marcus and Lutterodt, unpubl.). Such a technique can measure all six strain tensor components, and offers a direct measurement of strain without the involvement of other physical assumptions. However, the sample alignment is complicated, and the technique is extremely expensive. Micro-indentation, as a convenient way of measuring stress, has been used in the industry as an alternative. Sub-micron sized indentation mark analysis was made a long time ago (Doerner et al. 1986); however, it seems that the industry still has doubts about measurement interpretation when the substrate is of a multi-layer nature. Raman-microscopy has also progressed recently (Englert et al. 1980, Ajito et al. 1995). This technique can achieve a less than 1 μm spatial resolution and a 25 MPa sensitivity in Si. However, the technique has limited application in polycrystalline and amorphous materials.

In this paper, we propose a methodology to study the stress field in and around the patterned microstructure. Stress analysis of a Ti pad on a $\text{Si}_3\text{N}_4/\text{SiO}_2/\text{Si}$ composite diaphragm is used as an example. We etch the top layer of the Ti film to form a pad, and then etch the back of the Si wafer to form a Si diaphragm window beneath the Ti pad. Deformations on the Si diaphragm caused by residual stress in the Ti pad and two insulating layers are detectable by a Twyman-Green laser interferometer (TGLI). *Successive etching model*, a numerical approach based on discontinuous deformation analysis (Shi 1993, Shyu 1993, Chang 1994), is implemented to simulate a dynamic etching process and record all the changes in the mechanical fields of the Ti pattern, the insulating materials, and Si substrate. An iterative process is followed until the computed and measured deformation of the final Si diaphragm is reasonably matched.

2. THEORY

2.1 Background

The numerical etching algorithm is designed to simulate the random or sequential processes of dry and wet etching. The method of numerical etching process is developed on the basis of discontinuous deformation analysis (DDA). DDA, developed by Shi (Shi 1993), is a powerful numerical model for analyzing a system containing many solids. This technique uses the variation principle in solid mechanics. In order to resolve the stress re-distribution in a patterned thin film and its substrate, the simulation of an etching process in chip manufacturing is similar to the step-by-step sequential or random excavation in tunneling. Therefore, constituting from the theory and method of DDA, we developed a numerical model called "successive etching model" combining DDA with axially symmetric finite element model to effectively resolve stress distribution in patterned microstructure.

2.2 Successive Etching Model

Etching is an irreversible process. The process of mass or energy loss from the system cannot be reversed. For a specified patterning, energy loss will be different for various methods used in the etching procedure. If we etch portions A and B instantaneously in case I and sequentially in case II as shown in Figure 1, the energy loss in case II is approximately five times of that in case I.

During the process of substrate thinning, the substrate varies from a thick plate to a thin membrane, thus, the modeling problem involves a solid/plate problem, through combined

membrane plus plate (M+P) transition stage, and to the membrane stage. For a very thin diaphragm that is traditionally considered a membrane problem, combined M+P effects still need to be considered due to the fixed-end boundary condition near the corners of the substrate window.

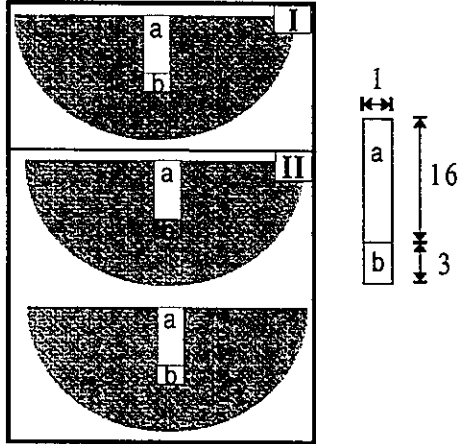


Figure 1. Energy loss for different patterning

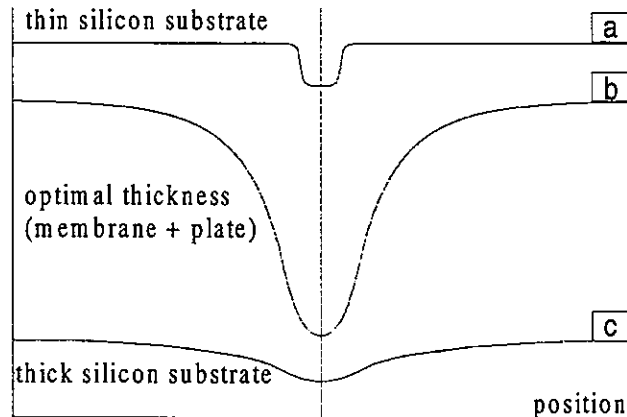


Figure 2. Deformation profile at different thickness

Plate and membrane have totally different mechanisms. Bending and shearing are considered in a plate problem to support the vertical load. On the other hand, when the membrane effect governs, in-plane stress produces vertical forces due to local curvature to balance the vertical load. The plate effect is neglected in a membrane case, and a plate problem does not include the membrane effect. One may think that with a patterned thin film on top of the substrate, the thinner the substrate, the larger the substrate deformation caused by the residual stress in the thin film. However, calculations show that there exists an optimal thickness such that the diaphragm deflection reaches its maximum. This creates the highest measurable deflection profile under the fixed TGLI resolution. This optimal thickness lies in the mechanical transition zone of M+P behavior.

With the complexity of mechanical behaviors involved during the substrate etching process, and because of the desired optimal thickness of a substrate required to obtain the best or largest

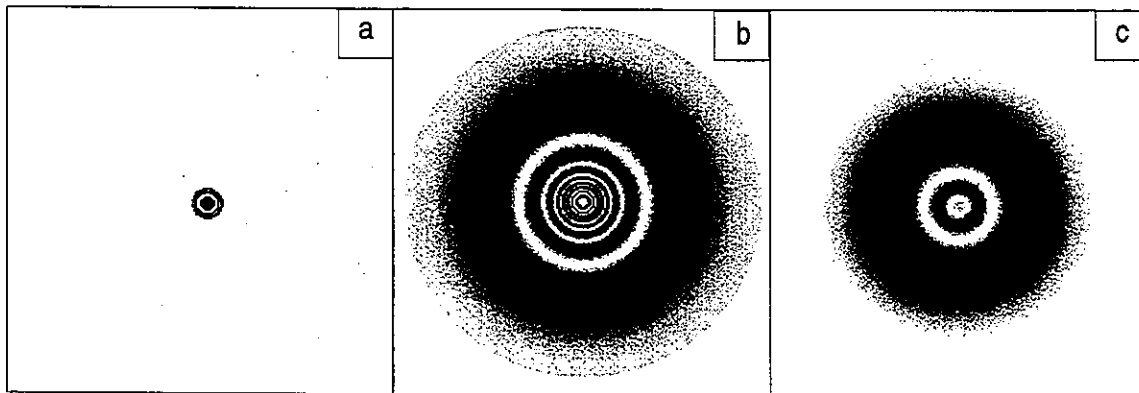


Figure 3. Computed interferometric pattern for Si thickness of (a) $0.5 \mu\text{m}$, (b) $3 \mu\text{m}$ (optimal thickness), (c) $10 \mu\text{m}$

deformation pattern, this numerical modeling problem becomes a highly nonlinear one. An iteration method called nonlinear sequential analysis (NSA) (Biao and Qing 1984) was developed to break through the impasse in the numerical etching process, especially in the combined plate/membrane problem. An interferometer pattern generated from numerical simulation output was compared with the experimental result. Figure 2 illustrates the profiles of the deformation field of an etched substrate at different thickness with a patterned thin film located at its center. Figure 3 demonstrates that *successive etching model* can perform predictive analysis and find an optimal substrate thickness of Si for local stress measurement.

3 COUPLED EXPERIMENTAL AND NUMERICAL ANALYSIS ON MECHANICS OF PATTERNED MICROSTRUCTURE

3.1 Procedure

This analysis involves coupled experimental work and computer simulation, as illustrated in Figure 4.

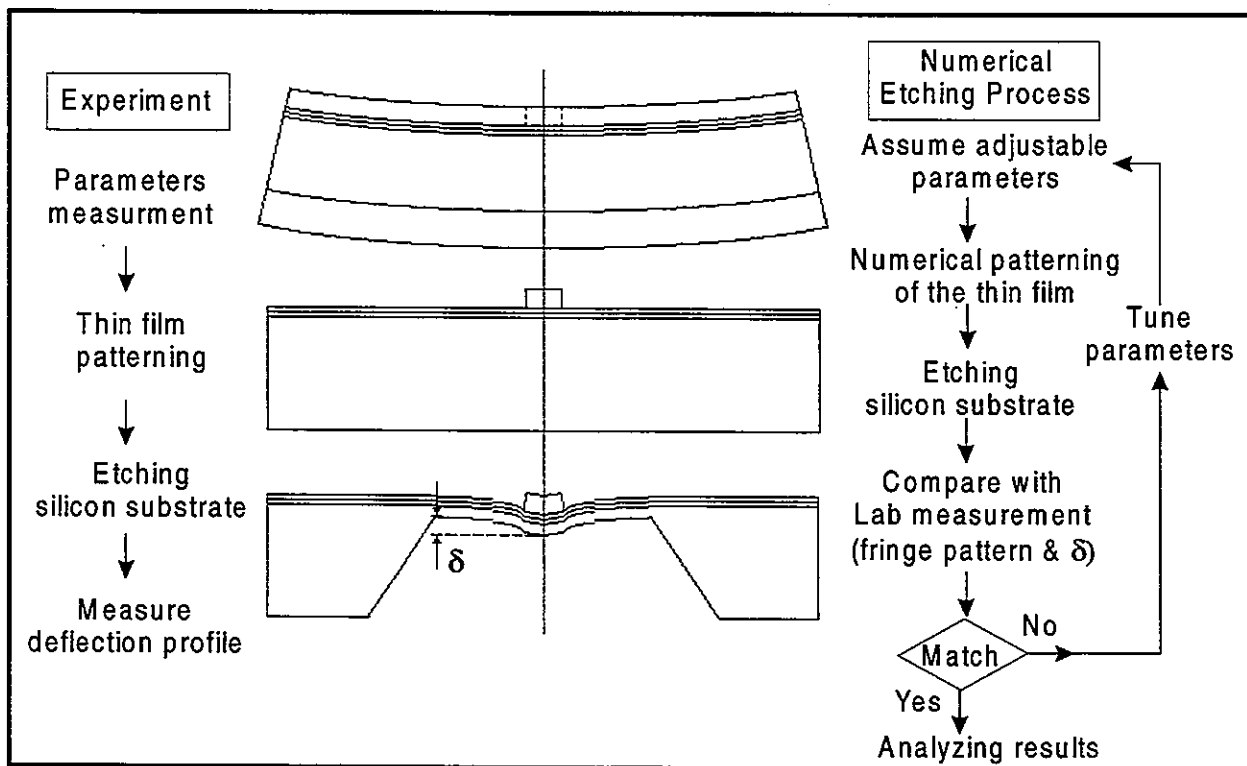


Figure 4. Schematic diaphragm for coupled experimental and numerical analysis

The experimental work includes the following steps:

- (1) provide testing sample's geometric configuration and elastic properties such as Young's modulus and Poisson's ratio;
- (2) test thin film patterning;

- (3) perform substrate etching to its required thickness and obtain its deformation using profile TGLI; and
- (4) repeat steps 1-3 with a different setting of substrate thickness to obtain optimal thickness and the best fringe patterns based on predictive numerical result of *successive etching model*.

Computer simulations perform the following steps:

- (1) prepare the sample's configuration and assume some adjustable parameters such as initial stresses of thin films and the substrate;
- (2) start the numerical etching process according to the experiment's procedure;
- (3) compare the output of computed substrate displacement and numerical interference picture with the experiment;
- (4) if results from the computer simulation do not match with those from the experiment, adjust certain parameters, and restart steps 1-3 until the data matches; and
- (5) once a match is achieved, output the stress and deformation distributions of the patterned thin film on the solid substrate. These are results for the patterned microstructure problem.

3.2 Example

A titanium pad with a radius of $100\text{ }\mu\text{m}$ and thickness of $0.525\text{ }\mu\text{m}$ is patterned on top of a composite substrate of Si_3N_4 ($0.142\text{ }\mu\text{m}$, top) / SiO_2 ($0.1125\text{ }\mu\text{m}$) / Si (substrate $525\text{ }\mu\text{m}$). The etching processes were conducted according to the procedures mentioned previously. During the etching processes, all the stress, strain, and deformation fields in and around the patterned microstructure show dramatic changes. Figure 5 compares the results of interference patterns from the laboratory test with numerical etching.

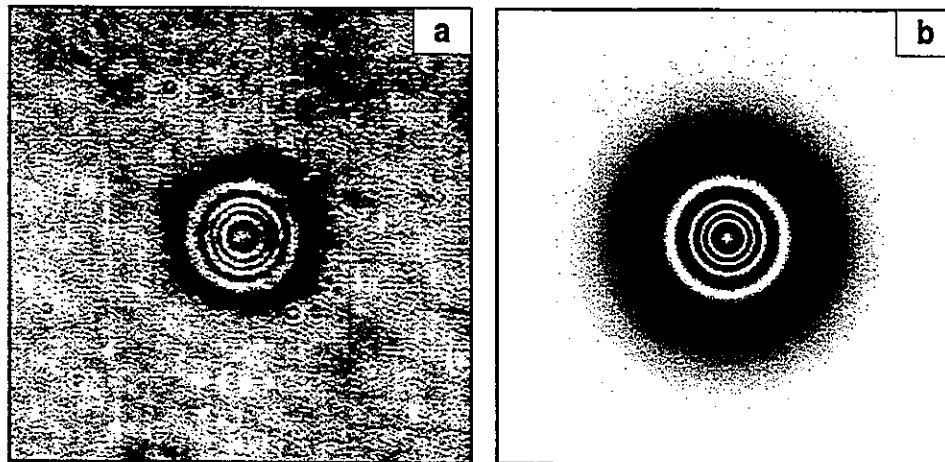


Figure 5. Comparison between (a) lab interferometric and (b) computed fringe patterns for a $100\text{ }\mu\text{m}$ Ti pattern on a $4.5\text{ }\mu\text{m}$ thick composite Si diaphragm

A magnified displacement field near the edge of the Ti pad is shown in Figure 6. Large distortion occurs after the Ti layer has been patterned. The Ti pad tends to shrink toward its center position (left), thus pulling the insulating layers and Si substrate up to the left. The area around Point A in Figure 6 is shown to be a critical region.

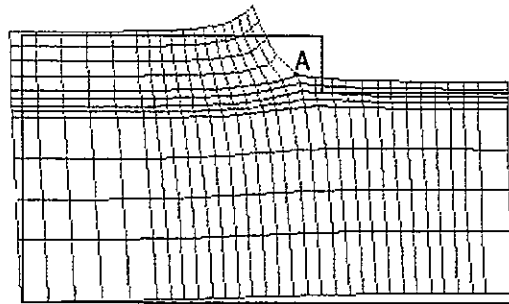


Figure 6. Deformation field near the edge of the Ti pad

Figure 7 illustrates the distribution of in-plane stress σ_{xx} in the vicinity of point A. The top legend is for stress fields of the Ti pad and the two insulating layers, while the bottom legend is for the Si substrate. Stress concentrations, with both tensile and compressive values, are found in all materials around point A. The highest tensile stress is found in the Si_3N_4 layer under Point A that reaches over 1,500 MPa. If there is any defect or material non-homogeneity in this area, cracks will form and spread rapidly to the Si substrate. It could be demonstrated that (a) adding an oxide layer between Ti and nitride will make the device stiffer and less likely to fail as before; and (b) changing nitride to a more ductile material or increasing its plasticity will make the device even stiffer and perform better.

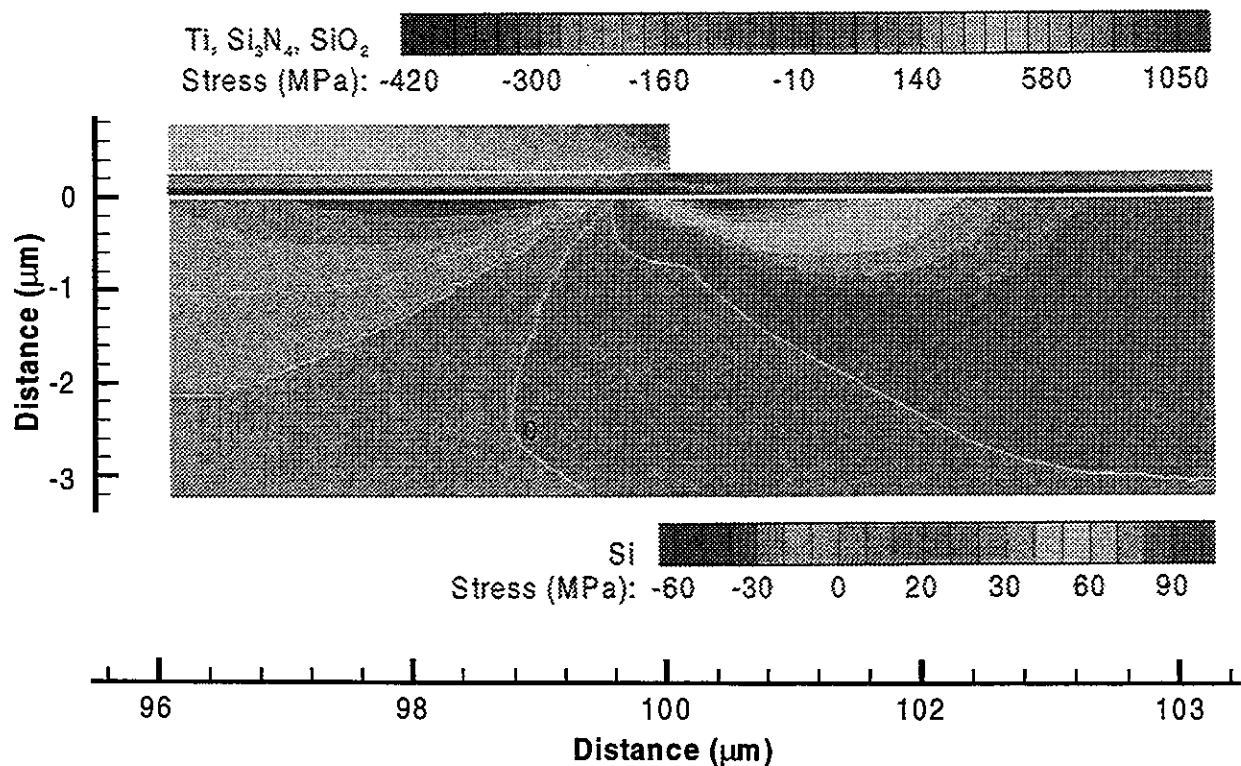


Figure 7. Stress contour near the edge of a Ti pad on a solid composite Si diaphragm

4 DISCUSSIONS

The idea of coupling experimental and numerical analysis on stress distribution in a patterned microstructure utilizes only the mechanical behavior of the stress pattern. Therefore, this approach is not limited by the crystalline properties of the materials to be studied. The above example could be used for measuring the residual stress in electroless Ni for flip-chip packaging applications. Semitech[®] has been trying to evaluate this problem, however, it has been hampered by the fact that X-ray does not apply readily, since electroless Ni consists of an amorphous matrix with dispersed Ni₃P nano-crystals after annealing. Micro-indentation also has a problem because the typical thickness of Ni used is about 5-10 μm depending on solder array pitch. This coupled experimental and numerical analysis could be a candidate to resolve the problem. We have performed some preliminary research and the result will be published elsewhere (Zheng et al., unpubl.).

5 CONCLUSIONS

The simulation of an etching process in chip manufacturing is similar to the step-by-step sequential or random excavation in tunneling using DDA. An iteration method called nonlinear sequential analysis (NSA) was developed to solve highly nonlinear problems due to the complexity of combined membrane plus plate (M+P) behaviors involved during the substrate etching process. It has been demonstrated that coupling experimental and numerical analysis using the *successive etching model* and sample deflection measurements appears to be a solid approach to resolve stress in a patterned microstructure problem, which is a typical reliability concern in IC and MEMS industries.

ACKNOWLEDGEMENTS

The authors would like to thank Professor King-Ning Tu, and Dr. Weijia Wen at the Department of Materials Science and Engineering of UCLA for performing experiments and valuable discussions.

REFERENCES

- Ajito, K., Sukanto, J. P. H., Nagahara, L.A., Hashimoto, K. and Fujishima, A. 1995. Strain imaging analysis of Si using Raman microscopy. *J. Vacuum Sci. Tech.* 13: 1234-1238.
- Biao, Xie-Ru and Qing, Jiang-Pei. 1984. *Nonlinear Numerical Analysis*. Shang Hai Jiao Tong university press.
- Chang, C.-T. 1994. Nonlinear Dynamic Discontinuous Deformation Analysis with Finite Element Meshed Block System. *Ph.D. Dissertation*, Department of Civil Engineering, University of California at Berkeley.

- Doerner, M.F., Gardner, D.S. and Nix, W.D. 1986. Plastic properties of thin films on substrates as measured by submicron indentation hardness and substrate curvature techniques. *J. Mater. Res.* 1: 845-851.
- Englert, T., Abstreiter, G. and Pontcharra, J. 1980. Determination of existing stress in silicon films on sapphire substrate using Raman spectroscopy. *Solid-State Elec.* 23: 31-33.
- Malhotra, S.G., Rek, Z.U., Yalisove, S.M. and Bilello, J.C. 1996. Depth dependence of residual strains in polycrystalline Mo thin films using high-resolution X-ray diffraction. *J. Appl. Phys.* 79: 6872-6879.
- Marcus, M.A. and Lutterodt, K.E., e.d. Isaacs. 1998. Presentation at Mater. Res. Soc. Spring meeting, San Francisco.
- Shi, G. 1993. *Block System Modeling by Discontinuous Deformation Analysis*. Computational Mechanics Publications, Southampton, UK and Boston, USA.
- Shyu, K. 1993. Nodal Based Discontinuous Deformation Analysis. *Ph.D. Dissertation*, Department of Civil Engineering, University of California at Berkeley.
- Tu, King-Ning, Mayer, James W. and Feldman, Leonard C. 1992. *Electronic Thin Film Science for Electrical Engineers and Materials Scientists*. Macmillan Publishing company, NY: 84-88.
- Zheng, D. W., Wang, Xinhua, Shyu, K., Chang, C.-T., Guo, Y., Sarihan B., Wen, Weijia, and Tu, K. N. 1999. A Study of Local Stress Using Stress-absorbing Si Diaphragm (unpublished).

MODELING EXCAVATION-INDUCED RESPONSE OF JOINTED ROCK USING DDA

Chihsen T. Lin, Shoung Ouyang, Chen-Tair Huang, and Cy C. Chen
Energy & Resources Laboratories, Industrial Technology Research Institute
195-6, Sec. 4, Chung Hsing Rd., Chutung, Hsin-chu, Taiwan, R.O.C.

Paul T. H. Huang, Chung-Cheng Lee, and Jiannlin Liu
Taiwan Power Company
2, Alley 15, Lane 196, Sec. 4, Roosevelt Rd., Taipei, Taiwan, R.O.C.

ABSTRACT: This paper presents three newly developed extensions of the DDA (Discontinuous Deformation Analysis) method for modeling excavation-induced response of jointed rock. The first extension introduces the plane strain condition to Dr. Shi's original DDA program in which only plane stress condition was available. All the examples shown in this paper are conducted in plane strain condition. It is mostly suited boundary condition for the analysis related to underground excavations. The second extension provides the capability of simulating the progressive excavation-induced response of jointed rock around tunnels. The induced stresses and deformations in the jointed rock can be captured at different excavation stages. The third extension provides more extensive capability of bolt installation in rocks along with the progressive excavation process. The optimum layout of rock bolts for tunnels can then be determined by the analysis. This paper also includes some practical excavation examples using the newly developed DDA programs.

1 INTRODUCTION

A final disposal program for spent nuclear fuel has been conducted in Taiwan for more than 10 years. ITRI (Industrial Technology Research Institute) has been authorized by Taiwan Power Company to conduct the Phase III work (regional investigation stage) of the final disposal program. In order to safely dispose of the spent nuclear fuel, the widely accepted concept of Deep Geological Disposal is also recognized in this program.

Rock mechanics was introduced to this program about two years ago. Various techniques of numerical modeling of rock masses are being evaluated. The DDA method originally developed by Dr. Shi in 1984 was readily introduced into this program. In the past year, three extensions to the method have been accomplished as a part of the establishment of numerical modeling ability for underground excavations. The first extension follows the classical theory of mechanics. The constitutive law between stresses and strains is modified to meet the plane strain condition. Since it is a very straightforward modification, it will not be introduced in this paper. All the details of the other two extensions are presented in the following sections.

2 PROGRESSIVE TUNNELING EXCAVATION

Underground structures such as tunnels can be excavated using full face or partial face excavation method. The choice of excavation methods should consider the geological condition nearby the tunnel and the possible extent of the induced excavation disturbed zone (EDZ) if necessary.

This extension to the DDA method provides both excavation methods. All the jointed rocks in tunnel face can be "excavated" (or removed) in any specified time step. Any one of the excavated blocks disappears when its specified time step given by the users is reached. All the "remaining" rocks and their stresses (or strains) need to be updated and carried through the rest of the analysis. This excavating process can be continuously implemented till all the given time steps for excavations are executed.

In order to make the excavated blocks disappeared from the analysis, three things are required in the rest of the analysis. The first thing is to release all the possible contacts between the excavated blocks and existing blocks in the rest of time steps. In other words, the stiffness matrix of $[K]_{ij}$ should be zero if either i or j belongs to any one of the excavated blocks. The second thing is to update the zero stress and strain for the disappeared blocks in the rest of time steps. The last thing is to modify pre-processor and post-processor programs for the new DDA main program. The pre-processor program should include the desirable excavating process that consists of the order and excavated blocks for every excavation. The post-processor program should only plot the existing blocks for any time step. The information of the existing blocks in any time step is obtained from the analysis of running the new DDA main program. The major advantage of this developed method is that a minimum change of the original DDA program is required. Only the timing of excavations and the stiffness matrix $[K]_{ij}$ of excavated blocks are needed to be located and modified during the analysis.

3 INSTALLING ROCK BOLTS WITH PROGRESSIVE TUNNELING EXCAVATION

The geological condition near excavated tunnels is always a very important factor to the deformation of the tunnels. The installation of rock bolts is to improve the geological condition. The efficiency of installing the rock bolts would be dramatically increased if the bolts were installed with right numbers and right depths along with right directions as well. The good efficiency might obtain limit deformations from the tunnel surface with minimum number of bolts

The DDA method treats rock mass as real isolated blocks bounded by preexisting discontinuities. The installation of rock bolts can be possibly simulated by the following manner. The methodology to be introduced in this section was first introduced in Dr. Shi's thesis published in 1988.

Consider a bolt or a bar (as shown in Fig. 1) connected at point (x_1, y_1) of block i and point (x_2, y_2) of block j . The length of the bar is

$$l = \sqrt{(x_1 - x_2)^2 + (y_1 - y_2)^2} . \quad (1)$$

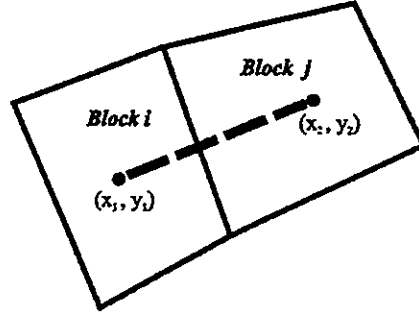


Figure 1. A bar connected to block i and block j.

The displacements at the end points of the bar are

$$\begin{aligned}
 dx_1 &= u_1 = u(x_1, y_1) \\
 dy_1 &= v_1 = v(x_1, y_1) \\
 dx_2 &= u_2 = u(x_2, y_2) \\
 dy_2 &= v_2 = v(x_2, y_2).
 \end{aligned} \tag{2}$$

The deformation of the bar is then obtained by taking the total derivatives of Equation (1) as follows

$$\begin{aligned}
 dl &= \frac{1}{l} [(x_1 - x_2)(dx_1 - dx_2) + (y_1 - y_2)(dy_1 - dy_2)] \\
 &= \frac{1}{l} [(x_1 - x_2)(u_1 - u_2) + (y_1 - y_2)(v_1 - v_2)] \\
 &= [(u_1 \quad v_1) \begin{pmatrix} l_x \\ l_y \end{pmatrix} - (u_2 \quad v_2) \begin{pmatrix} l_x \\ l_y \end{pmatrix}] \\
 &= \{[D_i]^T [T_i]^T \begin{pmatrix} l_x \\ l_y \end{pmatrix} - [D_j]^T [T_j]^T \begin{pmatrix} l_x \\ l_y \end{pmatrix}\}
 \end{aligned} \tag{3}$$

where $[D_i]$ and $[D_j]$ are the deformation matrices of block i and block j, respectively, and $[T_i]$ and $[T_j]$ enable the calculation of the displacements at any point within the block i and block j, respectively. The direction cosines of the bar l_x and l_y can be defined as

$$\begin{pmatrix} l_x \\ l_y \end{pmatrix} = \begin{pmatrix} \frac{1}{l}(x_1 - x_2) \\ \frac{1}{l}(y_1 - y_2) \end{pmatrix} \tag{4}$$

Assuming the stiffness of the bar is s , the bar force is

$$f = -s \frac{dl}{l}. \quad (5)$$

The strain energy of the bar is then

$$\Pi_b = \frac{1}{2} f dl = \frac{s}{2l} (dl)^2. \quad (6)$$

Substitute Equation (3) into Equation (6), therefore

$$\Pi_b = \frac{s}{2l} \left\{ [\mathbf{D}_i]^T [\mathbf{T}_i]^T \begin{pmatrix} l_x \\ l_y \end{pmatrix} - [\mathbf{D}_j]^T [\mathbf{T}_j]^T \begin{pmatrix} l_x \\ l_y \end{pmatrix} \right\}^2. \quad (7)$$

After the curl bracket is expanded and rearranged in Equation (7), we then get

$$\Pi_b = \frac{s}{2l} [\mathbf{D}_i]^T [\mathbf{E}_i] [\mathbf{E}_i]^T [\mathbf{D}_i] - \frac{s}{l} [\mathbf{D}_i]^T [\mathbf{E}_i] [\mathbf{G}_j]^T [\mathbf{D}_j] + \frac{s}{2l} [\mathbf{D}_j]^T [\mathbf{E}_j] [\mathbf{G}_j]^T [\mathbf{D}_j] \quad (8)$$

where

$$[\mathbf{E}_i] = [\mathbf{T}_i]^T \begin{pmatrix} l_x \\ l_y \end{pmatrix} = \begin{pmatrix} e_1 \\ e_2 \\ e_3 \\ e_4 \\ e_5 \\ e_6 \end{pmatrix} \quad \text{and} \quad [\mathbf{G}_j] = [\mathbf{T}_j]^T \begin{pmatrix} l_x \\ l_y \end{pmatrix} = \begin{pmatrix} g_1 \\ g_2 \\ g_3 \\ g_4 \\ g_5 \\ g_6 \end{pmatrix}. \quad (9)$$

The derivatives of Π_b in Equation (8) are 6x6 stiffness sub-matrix of block i or j. They can be computed as follows

$$k_{rs} = \frac{\partial^2 \Pi_b}{\partial d_{ri} \partial d_{sj}} = \frac{s}{2l} \frac{\partial^2}{\partial d_{ri} \partial d_{sj}} ([\mathbf{D}_i]^T [\mathbf{E}_i] [\mathbf{E}_i]^T [\mathbf{D}_i]) = \frac{s}{l} e_r e_s, \quad r, s = 1 \rightarrow 6 \quad (10)$$

which form a series of 6x6 matrix as

$$\frac{s}{l} \begin{pmatrix} e_1 \\ e_2 \\ e_3 \\ e_4 \\ e_5 \\ e_6 \end{pmatrix} (e_1 \ e_2 \ e_3 \ e_4 \ e_5 \ e_6) \rightarrow [K_{ii}] \quad (11)$$

added to the sub-matrix of $[K_{ij}]$ in global stiffness matrix;

$$-\frac{s}{l} \begin{pmatrix} e_1 \\ e_2 \\ e_3 \\ e_4 \\ e_5 \\ e_6 \end{pmatrix} (g_1 \ g_2 \ g_3 \ g_4 \ g_5 \ g_6) \rightarrow [K_{ij}] \quad (12)$$

added to the sub-matrix of $[K_{ij}]$ in global stiffness matrix;

$$-\frac{s}{l} \begin{pmatrix} g_1 \\ g_2 \\ g_3 \\ g_4 \\ g_5 \\ g_6 \end{pmatrix} (e_1 \ e_2 \ e_3 \ e_4 \ e_5 \ e_6) \rightarrow [K_{ji}] \quad (13)$$

added to the sub-matrix of $[K_{ji}]$ in global stiffness matrix;

$$-\frac{s}{l} \begin{pmatrix} g_1 \\ g_2 \\ g_3 \\ g_4 \\ g_5 \\ g_6 \end{pmatrix} (g_1 \ g_2 \ g_3 \ g_4 \ g_5 \ g_6) \rightarrow [K_{jj}] \quad (14)$$

added to the sub-matrix of $[K_{jj}]$ in global stiffness matrix.

The function of installing a bar between blocks i and j would be successfully implemented in the DDA main program when all the computations as shown in Equations (11)-(14) are conducted and correctly added into the global stiffness matrix. More extensively, the newly developed main program is able to progressively install the rock bolts in any given time step. All the designed rock bolts are given when executing the newly developed pre-processor program. The installing time steps for all rock bolts are then given when the main program is executed. All the bolting process should be recorded in an output file that is required for the later use by the post-processor program. All the programs need to be modified to accomplish this extension.

3 EXAMPLES

All the extensions introduced in previous sections are employed to the analysis of underground excavations to demonstrate the capability of the newly developed programs in this section. This section is composed of two examples. The first example introduces the simulation of a series of progressive excavations in a tunnel using the newly developed DDA programs. The second example demonstrates a more extensive capability of installing rock bolts in a progressive process of tunneling excavations. Both examples utilize the same tunnel, material properties and geological conditions of excavated rock masses.

Consider a 10m wide and 11.25m high tunnel constructed in 30m wide and 32.5m high jointed rock masses, consisting of 203 blocks as shown in Figure 2. Two sets of joint spacing are formed in examples. One set is 1.77m at a dip angle of 45° upward from the horizontal. The other set is 3.54m at a dip angle of 45° downward from the horizontal. A uniform vertical stress of 10.6 MPa is applied downward on top of the model to simulate the overburden of 393m. Three boundary blocks are used and firmly fixed so that no lateral displacement is allowed along the vertical and bottom boundaries. The intact rock has a unit weight $\gamma=0.027$ MPa, a Young's modulus $E=60$ GPa, and a Poisson's ratio $\nu=0.2$. The angle of frictional resistance in rock joints is 20° . The stiffness of rock bolts is assumed to be 200 GPa. No bolt was installed to rock mass around the tunnel for Example 1 but 6 rock bolts were installed on "key" blocks around the tunnel for Example 2. The definition of key blocks can be seen in Shi's key block theory (1985).

Figures 3a-f of Example 1 demonstrate the capability of progressive excavation of jointed rock masses in a tunnel. Figures 4a-f of Example 2 show another capability of installing rock bolts in the progressive excavation of jointed rock masses in a tunnel as shown in Example 1. The time increment is 0.001 seconds. A maximum of 15,000 time steps was conducted in both examples. Table 1 shows the measured displacements from the locations of installed rock bolts as shown in Figure 4f. The bolts are numbered 1 to 6 from top to bottom of the tunnel. The results demonstrate that the deformations on the tunnel side wall were largely decreased when the rock bolts were installed. It could be explained that the frictional resistance in rock joints was induced much more if rock bolts were installed. The jointed rocks in the tunnel side wall had a tendency to deform and slide down together. However, the block deformation on the top of the tunnel was decreased but not much even if the rock bolts were installed. Figure 5 shows that the blocks on top part of the tunnel deformed much more than the blocks on the lower part in the case of no installation of rock bolts.

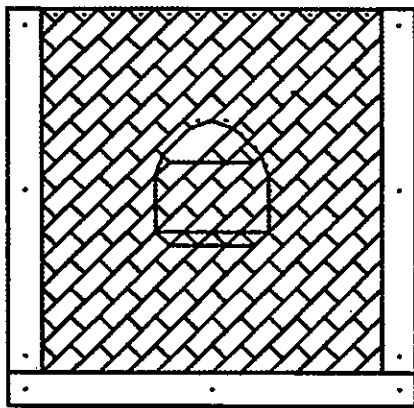
4 CONCLUSIONS

This paper presents the first attempt of using the DDA method to simulate progressive underground excavation and rock bolt installation in a tunnel. The analytical results shown in examples demonstrate that the newly developed DDA programs work quite well. This capability indeed provides the possibility of determining the optimum layout of rock bolts in tunneling excavations if the geological condition near the tunneling surface is obtained. Further applications of the capability will be studied in the near future.

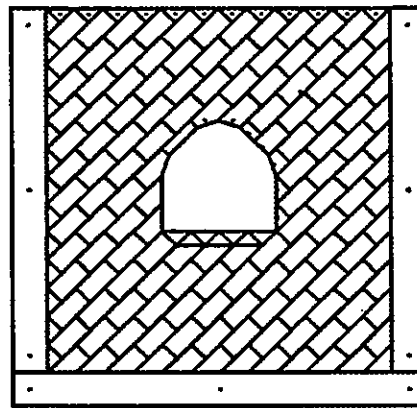
One of the other methods to decrease the deformation of tunneling excavation is to install the lining system to the excavated tunnel surface. This work can be implemented using the DDA method if the sub-block method originally proposed by Lin et. al. 1996 is employed and associated with the presented extensions in this paper. The irregular shape of the lining system can be constituted by small sub-blocks which also give stress (or strain) distribution in the lining.

REFERENCES

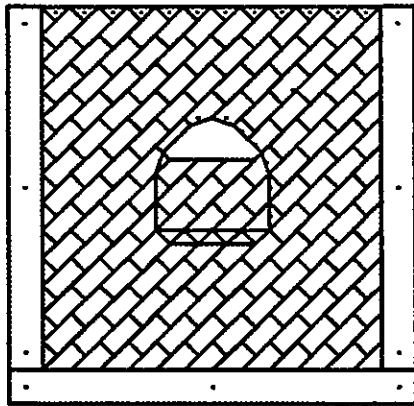
- Goodman, R.E. and Shi, G-H. 1985. Block theory and its application to rock engineering. published by *Prentice-Hall Inc.*, Englewood Cliffs, NJ, USA.
- Lin, C.T., Amadei, B., Jung, J., and Dwyer, J. 1996. Extensions to the Discontinuous Deformation Analysis for Jointed Rock Masses. *Int. J. of Rock Mech. and Mining Sci. & Geomech. Abstr.*, Vol. 33, No. 7, pp. 671-694.
- Shi, G-H. and Goodman, R.E. 1984. Discontinuous Deformation Analysis. *Proc. 25th US Symposium on Rock Mechanics*, pp. 269-277.
- Shi, G-H. 1988. Discontinuous Deformation Analysis: a new numerical model for the statics and dynamics of block systems. Ph.D thesis, University of California, Berkeley, USA.



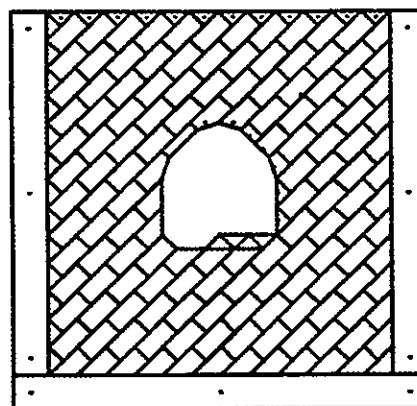
(a) 300 time steps



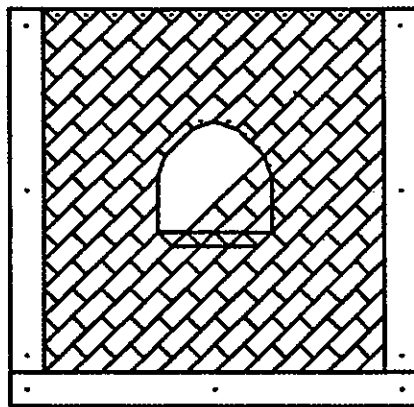
(d) 600 time steps



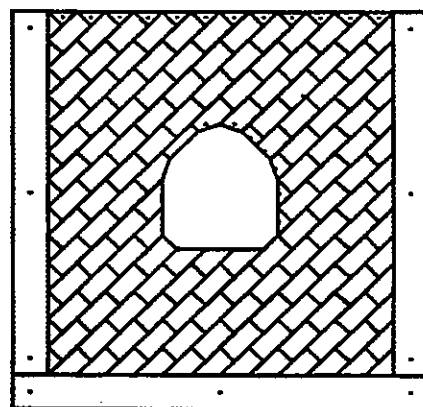
(b) 400 time steps



(e) 700 time steps

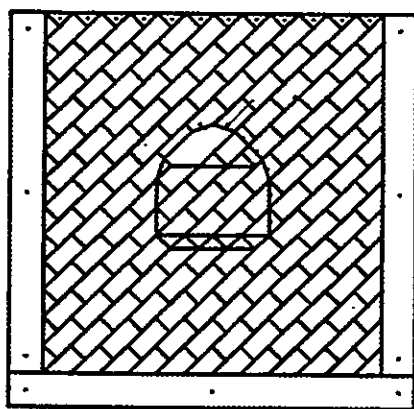


(c) 500 time steps

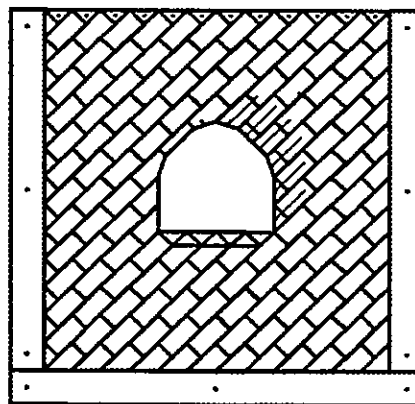


(e) 800 time steps

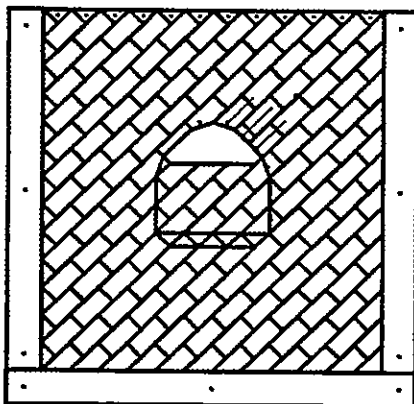
Figure 3. Example 1: progressive underground excavation in a tunnel.



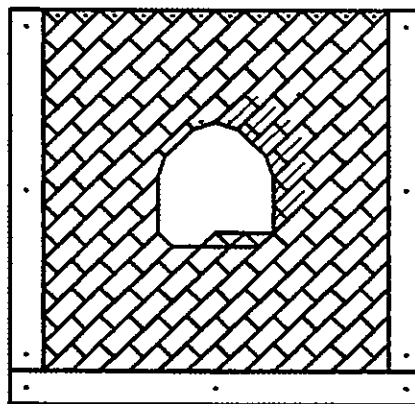
(a) 300 time steps



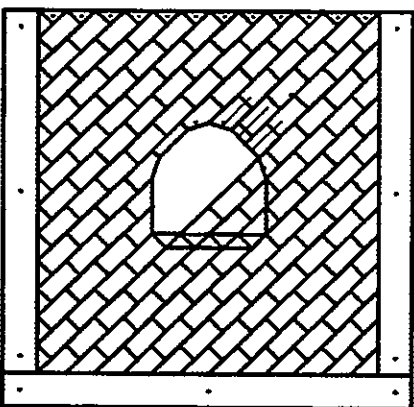
(d) 600 time steps



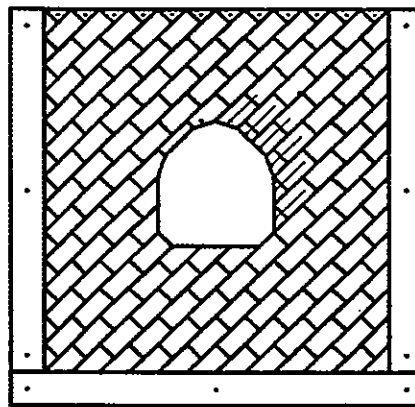
(b) 400 time steps



(e) 700 time steps



(c) 500 time steps



(f) 800 time steps

Figure 4. Example 2: progressive underground excavation with bolt installation in a tunnel.

Table 1. Measurements of rock bolts after 15,000 time steps for Examples 1 and 2.

Location No.	Displacements (no bolt) (cm)			Displacements (6 bolts) (cm)		
	dx	dy	dl	dx	dy	dl
1	22.2	26.3	34.4	21.1	24.8	32.6
2	-10.3	-11.1	15.1	-6.2	-7.3	9.6
3	-14.7	-15.4	21.3	-5.1	-6.0	7.9
4	-13.9	-14.5	20.1	-5.1	-5.7	7.6
5	-7.6	-8.1	11.1	-4.9	-5.4	7.3
6	-6.2	-6.8	9.2	-5.0	-5.1	7.1

Note: $dl = \sqrt{dx^2 + dy^2}$, the total displacement of the measured point.

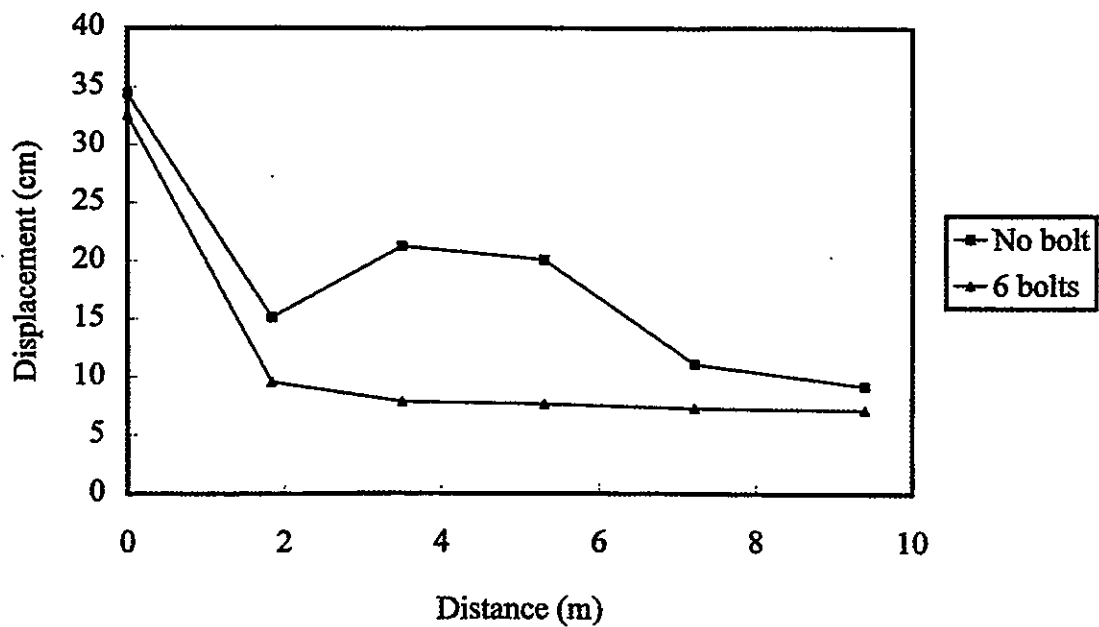


Figure 5. Displacement distributions on the same locations of rock bolts of tunnel face after 15,000 time steps.

Key-Block Analysis

TWO EXAMPLES OF THE APPLICATION OF KEY BLOCK THEORY IN CHINA

Jue-Min Pei,
Department of Hydraulic Engineering, Tsinghua University
Beijing 100084, PRC

Xiao-Chu Pen
Central South Institute of Investigation Design Research
Changsha 410014, PRC

Shan-Ru Hang
Water Conservancy Bureau of Shanxi Province
Taiyuan 030002, PRC

ABSTRACT: This paper introduces two examples of the application of key block theory in China. One is the collapse of a tunnel roof. The joint pyramid method of key block theory is used to check the accident. Another is the sliding of a dam abutment. A three dimensional chained key block method is used. The calculations of these two examples all are successful.

1 TUNNEL COLLAPSE

1.1 *Accident Situation*

Fen-he Reservoir was built on Fen-he River in Shanxi province of China in fifties. Due to the silt accumulation a new tunnel for sediment transport was excavated in 1991. The diameter of excavation is 9.6 meters. The total length of the tunnel is 1050 meters. The thickness of overburden is 40 meters. The rock mass consists of granite-gneiss and hornblende schist. The joints are well developed, they can be divided into three sets: (1) N50°W / NE40°; (2) N70°W / SW85°; (3) N48°E / NW88°. Otherwise, there is a fault across the tunnel with the strike and dip direction of (4) E270°W / NE80° at the location of stake No.0+728 – 0+760 (meters, beginning from intake). As the tunnel was excavated to this place, the collapse of tunnel roof occurred. Avoided the occurrence of similar accident in later excavation, key block theory is applied to predict the stability situation of the tunnel. At first the verification of the collapse is conducted. It proves that the calculated pyramid block of collapse is existent. It is very close to the prototype collapse in shape and size. Further searching, there is no other discovery of big fallen block existing in the remained part of tunnel. So the tunnel is safely excavated later in construction.

1.2 Measured Records

The measured records shows before collapsing that there was some presage to omen the damage. As the tunnel was excavated forward upstream to the stake No.0+760, there were five to six blocks of rock roof fallen down one after another. Due to the sizes of fallen rock blocks being not too big, no any support was done. As the excavation going from the stake No.0+760 to No.0+728, the tunnel happened to meet the fault. Its length of longitudinal section on the up-faulted plane is 25 meters. Three sets of joints on up-faulted plane are intersected very densely, that cause the crushed rock fallen and finally extended to form a big collapse with the volume of more than 300m^3 . Figure 1 shows its measured figuration of the collapse. It indicates that the first set of joints cut across the tunnel obliquely from 2 meters to 9 meters above the tunnel top and the second set of joints cut two sides of the tunnel in high angle. The thickness of joint layer is 4 to 6 cm filled with the soft clay and fragments. The third set of joints cut the tunnel at upstream and the fault cut the tunnel at downstream. The shape of collapse formed by this consists of five faces with a height of 9 meters and a length of 25 meters.

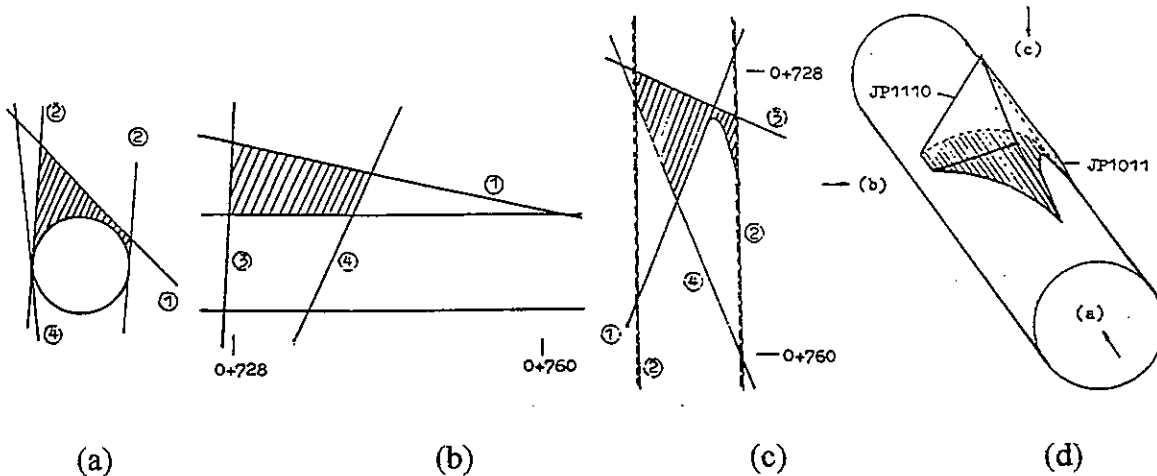


Figure 1. Shape of measured collapse

1.3 Key Block Calculation

Key block theory is used to check the collapse and to find its causality. According to the field observation, the up-faulted rock is cut by joint sets very densely, that forms a crushed band. Figure 2 shows the statistic distribution of key blocks near and in the crushed band. In Figure 2, it indicates that there are five smaller key blocks distributed on the roof of tunnel. It is similar with the actual situation happened as the excavation reaching to the stake No.0+760, there five to six blocks are fallen down. In the crushed band on up-faulted disk a huge rock collapse appears, which is possible to divide two parts to fall. The shadow part is fallen down first, then the dash part is fallen, seen as in Figure 2.

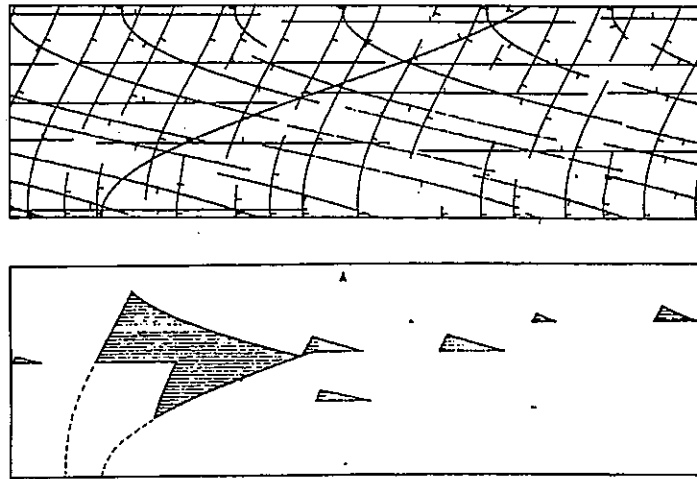


Figure 2. Statistical distribution of key blocks

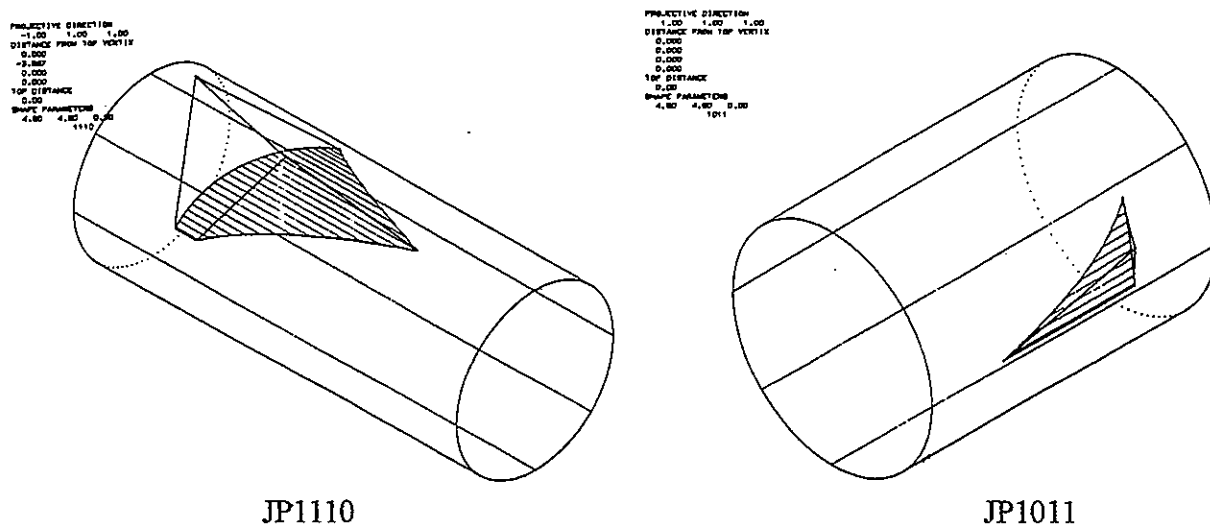


Figure 3. Maximum key block of JP1110 and JP1011

The maximum key block shows in Figure 3. It consists of joint pyramid codes: JP1110 and JP1011. These two parts combine into a big block. Its total volume is 316 cubic meters, which is very close to the measured one in field. As seen in figure, this maximum key block is bigger on the top of block. If the block is in a whole, the collapse is very hard to occur. Just the rock to be crushed, the scattered small blocks involved in the huge block can fall down. This result is the same as in actual process.

1.4 Sliding Modes

The sliding modes and critical angles of the key blocks of JP1110 and JP1011 are shown in

Figure 4. From the figure, it can see that block JP1110 slides on the combined plane of third joint set and the fault, and block JP1011 slides on the plane of second joint set. Their critical friction angles are individually 55° and 85° . Because the actual friction angles are less than those, the collapse is not able to avoid. It has been proved by the actual collapse of tunnel roof.

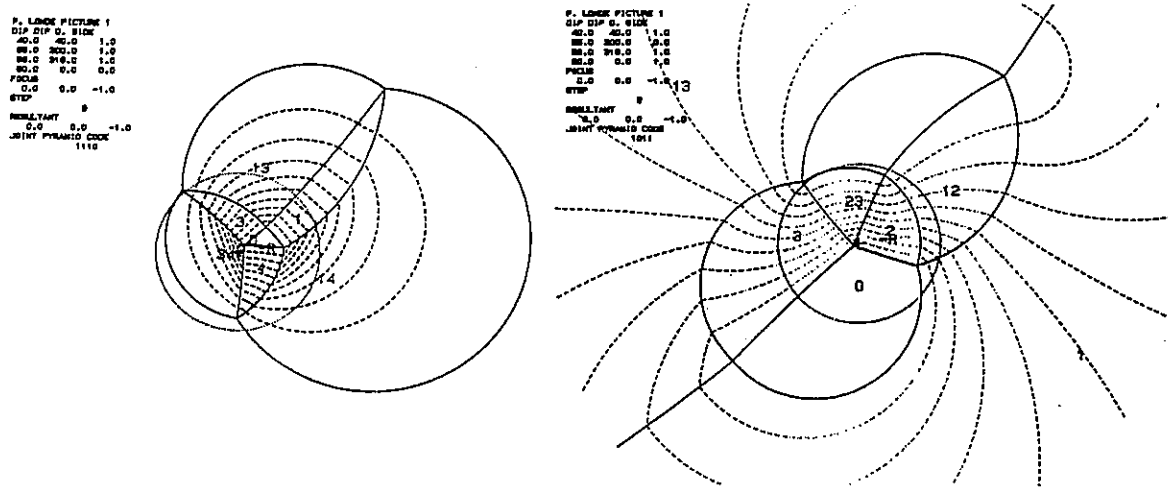


Figure 4. Sliding modes and critical angles

1.5 Conclusion

The application of key block theory on the tunnel collapse proved its correction on theory and method. The further analysis for later excavation is conducted. According to the exploration, the prediction by key block method is done. It shows that the tunnel in later excavation stage is impossible to further produce any large scale of collapse. But the scattered key blocks as JP111 (on roof), JP010 and JP011 (on right wall), and JP101 and JP100 (on left wall) are able to appear. This conclusion is also proved by the later construction.

2 SLOPE SLIDING

2.1 Brief Introduction

Man-wan Dam is located on Lan-chang-jiang River in Yunan province of China. Its left dam abutment slid on a large scale at half-hour later after a blasting excavation in 1989. The total volume of the sliding is about 80 thousand cubic meters with a depth of 20 meters. At sliding place four sets of joints are well developed. Their attitudes are (1) $N15\sim30^\circ W / SW42\sim52^\circ$, (2) $N40\sim60^\circ W / SW50\sim60^\circ$, (3) $EW / SN75\sim85^\circ$ and (4) $N50\sim60^\circ E / NW70\sim50^\circ$.

Because the above pyramid block method can not depict the real situation, a new three dimensional chained key block method is developed to analyze the sliding of dam abutment. It

generates the 3-d joint plane meshes by statistical joint rosettes of an exploration tunnel in the slope mass and finds 3-d blocks by searching closed loops of block edges in the rock space. According to the order of the stability of blocks, first take off the block, which has the lowest safety factor, thus a new free surface can be formed. In the second round the searching can be done on the new free surface. Step by step then the chained key blocks can be found. This paper shows the result of calculations and the sliding order of blocks. It indicates that the final sliding plane is stable and the anchorage scheme is sure enough.

2.2 Statistical Joint Distribution

The geotectonic stress field controlled the development of joints in rock mass. In the rock mass, the joints are distributed according to the statistical character. We can measure the local joint distribution in exploratory tunnel so as to model the statistical distribution of joints in certain limits of rock slope mass. The pole density graph is usually used in statistical analysis of joint attitudes. Figure 5 is a pole density graph of rock slope mass. It is measured in the exploratory tunnel. The total measured dots are seventy joints. Figure 5a shows its statistical raw data in exploratory tunnel. Then we use the Monte Carlo method to simulate the sample data in whole slope mass. Figure 5b shows its simulated pole density graph with 300 dots. Comparing two graphs, we can see that the simulation is very close.

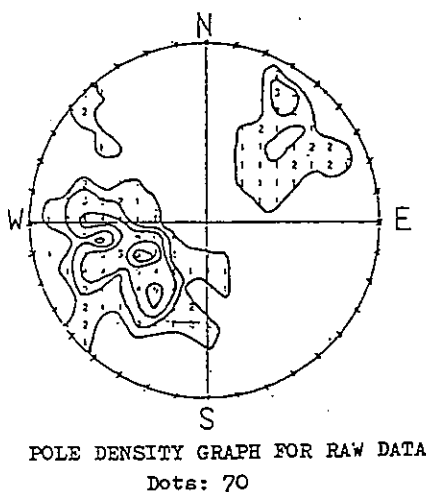


Figure 5a. Pole density graph of raw data

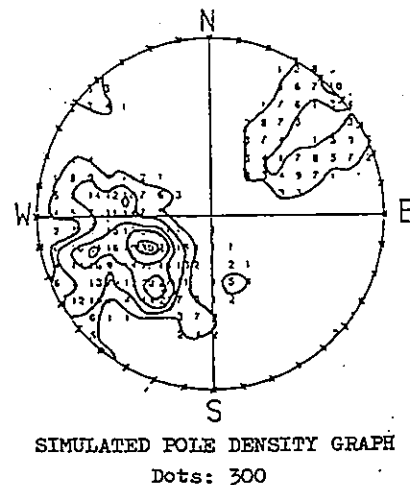


Figure 5b. Simulated pole density graph

Figure 5. Pole density graph

2.3 Three Dimensional Net Work and Blocks

Figure 6 shows the three dimensional joint net, which is drawn in light of simulated pole density

graph. The distribution of faults is confirmed by field measurement as shown in Fig.6a and the distribution of joints is confirmed by the statistics. Figure 6b shows the distribution of faults and

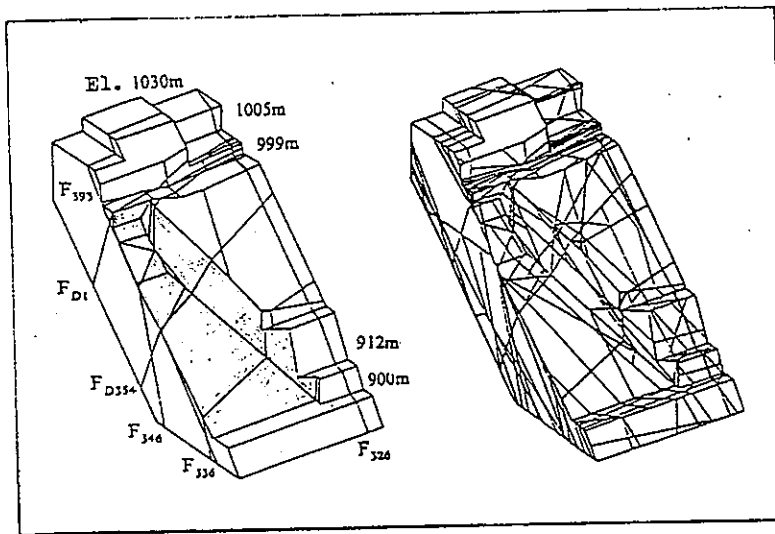


Figure 6. The net work of joint and faults

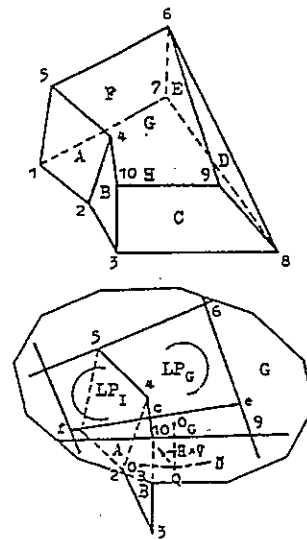


Figure7 Block and Loops

joints. In Figure 6 the shadow area is the dam pit, which is dug down to the dam foundation. The calculated section of the slope mass is taken from the abutment of left bank. The calculated section involves the dam pit. The total height of the calculated section is 150 meters with a width of 60 meters. With the statistical densities, diameters and attitudes of joints, the joint planes are simplified as disks and distributed in space. Then we can get a three dimensional net work of intersecting planes of statistical joint disks and confirmed faults. The intersecting lines in figure are the edges of different blocks. Each plane of block is a closed loop of edges. As long as we find out all loops of the block, its shape, location and size can be exactly fixed. Figure 7 shows an arbitrary block and its loops. The searching of loops can begin from an arbitrary plane such as G. Assume that LP_1 and LP_G are two loops of disk G, then judge which loop belonging to the block. As all the loops are judged, the block is found.

2.4 Chained Key Blocks

The unstable blocks in net work are chained with stability sequence. Figure 8 shows the sliding process of sequence 31 and 32. In the figure, the shape and location of unstable block 31 and 32 are shown. If we take off the unstable block 31, then the new free surface is formed. The next step is to take off the chained unstable block 32, then a newer free surface can be found. So on till no new free surface and chained key block generate, the searching can stop. This method can step by step find out all unstable blocks, which slide in a chain with their sliding sequence.

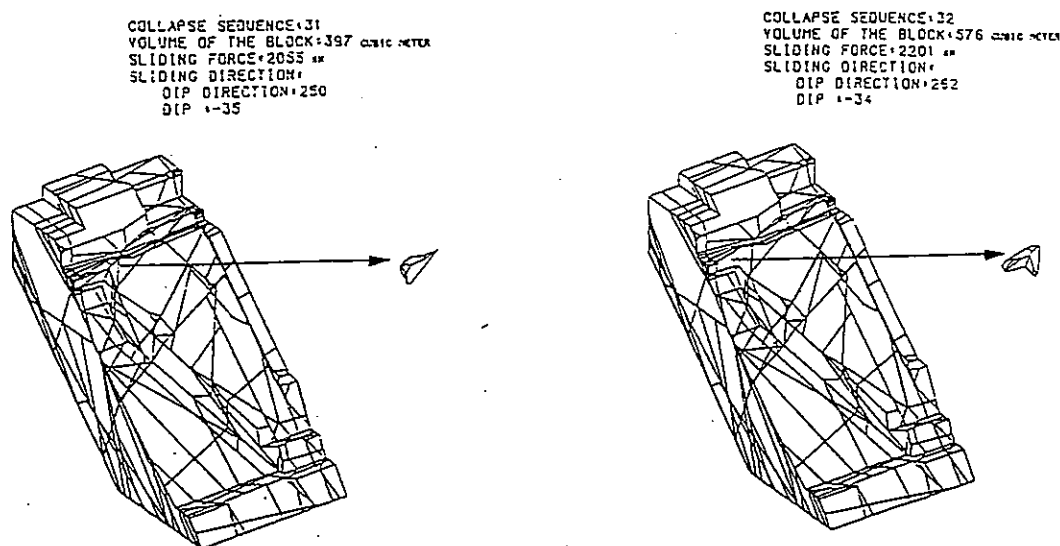


Figure 8. Sliding chained key block and its location

Figure 9 shows the slope surface before and after the sliding and its distribution of sliding force contour map: (a) the unstable block location on original slope plane; (b) the final sliding plane after sliding and (c) the contour map of sliding forces on final sliding plane. In the figure, the dash point zone is the limits of chained key blocks on original slope plane, the shadow area is the final sliding plane and the contour lines is its sliding force. The total volume of sliding blocks in the calculated section is 254,959 m³, converted into whole sliding slope is 80 thousands m³. The calculated sliding depth is 20 meters. These results are very close to the actual situation. The total sliding force is 168,829 KN. It means that the average unit sliding force is 6.6 KN/m³. The dip direction and dip angle of sliding blocks is 220° to 267° and 33° to 59° individually.

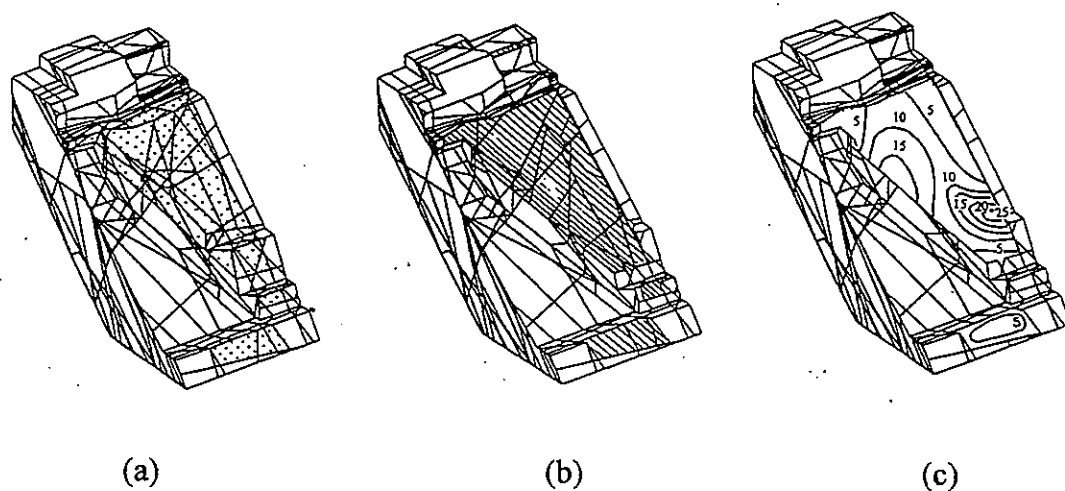


Figure 9. Chained key block location, final sliding planes and contour map of sliding forces

2.5 Collapse Sequence

Figure 10 shows the collapse sequence of the sliding. There are four sets of key blocks. The single key block 4 is on the elevation of 900 to 912 m. The chained key blocks 5, 6, 7 are on the elevation of 885 to 900 m. The chained key blocks 2, 3, 8, 9, 12, 13, 14, 15, 16, 17, 18, 19, 20, 21, 22, 23, 24, 25, 26, 27, 28, 29, 30, 31 and 32 are on the elevation of 912 to 999m. The chained

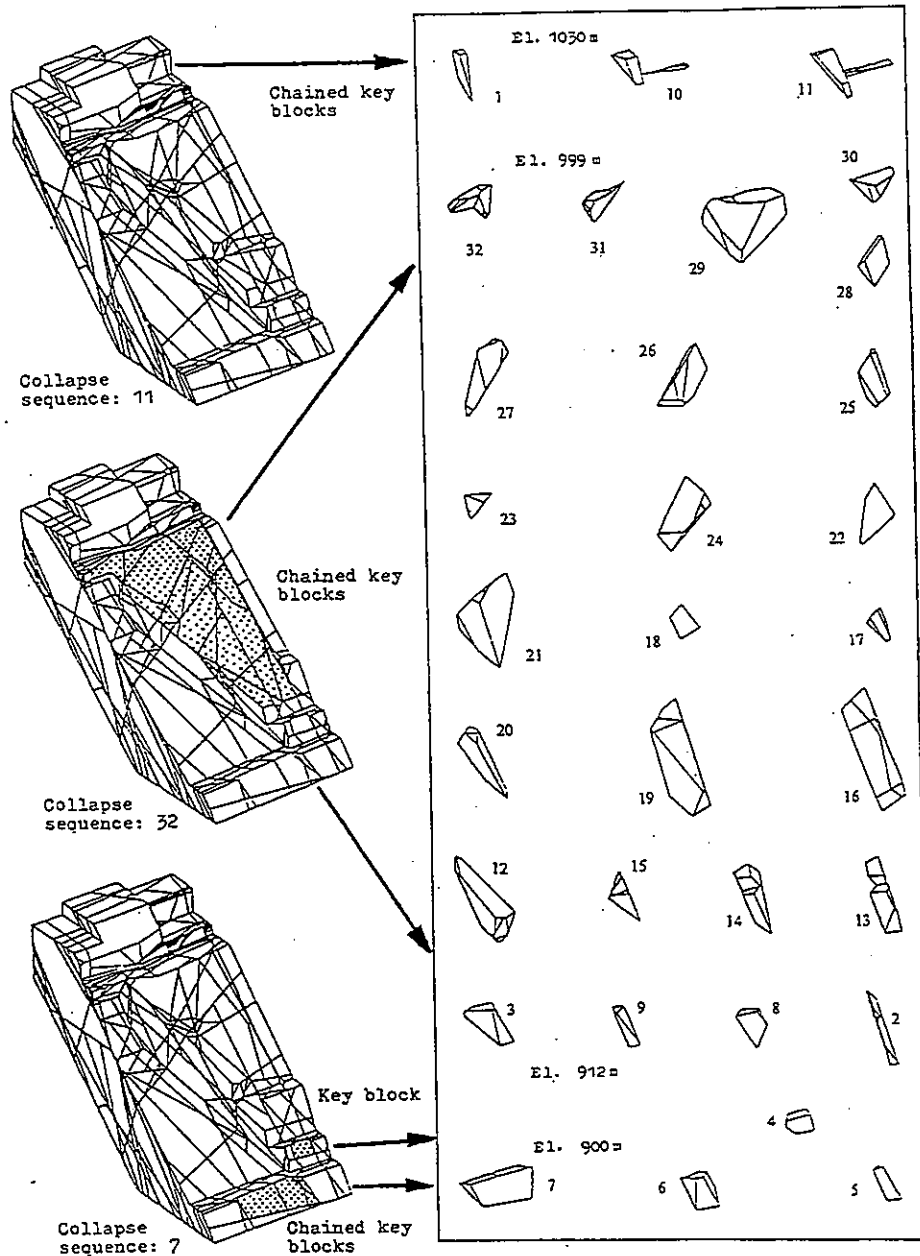


Figure 10. Collapse sequence

key blocks 1, 10, 11 are on the elevation of 1005 to 1030m. The numbers of blocks stand for the sliding sequences of chained key blocks. In the figure, the dashed area is the location of slid blocks and the number 1 to 32 is the sequence of block sliding and the block number. The shapes and sizes of blocks are plotted out. The block shapes are very different from the joint pyramids. Some blocks are very complicated in shapes and their planes even are more than twenty. Compared with the maximum key block theory, it is more reality, because the joint planes are not extended infinitely and are cut each other. The difference of sizes of blocks also is rather large. There are four sliding zones on slope. On the main sliding zone, the sliding sequence essentially is from lower to upper. The collapse is chained block by block. It indicates that the causality of the slope sliding is the excavation at slope toe. Obviously the failure of slope toe causes the upper slope sliding. If the slope can be strengthened before hand, may be the slope can avoid from sliding. Unfortunately, it is anchored after sliding and the calculation shows after sliding the new plane of slope has been stable. The anchorage scheme is to anchor the slope after sliding with more than one thousand pre-stressed steel cables with length of 30 to 50 meters and with the pre-stress of 100 to 300 tons per cable.

2.6 Conclusion

Using statistical method to generate a three dimensional random net work of joint planes can search out the probability distribution of chained key blocks. If the statistical data are simply reliable, it can predict and judge the stability and possibility of slope sliding statistically. The three dimensional chained key block method and program developed by authors can analyze the chained action of slope sliding, describe the complex shapes of rock blocks and evaluate the slope stability and the support safety. The calculation of Man-wan slope proves that the new slope plane generated after original slope sliding is stable, there is no need to reinforce if the base of slope is not cut down again. The pre-stressed anchorage, which has adapted, can increase the stability safety of the slope additionally. The best way to increase the slope safety is to move the power plant to a certain distance for diminishing the base cut, that has done together with the anchorage. So the reinforced slope is very stable at present.

REFERENCES

- Pei, Jue-Min and Hang, Shan-Ru, 1991. *The application of Block theory on the prediction of collapse of Fen-He tunnel*. Research report.
- Pei, Jue-Min and Pen, Xiao-Chu, 1992. *The three dimensional random net work of joints and the chained key blocks of rock slope*. Research report.

APPLICATIONS OF KEY BLOCK THEORY AND DDA AT YERBA BUENA ISLAND TUNNEL PORTALS UNDER EARTHQUAKE LOADING

Hubert K. Law
Earth Mechanics, Inc.
Fountain Valley, CA 92708, USA

Ignatius P. Lam
Earth Mechanics, Inc.
Fountain Valley, CA 92708, USA

ABSTRACT: Slope stability at the portals of Yerba Buena Island Tunnel is presented as a case history. The key block theory along with the Newmark's sliding on two planes was used to assess deformations of a potential failure wedge at the west portal slope. Discontinuous Deformation Analysis (DDA) was utilized at the east portal slope to evaluate a toppling mode of failure. Field measurements for these analyses are critical as the outcomes of the studies largely depend on the input parameters. The major emphasis was placed at gathering site specific data which led to a very comprehensive field investigation program to assist in selection of appropriate input parameters to be used in the analysis procedures. Rational judgements based on understanding of fundamental mechanics are needed because no amount of field investigation can fully reveal the complete geologic data.

1 INTRODUCTION

Yerba Buena Island is comprised of Franciscan Formation located between the cities of San Francisco and Oakland. The rock outcrop forming the island rises over 100 m above the sea level providing a natural break between the east and west spans of the San Francisco-Oakland Bay Bridge, as shown in Figure 1. The construction of the tunnel started in 1933 and completed in 1936, and the excavation into bedrock created slopes at the east and the west portals. As a part of the earthquake retrofit program for California Toll Bridges initiated by the California Department of Transportation, seismic vulnerability studies have been conducted at the Yerba Buena Island Tunnel. From the tunnel performance around the world, the tunnel portal is one of the most vulnerable areas to damage during earthquakes which is often caused by slope failure.

A geologic study was conducted as a part of the larger investigation to assess the seismic vulnerability of the tunnel liner and the tunnel portals. The complete field investigations included geologic mapping, continuous rock coring, laboratory and field rock-strength testing, down-hole pressure-meter testing, down-hole digital video imaging, down-hole seismic velocity measurements, and specialized testing for Spectral Analysis of Surface Waves (SASW). Although some of these investigations were intended to study the performance of the tunnel liner, they also provided important information for assessment of rock slope stability at the portals.

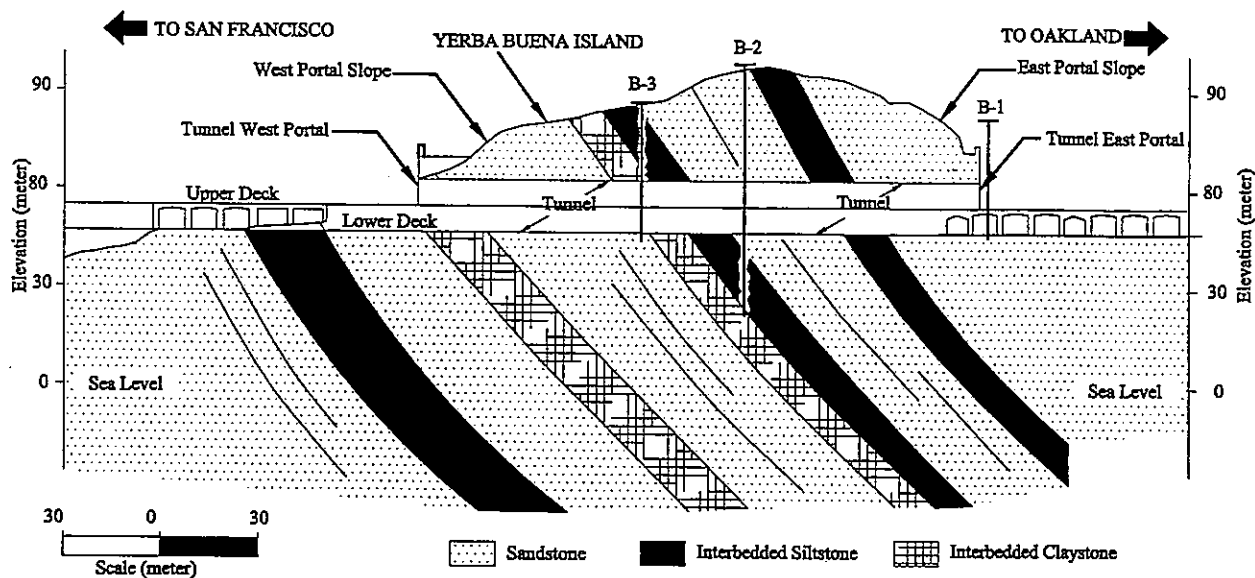


Figure 1. Geologic Cross Section of the Yerba Buena Island Tunnel

2 GEOLOGIC DATA AND SITE INVESTIGATION

Figure 1 is the longitudinal cross-section along the tunnel showing the general geological structure and rock types. Rocks at the tunnel area are primarily sandstone of the Mesozoic-age Franciscan Formation (100-200 million years old). The bedrock formation is generally covered by a thick blanket of sandy soil. Exposures of bedrock in the tunnel area occur primarily in excavations made for the various roads and the tunnel. The rocks exposed at the surface are generally weathered yellowish-brown, medium-grained graywacke sandstone. At depth, weathering decreases and the rocks are predominantly gray and black. The rocks are moderately hard to very hard except in highly fractured zones.

During the field investigation, geologic mapping was conducted mostly at the portal areas to collect information on orientations of discontinuous planes, characteristics of joint surfaces, and weathering conditions. Rock was cored at three locations as shown in Figure 1; and the boring depths range from 32 m to 75 m. Point load tests and unconfined compression tests have been conducted on selected intact cores while direct shear tests were conducted on samples with the existing joints. Seismic wave velocities were measured in the boreholes with down-hole geophysical sounding using OYO Model 170 suspension P-S wave logging system which provided important information on weathering conditions of rock. Also, down-hole pressure-meter tests were conducted in one of the boreholes to measure Young's modulus of the rock. Upon completion of drilling, the boreholes were photographed continuously by a down-hole digital video camera. The digital video imaging provided important features on bedding and joint orientation, and joint aperture. A specialized geophysical testing technique called SASW (spectral analysis of surface waves) was also performed in this project to obtain shear wave velocity of the rock behind the tunnel liner along the length of the tunnel wall without drilling through the tunnel liner.

3 ORIENTATIONS OF JOINTS

During the field mapping, several hundred discontinuities (including beds, faults, joints, fractures) were recorded using a scan-line mapping technique. This approach was used because it is not practical to map every single joint in the extensive exposures at the portals which consist of steep cliff faces comprising areas more than 30 m long and 15 m high. As results, both vertical and horizontal scan lines were established on the slope and each geologic feature that intercepts the scan lines is recorded. Statistical studies have shown that fractures can be adequately characterized if more than 60 joints are recorded along the scan line, and adding more joints may increase the confidence level but does not necessarily increase the accuracy of the results.

The poles of these discontinuous planes were plotted on a polar net and were analyzed for pole concentrations. Based on the study of pole population, the following most dominant joint sets were found at the two portal slopes.

Table 1. Joint Orientations at West and East Portal

West Portal Slope			East Portal Slope		
Joint Set	Strike	Dip	Joint Set	Strike	Dip
Set A	N18°E	73°SE	Set A	N10°E	85°SE - 80°NW
Set B	N70°W	58°NE	Set H	N59°W	72°NE
Set C	N51°W	70°SW	Set I	N62°E	63°SE
Set D	N45°W	32°SW			

4 CHARACTERIZATION OF JOINTS AND BEDDING PLANES

Joints exposed at the surface in the portal areas are generally tight with little aperture. Most joints have an oxide coating composed primarily of iron oxide (FeO_2) which is yellowish brown to reddish brown, but black manganese oxide (MnO_2) coatings are also common. Several joints are filled with a hard silica filling while other joints, typically at the shallow subsurface, have clay films. Thirteen samples from the boreholes with typical joints were subjected to direct shear tests. As expected, the sandstones have higher friction angles than the claystones (30° to 40° vs 20°). However, some joints in claystone have wavy irregular joints or are partly healed and calcite-lined. These have substantially higher (20° to 40°) friction angles than other claystone joints and have friction angles more similar to sandstone joints. The uniaxial compressive tests conducted on seven intact core samples show that the unconfined compression strengths range from 6 to 130 MPa.

The joint continuity (persistence) in the form of joint length was recorded in the field which ranges from discontinuous to highly continuous. Table 2 lists the percentages of joints that have certain joint lengths. Table 3 describes the characteristics of joint roughness and the percentage that falls in each roughness category. For rock slope stability evaluation, it is important to examine all these data and to make rational judgements in selecting reasonable sets of input data. It would be inappropriate to solely rely on a particular type of test data (e.g., direct shear test data) as the potential failure plane is likely to go through the existing discontinuities and to shear the intact rock that bridges the joint planes. As results, the shear strength parameters assigned to the potential

failure plane in a limit equilibrium analysis should include some portion of the intact strength. Furthermore, laboratory direct shear tests are usually conducted on small rock specimens, and thus dilation due to waviness (undulatory nature) of the joint that has a wave length of 0.5 m or longer is not captured in the test. These considerations would increase the gross shear strength properties of the joint planes that compose a reasonable size failure wedge. The equation of the following form may be used to assign shear strength (τ) on a potential failure plane:

$$\tau = \tau_i + c + \sigma_n \tan(\phi + \delta) \quad (1)$$

where τ_i = portion of intact rock strength, c = shear intercept of the existing rock joint, σ_n = normal stress on the failure plane, ϕ = friction angle of existing rock joint, δ = added friction angle due to dilation. The contribution of τ_i and δ becomes rather important as the size of potential failure block increases because shearing of intact rock by the failure plane is likely to occur as well as the failure plane tends to weave. On the other hand for a small size failure block, τ_i and δ become negligible and thus should not be accounted for.

Table 2. Joint Continuity (Persistence)

West Portal Slope ⁽¹⁾			East Portal Slope		
Joint Set	Joint Length, meter	Percentage	Joint Set	Joint Length, meter	Percentage
Set A	15 or more	5	Set A	15 or more	4
	10-15	7		10-15	5
	7-10	10		7-10	17
	3-7	20		3-7	10
	1.5-3	23		1.5-3	20
	0-1.5	35		0-1.5	39
Set C	6-7	15	Set I	6-7	0
	3-6	20		3-6	5
	1.5-3	30		1.5-3	15
	0-1.5	35		0-1.5	80
Set D	6-7	15	Set H	15 or more	50
	3-6	20		9-15	30
	1.5-3	30		3-9	20
	0-1.5	35		<3	<1

Note: ⁽¹⁾ Data for Joint set B at the west portal slope was not compiled since it does not affect stability

Table 3. Joint Roughness

West Portal Slope Data ⁽²⁾			East Portal Slope		
Joint Set	Joint Length	%	Joint Set	Joint Length	%
Set A	Smooth and Planar	70	Set A	Smooth and Planar	70
	Moderately Rough to Rough	20		Moderately Rough to Rough	20
	Discontinuous ⁽¹⁾	10		Discontinuous ⁽¹⁾	10
Set C	Smooth and Planar	60	Set I	Smooth and Planar	30
	Moderately Rough to Rough	30		Moderately Rough to Rough	10
	Discontinuous ⁽¹⁾	10		Discontinuous ⁽¹⁾	60
Set D	Smooth and Planar	35	Set H	Smooth and Planar	35
	Smooth & Undulatory (Wavy)	35		Smooth & Undulatory (Wavy)	45
	Moderately Rough to Rough	20		Moderately Rough to Rough	20
	Discontinuous ⁽¹⁾	10			

Note:

⁽¹⁾ Terminated by or is offset by a major step at another joint within lengths of less than 1.3 m long.

⁽²⁾ Data for Joint set B at the west portal slope was not compiled since it does not affect stability

5 WEST PORTAL SLOPE

Figure 2 shows the stereo-graphic projections of joint sets A, B, C and D, and the orientation of the rock slope. Markland's test of kinematic stability was conducted at the west portal slope; it seemed that the wedge formed by joint sets A, B and D has a potential for instability. As a lower bound scenario, a friction angle of 33 degrees was assigned to joint sets A and D, and that of 25 degrees was assigned to joint sets B and C to evaluate static stability without considerations for dilation and contribution of the intact rock strength. A static factor of safety of 1.61 was estimated under gravity loading, and from the key block analysis the maximum volume for this removable wedge formed by joint sets A, B and D was calculated to be 77 cubic meters. For evaluation of seismic stability, a method similar to P. Londe solution was used. The P. Londe stereo-graphic projection solution is well known for dam foundation and dam abutment stability analysis, and is also suitable for earthquake loading. The three-component acceleration time histories developed for the Yerba Buena Island Tunnel seismic retrofit program were used as input loads to the potential failure wedge. The trajectories of the inertia force as exerted by seismic loading are graphically presented

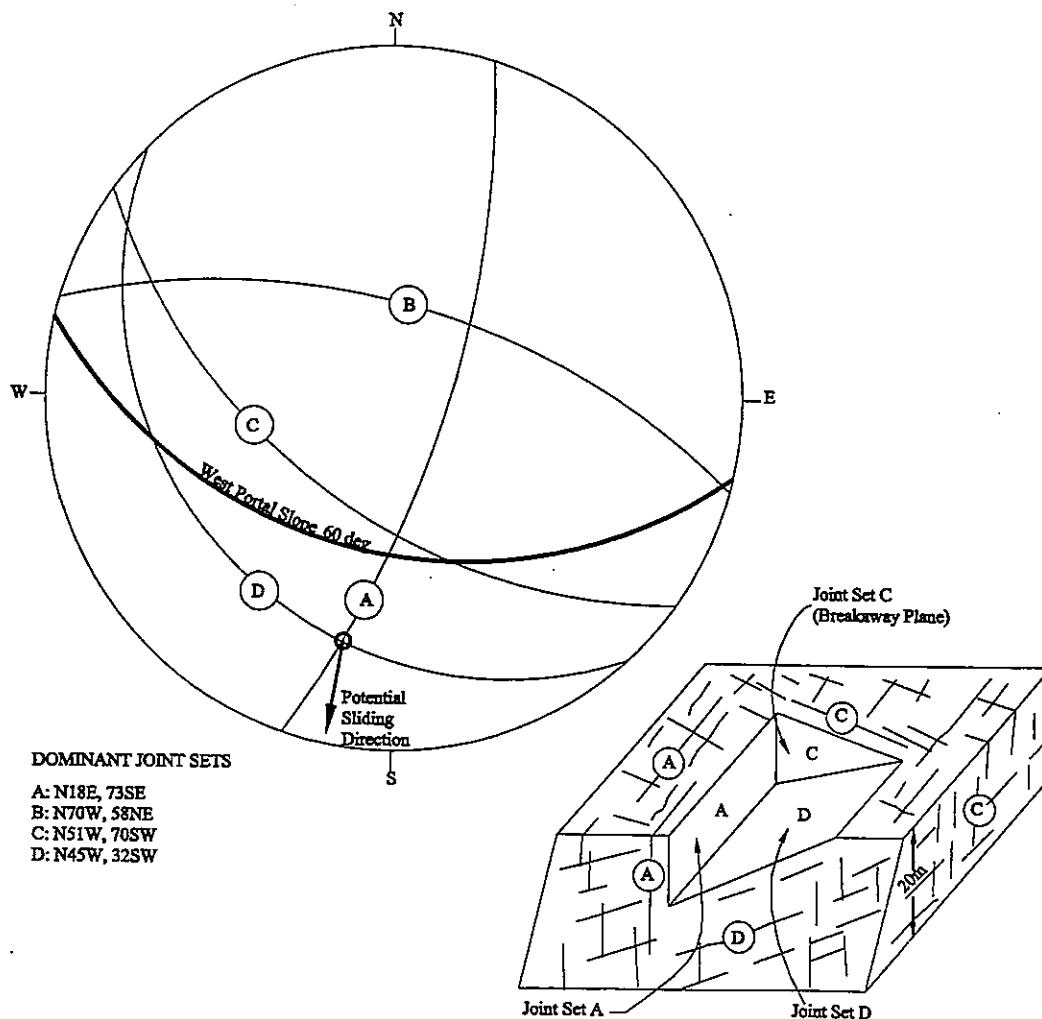


Figure 2. Orientations of Dominant Joint Sets at the West Portal Slope

in Figure 3. The region closed by the friction circles of the poles A and D is shown on the figure. When the resultant force falls within this region, no movement of the wedge will take place; otherwise sliding will occur. To compute the amount of wedge displacement, the Newmark type analysis was extended for sliding on two planes under three-dimensional loading. The vector of body force acting onto each joint plane due to the three-component acceleration was checked against the joint's yield acceleration. Sliding can take place on the either plane or along the interception of the two planes depending on the direction of load at any given instance of time. The permanent displacement of the wedge as obtained from the Newmark integration is compared with the input accelerations in Figure 4. The maximum permanent displacement is 1.3 meters and the all-time maximum sliding velocity is 0.7 meter per second.

From the discussion of assigning shear strengths on a potential failure plane in the previous section, it would be justifiable to include additional components. In addition to $\phi = 33$ degrees, it was elected to use τ_i of 300 kPa and δ of 7 degrees as the upper bound strength scenario. This additional shear strength (τ_i) of 300 kPa corresponds to 5% of the smallest shear strength measured on the intact core samples (assuming that 5% of failure plane intercepts the intact rock), and δ of

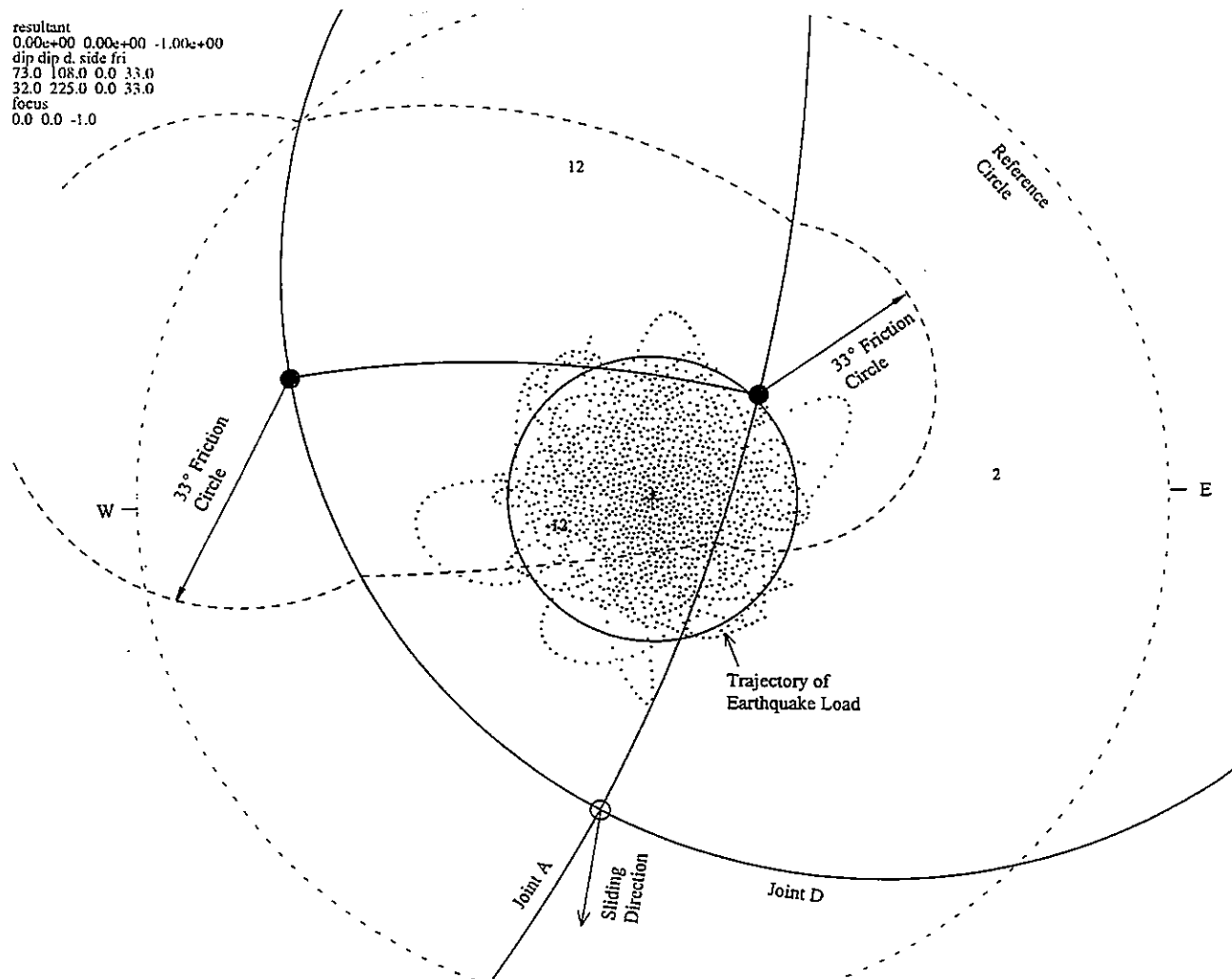


Figure 3. Trajectories of Seismic Loads

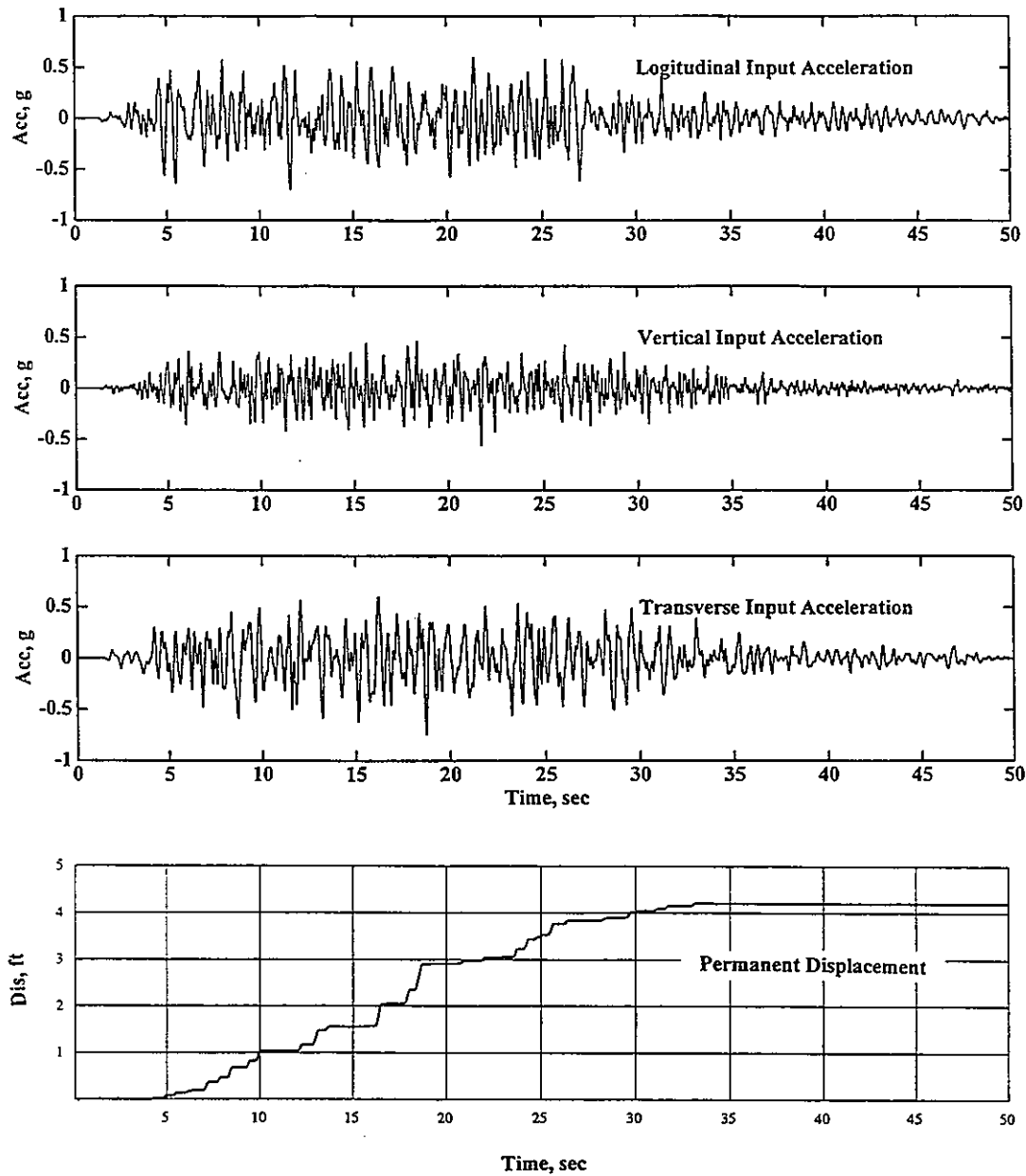


Figure 4. Time Histories of Permanent Deformation and Input Accelerations

7 degrees is based on the field measurements. The Newmark sliding analysis with the upper bound shear strength indicates no permanent movement under the same earthquake loading. The additional analyses showed that all it needs to maintain a stable condition under the given earthquake is to use τ_i of 28 kPa even without dilation contribution ($\delta = 0$). This clearly shows that the intact rock strength is a very important factor controlling stability.

6 EAST PORTAL SLOPE

From the stereo-graphic projections of joint sets A, H, and J at the east portal slope as shown in

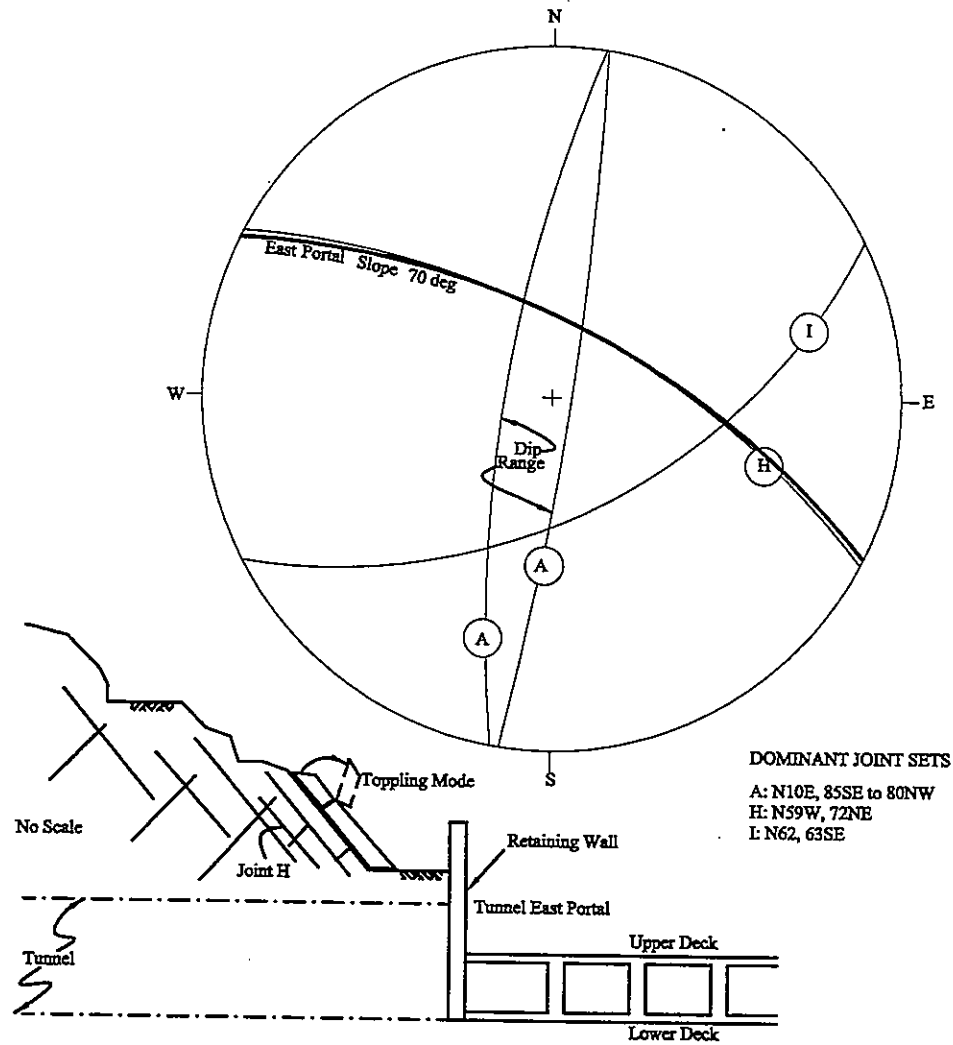


Figure 5. Orientations of Dominant Joint Sets at the East Portal Slope

Figure 5, no key block was found to be kinematically unstable. However, due to the large dip angle of the slope which is parallel to the joints, a rotational mode of failure was considered. A two-dimensional Discontinuous Deformation Analysis (DDA) with a seismic capability was used to compute multi-block toppling and buckling. Based on the natural contact phenomena, the algorithm for "open-close" iteration implemented in the DDA ensures no tension and no penetration for all blocks, and yet the computation offers deformations, stresses and strains for each block. A graphical presentation of DDA results under seismic loading can be seen in Figure 6 for a few snap-shots. Based on the DDA computation, toppling of rock is confined to the surficial rock of no more than 2 m from the east portal slope face, and no block bounces over the retaining wall located about 7 m away from the toe. In fact this counter-fort retaining wall was built to prevent rockfalls onto the highway at the tunnel portal. The crown of the tunnel is located about 10 m below the top of the retaining wall. The area between the toe of the slope and the retaining wall has massive lean concrete fills, as much as 5 meter thick, and provides as a good buffer zone for a potential impact.

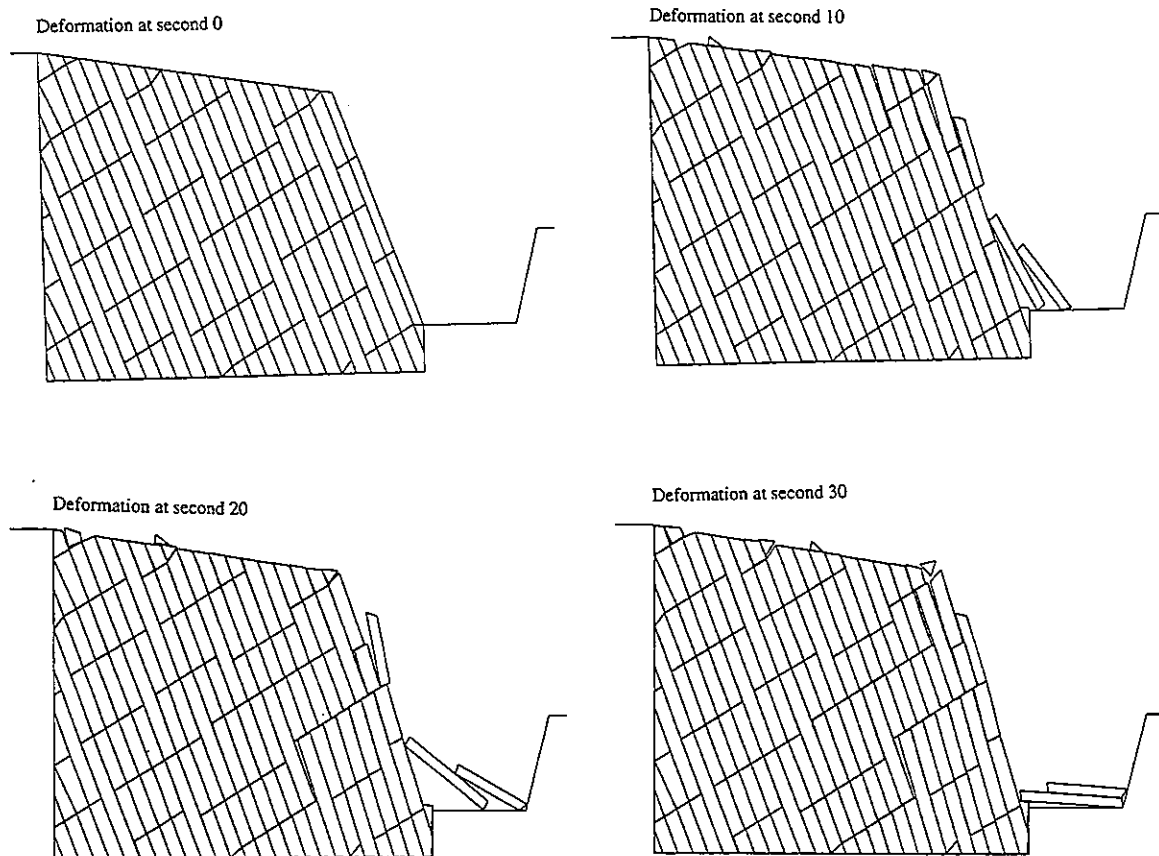


Figure 6. Snap-shot Deformations for Toppling at East Portal Slope

7 CONCLUSIONS

The field data and analysis results presented in this paper are a part of the larger investigation to develop a retrofit strategy to keep the tunnel opened to traffic in event of future earthquakes. A system of rock bolts has been recommended to stabilize the potential failure wedge at the west portal slope. At the east portal slope, only a few spots need rock bolts.

8 ACKNOWLEDGMENTS

The authors acknowledge the professional assistance of the Caltrans Contract Management team, the peer review panel members, and all the consultants working on this project. HNTB Corporation conducted the studies on seismic vulnerability assessment of the tunnel liner while Shannon & Wilson Inc. designed rock-bolts at the portal slopes. Mr. Bruce Schell conducted the site investigation, and Dr. Gen-hua Shi performed DDA and Newmark analysis for sliding on two planes. Drs. Tor Brekke and Geoffrey Martin served as technical consultants.

REFERENCES

- Earth Mechanics, Inc. (1998), "Report on Field Investigation," Prepared for HNTB and Caltrans, Division of Structures, Sacramento CA, Contract No. 59X855, February
- Earth Mechanics, Inc. (1998), "Report on Wave Propagation Analyses," Prepared for HNTB and Caltrans, Division of Structures, Sacramento CA, Contract No. 59X855, March
- Goodman, R. E. (1976), *Methods of Geological Engineering in Discontinuous Rock*, West Pub. Co.
- HNTB Co. (1998), "Seismic Vulnerability Assessment and Conceptual Retrofit of Yerba Buena Island Tunnel," Prepared for Caltrans, Division of Structures, Sacramento, CA, Contract No. 59X855-A/1, March
- Hoek, E. and Bray, J. W. (1981), *Rock Slope Engineering*, The Institution of Mining and Metallurgy, London
- Shannon & Wilson, Inc. (1998), "Slope Criteria/Analysis Report at Yerba Buena Island Tunnel," Prepared for HNTB and Caltrans, Division of Structures, Sacramento CA, Contract No. 59X855, May
- Shi, G.H.(1993), "Block System Modeling by Discontinuous Deformation Analysis," *Computational Mechanics* Publication, Southampton, UK
- Shi, G. H. (1998), "Numerical manifold Method," *International Journal for Numerical and Analytical Methods in Geomechanics* (in press)

Manifold Method

MANIFOLD METHOD WITH COMPLETE FIRST ORDER DISPLACEMENT FUNCTION ON PHYSICAL COVER

Wang Shuilin, Ge Xiurun & Zhang Guang
Institute of rock and Soil Mechanics, Chinese Academy of Sciences
Wuhan 430071, PRC

ABSTRACT: Complete first order displacement function is used on physical covers of manifold element. The analyzing formulas for numerical implementation are presented for the first time in this paper. A continuous stress distribution is obtained through projection techniques proposed by Zienkiewicz et al so that results can be compared with those published. Two examples are investigated and the numerical results show that a high accuracy can be achieved by the adoption of the function on physical covers.

1 INTRODUCTION

Manifold method, proposed by Genhua Shi(1991), is a recently developed numerical technique. It is studied by some scholars (Lin et al.1996, Qiu 1996, Shi 1996a,b, Wang et al.1997, Wang 1998, Wang et al. 1998), and the published results show that the new method is effective in discontinuous deformation analysis, large deformation analysis, simulation of crack propagation and seepage problem with free surface, etc. Compared with finite element method, this one is a general one and has its own advantages. The manifold element is composed of the overlapped physical covers, and the displacement function on elements is the average of the weighted cover function (displacement function) on physical covers. Therefore, there is flexibility in composing displacement function in the elements by means of choosing displacement functions on physical covers. In addition, the displacement compatibility between elements can be guaranteed for continuous region.

In this paper, the complete first order cover functions on physical covers are used, the analyzing formulas for numerical implementation are presented for the first time. In order to compare the results with those published, projection techniques suggested by Zienkiewicz and Zhu(1987) are used to get a continuous stress distribution. Two numerical examples are studied and their results illustrate that the adoption of complete first order approximation on physical covers is efficient and can achieve a high accuracy.

2 MANIFOLD ELEMENTS WITH COMPLETE FIRST ORDER APPROXIMATION ON PHYSICAL COVERS

2.1 Displacement function on manifold element

For finite covers of manifold method, finite element mesh is usually adopted to cover the problem geometry. In this paper, triangular elements are used to define mathematical covers of manifold method for 2-D problems. Figure 1 shows that a triangular element covers a triangular domain. They are overlapped each other. The mathematical cover, physical cover and manifold

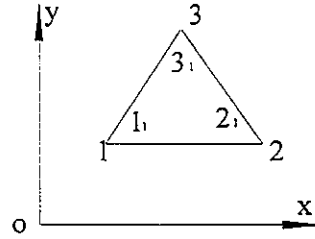


Figure 1. A triangular mesh covers a triangular

element are defined according to Shi (1996a). In Figure 1, there are 3 mathematical covers denoted by 1, 2 and 3, and 3 physical covers denoted by 1_1 , 2_1 , and 3_1 , and 1 manifold element. The manifold element takes the shape of the triangular domain and it is expressed by $1_1 2_1 3_1$. If complete first order approximation function is used on the i th physical cover of the manifold element in Figure 1, the function on that cover can be written as

$$\{u_i\} = [fun] \{D_i\} \quad (i = 1, 2, 3) \quad (1)$$

Where $\{u_i\} = \begin{Bmatrix} u_i(x, y) \\ v_i(x, y) \end{Bmatrix}$, $[fun] = \begin{bmatrix} 1 & 0 & x & 0 & y & 0 \\ 0 & 1 & 0 & x & 0 & y \end{bmatrix}$ and $\{D_i\}^T = \{d_{i1} \ d_{i2} \ d_{i3} \ d_{i4} \ d_{i5} \ d_{i6}\}$.

So the displacement function within the element is

$$\begin{Bmatrix} u(x, y) \\ v(x, y) \end{Bmatrix} = \begin{bmatrix} W_1(x, y) & 0 & W_2(x, y) & 0 & W_3(x, y) & 0 \\ 0 & W_1(x, y) & 0 & W_2(x, y) & 0 & W_3(x, y) \end{bmatrix} \begin{Bmatrix} u_1(x, y) \\ v_1(x, y) \\ u_2(x, y) \\ v_2(x, y) \\ u_3(x, y) \\ v_3(x, y) \end{Bmatrix} \quad (2)$$

in which $W_i(x, y)$ ($i=1, 2$ or 3) is the weighted function. It takes the form of the shape function of the corresponding triangular element, i.e. $W_1(x, y) = a_1 + b_1 x + c_1 y$, $W_2(x, y) = a_2 + b_2 x + c_2 y$, $W_3(x, y) = a_3 + b_3 x + c_3 y$, where x_i , y_i ($i=1, 2, 3$) are node coordinates of the corresponding triangular element, whose area is denoted by A . $a_i = (x_j y_k - x_k y_j) / (2A)$, $b_i = (y_j - y_k) / (2A)$, $c_i = (x_k - x_j) / (2A)$, and the

subscript i, j and k permulate like 1,2,3.

Denote $I = \begin{bmatrix} 1 & 0 \\ 0 & 1 \end{bmatrix}$, $W_1 = W_1(x, y) \bullet I$, $W_2 = W_2(x, y) \bullet I$, $W_3 = W_3(x, y) \bullet I$, and $\{u\} = \begin{Bmatrix} u(x, y) \\ v(x, y) \end{Bmatrix}$.

Thus, equation (2) can be rewritten as

$$\{u\} = \begin{bmatrix} W_1 \bullet fun & W_2 \bullet fun & W_3 \bullet fun \end{bmatrix} \begin{Bmatrix} D_1 \\ D_2 \\ D_3 \end{Bmatrix} \quad (2a)$$

in which $\begin{Bmatrix} D_1 \\ D_2 \\ D_3 \end{Bmatrix}$ is unknown variable vector.

2.2 Element stiff matrix and force vector

From equation (2a), the strains within the manifold element are

$$\begin{Bmatrix} \varepsilon_x \\ \varepsilon_y \\ \varepsilon_{xy} \end{Bmatrix} = \begin{bmatrix} B_1 & B_2 & B_3 \end{bmatrix} \begin{Bmatrix} D_1 \\ D_2 \\ D_3 \end{Bmatrix} \quad (3)$$

where

$$[B_i] = \begin{bmatrix} b_i & 0 & a_i + 2b_i x + c_i y & 0 & b_i y & 0 \\ 0 & c_i & 0 & c_i x & 0 & a_i + b_i x + 2c_i y \\ c_i & b_i & c_i x & a_i + 2b_i x + c_i y & a_i + b_i x + 2c_i y & b_i y \end{bmatrix} \quad (i=1,2,3)$$

Relationship between stress and strain can be written as $\{\sigma\} = [D]\{\varepsilon\}$, in which $\{\sigma\}$ and $\{\varepsilon\}$ are stress and strain vector respectively, and $[D]$ is relationship matrix. Accordingly, the strain energy done by the elastic stresses in the element is

$$\pi_e = \frac{1}{2} \iint_{s_e} \{\varepsilon\}^T \{\sigma\} dx dy = \frac{1}{2} \{d\}^T [K_e] \{d\} \quad (4)$$

in which $\{d\}^T = \{D_1^T \quad D_2^T \quad D_3^T\}$, $[K_e] = \iint_{s_e} \begin{bmatrix} B_1^T \\ B_2^T \\ B_3^T \end{bmatrix} [D] \begin{bmatrix} B_1 & B_2 & B_3 \end{bmatrix} dx dy$, and s_e is the area of

the manifold element. Numerical integration in element stiff matrix $[K_e]$ can be done by simplex integration (Shi 1996b).

In equation (4), $[K_e]$ is an 18 by 18 matrix and $\iint_{\Omega_e} [B_i^T DB_j] dxdy$ ($i,j=1,2,3$) is a 6 by 6 sub-matrix.

$$\text{If plane stress condition is assumed, } [D] = \frac{E}{1-\gamma^2} \begin{bmatrix} 1 & \gamma & 0 \\ \gamma & 1 & 0 \\ 0 & 0 & \frac{1-\gamma}{2} \end{bmatrix}. \text{ Denote } d_{00}=d_{11}=\frac{E}{1-\gamma^2},$$

$$d_{01}=d_{10}=\frac{\gamma \cdot E}{1-\gamma^2}, d_{22}=\frac{E}{2(1+\gamma)} \text{ (E will be substituted by } \frac{E}{1-\gamma^2} \text{ and } \gamma \text{ by } \frac{\gamma}{1-\gamma} \text{ if plane strain}$$

condition is assumed.), and $[SK] = \iint_{\Omega_e} [B_i^T DB_j] dxdy$. Each element of matrix $[SK]$ is in analytical formulation and is given in the Appendix.

Suppose that a point load \bar{p} ($\bar{p} = p_x \bar{i} + p_y \bar{j}$), in which p_x and p_y are projection of \bar{p} on Cartesian coordinates and \bar{i} and \bar{j} are the corresponding unit vector, acts on point (x_0, y_0) of the element. The potential energy due to the point load is

$$\pi_p = -\{u \quad v\} \begin{Bmatrix} p_x \\ p_y \end{Bmatrix}_{(x_0, y_0)} = -\{D_1^T \quad D_2^T \quad D_3^T\} \begin{bmatrix} fun^T \bullet W_1 \\ fun^T \bullet W_2 \\ fun^T \bullet W_3 \end{bmatrix}_{(x_0, y_0)} \begin{Bmatrix} p_x \\ p_y \end{Bmatrix} \quad (5)$$

Potential energy produced by surface loading is

$$\pi_q = -\{D_1^T \quad D_2^T \quad D_3^T\} \iint \begin{bmatrix} fun^T \bullet W_1 \\ fun^T \bullet W_2 \\ fun^T \bullet W_3 \end{bmatrix} \begin{Bmatrix} q_x \\ q_y \end{Bmatrix} dl \quad (5a)$$

q_x and q_y are projection of surface load acting on the element in x and y direction respectively. If a unit thickness is considered, l will be the area on which the load acts.

Assuming $\begin{Bmatrix} g_x \\ g_y \end{Bmatrix}$ is the body force. The potential energy due to the force is

$$\pi_g = -\{D_1^T \quad D_2^T \quad D_3^T\} \iint_{\Omega_e} \begin{bmatrix} fun^T \bullet W_1 \\ fun^T \bullet W_2 \\ fun^T \bullet W_3 \end{bmatrix} \begin{Bmatrix} g_x \\ g_y \end{Bmatrix} dxdy \quad (5b)$$

By minimizing the total potential energy of the system, the governing equation can be obtained in the same way as in finite element method. According to equation (4), an 18 by 18 sub-matrix is added to globe stiff matrix for each of the manifold elements, and an 18 by 1 vector to force vector by point load, surface load and body force respectively.

3 NUMERICAL EXAMPLES

The behavior of the adoption of complete first order approximation on physical cover is studied in the following two problems. In order to compare numerical results with those published, projection technique is used, in which constant stresses on physical cover is assumed. For simplicity, the generated triangular meshes in the interested domain constitute the finite cover system.

3.1 Cantilever Beam

A cantilever beam in two loading cases is showed in Figure 2a. The problem was solved for plane stress case. Figures 2b and 2c are two cover systems, and they correspond to regular 4-node quadrilateral (Fig. 2d) and irregular ones (Fig. 2e). The results are compared with the analytical ones in table 1 and table 2. Moreover, finite element solutions were also obtained using regular and irregular quadrilateral Q4 and QA4 (Chen et al.1993).

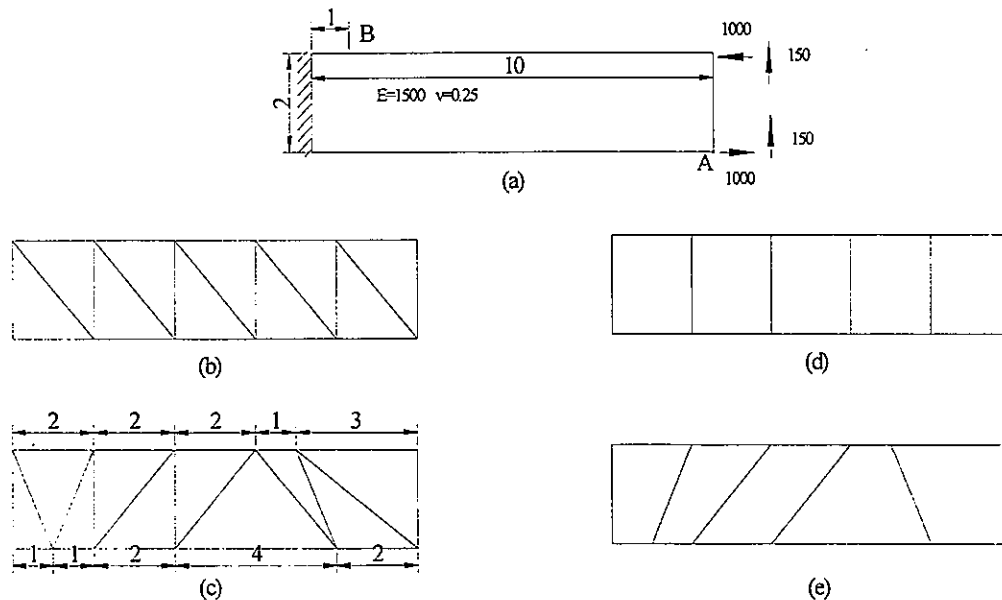


Figure 2. Cantilever beam

Table 1. Comparison of results of the beam subjected to bending

Element Type	regular mesh		irregular mesh	
	V_A	σ_{xB}	V_A	σ_{xB}
Q4	67.41	-2222.2	38.92	-2111.1
QA4	100.0	-3000.0	97.38	-2891.6
This paper	99.97	-3000.0	100.0	-3000.0
Analytical solution	100.0	-3000.0	100.0	-3000.0

Table 2. Comparison of results of the beam subjected to shear

Element Type	regular mesh		irregular mesh	
	V_A	σ_{xB}	V_A	σ_{xB}
Q4	70.00	-2945.5	45.11	-2939.4
QA4	101.51	-4049.9	98.90	-4077.8
This paper	101.7	-4009.0	101.2	-3841.0
Analytical solution	103.0	-4050.0	103.0	-4050.0

3.2 Cook problem

Figure 3a shows the cook problem. Two kinds of finite cover system are used as showed in Figure 3b and 3c, and they also correspond to regular 4-node quadrilateral (Fig. 3d) and irregular ones (Fig. 3e). Table 3 presented the comparison of the results.

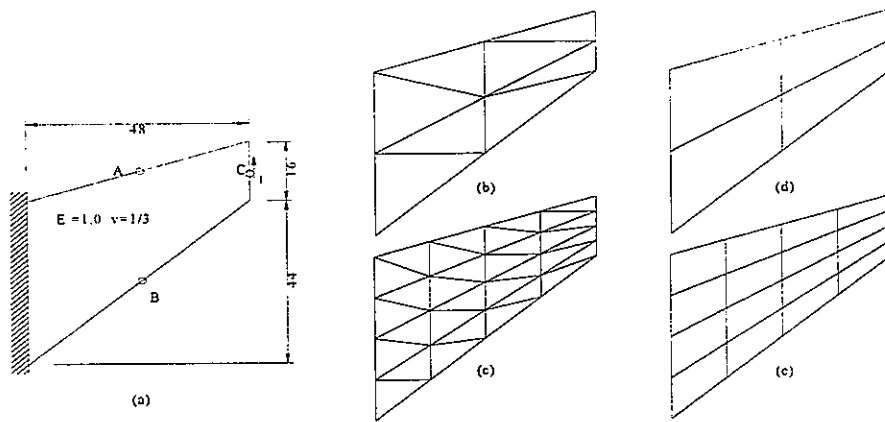


Figure 3. Cook problem

Table 3. Comparison of results of Cook problem

Element Type	4 × 4 mesh			8 × 8 mesh		
	V_C	$\sigma_{A \max}$	$\sigma_{B \min}$	V_C	$\sigma_{A \max}$	$\sigma_{B \min}$
Q4	11.85	0.1078	-0.0763	18.30	0.1814	-0.1429
QA4	23.29	0.1883	-0.1849	23.78	0.2226	-0.1888
This paper	22.79	0.2193	-0.2194	23.64	0.2339	-0.2017
Analytical solution	23.9	0.2360	-0.2010	23.9	0.2360	-0.2010

4 CONCLUSION

Numerical manifold method with complete first order approximation function on physical cover is presented in this study. Surprising accuracy is achieved. It is promising that the method can get a balance between accuracy and efficiency. In fact, application of the method to p-adaptivity, which is being carried out by the author, has been observed for the reason that cover function on physical cover can be defined as one's wish. Some results will be available soon.

REFERENES

- Chen, W.J. and Li, Y.D. 1993. Refined non-conforming quadrilateral plane isoparametric element with drilling degrees of freedom. *Computational structural mechanics and applications*. 10:22-29.
- Lin, J.S. and Lee, D.H. 1996. Manifold method using polynomial basis functions of any order. *Proc. of the 1st Int. Forum on DDA Simulation of Discontinuous Media*, Bekerley, california, USA:365-372.
- Qiu, X.J. 1996. Manifold method without use of penalty springs. *Proc. of the 1st Int. Forum on DDA Simulation of Discontinuous Media*, Bekerley, california, USA:407-414.
- Shi, G.H. 1991. Manifold method of material analysis. Transaction, *Ninth Proc. of the 1st Int. Forum on DDA Simulation of Discontinuous Media*, Bekerley, california, USA:52-204.
- Shi, G.H. 1996a. Manifold method. *Proc. of the 1st Int. Forum on DDA Simulation of Discontinuous Media*, Bekerley, california, USA:52-204.
- Shi, G.H. 1996b. Simplex Integration for manifold method. *Proc. of the 1st Int. Forum on DDA Simulation of Discontinuous Media*, Bekerley, california, USA:205-249.
- Wang, S.L. and Ge, X.R. 1997. Application of manifold method in simulating crack propagation. *Chinese Journal of Rock Mechanics & Engineering*, 16(5):405-410.
- Wang, S.L. 1998. Numerical manifold method and simulation of crack propagation. [Ph.D. dissertation]. Institute of Rock and Soil Mechanics, Chinese Academy of Sciences.
- Wang, S.L. and Ge, X.R. 1998. Analysis of seepage problem with free surface by manifold method. *The 6th National Conference on Numerical and Analytical Methods on Geomechanics*. Guangzhou, PRC:494-497.
- Wang, Z.Y. and Li, Y.P. 1997. Manifold method in large deformation for rock, *Computer Methods and Advances in Geomechanics, ACMAG*. Wuhan, PRC:513-516.
- Zienkiewicz, O.C. and Zhu, J.Z. 1987. A simple error estimator and adaptive procedure for practical engineering analysis. *Int. J. Num. Meth. Eng.* 24:237-357.

APPENDIX

For the completeness of the study, each element of the sub-matrix [SK] is presented here in analytical formulation. They are needed when integrals are computed in general manifold elements.

$$\begin{aligned}
 SK_{11} &= \iint_{s_e} (b_i d_{00} b_j + c_i d_{22} c_j) dx dy \\
 SK_{12} &= \iint_{s_e} (b_i d_{01} c_j + c_i d_{22} b_j) dx dy \\
 SK_{13} &= \iint_{s_e} [b_i d_{00} (a_j + 2b_j x + c_j y) + c_i d_{22} c_j x] dx dy \\
 SK_{14} &= \iint_{s_e} [b_i d_{01} c_j x + c_i d_{22} (a_j + 2b_j x + c_j y)] dx dy \\
 SK_{15} &= \iint_{s_e} [b_i d_{00} b_j y + c_i d_{22} (a_j + b_j x + 2c_j y)] dx dy \\
 SK_{16} &= \iint_{s_e} [b_i d_{01} (a_j + b_j x + 2c_j y) + c_i d_{22} b_j y] dx dy \\
 SK_{21} &= \iint_{s_e} (c_i d_{10} b_j + b_i d_{22} c_j) dx dy \\
 SK_{22} &= \iint_{s_e} (c_i d_{11} c_j + b_i d_{22} b_j) dx dy \\
 SK_{23} &= \iint_{s_e} [c_i d_{10} (a_j + 2b_j x + c_j y) + b_i d_{22} c_j x] dx dy \\
 SK_{24} &= \iint_{s_e} [c_i d_{11} c_j x + b_i d_{22} (a_j + 2b_j x + c_j y)] dx dy \\
 SK_{25} &= \iint_{s_e} [c_i d_{10} b_j y + b_i d_{22} (a_j + b_j x + 2c_j y)] dx dy \\
 SK_{26} &= \iint_{s_e} [c_i d_{11} (a_j + b_j x + 2c_j y) + b_i d_{22} b_j y] dx dy \\
 SK_{31} &= \iint_{s_e} [(a_i + 2b_i x + c_i y) d_{00} b_j + c_i x d_{22} c_j] dx dy \\
 SK_{32} &= \iint_{s_e} [(a_i + 2b_i x + c_i y) d_{01} c_j + c_i x d_{22} b_j] dx dy \\
 SK_{33} &= \iint_{s_e} [(a_i + 2b_i x + c_i y) d_{00} (a_j + 2b_j x + c_j y) + c_i x d_{22} c_j x] dx dy \\
 SK_{34} &= \iint_{s_e} [(a_i + 2b_i x + c_i y) d_{01} c_j x + c_i x d_{22} (a_j + 2b_j x + c_j y)] dx dy \\
 SK_{35} &= \iint_{s_e} [(a_i + 2b_i x + c_i y) d_{00} b_j y + c_i x d_{22} (a_j + b_j x + 2c_j y)] dx dy \\
 SK_{36} &= \iint_{s_e} [(a_i + 2b_i x + c_i y) d_{01} (a_j + b_j x + 2c_j y) + c_i x d_{22} b_j y] dx dy
 \end{aligned}$$

$$\begin{aligned}
SK_{41} &= \iint_{s_e} [c_i x d_{10} b_j + (a_i + 2b_i x + c_i y) d_{22} c_j] dx dy \\
SK_{42} &= \iint_{s_e} [c_i x d_{11} c_j + (a_i + 2b_i x + c_i y) d_{22} b_j] dx dy \\
SK_{43} &= \iint_{s_e} [c_i x d_{10} (a_j + 2b_j x + c_j y) + (a_i + 2b_i x + c_i y) d_{22} c_j x] dx dy \\
SK_{44} &= \iint_{s_e} [c_i x d_{11} c_j x + (a_i + 2b_i x + c_i y) d_{22} (a_j + 2b_j x + c_j y)] dx dy \\
SK_{45} &= \iint_{s_e} [c_i x d_{10} b_j y + (a_i + 2b_i x + c_i y) d_{22} (a_j + b_j x + 2c_j y)] dx dy \\
SK_{46} &= \iint_{s_e} [c_i x d_{11} (a_j + b_j x + 2c_j y) + (a_i + 2b_i x + c_i y) d_{22} b_j y] dx dy \\
SK_{51} &= \iint_{s_e} [2b_i y d_{00} b_j + (a_i + b_i x + 2c_i y) d_{22} c_j] dx dy \\
SK_{52} &= \iint_{s_e} [b_i y d_{01} c_j + (a_i + b_i x + 2c_i y) d_{22} b_j] dx dy \\
SK_{53} &= \iint_{s_e} [b_i y d_{00} (a_j + 2b_j x + c_j y) + (a_i + b_i x + 2c_i y) d_{22} c_j x] dx dy \\
SK_{54} &= \iint_{s_e} [b_i y d_{01} c_j x + (a_i + b_i x + 2c_i y) d_{22} (a_j + 2b_j x + c_j y)] dx dy \\
SK_{55} &= \iint_{s_e} [b_i y d_{00} b_j y + (a_i + b_i x + 2c_i y) d_{22} (a_j + b_j x + 2c_j y)] dx dy \\
SK_{56} &= \iint_{s_e} [b_i y d_{01} (a_j + b_j x + 2c_j y) + (a_i + b_i x + 2c_i y) d_{22} b_j y] dx dy \\
SK_{61} &= \iint_{s_e} [(a_i + b_i x + 2c_i y) d_{10} b_j + b_i y d_{22} c_j] dx dy \\
SK_{62} &= \iint_{s_e} [(a_i + b_i x + 2c_i y) d_{11} c_j + b_i y d_{22} b_j] dx dy \\
SK_{63} &= \iint_{s_e} [(a_i + b_i x + 2c_i y) d_{10} (a_j + 2b_j x + c_j y) + b_i y d_{22} c_j x] dx dy \\
SK_{64} &= \iint_{s_e} [(a_i + b_i x + 2c_i y) d_{11} c_j x + b_i y d_{22} (a_j + 2b_j x + c_j y)] dx dy \\
SK_{65} &= \iint_{s_e} [(a_i + b_i x + 2c_i y) d_{10} b_j y + b_i y d_{22} (a_j + b_j x + 2c_j y)] dx dy \\
SK_{66} &= \iint_{s_e} [(a_i + b_i x + 2c_i y) d_{11} (a_j + b_j x + 2c_j y) + b_i y d_{22} b_j y] dx dy
\end{aligned}$$

MANIFOLD METHOD WITH FOUR PHYSICAL COVERS FORMING AN ELEMENT AND ITS APPLICATION

Wang Shuilin & Ge Xiurun

Institute of rock and Soil Mechanics, Chinese Academy of Sciences
Wuhan 430071, PRC

ABSTRACT: Based on the theories of numerical manifold method proposed by Dr. Genhua Shi, this paper presents an extension of it, which improves manifold elements from three physical covers to four. Constant displacement function on physical cover is used and the weight functions take the form of the shape functions of the corresponding finite element. The manifold elements are transformed into squares so that numerical integration can be conducted by Gauss quadrature formula. With the extension, crack propagation is simulated and the results show that manifold method is effective in solving this class of problems.

1 INTRODUCTION

The manifold method, a new member of the families of numerical methods, is increasingly capturing attentions of researchers (Lin et al.1996, Qiu 1996, Shi 1996a,b, Wang et al.1997, Wang 1998, Wang et al. 1998), and more and more applications were found from recently published papers. One of the applications is the simulation of crack propagation.

In this paper, we present an extension of the method for 2-D problem, The manifold element is extended from three physical covers to four. Displacement function and numerical integration on manifold element are discussed, and crack propagation is modeled by the extension at last.

2 ELEMENT FORMED BY 4 PHYSICAL COVERS

2.1 *Manifold elements and displacement functions on them*

Figure 1 shows that 3 quadrilateral meshes cover a region, in which a crack exists. By the definition of mathematical cover, physical cover and manifold element of Shi, there are 8 mathematical covers, denoted by 1, 2, 3, 4, 5, 6, 7 and 8, 10 physical covers, by 1_1 , 1_2 , 2_1 , 3_1 , 4_1 , 5_1 , 5_2 , 6_1 , 7_1 and 8_1 . The relationship between the finite meshes and the manifold elements is given in table 1.

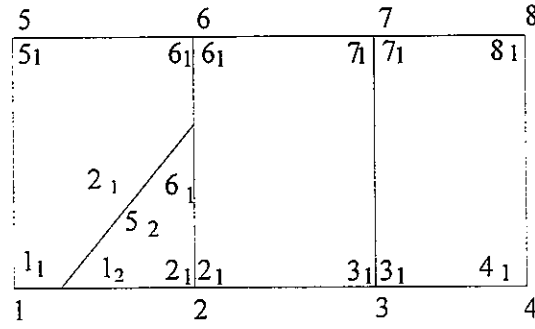


Figure 1. Mathematical covers, physical covers and manifold elements

Table 1. Manifold elements and its corresponding finite meshes

Finite mesh	1 2 6 5	2 3 7 6	3 4 8 7
Manifold element	$1_2 2_1 6_1 5_2$	$1_2 2_1 6_1 5_1$	$2_3 3_1 7_1 6_1$
			$3_4 4_1 8_1 7_1$

In this study, displacement functions on manifold element, say $1_2 2_1 6_1 5_2$, is in the following form.

$$\begin{Bmatrix} u(x,y) \\ v(x,y) \end{Bmatrix} = \begin{bmatrix} W_{\alpha(1_2)}(x,y) & 0 & W_{\alpha(2_1)}(x,y) & 0 & W_{\alpha(6_1)}(x,y) & 0 & W_{\alpha(5_2)}(x,y) & 0 \\ 0 & W_{\alpha(1_2)}(x,y) & 0 & W_{\alpha(2_1)}(x,y) & 0 & W_{\alpha(6_1)}(x,y) & 0 & W_{\alpha(5_2)}(x,y) \end{bmatrix} \begin{Bmatrix} u_{1_2} \\ v_{1_2} \\ u_{2_1} \\ v_{2_1} \\ u_{6_1} \\ v_{6_1} \\ u_{5_2} \\ v_{5_2} \end{Bmatrix} \quad (1)$$

where u_i and v_i are cover functions on the physical covers in xy -plane, $W_{\alpha(i)}(x,y)$ is weight function and subscript i represents physical covers 1_2 , 2_1 , 6_1 and 5_2 . The weight function takes the form of the shape functions of the corresponding finite element. $W_{\alpha(i)}(x,y) \geq 0$ and $\sum_i W_{\alpha(i)}(x,y) = 1$ on element $1_2 2_1 6_1 5_2$ are obvious. A detail explanation can be found in Wang (1998).

2.2 Numerical integration on manifold element

After manifold elements and displacements function on them are defined, numerical integration on the elements is carried out to obtain element matrix. Usually, there are two kinds of elements in this paper while crack propagation is simulated. One is that the elements share the same domain with the finite meshes and the other is that the corresponding finite meshes, which are

divided by cracks or fractures, produce the manifold elements. For the former one, numerical integration can be done in the same way as in finite element method; whereas for the latter, the shape of the element may be triangle, quadrilateral, pentagon and other ones. Integration on them is dealt with as follows.

If a crack crosses an element from one corner of it as showed in Figure 2a-c, Three cases will appear; and while a crack crosses an element from one side of it as showed in Figure 3a-e five cases are possible. In Figures 2, 3, dash lines represent crack paths. Transform the elements in xy -

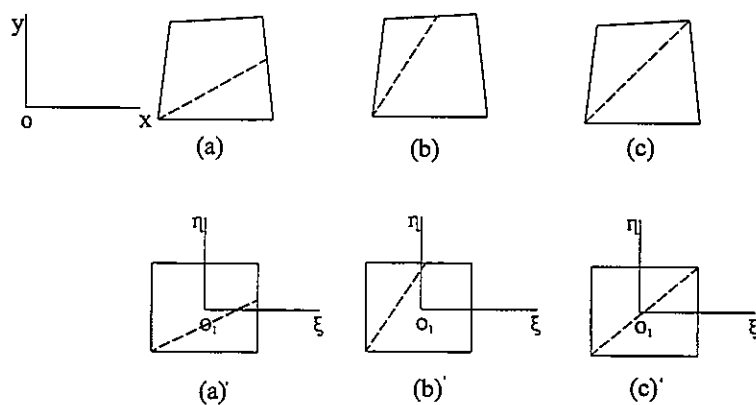


Figure 2. A crack crossing an element and its transformation.

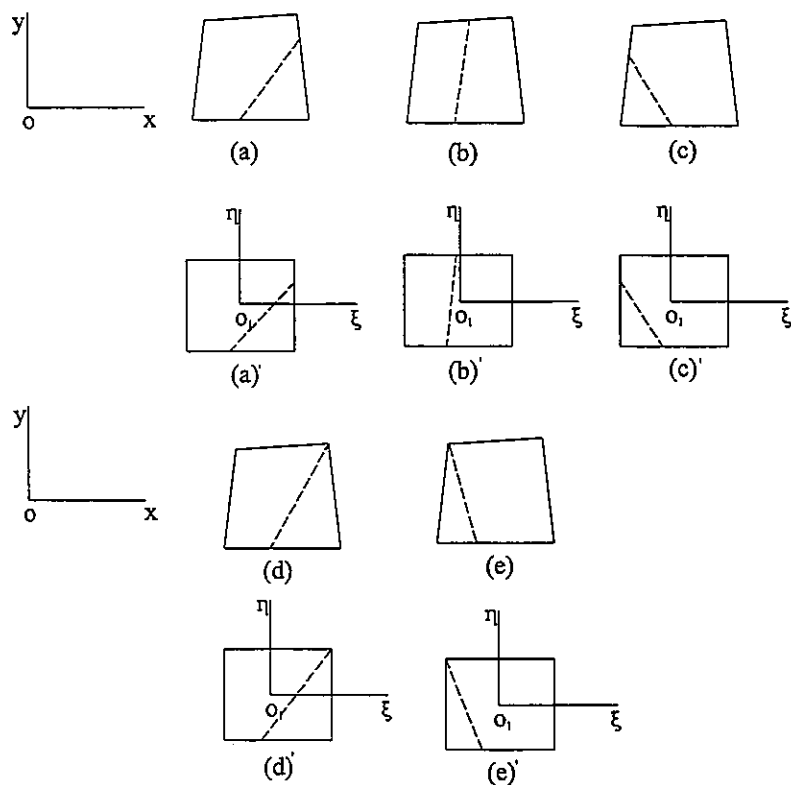


Figure 3. A crack crossing an element and its transformation.

plane into the square $\Omega = [-1, 1] \times [-1, 1]$ in $\xi\eta$ -plane. Their images are shown in Figure 2a'-c' and Figure 3a'-e'. In $\xi\eta$ -plane, further transformation is needed to conduct numerical integration for these elements

For example, two typical elements in Figure 1 are $1_2 2_1 6_1 5_2$ and $1_1 2_1 6_1 5_1$. They correspond to the finite mesh 1265 (Fig.1), and they are formed by a crack propagating from one point of side 12 and ending at a point of side 26 of the mesh 1265. The 2 manifold elements and their shapes in plane $\xi o_1 \eta$ are shown in Figure 4. Pentagon $abdf e$, corresponding to element $1_1 2_1 6_1 5_1$, is divided into 2 quadrilateral $abdc$ and $cdfe$. Each of them is transformed into a square in plane $ro_2 s$ so that Gauss quadrature can be conducted. Numerical integration on the pentagon is the sum of integration on quadrilateral $abde$ and $cdfe$. As for triangle ghi (corresponding to element $1_2 2_1 6_1 5_2$), it is considered as a degenerated quadrilateral and is also transformed into a square on plane $ro_2 s$, therefore, integration can be conducted easily.

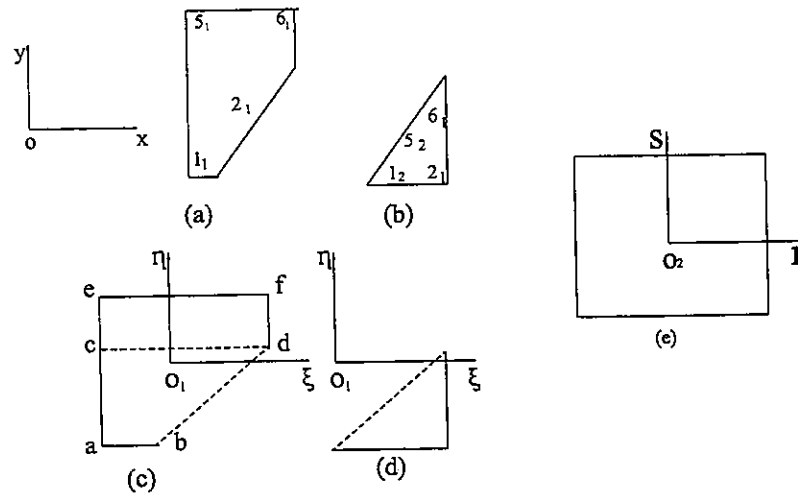


Figure 4. A transformation from $\xi\eta$ -plane to rs -plane

Note that if the finite mesh used as mathematical cover is parallelogram, the crack path, assumed as a line, is also a line after it is transformed from xy -plane into $\xi\eta$ -plane. If it is not, the crack path, even though considered as a line in plane xoy , will not be a line in plane $\xi o_1 \eta$. Hence, there is a little error in the above treatment of integration, but it will be negligible. However, if we think that the image of the crack path in $\xi\eta$ -plane is a line and the crack path is mapped from the dash line in $\xi\eta$ -plane, the above treatment will be all right.

2.3 Crack propagation simulation

The maximum principal stress criterion (Erdogan et al 1963), which states that the crack will propagate in the direction perpendicular to the maximum principal stress, is used while crack propagation is simulated. It can be written as

$$K_{Ic} = K_{eq} = \cos \frac{\theta}{2} (\cos^2 \frac{\theta}{2} - K_2 \sin \theta) \quad (2)$$

Where θ , the propagation angle relative to the current crack segment, can be determined by solving $K_1 \sin \theta + K_2 (3 \cos \theta - 1) = 0$; K_1 and K_2 are stress intensity factor, and they are calculated by a contour integration method (Yang 1996), whose accuracy has been verified by Yang (1996) and Wang (1998).

Once a crack has started to propagate at a given level, stable and unstable propagation will appear. Ingraffea(1985) and Scavia (1995) explained how stable and unstable conditions were judged during simulation. In the processes of crack extension, mathematical covers are kept changeless and physical covers and manifold elements are added. Computer code based on the proposed method was developed, and a flow chart of the program is shown in Figure 5.

3 EXAMPLES OF CRACK PROPAGATION

3.1 A half-disk with a crack

In this example, a half-disk with a crack subjected to a point load is modeled. The setup is showed in Figure 6a. Lim(1993) carried out an experiment on a similar structure. Crack propagation is simulated with plane stress case assumed. The material properties here are $E=10\text{Gpa}$ and $\gamma=0.3$. The supporting distance of the setup is $2s=0.14\text{m}$ and the half-disk has an initial crack length $a=0.028\text{m}$ and radius $r=0.1\text{m}$. The progression of crack propagation at two different stages is shown in Figures 6b,c (The deformation in Figures 6 and 7 is scaled up a little so that crack paths can be seen clearly).

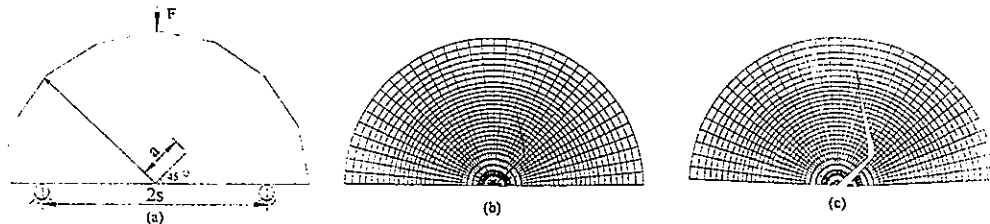


Figure 6. (a) A half-disk with an initial crack subjected to point load, (b) and (c) the progression of crack propagation at two different stages.

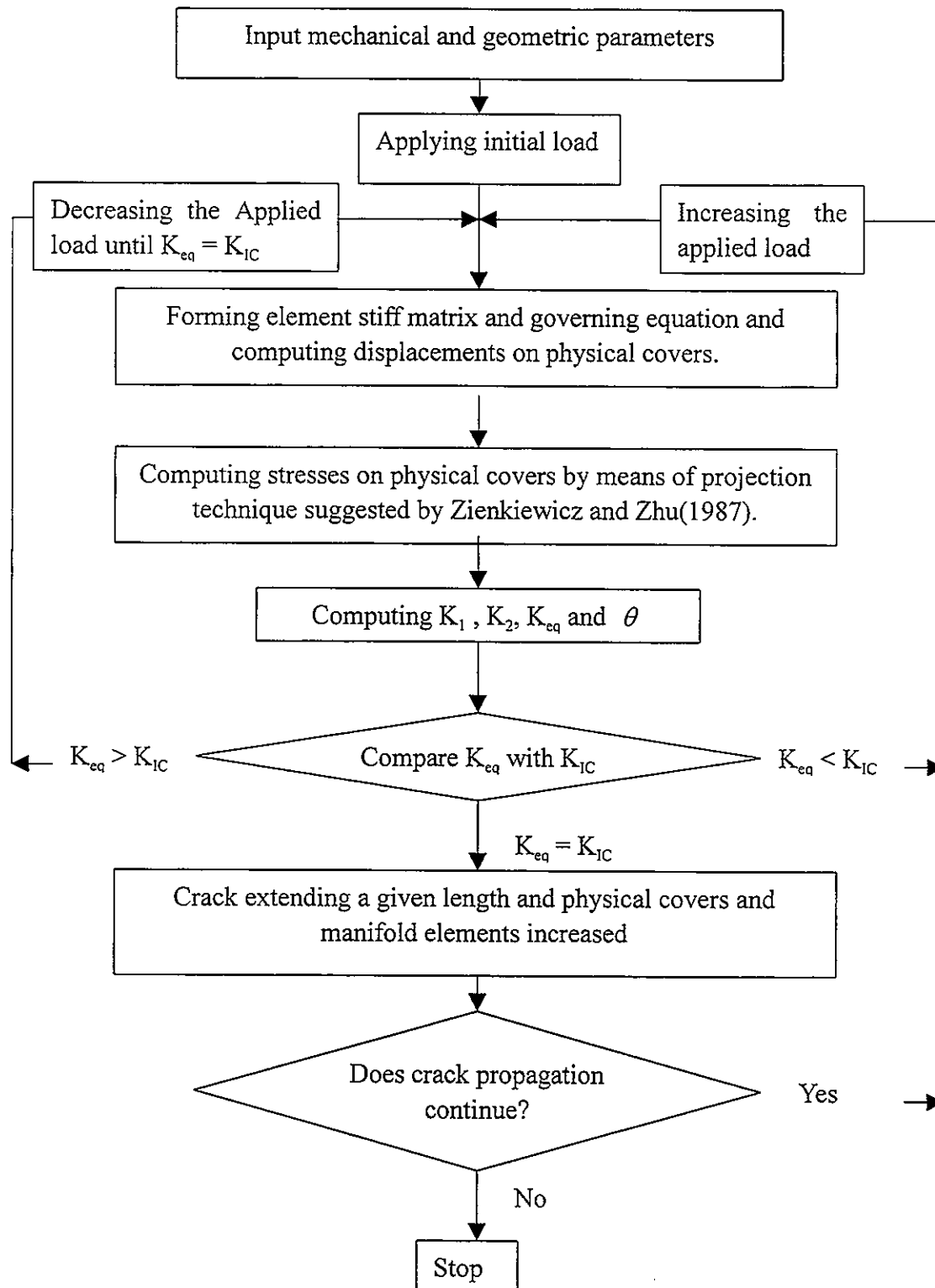


Figure 5. Proposed method

3.2 Three-point-bend specimen with a crack

This example presents a crack growth in a three-point-bend beam as showed in Figure 7a. A plane stress condition is assumed with elastic modules $E=24.8\text{Gpa}$, Poisson ration $\gamma=0.18$ and material toughness $K_{IC}=1.5\text{MPa}\sqrt{m}$. The geometric parameters are $a=80\text{mm}$, $b=50\text{mm}$, $c=30\text{mm}$, $H=300\text{mm}$, $L=900\text{mm}$. Figure 7b shows the evolution of the crack paths. Obviously, the propagating crack goes toward the load point. A diagram of vertical load against loading point displacement is given in Figure 7c. Meanwhile, crack path progression for $b=230\text{mm}$ is shown in Figure 7d. It is reasonable that the farther the loading point is away from the centerline, the more the crack path diverges.

In the above examples, crack growth displays an unstable propagation.

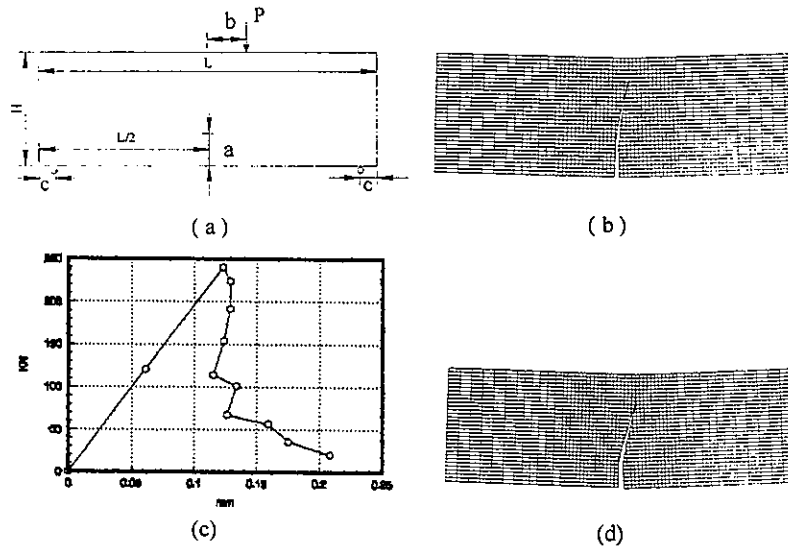


Figure 7. (a) 3-point-bend-beam; (b) Crack path for $b=50\text{mm}$; (c) A diagram of load against load point displacement; (d) Crack path for $b=230\text{mm}$.

During the progression of crack propagation, the calculations are completely automatic in the proposed method. Compared with finite element method, it eliminates the burden associated with remeshing throughout the evolution of the problem; compared with boundary element method, it can apply to complex media. In our opinion, the manifold method has the advantages of both FEM and BEM in modeling crack propagation. In addition, The meshless method (Belytschko, 1996), another recently developed numerical method, also has the great promise in dealing with evolving crack problem, but considerable improvement is required at present.

REFERENCES

- Belytschko, T., Krongauz, Y., Organ, D., Fleming, M. And Krysl, P. 1996. Meshless method: an overview and recent developments. *Comput. Methods Appl. Mech. Engrg.* 139:3-47.
- Erdogan, F. and Sih, G.H. 1963. On the crack extension in plates under plane loading and transverse shear. *J. Basic Engng. Am. Soc. Mech. Engrs.* 85:519-527.
- Ingraffea, A.R. 1985. Fracture propagation in rock. In: *Mechanics of Geomaterials Rock, Concrete, Soils* (Ed, Bazant, Z.P.) Noriwh: John Wiley & Sons Ltd: 219-258.
- Lim, I.L., Johnson, I.W. and Choi, S.K. 1993. Numerical methods in simulating crack propagation of rock. *Computer Methods in Application of Rock Mechanics* (Ed, Ge, X.R.) Wuhan: 289-296.
- Lin, J.S. and Lee, D.H. 1996. Manifold method using polynomial basis functions of any order. *Proc. of the 1st Int. Forum on DDA Simulation of Discontinuous Media*, Bekerley, california, USA:365-372.
- Qiu, X.J. 1996. Manifold method without use of penalty springs. *Proc. of the 1st Int. Forum on DDA Simulation of Discontinuous Media*, Bekerley, california, USA:407-414.
- Scavia, C. 1995. A method for the study of crack propagation in rock structures. *Geotechnique*. 45(3):447-463.
- Shi, G.H. 1991. Manifold method of material analysis. Transaction, *Ninth Proc. of the 1st Int. Forum on DDA Simulation of Discontinuous Media*, Bekerley, california, USA:52-204.
- Shi, G.H. 1996a. Manifold method. *Proc. of the 1st Int. Forum on DDA Simulation of Discontinuous Media*, Bekerley, california, USA:52-204.
- Shi, G.H. 1996b. Simplex Integration for manifold method. *Proc. of the 1st Int. Forum on DDA Simulation of Discontinuous Media*, Bekerley, california, USA:205-249.
- Wang, S.L. and Ge, X.R. 1997. Application of manifold method in simulating crack propagation. *Chinese Journal of Rock Mechanics & Engineering*, 16(5):405-410.
- Wang, S.L. 1998. Numerical manifold method and simulation of crack propagation. [*Ph.D. dissertation*]. Institute of Rock and Soil Mechanics, Chinese Academy of Sciences.
- Wang, S.L. and Ge, X.R. 1998. Analysis of seepage problem with free surface by manifold method. *The 6th National Conference on Numerical and Analytical Methods on Geomechanics*. Guangzhou, PRC:494-497.
- Wang, Z.Y. and Li, Y.P. 1997. Manifold method in large deformation for rock, *Computer Methods and Advances in Geomechanics, ACMAG*. Wuhan, PRC:513-516.
- Yang, X.X., Fan, J.Q. and Kuang, Z.B. 1996. A contour integral method for stress intensity factors of mixed-mode crack. *Computational structural mechanics and applications*. 13:84-89.
- Zienkiewicz, O.C. and Zhu, J.Z. 1987. A simple error estimator and adaptive procedure for practical engineering analysis. *Int. J. Num. Meth. Eng.* 24:237-357.

APPLICATION OF MANIFOLD METHOD TO JOINTED DAM FOUNDATION

Guo-Xin Zhang

River Technology Department, I.N.A. Corporation
Sekiguchi 1-44-10, Bunkyo-ku, Tokyo, 112-8668, Japan

Yasuhito Sugiura

River Technology Department, I.N.A. Corporation
Sekiguchi 1-44-10, Bunkyo-ku, Tokyo, 112-8668, Japan

Kozo Saito

River Technology Department, I.N.A. Corporation
Sekiguchi 1-44-10, Bunkyo-ku, Tokyo, 112-8668, Japan

ABSTRACT: Manifold Method (MM) is a newly developed numerical tool in analyzing both continuous and discontinuous problems. By employing the concept of cover and two sets of meshes, MM can simulate the small and large-scale deformation of materials as well as the failure and movement of block system. In the present paper the original MM is extended by adding the consideration of crack propagation in failure process into the numerical procedure. The extended version of MM is then applied to simulate the initiation and propagation of cracks in dam foundation with weak zone such as faults and joints. The failure process and corresponding bearing capacity are predicted, and the computed results are compared with those of the experiment. It is convinced that the extended version of MM can reproduce the initiation of cracks and the failure process reasonably well.

1. INTRODUCTION

Several numerical methods are used in simulating the failure and response of structure and rock foundation with discontinuities. These methods include the Finite Element Method (FEM), the Boundary Element Method (BEM), the Discrete Element Method (DEM) and the Discontinuous Displacement Analysis (DDA). Although discontinuities in structure and rock mass can be modeled in a discrete manner with FEM and BEM by using special joint elements (such as Goodman Element), it is difficult to describe the discontinuities numerically, and small deformation restriction is usually needed. And also the number of discontinuities that can be handled is limited. Therefore, problems of many discontinuities or large-scale deformation can not be analyzed by such kind of methods. DEM and DDA can be utilized to model the behavior of structure with many discontinuities or block system, but the stress distribution inside the blocks can not be calculated properly, and, therefore, the propagation of cracks through blocks can not be well modeled.

Manifold Method (MM) proposed by Shi in 1991 is a new numerical method. It provides a unified framework for solving problems with both continuous and discontinuous media. The concept and potential application of this method have drawn a great attention from international researchers in engineering fields (Chang et al. 1996, MacLaughlin 1996, Zhang et al. 1997, Chiou et al. 1997, Zhang et al. 1998).

By employing the concept of cover and two sets of meshes, manifold method combined the advantages of FEM and DDA. It can not only deal with discontinuities, contact, large scale deformation and block movement as DDA dose, but also provide the stress distribution inside each block as accurately as FEM can.

In rock foundation or concrete structure, cracks occur usually from weak zone like faults, joints and interfaces of different materials. With the propagation, the cracks break the mass material and lead to the final failure. Modeling the failure must simulate both the opening of existing joints and the fracturing of mass materials. In the present paper, the original manifold method is extended to simulate the failure of existing joints and the propagation of cracks inside blocks. The newly developed code is used to simulate the failure of two dam foundations and the results are compared with those of the experiments.

2. MODELING THE EXISTING JOINT

For an existing joint, there are two possibilities: 1) unfailed, namely the joint can be treated as continuous, and it can transfer both normal and shear stresses, and the displacement is continuous along the joint. 2) failed, that means the joint can only transfer normal compression stress or limited shear stress if the friction angle ϕ is not zero, discontinuity can occurs on two sides of joint.

Modeling of the existing joint considers these two possibilities. Figure 1 shows schematically the treatment of the joint by adding normal and shear springs at the joint. For the former case, if the thickness of joint layer is idealized as zero, there must be no relative normal displacement between two surfaces of the joint since they keep moving together under load. A very hard spring p (penalty) is therefore added in the normal direction to the joint to hold the possible relative normal displacement between two surfaces back to zero. In the tangent direction, however, a small relative shear displacement is usually permitted, especially when a soft layer is included in the joint. This condition is satisfied by adding a comparatively soften shear spring K_s in the tangent direction. For the later case in which joint failed, normal penalty and shear springs are added at the joint when the joint is loaded by compression and the shear stress is less than the friction between two surfaces. If the shear stress is larger than the friction, shear spring is removed and only normal spring is needed. If the joint opens, both normal and shear springs are removed from the joint.

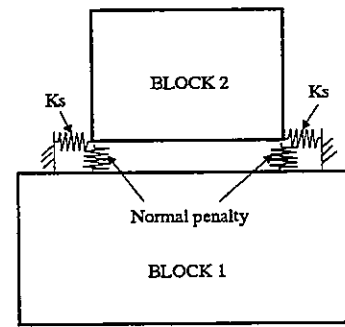


Figure 1. The normal and shear springs of contact blocks

The failure of existing joints follows Mohr-Coulomb's law with three parameters. Taking σ'_y as the normal stress and τ'_{xy} as the shearing stress on a joint, the failure criterion is defined as bellow:

$$\begin{aligned}
 \text{Tensile failure : } & \sigma_1 = T_0. \\
 \text{Shearing failure : } & \frac{(\sigma_1 - \sigma_3)}{2} = C \quad \text{if } \frac{(\sigma_1 + \sigma_3)}{2} > 0 \text{ and } 0 < \sigma_1 < T_0, \\
 & \frac{(\sigma_1 - \sigma_3)}{2} = C \cos \phi - \frac{(\sigma_1 + \sigma_3)}{2} \sin \phi \quad \text{if } \frac{(\sigma_1 + \sigma_3)}{2} < 0 \text{ and } 0 < \sigma_1 < T_0.
 \end{aligned} \tag{1}$$

where T_0 represents the tension strength of joint, C represents cohesion, ϕ is the friction angle.

3. CRACK PROPAGATION IN SOLID BLOCK

When a new crack occurs or an old crack propagates the physical meshes and the mathematical meshes that contain this crack should be regenerated. If no physical cover is broken by the new crack, only the physical meshes need to be reformed, the mathematical meshes keep unchanged. But if the new crack breaks a physical cover into two parts, then a new physical cover is produced, hence both the physical and mathematical meshes must be regenerated.

Figure 2 is given here to illustrate the crack propagation and corresponding regeneration of the physical and mathematical mesh system in the numerical simulation. In Figure 2(a) a new crack ab occurs. Since it does not break the physical cover that contains it into two parts, only physical meshes need to be regenerated by adding ab into the physical meshes. The mathematical meshes keep unchanged. Whereas in Figure 2(b), new occurred crack bc together with the existing crack ab break the cover that covers the area 4-5-8-10-9-6 into two parts as showed by shadow, therefore a new cover 7^1 must be added to the previous physical cover system, and both the physical and mathematical meshes need to be reformed.

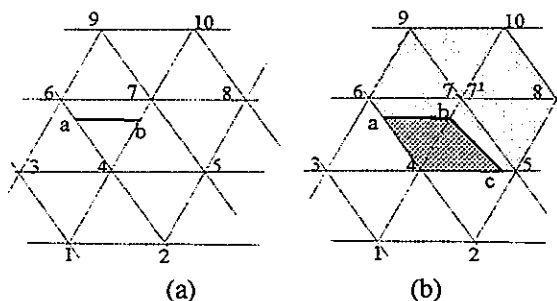


Figure 2. The relationship between new crack and covers

In simulating the failure of solid block, formula (1) is also taken as the failure criterion. But in the present study, it is supposed that cracks can only propagate along the mathematical meshes.

4. FAILURE SIMULATION OF ROCK FOUNDATIONS

The safety of an arch dam depends mainly on the stability of the arch abutments. The stability and bearing capacity of the dam foundation are usually studied by experiment (Iida 1992). In this section the newly extended version of manifold method is applied to analyze the stability and bearing capacity of dam foundation and to simulate their failure process. The numerical results are compared with the experimental ones (Nakamura et al. 1964, Takano 1962).

4.1 Failure Simulation of an Arch Dam Abutment with Faults

Figure 5 shows the model of the abutment of an arch dam in Japan. The location of existing faults is denoted in this figure as F. 1, F. 7 etc. The stability and bearing capacity of this abutment before and after strengthened by concrete wall were studied by experiment in Public Works Research Institute Ministry of Construction,

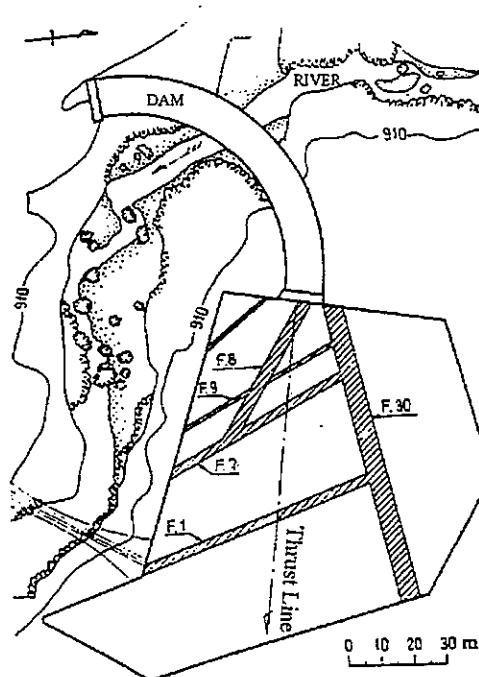


Figure 3. Model of an arch dam abutment

Japan (Nakamura et al. 1964). Here, by using the same model, the failure process and bearing capacity are simulated by manifold method.

Table 1. Fault width and parameters

Fault	Width (m)	E (kg/cm ²)	T ₀ (kg/cm ²)	C (kg/cm ²)	ϕ
F-30	5.0	3320	0.52	1.7	30
F-1	3.0	16530	2.87	9.0	30
F-7	2.0	22440	3.89	13.0	30
F-8	3.0	22440	3.89	13.0	30
F-9	0.5	16530	2.87	9.0	30
Good rock		68240	12.9	40.0	30
Concrete wall		267000	29.0	70.0	30

The width of faults and the controlling parameters used in the calculation are listed in Table 1 (Nakamura et al. 1964, Takano 1962). The arch thrust force along the direction of arch axis was taken as $P=5200$ ton/m, calculated according to water pressure and temperature change. The mathematical and physical meshes used in MM simulation are shown in Figure 4, with thin lines referring to the mathematical meshes and thick lines referring to the physical meshes.

Three cases are calculated in the numerical simulation: (1) no foundation treatment, (2) foundation strengthened by 2m thick concrete wall, (3) foundation strengthened by 3.5m thick concrete wall.

Figure 5 shows the experimental result of failing process and bearing capacity of the abutment with no foundation treatment. Numbers in this figure denote the order of crack occurrence, and the corresponding bearing capacity is listed in Table 2.

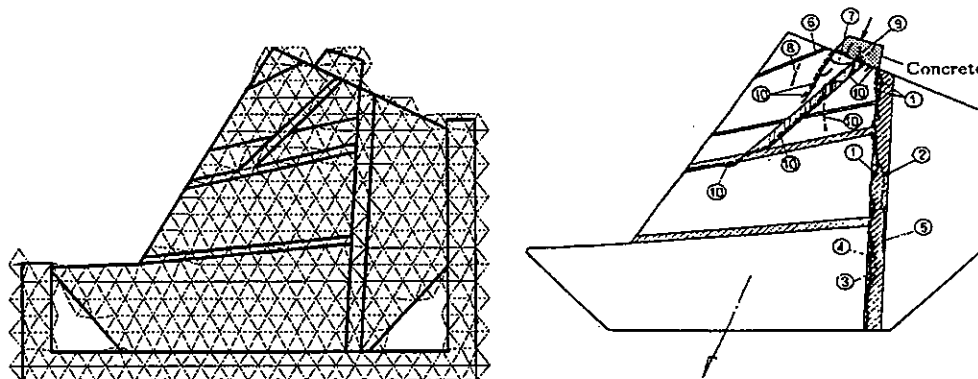


Figure 4. Mesh system used in MM. Figure 5. Experimental result of case 1

Table 2. Bearing capacity in case 1 of experiment

Number	Bearing capacity ($\times P$)	Number	Bearing capacity ($\times P$)
1	0.5	6	1.1
2	0.6	7	1.0
3	0.6	8	1.15
4	0.7	9	1.20
5	0.9	10	1.20

Figure 6 shows the calculating result of the abutment failure in case 1. Cracks start occurring at the fault of F-30, as depicted in Figure 6(a) by thick line, because the material strength here is much smaller than that in the other areas. With the increase of load from $1.0P$ in Figure 6(b) to $1.3P$ in Figure 6(d), the abutment fails progressively at the fault location of F-7, F-8 and F-9. The computed failure process and the corresponding bearing capacity agree reasonably well with the experiment.

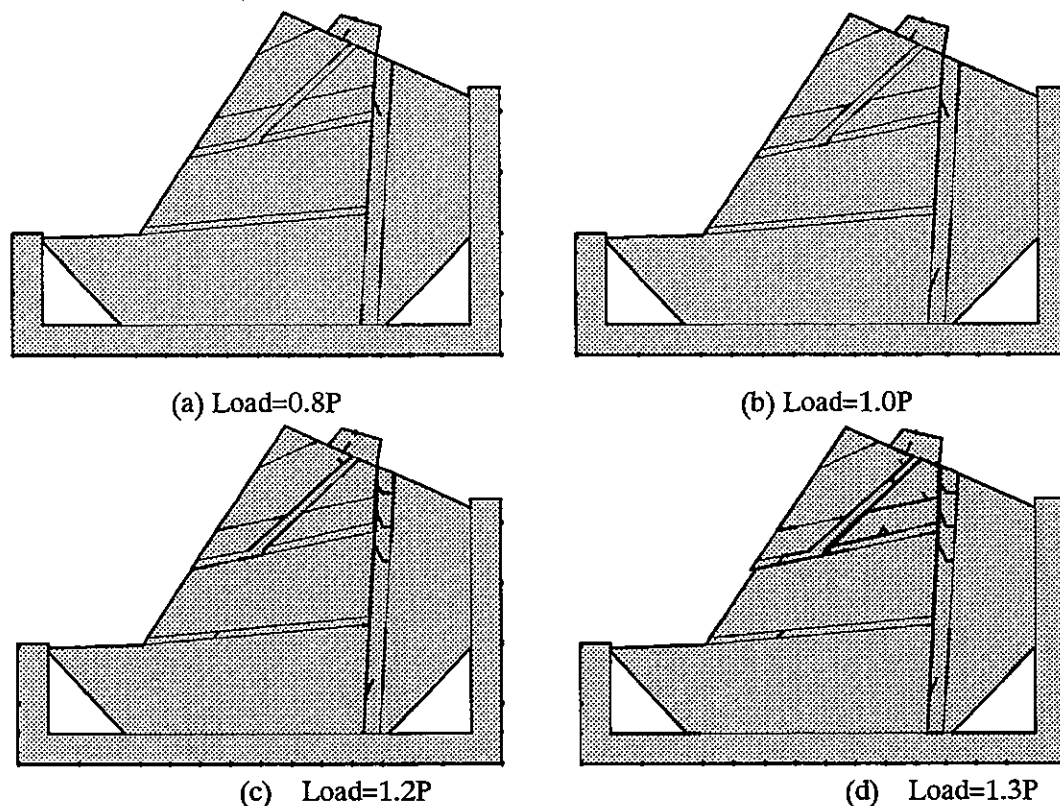


Figure 6. Computed failure process of abutment in case 1

Figure 7 gives the experimental result of the abutment failure process after strengthened by 2m thick concrete wall. Bearing capacity of the abutment obtained by experiment is listed in Table 3. From the results it can be seen that the bearing capacity of the foundation increases from $1.2P$ in case 1 to $2.8P$ after foundation treatment.

Table 3. Bearing capacity in case 2 of experiment

Number	Bearing capacity ($\times P$)	Number	Bearing capacity ($\times P$)
1~5	1.0	10	1.65
7	1.0	12~13	2.65
8	1.25	14~15	2.70
9	1.40	16	2.80

Figure 8 shows the calculated result of failure process for case 2. In this case cracks start occurring at the fault F-30 when load reaches $0.6P$, as shown in Figure 8(a). In Figure 8(b) when load reaches $2.0P$, almost all the area of F-30 fails, and faults of F-8 and F-9 start opening. When load further increase to $2.6P$, shown in Figure 8(c), the concrete wall begins to fail leading to the failure of the foundation along F-30 to F-1. Following the failure of foundation, blocks lose their stability and begin to move. Figure 8(d) shows the movement of blocks after the foundation failure.

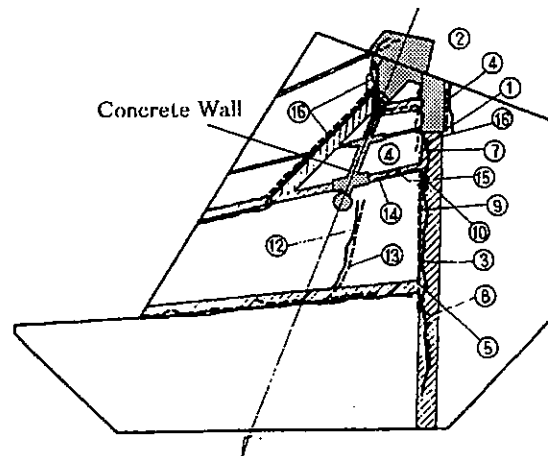


Figure 7. Experimental result of the abutment failure in case 2

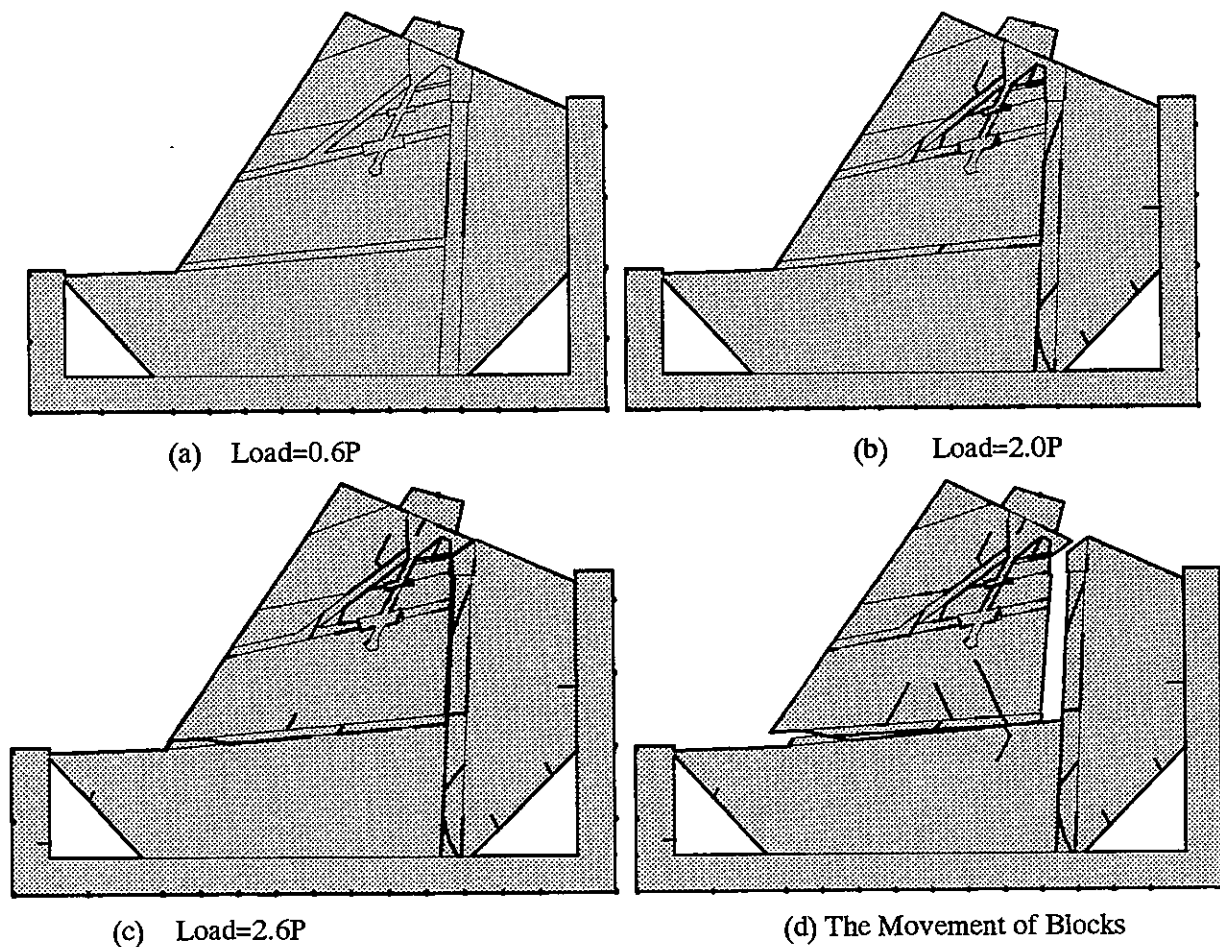


Figure 8. Computed failure process of the abutment in case 2

Experimental result of the abutment failure for case 3 is given in Figure 9 and the corresponding bearing capacity is listed in Table 4. The bearing capacity increases to 4.0P due to the treatment of foundation by 3.5m thick concrete wall. The simulation result for the same case is shown in Figure 10. The prediction of bearing capacity is slightly larger than the experimental one. The failure process is similar to the experiment.

Table 4. Bearing capacity in case 3

Number	Bearing capacity ($\times P$)	Number	Bearing capacity ($\times P$)
1	1.3	7~10	2.5
2	1.5	11	3.25
3	1.75	12~13	3.5
4~5	1.8~1.9	14	3.5~4.0
6	2.25	15~18	4.0

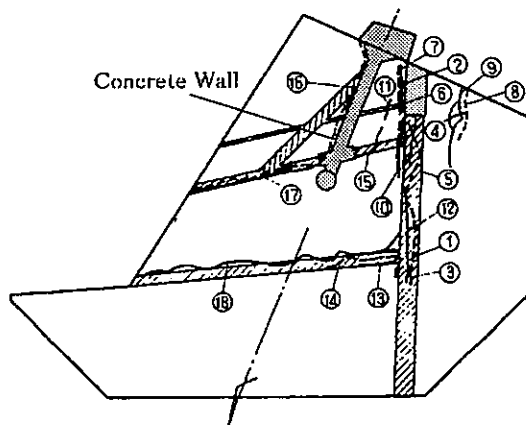


Figure 9. Experimental result after the foundation treatment by 3.5m concrete wall

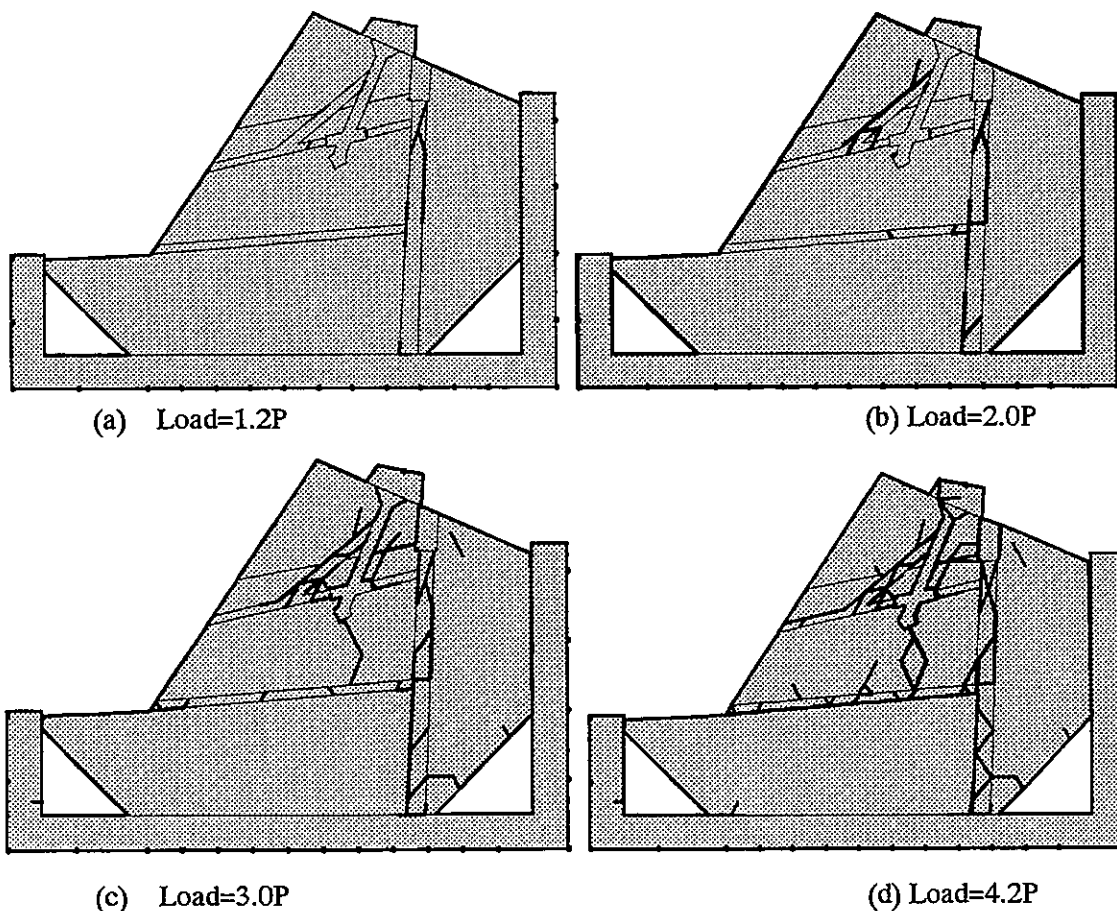


Figure 10. The failure of abutment after strengthened by 3.5m concrete wall

4.2 Failure of a Dam Abutment with a Set of Joints

Second application of the extended MM is made in simulating the failure of an arch dam foundation with a set of joints. The experiment was carried out by Takano (1962). Figure 11 shows the diagram of the arch dam foundation. A set of joints exists paralleling to the direction of thrust force. Water pressure acts at the upper surface of the arch. The controlling parameters in the experiment are listed in Table 5. The experimental result showed that the abutment failed as shown in Figure 12 when the water pressure $q=9.3\text{kg/cm}^2$.

Table 5. Calculation parameters

	E (kg/cm^2)	ν	Compression Strength (kg/cm^2)	T_0 (kg/cm^2)	C (kg/cm^2)	ϕ
Arch	200000	0.2	250	-----	-----	-----
Left Abutment	20000	0.2	60	6	20	30
Right Abutment	20000	0.2	30	3	10	30
Joint	-----	-----	-----	0.6	1.2	18

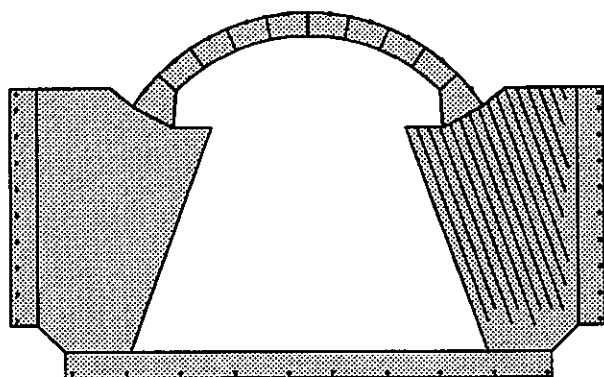


Figure 11. Abutment with one set of joints

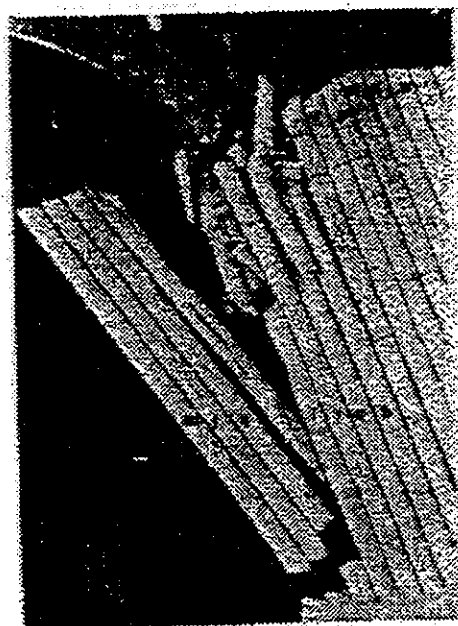


Figure 12. Experimental result

Figure 13 gives the simulating result by MM. Because the strength of joint is less than that of the mass material, some joints firstly open because of the tension and shear failure {Fig. 13 (a)}. The blocks contacting with the arch mainly support the load conducted by arch, and the principal stress is parallel to the thrust direction {Fig. 13 (a)}. This point is same with the experimental conclusion. When the pressure on arch increases to 7.0 kg/cm^2 , some cracks occur in mass blocks {Fig.13 (b)}, and when the load reaches to 7.5 kg/cm^2 , the foundation fails {Fig. 13 (c), (d)}. The bearing capacity obtained by MM is less than the experimental result and the failure pattern has some differences. In the experiment, the failure is mainly caused by compression near the arch abutment, but in MM analysis, the failure is mainly caused by shear.

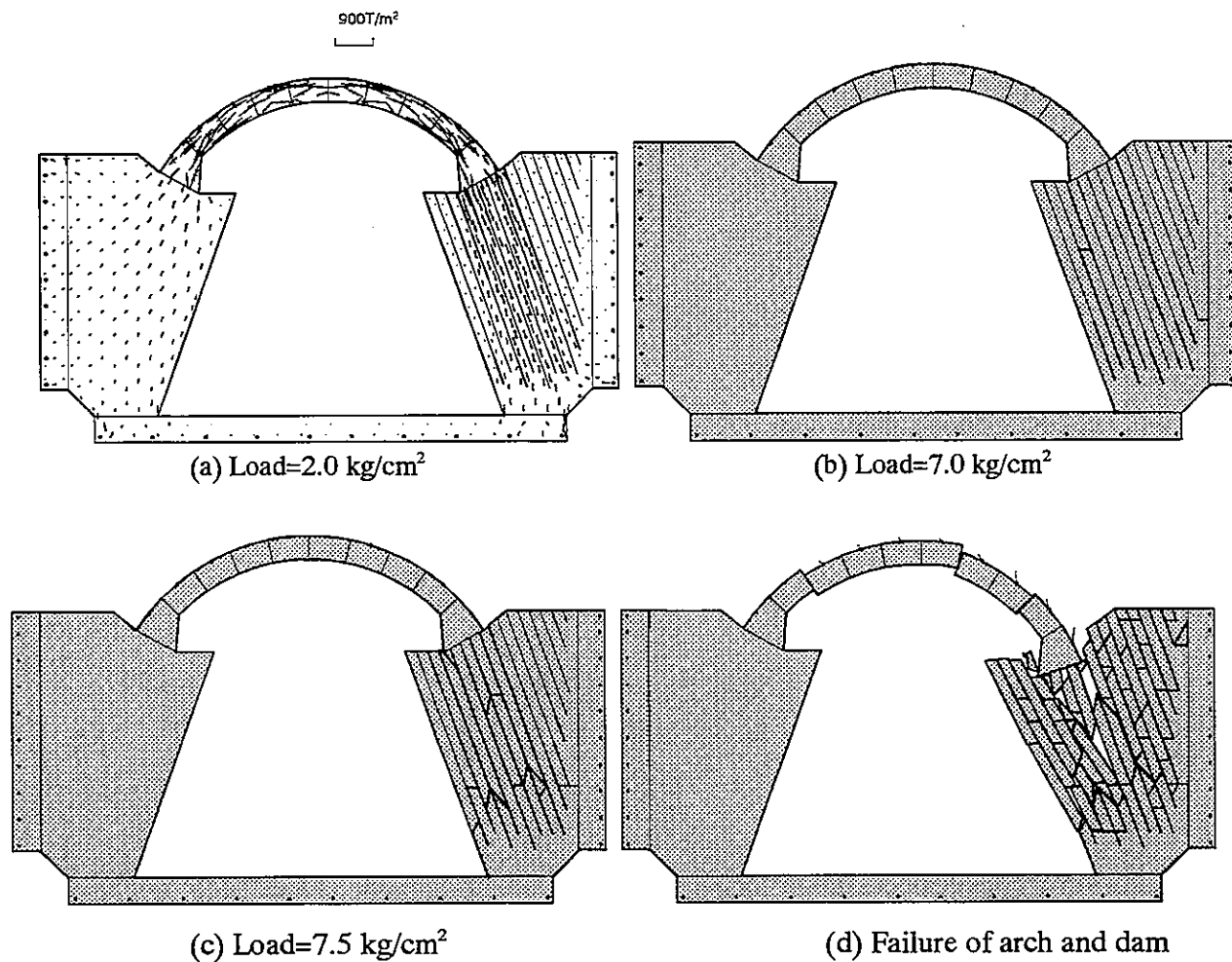


Figure 13. Computed failure of arch foundation by MM

5. CONCLUSION

Manifold method was extended by adding the consideration of crack propagation in failure process into the numerical procedure in the present paper. The extended version of MM is capable of dealing with the failure of structure or foundation with joints or faults. The failure of foundation with discontinuities usually begins from weak places like joints or faults, and then breaks the mass material to lead to the final failure. The extended MM can simulate this process very well. The numerical simulation proved the effect of foundation treatment and the prediction of bearing capacity is also in good agreement with the experiment results. From engineering practical point of view, the numerical method developed in the present study would be a useful tool in simulating the failure process of structure with discontinuities.

The numerical result is mainly affect by the parameters used in calculation, further studies should be performed on characteristics of parameters.

ACKNOWLEDGMENT: The author would like to thank Dr. G. H. Shi and Professor Yuzo OHNISHI for suggestions.

REFERENCE

- Chang, C. T. 1996. Nonlinear level manifold method. *Working Forum on the Manifold Method of Material Analysis*. Jenner, California, U. S. A., Vol. 1, pp. 127-146.
- Chiou, Y. J. 1997. Crack propagation using manifold method. *Proceedings of the Second International Conference on Analysis of Discontinuous Deformation*. Kyoto Japan, pp.298-308.
- Iida, R. 1992. *Design method of concrete dam*. GIHODO Press.
- MacLaughlin, M. 1996. Manifold application: tunnel roof deflection. *Working Forum on the Manifold Method of Material Analysis*. Jenner, California, U. S. A., Vol. 1, pp. 241-244.
- Nakamura, K., Iida, R. and Tsutaya, T. 1964. Model study on foundation rocks of Kawamata dam. Report of the Public Works Research Institute Ministry of Construction. Vol. 120, No.78, pp. 1-11.
- Shi, G. H. 1991. Manifold method of material analysis. *Proc. Ninth army conference on applied mathematics and computing*. Minneapolis, Minnesota, U. S. A., pp. 51-76, June 18-21.
- Shi G. H. 1996. Manifold method, *Discontinuous Deformation Analysis (DDA) and Simulations of Discontinuous Media*, pp. 52-204, TSI Press.
- Takano, M. 1962. Studies on experimental method of measuring safety of arch dam foundation. *Transactions of the Japan Society of Civil Engineers*. No. 78, pp. 43-69.
- Zhang, G. X., Sugiura Y. and Hasegawa, H. 1997. Crack propagation and thermal fracture analysis by manifold method. *Proceedings of the Second International Conference on Analysis of Discontinuous Deformation*. Kyoto Japan, pp.282-297.
- Zhang, G. X., Sugiura Y. and Saito, K. 1998. Failure simulation of foundation by manifold method and comparison with experiment. *Journal of Applied Mechanics (JSCE)*. Vol. 1, pp. 427-435.

Manifold Method in Saturated-unsaturated Unsteady Groundwater Flow Analysis

Yuzo OHNISHI¹, Makoto TANAKA¹, Tomofumi KOYAMA¹ and Ko MUTOH²

¹School of Civil Engineering, Kyoto University, Kyoto, Japan

²Kyoto Branch, Hazama Co., Kyoto, Japan

Abstract: In this paper a new technique was implemented in Manifold Method (MM) to solve groundwater flow problems. MM was originally developed for analysis of solid deformation. Here, saturated-unsaturated unsteady groundwater flow problem in porous medium was solved by MM in the way similar to the stress-deformation analysis. Only water pressure or potential is unknown in groundwater flow analysis which uses time-dependent continuity equation and nonlinear Darcy's law. The time-independent terms of the governing equation are discretized using MM while backward finite difference scheme is used to take into account time domain. The authors have developed an analysis code and applied it to some example problems. The code showed a power of MM in which the mesh generation was very easy. The results of the analysis by MM were compared with ones by the conventional FEM.

1 INTRODUCTION

When one deal with the flow of groundwater through porous media from an analytical viewpoint, the behavior of groundwater is modeled as a boundary-value problem. The typical methods to solve the boundary-value problem are summarized as follows: 1) Direct method 2) Graphical method 3) Numerical method.

The first method corresponds to the methodology to obtain the solution directly by solving the governing equation under some limited very simple boundary conditions. The second method corresponds to the methodology to solve problems graphically by drawing both equi-potential lines and flow lines, which is so-called flow net. However, the solution by means of the graphical method heavily depends on individual skill and experience, and the method is applicable only to simple problems. Therefore, at present, both methods mentioned above are not common.

On the other hand, the third method corresponds to the methodology to obtain an approximate solution using numerical method such as Finite Differential Method (FDM), Finite Element Method (FEM), Boundary Element Method (BEM) and so on. At present, these numerical methods are the most common.

In the seepage analysis, FEM is the most popular. Since the analyzed geotechnical problems become more large-scale and complex these days, however, the finite element mesh generation, which is related to the shape of the model boundary, becomes more and more difficult. So making finite element model takes us a lot of time and effort. MM, which uses the independent mathematical and physical meshes, can use a very simple mesh, which will solve this problem.

2 FORMULARIZATION BY MANIFOLD METHOD

2.1 Governing Equation of Saturated-unsaturated Unsteady Groundwater Flow

Akai *et al.* (1977) derived the governing equation of the saturated-unsaturated unsteady flow problem. Followings are re-formulation by the authors.

Assume that the density of the water is constant, continuity equation is expressed as follows:

$$-v_{i,j} = \partial\theta/\partial t \quad (1)$$

And the Darcy's law in saturated-unsaturated area is expressed as follows:

$$v_i = -K_r(\psi)K_{ij}h_{,j} \quad (2)$$

$$h = \psi + x_3 \quad (3)$$

From these equations, we get

$$\{K_r(\psi)K_{ij}h_{,j}\}_{,i} = \partial\theta/\partial t \quad (4)$$

where v_i is the velocity of the flow in x_i -direction, θ is the volumetric water content, $K_r(\psi)$ is the relative permeability, K_{ij} is permeability tensor of saturated state, h is the total head, ψ is the pressure head and x_3 is the gravitational potential. Let n the porosity of the medium and S_w the degree of saturation,

$$\theta = nS_w \quad (5)$$

Hence,

$$\frac{\partial\theta}{\partial t} = \frac{\partial}{\partial t}(nS_w) = \frac{d}{d\psi}(nS_w)\frac{\partial\psi}{\partial t} = \left\{S_w \frac{dn}{d\psi} + n \frac{dS_w}{d\psi}\right\} \frac{\partial\psi}{\partial t} \quad (6)$$

Assume that porosity change is not caused by the pressure change in unsaturated area, $dn/d\psi$ is 0, and $dS_w/d\psi$ has some non-zero value. While, in the saturated area, S_w is always 1, and $dn/d\psi$ has some non-zero value. So we get the following equation, substituting Eqs.(6) and (3) into Eq.(4).

$$\{K_r(\psi)K_{ij}(\psi + x_3)_{,j}\}_{,i} = \{c(\psi) + \alpha S_w\} \partial\psi/\partial t \quad (7)$$

where $S_s = dn/d\psi$ is the specific storage, $c(\psi) = d\theta/d\psi$ is the specific capacity and α is 1 in saturated area ($\psi \geq 0$) and is 0 in unsaturated area ($\psi < 0$). Eq. (7) is the governing equation. In the unsaturated area, ψ and θ have a relationship. The functional relationship between ψ and θ (so-called water retention curve) is shown in Figure 1. As seen from Figure 1, θ tend to become constant which is equal to n , and K_r is 1 in the saturated area. Generally, water retention curve follows the different path in the saturation and dewatering processes, but in this study, we assume that water retention curve follows the same path.

2.2 Discretization of Governing Equation

If there are n physical covers or nodes in the manifold, the governing equation (simultaneous) equation becomes Eq. (8)

$$\begin{bmatrix} K_{11} & K_{12} & \cdots & K_{1n} \\ K_{21} & K_{22} & \cdots & K_{2n} \\ \vdots & \vdots & \ddots & \vdots \\ K_{n1} & K_{n2} & \cdots & K_{nn} \end{bmatrix} \begin{Bmatrix} H_1 \\ H_2 \\ \vdots \\ H_n \end{Bmatrix} = \begin{Bmatrix} Q_1 \\ Q_2 \\ \vdots \\ Q_n \end{Bmatrix} \quad (8)$$

In the deformation analysis, the matrix in the left-hand side and the vector in the right-hand are called stiffness matrix and external force vector respectively. In case of seepage problem, these are called permeability matrix and flux vector.

In MM, global stiffness matrix and global external force vector are derived from the principle of minimum potential energy. Physically, energy means "the ability to do work", but it can be thought that it is potential of force. Extending this idea, it is possible to show "potential" of velocities for element permeability, point flow, inflow/outflow, and to derive global permeability matrix in seepage problem. In this case, potential does not necessarily mean energy in terms of physics, which causes no mathematical problem.

2.3 Approximation functions

Approximation function is independent from the material boundary in MM. Even if the material occupies only a part of the element, approximation function is still the same.

For a triangular element (cover, or mathematical mesh), let the coordinate $i_i(x_i, y_i)$ for each nodes $i = 1, 2, 3$, and corresponding nodal heads $h_i (i = 1, 2, 3)$ are described as follows.

$$\begin{array}{ll} \text{coordinate} & \rightarrow \text{hydraulic head} \\ i_1 : (x_1, y_1) & \rightarrow h_1 \\ i_2 : (x_2, y_2) & \rightarrow h_2 \\ i_3 : (x_3, y_3) & \rightarrow h_3 \end{array}$$

The hydraulic head h in the element is described as follows.

$$h = a + bx + cy \quad (9)$$

where a, b, c are unknown coefficients. The nodal heads are

$$\{H_e\} \equiv \begin{Bmatrix} h_1 \\ h_2 \\ h_3 \end{Bmatrix} = \begin{bmatrix} 1 & x_1 & y_1 \\ 1 & x_2 & y_2 \\ 1 & x_3 & y_3 \end{bmatrix} \begin{Bmatrix} a \\ b \\ c \end{Bmatrix} \quad (10)$$

2.4 Element Permeability Matrix

In FEM, the integration domain of the permeability matrix is the whole element that usually has a boundary. In MM, the domain is physical cover, which might be only a part of the element.

In case of isotropic medium, Darcy's law is described as following equation, same as FEM.

$$\begin{Bmatrix} v_x \\ v_y \end{Bmatrix} = \begin{bmatrix} k & 0 \\ 0 & k \end{bmatrix} \begin{Bmatrix} i_x \\ i_y \end{Bmatrix} = [k_e] \begin{Bmatrix} i_x \\ i_y \end{Bmatrix} \quad (11)$$

Where $k(=K_r(\psi)K)$ is the permeability of the element. And

$$h = \{f_1 \ f_2 \ f_3\} \{h_1 \ h_2 \ h_3\}^T = \{f_1 \ f_2 \ f_3\} \{H_e\} \quad (12)$$

$$\begin{Bmatrix} i_x \\ i_y \end{Bmatrix} = - \begin{Bmatrix} \partial h / \partial x \\ \partial h / \partial y \end{Bmatrix} \quad (13)$$

where

$$\{f_1 \ f_2 \ f_3\} = \begin{bmatrix} 1 & x & y \end{bmatrix} \begin{bmatrix} f_{11} & f_{12} & f_{13} \\ f_{21} & f_{22} & f_{23} \\ f_{31} & f_{32} & f_{33} \end{bmatrix} \quad (14)$$

$$\begin{bmatrix} f_{11} & f_{12} & f_{13} \\ f_{21} & f_{22} & f_{23} \\ f_{31} & f_{32} & f_{33} \end{bmatrix} = \begin{bmatrix} 1 & x_1 & y_1 \\ 1 & x_2 & y_2 \\ 1 & x_3 & y_3 \end{bmatrix}^{-1} \quad (15)$$

Hence,

$$\begin{Bmatrix} i_x \\ i_y \end{Bmatrix} = \begin{bmatrix} \partial f_1 / \partial x & \partial f_2 / \partial x & \partial f_3 / \partial x \\ \partial f_1 / \partial y & \partial f_2 / \partial y & \partial f_3 / \partial y \end{bmatrix} \begin{Bmatrix} h_1 \\ h_2 \\ h_3 \end{Bmatrix} = \begin{bmatrix} f_{21} & f_{22} & f_{23} \\ f_{31} & f_{32} & f_{33} \end{bmatrix} \begin{Bmatrix} h_1 \\ h_2 \\ h_3 \end{Bmatrix} \quad (16)$$

Now we define $[B_e]$ as follows.

$$[B_e] = - \begin{bmatrix} f_{21} & f_{22} & f_{23} \\ f_{31} & f_{32} & f_{33} \end{bmatrix} \quad (17)$$

Then, we can express hydraulic gradient as follows.

$$\begin{Bmatrix} i_x \\ i_y \end{Bmatrix} = [B_e] \{H_e\} \quad (18)$$

The potential Π_e of the element e is

$$\Pi_e = \iint_A \frac{1}{2} (i_x v_x + i_y v_y) dx dy \quad (19)$$

Here, the integration should be done over the whole area A where the material (physical domain) occupies in the element.

$$\begin{aligned} \Pi_e &= \iint_A \frac{1}{2} \begin{Bmatrix} i_x & i_y \end{Bmatrix} \begin{Bmatrix} v_x \\ v_y \end{Bmatrix} dx dy \\ &= \iint_A \frac{1}{2} \{H_e\}^T [B_e]^T [k_e] [B_e] \{H_e\} dx dy \\ &= \frac{1}{2} \{H_e\}^T \left[\iint_A [B_e]^T [k_e] [B_e] dx dy \right] \{H_e\} \\ &= \frac{1}{2} \{H_e\}^T (S^e [B_e]^T [k_e] [B_e]) \{H_e\} \end{aligned} \quad (20)$$

Where S^e means area of the element.

From the principle of minimum potential energy, the permeability matrix is

$$K_{ij} = \frac{\partial^2 \Pi_e}{\partial h_i \partial h_j} \quad (21)$$

then

$$S^e [B_e]^T [k_e] [B_e] = S^e \begin{bmatrix} f_{21} & f_{31} \\ f_{22} & f_{32} \\ f_{23} & f_{33} \end{bmatrix} \begin{bmatrix} k & 0 \\ 0 & k \end{bmatrix} \begin{bmatrix} f_{21} & f_{22} & f_{23} \\ f_{31} & f_{32} & f_{33} \end{bmatrix} \quad (22)$$

Here

$$S^e [B_r]^T [k_e] [B_s] \rightarrow [K_{i(r)j(s)}] \quad r, s = 1, 2, 3 \quad (23)$$

$$i(l) = \begin{cases} i_1, l = 1, \text{ first node} \\ i_2, l = 2, \text{ second node} \\ i_3, l = 3, \text{ third node} \end{cases}$$

2.5 Other Vectors

Other vectors can be given using the principle of minimum potential energy as well.

• Point flow vector

$$\Pi_Q = -Qh = -\{H_e\}^T \{f_1 \ f_2 \ f_3\}^T Q \quad (24)$$

$$Q_i = \partial \Pi_Q / \partial h_i \quad (25)$$

• Inflow/outflow vector

$$\Pi_q = -\iint_A h q dx dy = -\{H_e\}^T \left| \iint_A \{f_1 \ f_2 \ f_3\}^T dx dy \right| q \quad (26)$$

$$Q_i = \partial \Pi_q / \partial h_i \quad (27)$$

2.6 Treatment of Time-independent Terms and Unsaturated Area

In this study, it is assumed that element values K_{ij}^e and S_s^e are constant in each elements and

$K_r^e(\psi)$ and $c^e(\psi)$ are the mean of the 3 nodal values respectively as follows.

$$K_r^e(\psi) = \{ (K_r(\psi))_1 + (K_r(\psi))_2 + (K_r(\psi))_3 \} / 3 \quad (28)$$

$$(c(\psi) + \alpha S_s)^e = \{ (c(\psi) + \alpha S_s)_1 + (c(\psi) + \alpha S_s)_2 + (c(\psi) + \alpha S_s)_3 \} / 3 \quad (29)$$

$$\frac{1}{\Delta t} S^e (c + \alpha S_s)^e \begin{bmatrix} 1 & 0 \\ 0 & 1 \end{bmatrix} \rightarrow [K_{i(r)j(s)}] \quad r, s = 1, 2, 3 \quad (30)$$

$$\frac{1}{\Delta t} S^e (c + \alpha S_s)^e h \rightarrow \{Q_{i(r)}\} \quad r, s = 1, 2, 3 \quad (31)$$

In this study, the backward finite difference method is used for discretization of time. The governing equation becomes Eq. (32) using the backward finite difference for time.

$$\left(A_{nm}^{k+\frac{1}{2}} + \frac{1}{\Delta t^k} F_{nm}^{k+\frac{1}{2}} \right) h_m^{k+1} = Q_n^{k+\frac{1}{2}} + \frac{1}{\Delta t^k} F_{nm}^{k+\frac{1}{2}} h_m^k \quad (32)$$

$$\Delta t^k = t^{k+1} - t^k \quad (33)$$

3 TREATMENT OF FIXED HEAD BOUNDARY

In MM, there are two ways to fix the hydraulic head on certain boundaries. One is penalty method, the other is node shift method.

The heads at some points in the element are fixed to certain value h_0 . In MM, mathematical mesh is independent from physical mesh, so nodes are not always on the material boundary. Then, the hydraulic head is not fixed to certain value, and freedom degree of the system does not decrease, which is different from FEM. So we arrange the fixed head point inside the element, give the penalty for the head change at fixed head point, and consequently control the head change. We call this way penalty method.

Displacement in the deformation problems is equal to hydraulic head in the seepage problem. So, we apply penalty method to the head change. The potential Π_f due to the head change is expressed as follows.

$$\Pi_f = \frac{p}{2} (h - h_0)^2 = \frac{p}{2} \begin{Bmatrix} h_1 - h_0 \\ h_2 - h_0 \\ h_3 - h_0 \end{Bmatrix}^T \begin{Bmatrix} f_1 \\ f_2 \\ f_3 \end{Bmatrix} \{f_1 \quad f_2 \quad f_3\} \begin{Bmatrix} h_1 - h_0 \\ h_2 - h_0 \\ h_3 - h_0 \end{Bmatrix} \quad (34)$$

where p is penalty. The larger the penalty is, the smaller the head change is. From the principle of minimum potential energy, the permeability matrix is

$$K_{ij} = \frac{\partial^2 \Pi_f}{\partial h_i \partial h_j} \quad (35)$$

However, penalty method has some problems. Firstly, there is no definite basis how large the penalty for the head change should be. Secondly, in the seepage problems, unknown value (hydraulic head) varies in a wide range, differently from the deformation problems. So the analysis results may have non-negligible difference in cases that fixed head points are inside the element and on the material boundary. Figure 2 shows this problem.

Then we modified the mathematical mesh so that we can give the boundary conditions on the material boundary as it is done in FEM. Firstly, regular mathematical mesh was made which is independent on the physical mesh. Secondly, some nodes of the mathematical mesh were selected which were near the material boundary where the fixed head boundary conditions were given. Thirdly, these nodes were moved on the boundaries as shown in Figure 3. We call this method node shift method. In this method, the value of the hydraulic head can be given at the nodes that are on the material boundary. Consequently, the freedom degree of the global system decreases. Node shift method has an advantage that the total dimension of the governing equation is reduced. On the contrary, it may be a disadvantage that the shape of the mathematical mesh near the material boundary becomes complex. This problem will be an obstacle, when we develop 3-dimensional MM.

4. EXAMPLES

To verify the formulation and the analysis code developed by the authors, some simple example problems were analyzed.

4.1 1-dimensional Saturated Steady Seepage Analysis

Firstly, the authors analyzed 1-dimensional saturated steady seepage problem shown in Figure 4. The length of the analyzed model is d_0 . Hydraulic heads were fixed to h_0 and 0 at upstream and downstream boundaries respectively. The theoretical solution of this problem is as follows.

$$h(x)/h_0 = -x/d_0 + 1 \quad (36)$$

Figures 5 and 6 show the comparison of the calculated results and the theoretical solution, where Figure 5 shows the analysis result by penalty method and Figure 6 shows the one by node shift method. In this problem, calculated results correspond to the theoretical solution very well in both methods.

4.2 1-dimensional Saturated Unsteady Seepage Analysis

Next, the authors analyzed 1-dimensional saturated unsteady seepage to verify that this code can analyze unsteady problem. The problem is shown in Figure 7. The length of the model is d_0 . Initially, hydraulic head is 0 in the whole area, and it is fixed to h_0 on the left end and 0 on the right at $t = 0$. The theoretical solution of this problem is shown as follows.

$$\frac{h(x,t)}{h_0} = 1 - \frac{x}{d_0} - \frac{2}{\pi} \sum_{n=1}^{\infty} \frac{1}{n} \sin \frac{n\pi x}{d_0} \exp \left(-\frac{k}{S_s} \left(\frac{n\pi}{d_0} \right)^2 t \right) \quad (37)$$

Figures 8 and 9 show the comparison of the calculated results and theoretical solution, where Figure 8 shows the analysis result by penalty method and Figure 9 shows the one by node shift method. From Figure 8, we can see the difference between the calculated results and the theoretical solution. Especially, this difference is large when the normalized time is small. We can find that this difference is smaller in Figure 9 than in Figure 8.

This large difference shown in Figure 8 is caused by the fact that the fixed head points are inside the element.

4.3 2-dimensional Saturated-unsaturated Unsteady Seepage Analysis

The authors analyzed the model of groundwater flow in earth dam. This problem is 2-dimensional saturated-unsaturated unsteady seepage problem (see Figure 10). The analyzed water table at several times are shown Figures 11 and 12, where Figure 11 shows the analysis result by MM, and Figure 12 shows the one by FEM. Table 1 shows the comparison of the input data used in MM and FEM respectively. From Table 1, we can see that MM can save the task for preparing input data for the analysis. This fact proves the advantage of MM to FEM.

5 CONCLUSIONS

The MM could formulate the governing equation of the saturated-unsaturated unsteady groundwater flow problem. Simple examples to demonstrate the validity of the method were given. In this study, the authors get following conclusions.

- In saturated steady and unsteady analysis, calculated results by MM showed very good correspondences to the theoretical solutions.
- In MM, there are two methods to fix the hydraulic head, which are penalty method and node shift method. The former is superior to the latter in convergence of solution, but may have disadvantage that shape of mathematical mesh near the material boundary becomes complex.
- MM is superior to FEM in that we can save the task for preparing input data for the analysis.

REFERENCES

- Akai, K., Ohnishi, Y., and Nishigaki, M. 1977. Finite element analysis of saturated-unsaturated seepage in soil. *Proc. Japanese Soc. for Civil Eng.*, 264: 87-96 (in Japanese).
- Ohnishi, Y. and Tanaka, M. 1998. Manifold method in saturated-unsaturated unsteady groundwater flow analysis. *Proc. 8th KU-KAIST-NTU-NUS Seminar on Civil Eng.*, 440-445.
- Shi, G.-H. 1991. Manifold method of material analysis. *Trans. 9th Army Conf. on Applied Math. and Computing*, 92-1, U. S. Army Research Office.

Table 1. Comparison of input data between MM and FEM.

	Finite Element Method	Manifold Method (node shift method)
Total number of nodes	143 points (Fixed head points: 22 points) Freedom degree of the system: 121	143 points (Fixed head points: 22 points) Freedom degree of the system: 121
Total number of elements	240 elements (triangular mesh)	240 elements (triangular mesh)
Data of nodes	The number of nodes (143) x -coordinate of nodes (143) y -coordinate of nodes (143) Designation sign of fixed head point (143) Fixed head value (22)	Dividing number of mathematical mesh (1) x -coordinate of fixed head points (22) y -coordinate of fixed head points (22) Number of fixed head points (22) Fixed head value (22)
Data of elements	Element number (240) Node numbers of each element (720)	—
Data of material	Permeability in saturated area Specific storage Water retention curve	(same as FEM)
Other	Data of time step etc.	(same as FEM)

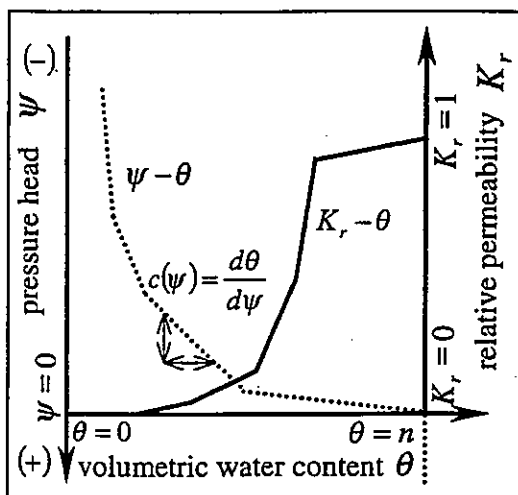


Figure 1. Water retention curve.

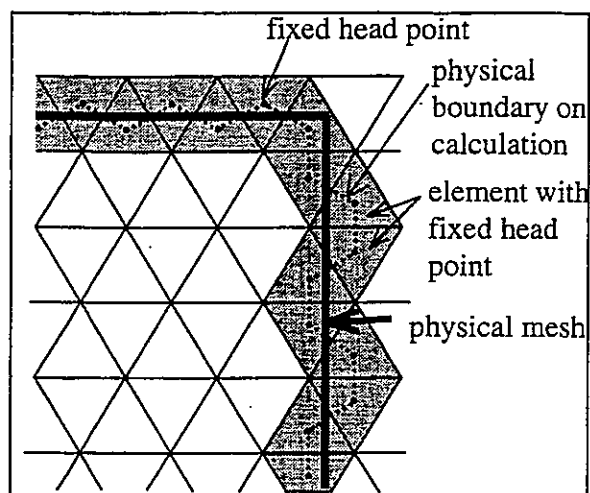


Figure 2. Fixed head points in penalty method.

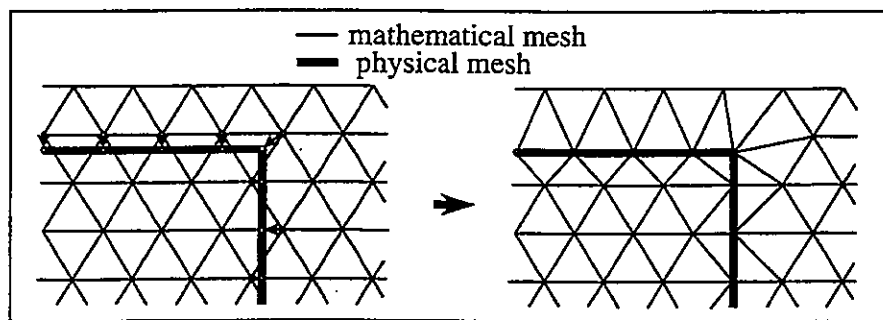


Figure 3. Modification of mathematical mesh.

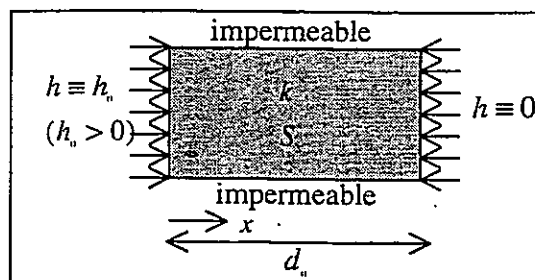


Figure 4. 1-dimensional saturated steady seepage problem.

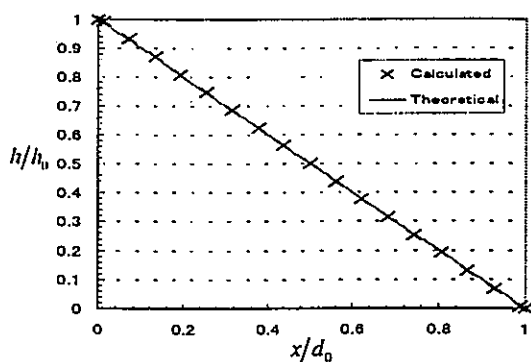


Figure 5. Result by penalty method.

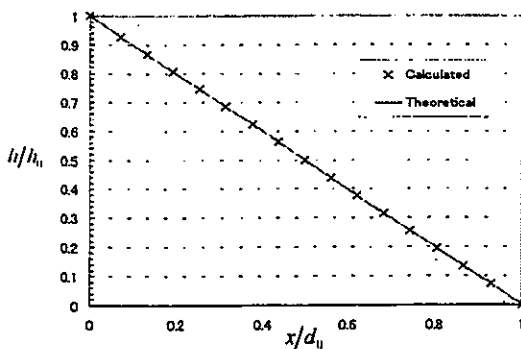


Figure 6. Result by node shift method.

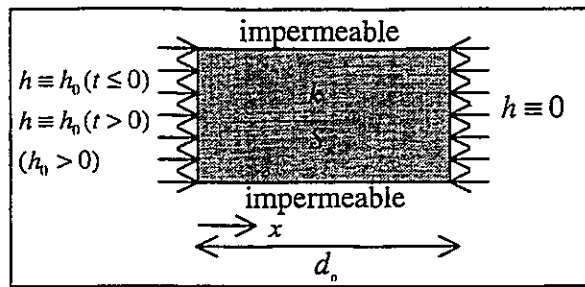


Figure 7. 1-dimensional saturated unsteady seepage problem.

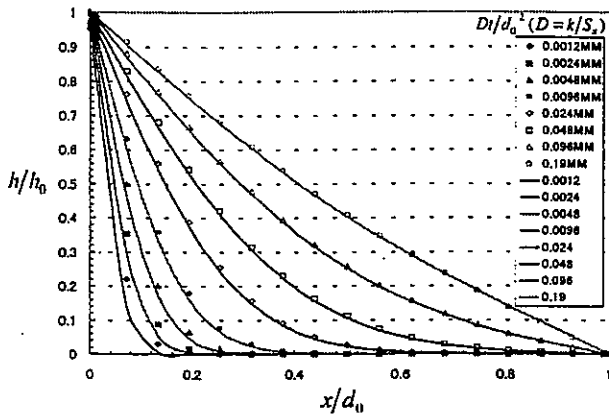


Figure 8. Result by penalty method.

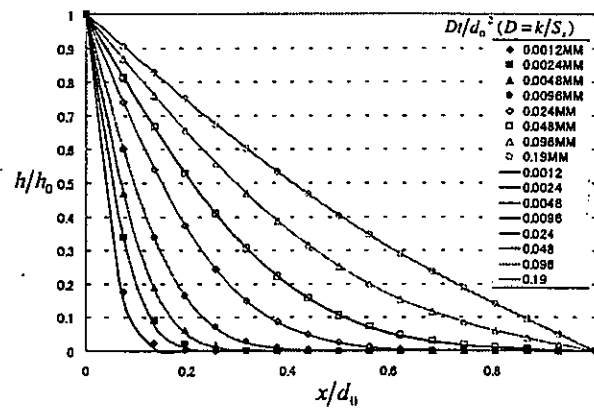


Figure 9. Result by node shift method.

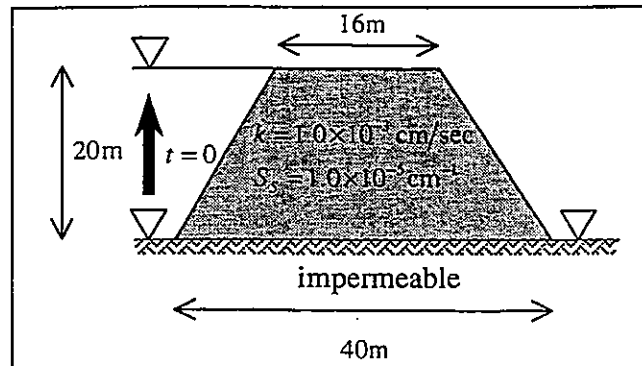


Figure 10. Groundwater flow in earth dam.

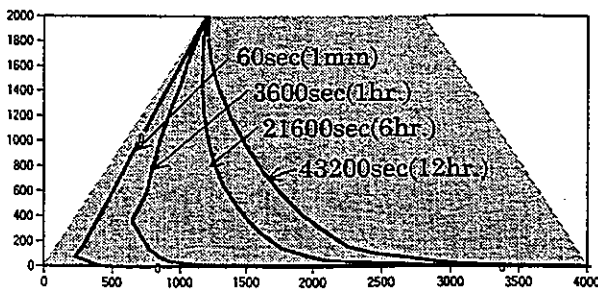


Figure 11. Calculated water table by MM.

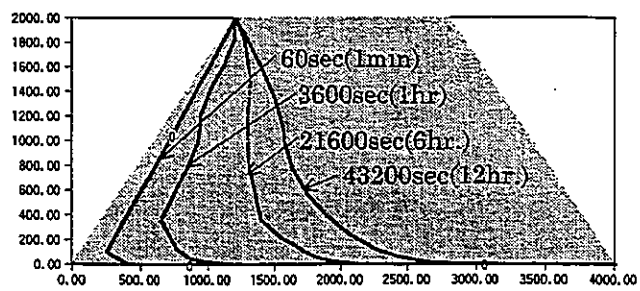


Figure 12. Calculated water table by FEM.

Manifold Method Analysis of Rock Masses Containing Joints of Two Different Scales

Jeen-Shang Lin and Cheng-Yu Koo

Department of Civil and Environmental Engineering
BEH949, University of Pittsburgh, Pittsburgh, PA 15261, USA

Jin-Ching Chern

Sinotech Engineering Consultants, Inc., Taipei, Taiwan, ROC

ABSTRACT: A manifold method formulation is presented here for analyzing rock masses that contain joints of two different geometric scales. When joint scales become very wide apart, it would not be feasible to model them with equal details. Reasonable simplification requires that at least the dominant kinematic constraints be preserved. This can be achieved through the combination of discrete and continuum methodologies. In this respect, manifold method comes in handy. This study models the primary set of joints as discontinuities that divide a rock mass into individual blocks. Within each block the secondary joint set is handled using an equivalent continuum constitutive model. Numerical experiments were conducted and implications discussed.

INTRODUCTION

Rock masses often contain more than one set of joints. In all likelihood, these joints may also have very different geometric scales. When the joint scales become wide apart, it would not be feasible to model them with equal details. The immediate question in dealing with such a rock mass is, "How much simplification can one make without jeopardize an analysis?" It is essential that good reasonable estimates of the displacement field be obtained even after simplification, as it is the base for evaluating failure modes and the stresses. To achieve this goal, an acceptable simplification should at least preserve the gross kinematics of a rock mass.

In the following discussion, only two sets of joints are considered: one dominant or primary and the other secondary. The primary joint set is the one that has a wider spacing, and that it governs the overall kinematics of a rock mass. To preserve the rock mass kinematics, it may be essential to model this joint set explicitly. This can be achieved in a discrete approach by modeling the joints as physical discontinuities. These discontinuities cut a rock mass into individual discrete blocks.

The secondary joint set is also the source of some relative movements. But being confined by the primary joint set, this movement per se is not important. It, however, has significant impact on the stress that a rock can withstand. The net effect of the secondary joint set may, therefore, be modeled satisfactorily using an equivalent continuum constitutive model.

In view of these, the present study will employ a mixed continuum-discrete method, the manifold method (Shi, 1997; Lin, 1995), in the analysis. The primary joint set is modeled as discontinuities, while the secondary set through an equivalent continuum. Numerical experiments and an application example are also presented.

MANIFOLD METHOD

In manifold method, a problem description is defined by a two-layer description. The first layer of the description is called a physical mesh. Within the present context, a physical mesh includes the problem boundaries and the discontinuities posed by the primary joint set. The second layer of description is called a mathematical mesh. A mathematical mesh can be a mesh of some regular pattern, or a combination of some of arbitrary figures. The mesh or shape size may be chosen according to the problem geometry, solution accuracy requirements, and the physical property zoning. In this study a regular triangular grid is employed as a mathematical mesh. The mathematical mesh is used for building covers and has to be large enough to cover every point of the physical mesh.

Figure 1(a) depicts a jointed rock sample which is placed between two caps ready for uniaxial test. This problem layout shows the physical boundaries and discontinuities encountered. Thus, this layout is served as a physical mesh in a manifold formulation. As for the rock itself, a discretization using a triangular mesh is selected. A mathematical mesh reflecting this consideration is depicted in Figure 1(b). In the manifold method, the two layers of meshes do not have to conform to each other. Putting these two meshes together gives a manifold description of a problem as illustrated in Figure 1(c).

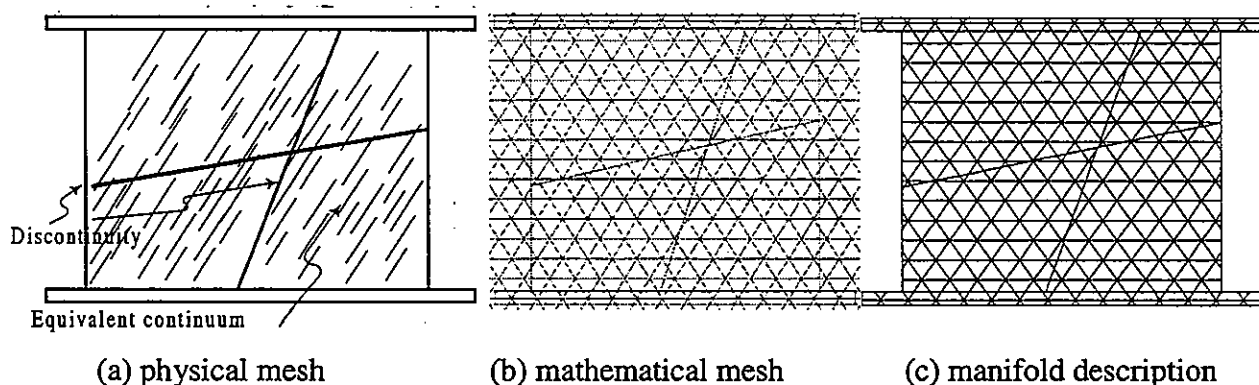


Figure 1. A manifold description of a rock sample under uniaxial test setup

Each discontinuity encountered can have distinct properties. Surface of discontinuities may be separated or come to contact with each other. When they are in contact, the normal force is obtained from no penetration requirement, while the shear force is determined from relative sliding movement together with Mohr-Coulomb failure criteria.

EQUIVALENT CONTINUUM MODELS

There are many equivalent continuum models for representing jointed rock masses. Analytical solution considering compliance and anisotropy induced by joints represent one approach (e.g., Gerrard, 1982; Amadei, 1982). Another approach requires numerical implementation but is much more versatile. Multi-laminated model is perhaps one of the most comprehensive model in this category. It was proposed by Zienkiewics and Pande (1977) to

model the “pronounced” anisotropy of rock due to the presence of two or three sets of weak planes. The normal and shear stresses on a typical weak plane can be found by Cauchy’s law, i.e.,

$$\begin{bmatrix} \sigma_n \\ \tau \end{bmatrix} = T_i \sigma \quad (1)$$

Each weak plane is associated with a yield function that is defined in terms of the stress state and stress history as follows,

$$F_i = F_i(\sigma_n, \tau, \varepsilon^p) \quad (2)$$

The surface may exhibit work-hardening or work-softening characteristics. A hardening parameter that is tied to a plastic strain measure can be used to model this effect. When there are many sets of weak planes, Zienkiewics and Pande suggested the intersection of the individual yield functions be used in representing the gross yield function of a rock element, i.e.,

$$F = F_1 \cap F_2 \dots \cap F_k = 0 \quad (3)$$

One may also adopt an associated or a non-associated flow rule to model the plastic sliding and dilatancy of weak planes.

Ubiquitous joint model (Flac, 1993) can be viewed as a simplified version of the multi-laminated model: the weak planes are considered perfectly smooth. As a result, no dilatancy takes place at yielding. This simple version is adopted for the present study. Whenever the yield function of a weak plane is reached, the stress exceeds the yield strength is relaxed.

Only one set of weak plane within each continuum element is considered in this study. Each weak plane is also assigned a residual strength once the yielding strain is exceeded.

TESTS ON SAMPLES CONTAINING ONE SET OF JOINTS

Plane stress numerical tests were conducted for rock samples that contain one single set of joint. First of all, each rock sample is modeled as a uniform continuum by adopting UBI model. Each sample is covered by 100 to 1000 triangular elements. Within each element, the displacement field is linear. All elements use the same set of parameters. Mathematical and physical meshes similar to Figure 1 are employed except that there is no physical discontinuity. Initially, the rock is elastic until its yielding strength is reached, then UBI model is triggered. Several joint orientations, defined by an angle θ , are considered. They are 30, 50 and 60 degrees from horizontal, respectively. Two sets of strength parameters are used for each case. For $\theta=60$ degree, the first case considers $\phi_p=\phi_r=30$ deg and $c_p=c_r=30$ kN/m²; the second case considers $\phi_p=\phi_r=30$ deg, $c_p=400$ kN/m² and $c_r=30$ kN/m².

Parallel sets of tests using discrete elements were also carried out. Each rock sample in this case consists of two discrete blocks. They are separated by one single joint that has the same orientation as its counter part in the continuum model. In the discrete model, the rock is elastic.

The displacement field within each block is linear.

Results from both sets of tests using same peak and residual strengths are shown in Figure 2(a) and (b). Both results show similar gross elasto-plastic stress-strain curve. The yielding strengths from both tests are about the same values. The main differences lie in the displacement. Since the two models employ vast different degrees of freedom, it is not unexpected to find significant differences in the elastic limit strain. In the discrete model, the failure is instantaneous. In the continuum model, the failure progresses also very fast, and the sample failed within a few time steps.

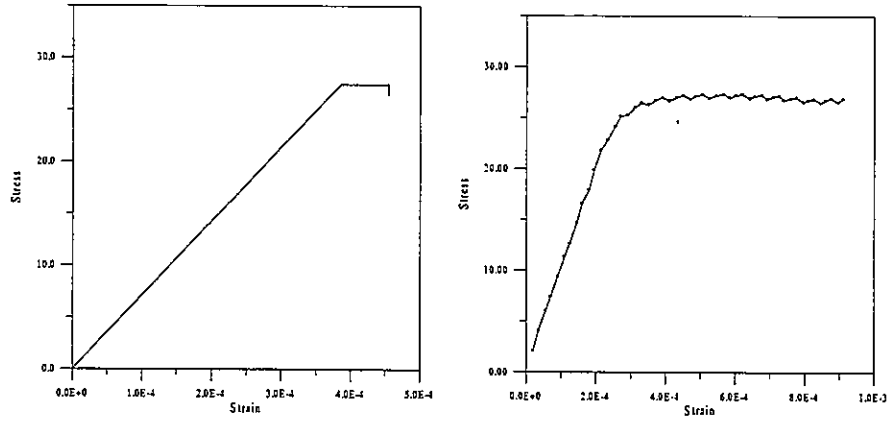
However, if rock joint strength is substantially reduced after first yield, results from the two sets of tests diverge. Their gross stress-strain curves are depicted in Figure 3. In the discrete model, once the peak strength is reached, it immediately drops to a residual level. In contrast, the continuum model gives a higher post-yield strength, which is also sensitive to the number of elements used. Figure 4 shows that the yielding zone within a continuum sample expands gradually. Failure starts from both ends and propagates toward the center. Even after a failure band is formed, some loading is still carried by elements outside the band. The residual strength from discrete model thus can be regarded as an asymptotic value.

Figure 5(a) depicts the deformation of a continuum sample after a large deformation. A significant sliding like deformation can be observed. It is clear that sliding takes place along many weak planes. This sliding pattern is also affected significantly by the evolution of failure zones within a sample. Moreover, presence of weak planes affects the principal stress orientation within a sample. UBI model is capable of achieving that. This can be observed from end-of-test results shown in Figure 5(b). In it, the failure band can also clearly be identified from the rotated principal stress.

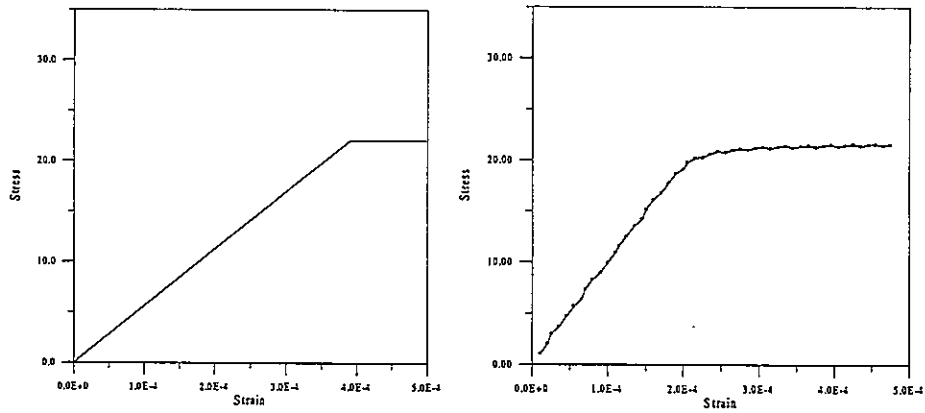
The preceding results demonstrate that a continuum model, when incorporate a proper constitutive law for joints, can provide a reasonable basis for estimating the mechanical behavior of a jointed rock.

TESTS ON SAMPLES CONTAINING TWO SET OF JOINTS

Tests were also conducted on a sample contains two sets of joints of different scales. This mainly serves as an illustration of the present approach. Only one single sample was used in this case, and the meshes used are depicted in Figure 1. The physical discontinuities used in this case do not undergo much relative movement under the applied load. Therefore, the load deformation curves is expected to be close to that contains only secondary joint set. Three cases were analyzed: (1) both primary and secondary joint sets are considered, (2) only secondary joint set is considered, and (3) only primary joint set is considered. The displacement vectors and principal stresses are depicted in Fig. 6. The stress-strain curves obtained are presented in Fig. 7. These results demonstrate that a wide range of complex behavior can be modeled with various combination of discrete and equivalent continuum modeling techniques.



(a) Joint angle $\theta = 50$ degree



(b) Joint angle $\theta = 60$ degree

Fig. 2 Stress-strain curve obtained by DDA(left) and Manifold method(right)

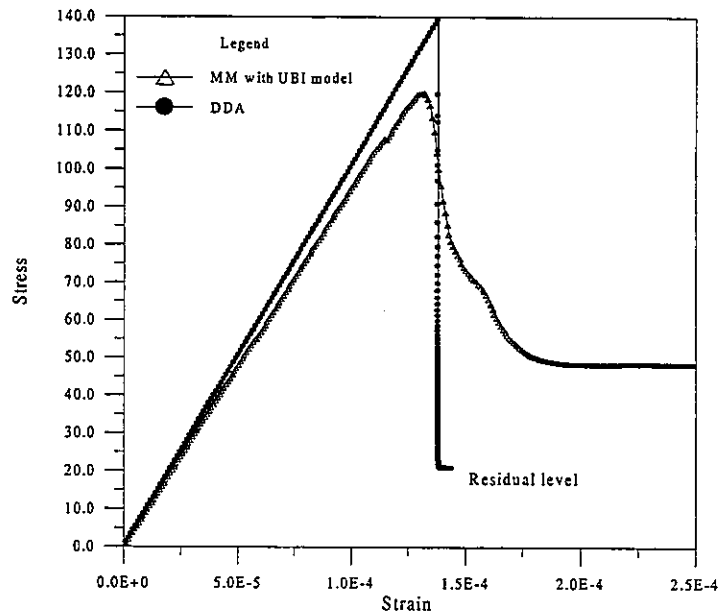


Fig. 3 Stress-strain curve obtained from discrete and continuum models, $\theta = 60$ degree.

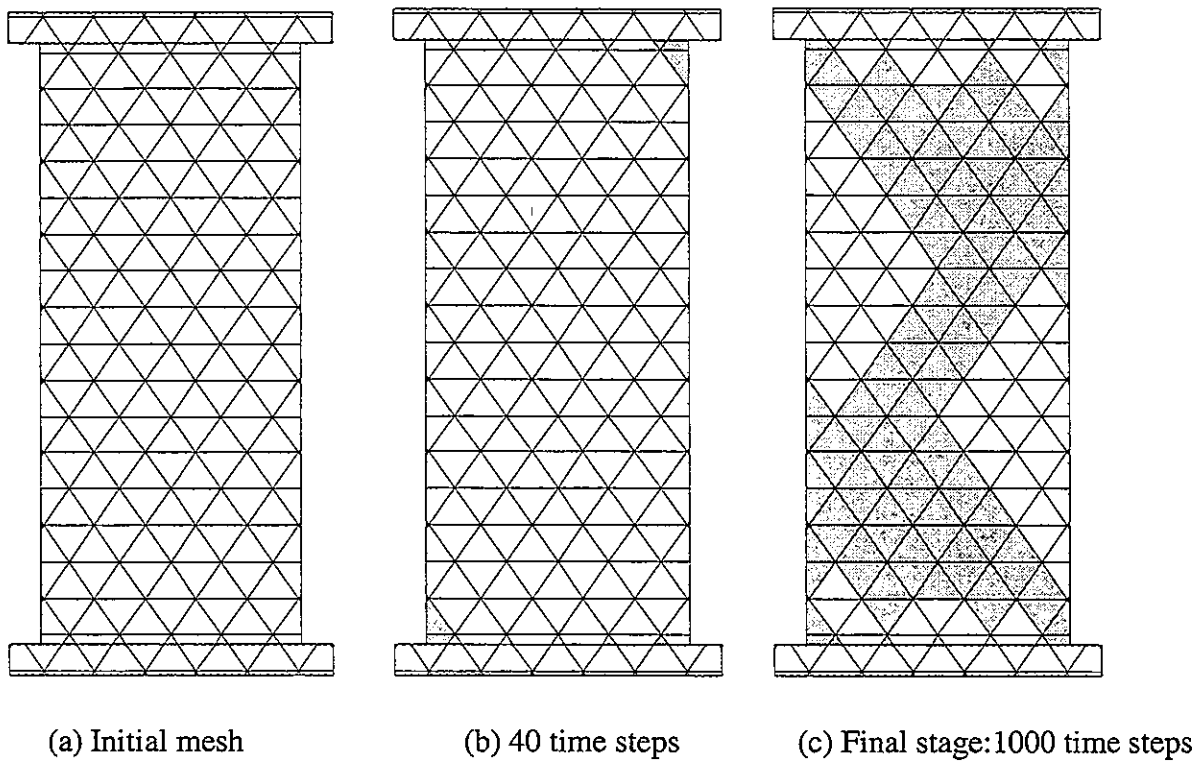


Fig. 4 Evolution of failure zone.

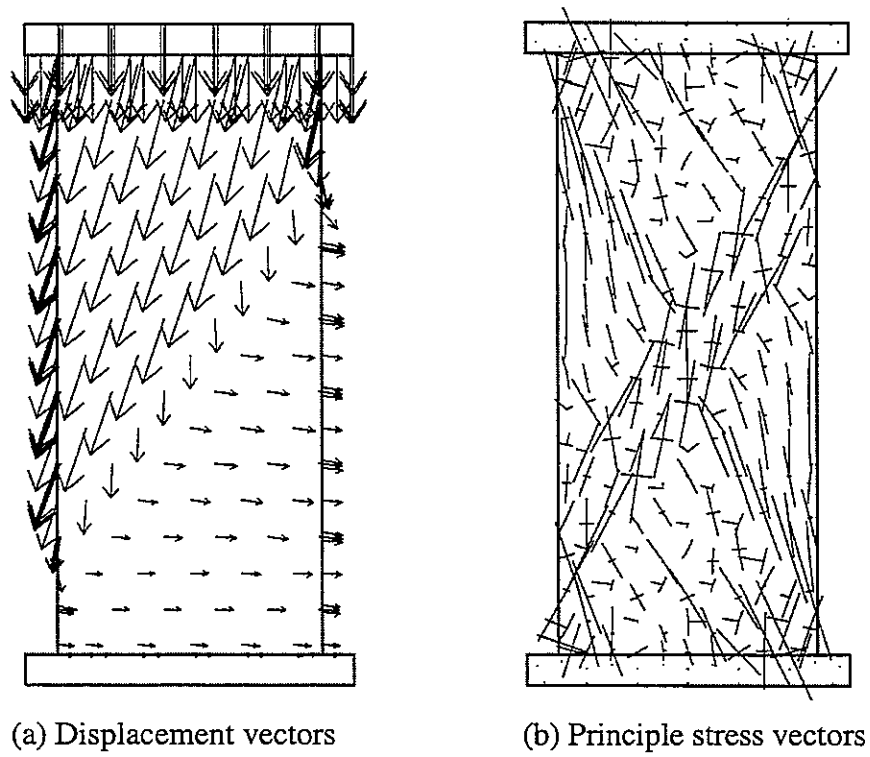
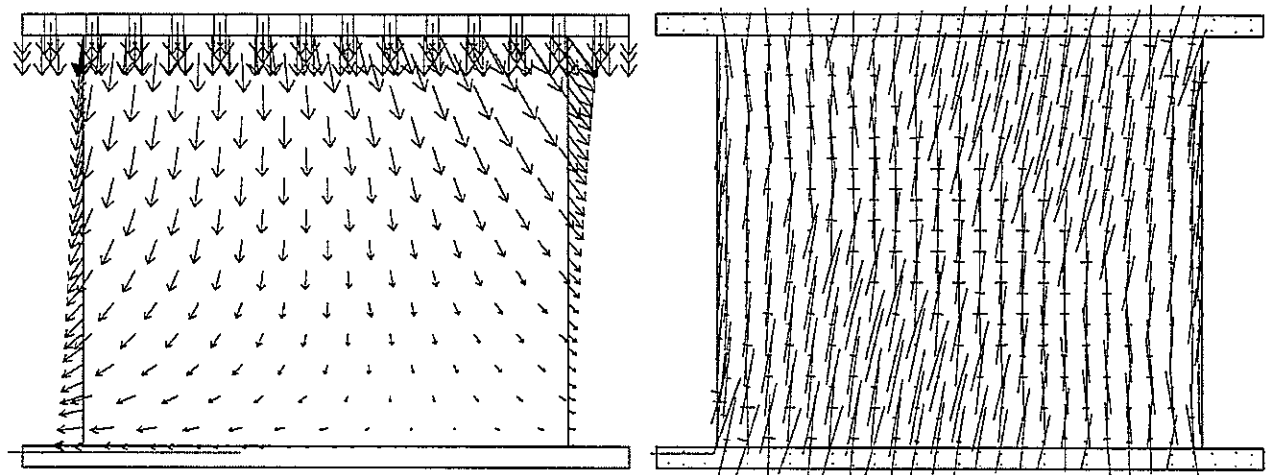
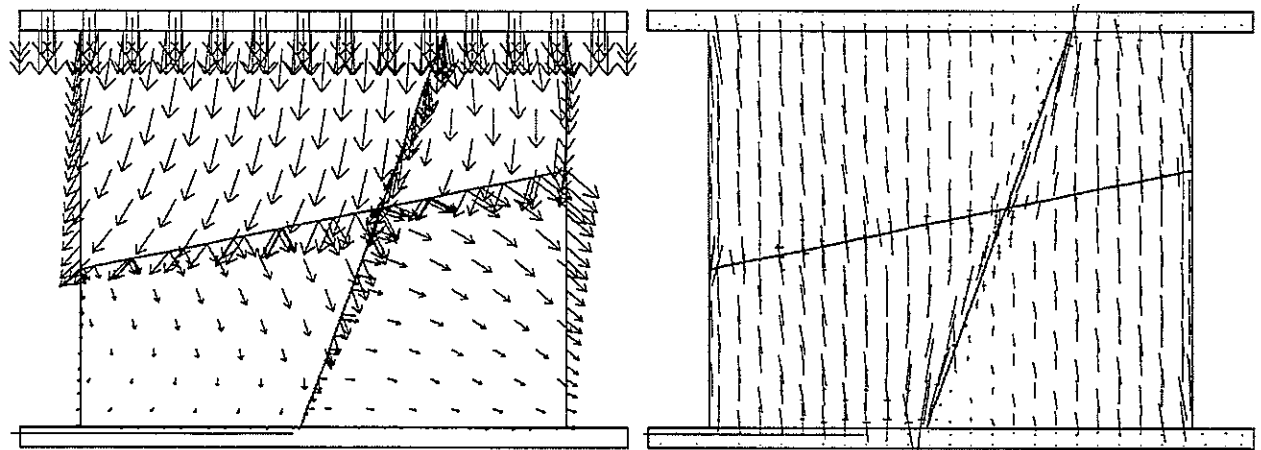


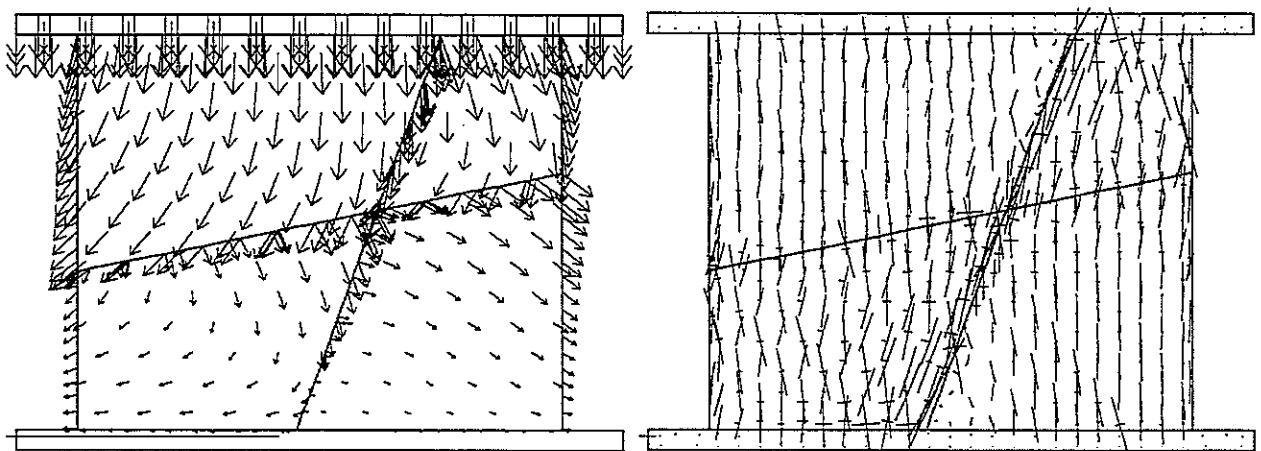
Fig. 5 Results from the continuum model, with $\theta = 60$ degree



(a) With only secondary joint set



(b) With only primary joint set



(c) With both primary and secondary joint sets

Fig. 6 Deformation vectors and principle stress distribution at the end of tests.

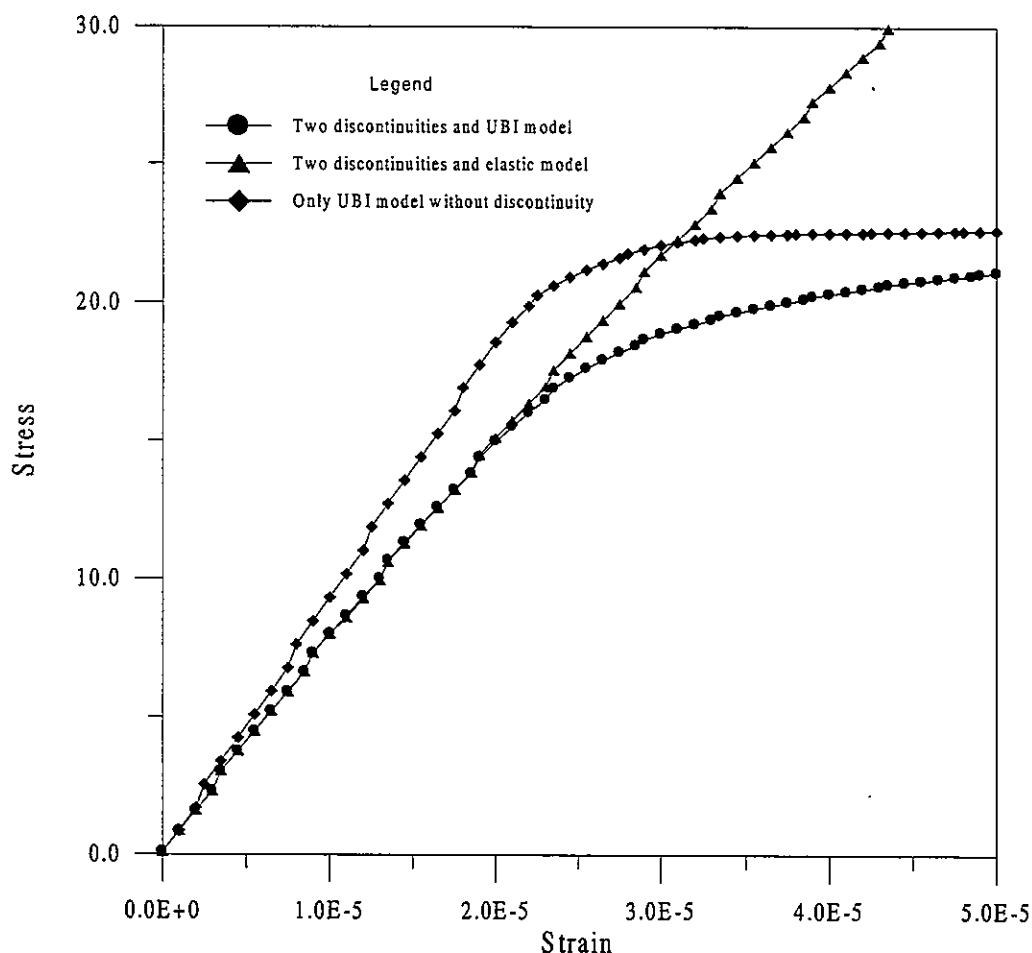


Fig. 7 Stress-strain curves with various combinations of joint sets.

CONCLUSIONS

This study shows the advance of discrete continuum interaction formulation, such as that based in manifold method, may provide a framework for enhancing the level of analysis that can be achieved. Moreover, it also shows even simple model, such as UBI, couple with explicit discrete model has the potential for describing a very complex behavior. Work is currently underway in further exploring the effects of various combinations and their implications. The present work can readily be employed in assessing large-scale rock mass strength and stability.

REFERENCES

- Amadei B. 1982. The influence of rock anisotropy on measurement of stresses in situ. Ph.D. thesis, University of California, Berkeley.
- Curran, J. H. and Ofoegbe G. I. *Modeling Discontinuities in Numerical Analysis*. 443-468. Constitutive laws and numerical modeling.

Gerrard, C. M. 1982. Joint compliances as a basis for rock mass properties and the design of supports. *Int. J. Rock Mech. Min. Sci. & Geomech. Abstr.* 9: 285-305.

ITASCA. Flac user's manual.

Koo C-Y and Chern J-C, 1997. Modeling of progressive fracture in jointed rock by DDA method. Proceeding of Second International Conference on the Analysis of Discontinuous Deformation. pp. 186-200. Kyoto, Japan.

Lin, J-S. 1995. Continuous and Discontinuous Analysis using the Manifold Method. *Proceeding of the Working Forum on the Manifold of Material Analysis.* pp. 1-20. California.

Shi, G. H. 1997. Numerical Manifold Method. *Proceeding of Second International Conference on the Analysis of Discontinuous Deformation.* pp. 1-36. Kyoto, Japan.

Zienkiewics, O. C. and Pande, G. N. 1977. Time-dependent multi-laminated model of rocks—a numerical study of deformation and failure of rock masses. *Int. J. of numer. anal. methods in geomechanics.* 1: 219-247.

Hybrid Numerical Analyses

DYNAMIC BEHAVIORS IN DISCONTINUOUS ELASTIC MEDIA USING DDA

Kuokai Shyu

Manifold Engineering, 18645 East Gale Avenue, Suite 200
Industry CA 91748-1345, USA

Xinhua Wang

Manifold Engineering, 18645 East Gale Avenue, Suite 200
Industry CA 91748-1345, USA

Chiao-Tung Chang

Manifold Engineering, 18645 East Gale Avenue, Suite 200
Industry CA 91748-1345, USA

ABSTRACT: In the study of wave propagation and dynamic contact analysis for discontinuous elastic media, few results have been reported by use of current numerical models, such as the Finite Element Method (FEM) and Discontinuous Deformation Analysis (DDA). An improved numerical model, DDA+FEM is presented to analyze these types of problems. This model, an enhancement of original DDA, can simulate the propagation of dynamic waves more accurately in discontinuous elastic media. In this paper the basic concept of DDA+FEM is presented, and applications of wave propagation in finite dimensions is demonstrated. Verification examples of the proposed model include the dynamic impact of two elastic bars and two spheres. Given the velocity structure and geological information, the proposed model can simulate dynamic wave propagation in tectonic media; while with known seismogram data, the geological information and velocity structure of tectonic media can be investigated.

1 INTRODUCTION

In the field of geophysics, the geological survey of the crust-mantle structure has been an important issue to explore. Better knowing the fundamental nature of the geological structure underneath can help mankind to understand and to be cautious about unexpected movements or other unsolved mysteries of the earth. For example, an earthquake pre-warning system can be established after understanding of the geological information of the faults and tectonic plates; energy exploration can be improved by knowing the distribution of the geological structure; the phenomenon of orogenic movements may be explained by geologists due to the unfolding information of the velocity structure; to locate the discontinuous interfaces or weak zones and to obtain the geological properties of the bedrock by reference to the velocity structure is an important issue for dam engineering.

To investigate the geological velocity structure, the classical theory of the wave (ray theory) has been intensively used to interpret the reflection and refraction of the dynamic waves generated through a wave source. The refraction depends on the material properties of the geological structures and the discontinuous media interfaces. The geological velocity properties are often characterized.

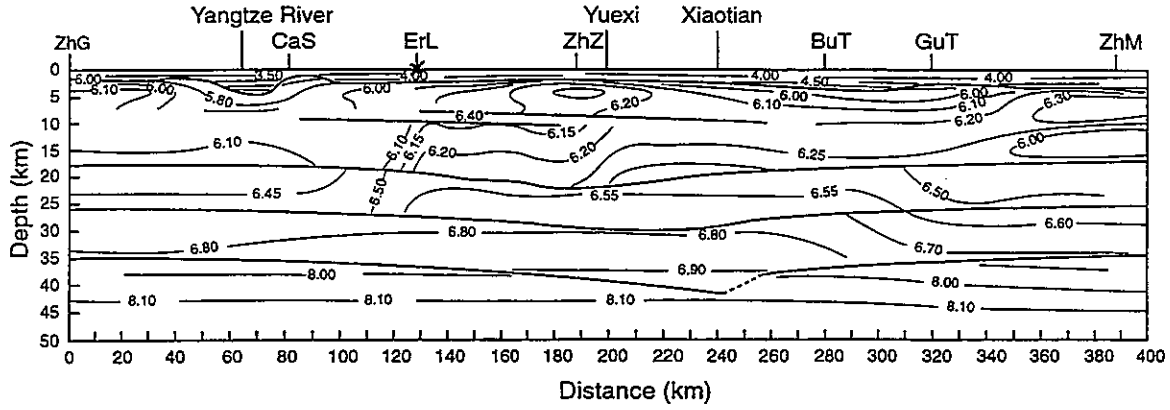


Figure 1. P wave velocity structure of the ultrahigh-pressure Dabie Shan orogenic belt.

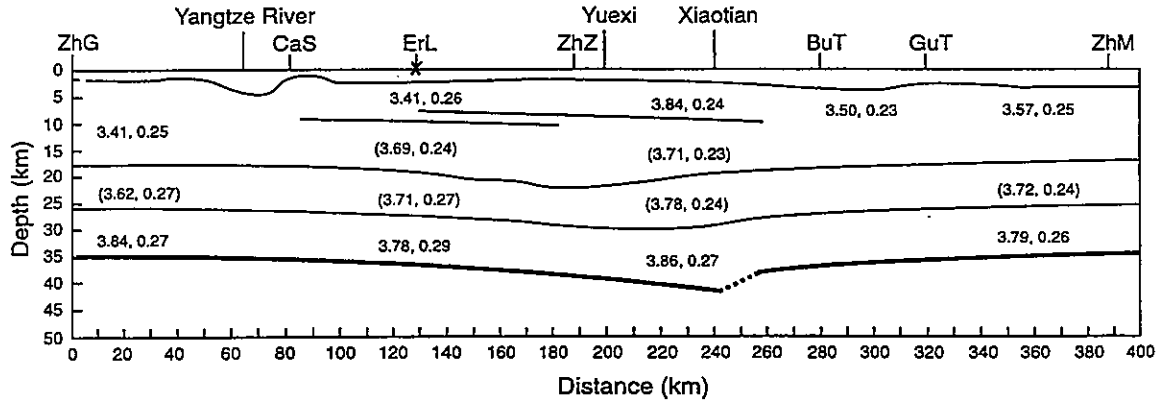


Figure 2. S wave velocity structure of the ultrahigh-pressure Dabie Shan orogenic belt.

as the P wave (pressure wave) and S wave (shear wave) velocities of the structure Figures 1 and 2 illustrate the typical P and S wave velocity structures. These velocities properties are related to the material properties of Young's modulus, Poisson's ratio, and mass density as follows:

$$V_p = \sqrt{\frac{E}{\rho} \frac{1 - \nu}{(1 + \nu)(1 - 2\nu)}} \quad (1)$$

$$V_s = \sqrt{\frac{E}{\rho} \frac{1}{2(1 + \nu)}} \quad (2)$$

where V_p and V_s are the P and S wave velocities; E , ν , and ρ are Young's modulus, Poisson's ratio, and mass density respectively. The wave source often is generated by seismic sounding, namely, borehole explosion or pile hitting. The response data, which are the superposition of various ray of waves, are captured by observation stations at certain locations. Thanks to digital computer technology, now these massive data and numerical modeling can be analyzed effectively.

Incorporated with dynamic wave propagation equations, Finite Difference Method (FDM) and Finite Element Method (FEM) are extensively used in geophysics studies. However, there are limitations. These two methods can only be effective in homogeneous and layered media, and can not well describe the reflection and refraction responses of the waves through discontinuous media.

Wave traveling through discontinuous interface involves complicated energy transfer, reflection, refraction of the wave, and contact of the discontinuous interface.

To better describe the dynamic wave propagation equation, the element size of a finite element mesh must be small enough to capture the traveling wave shape. A seismic sounding source is usually an impulse or shock wave for numerical simulation. An impulse-in-time-domain can be represented as the amplitude spectra in frequency domain by Fourier transformation that contains numerous trigonometric terms of different frequencies:

$$F(f) = \frac{1}{\sqrt{2\pi}} \int_{-\infty}^{+\infty} y(t) e^{ift} dt \quad (3)$$

where $F(f)$ is the amplitude spectra, $y(t)$ is the impulse, t and f are the time and frequency respectively. Each frequency by itself represents a wave of a certain length. To capture a short, high-frequency wave, a smaller element size is required; otherwise, the wave cannot be adequately represented, and the element will work as a wave filter that simply filters out the high-frequency portion. This makes dynamic wave propagation problems difficult to simulate.

As for the simulation of discrete media, Shi (1988) introduced Discontinuous Deformation Analysis (DDA), which includes complete block system kinematics to describe the contact mechanism of a discrete multi-body system. The block system kinematics basically contains three parts: contact scheme, contact transfer, and open-closed iteration to correctly find the contact position, contact status, and contact forces. DDA also incorporates a time marching scheme to simulate the characteristics of the true dynamics and to control the convergence of the open-closed iteration.

Since DDA's debut, many improvements have been developed to enhance a block's deformation ability. For example, Shyu (1993) and Chang (1994) have incorporated finite meshes into DDA blocks (DDA+FEM); Ke (1993) and Amadei *et al.* (1996) have introduced unique concepts to make fracture mechanics available; Lin and Lee (1996), Koo and Chern (1996), and Ma *et al.* (1996) have developed high order DDA blocks.

In geophysics studies, an investigation on finding the refraction profile possibly resulting from an orogenic movement has been processed in China (Wang *et al.* in press). Their report indicated that, by coupling the seismic sounding technique and FDM to analyze the time traveling curve and to trace the reflection and refraction formation of the waves, some velocity structures in the crust can be derived from the ultrahigh-pressure Dabie Shan orogenic belt in the mantle. Therefore, the geophysics field can be an important direction for DDA. For example, combining seismic sounding and DDA, the geological formation of underground structures can be found to help the exploration of oil and mining procedures; tectonic movements can be studied to understand the mechanism of the earthquake phenomenon, etc.

Due to the nature of DDA, dynamics and contact mechanisms can be easily overcome. However, few applications in geophysics studies including dynamic wave propagation problem through discontinuous media have been found by use of DDA modeling. The most recent one was demonstrated by Liu (1996), in that aseismic fault slips and block formation in Northern China has been modeled. To demonstrate the wave propagation behavior by use of DDA, two classical numerical examples will be illustrated to show the capacity of DDA+FEM. The dynamic wave propagation behavior induced from a shock wave through discontinuous media containing various velocity structures will be investigated using DDA+FEM to demonstrate the possible application for geophysics. Response signals captured from observation stations that characterize the reflection and refraction of the P waves and S waves through different velocity structures have been analyzed. In the last section, the conclusions are addressed.

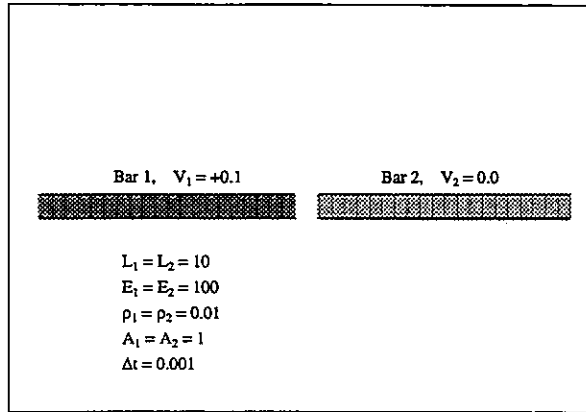


Figure 3. Input data and mesh of impact of two identical elastic bars.

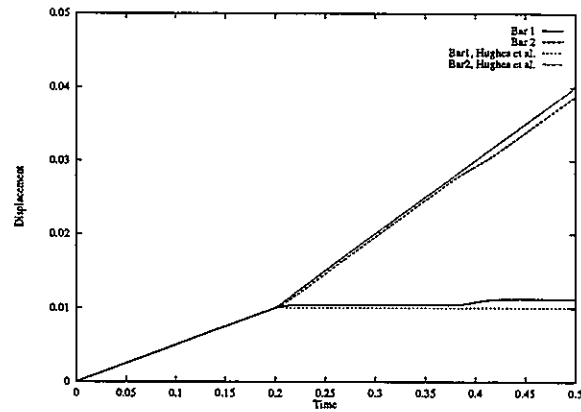


Figure 4. Impact of two identical elastic bars. Displacements of contact point vs. time.

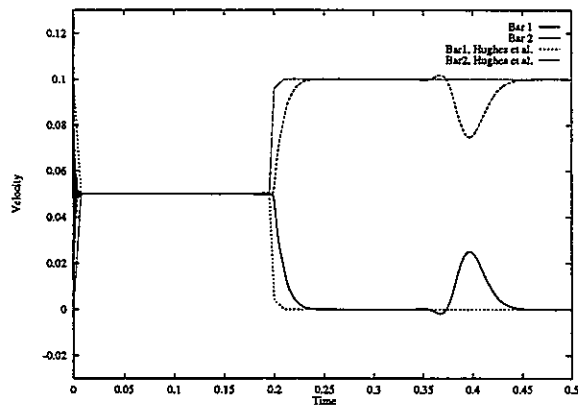


Figure 5. Impact of two identical elastic bars. Velocities of contact point vs. time.

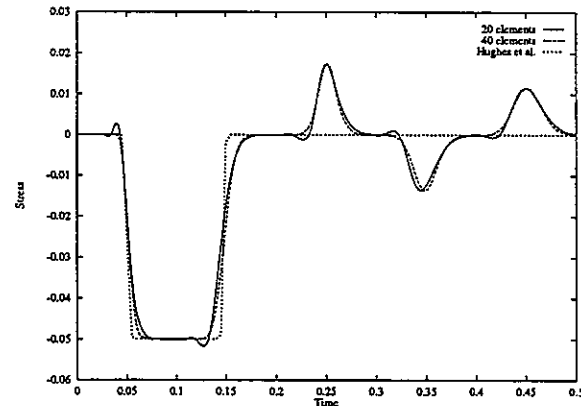


Figure 6. Impact of two identical elastic bars. Stress at mid point of bar 2 vs. time.

2 VERIFICATION

The following examples were first performed by Hughes *et al.* (1976) by use of contact finite element methods. The classical contact problems did involve energy transfer, dynamic wave propagation, and step function that are difficult for numerical models to simulate. Ma *et al.* (1996) have also been using high order DDA to verify their models, and the results were encouraging. Here, the proposed model considers the same configuration to validate the theory.

2.1 Impact of two identical elastic bars

As seen in Figure 3, two identical elastic bars are contacting at $t = 0$. Each bar is discretized with 20 elements. Figures 4–6 illustrate the results of displacement, velocity at contact point, and stress at mid point of bar 2 versus time. Compared with the results of Hughes *et al.*, the curves fit well. Using dynamic procedure, the contact-impact results and the phenomenon of reflecting waves can be easily observed after the impact waves reach the end of each bar. As a comparison, each bar is further discretized by 40 elements. The curve of stress at mid point of bar 2 versus time is also plotted in Figure 6.

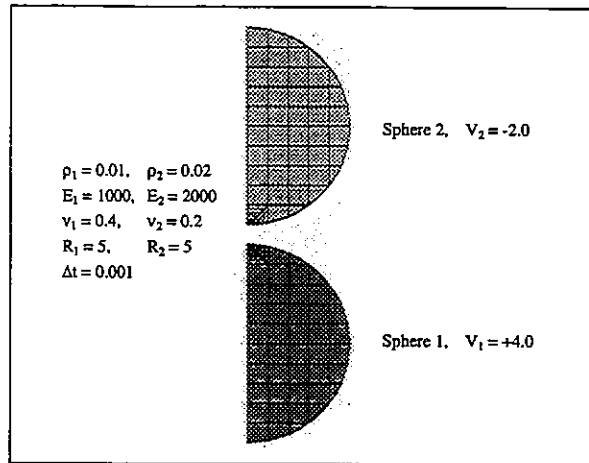


Figure 7. Input data and mesh of impact of two dissimilar elastic spheres.

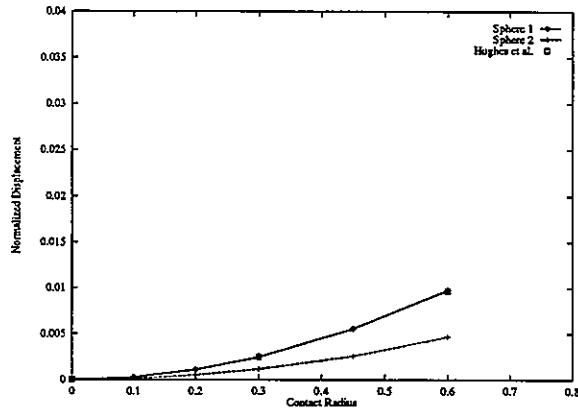


Figure 9. Impact of two dissimilar elastic spheres. Curve of normalized displacements of contact point vs. time.

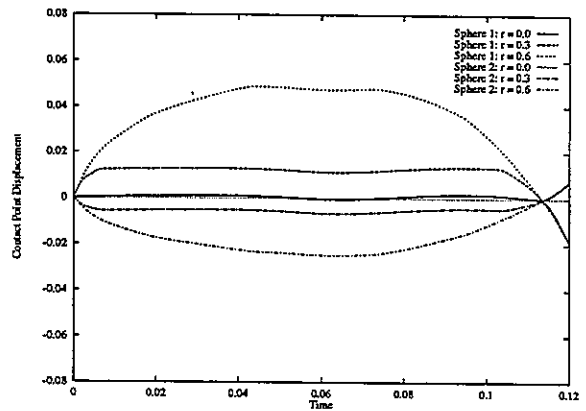


Figure 8. Impact of two dissimilar elastic spheres. Displacements of contact point vs. time.

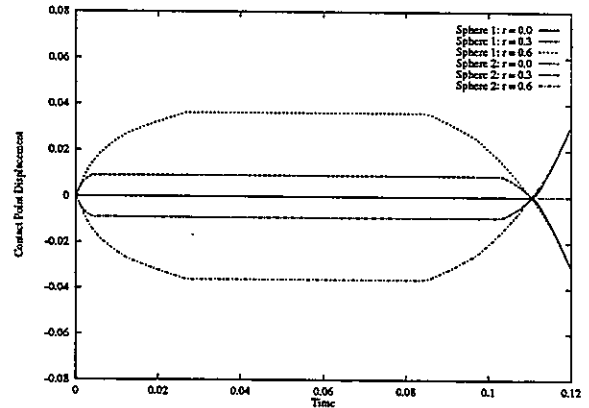


Figure 10. Impact of two identical elastic spheres. Displacements of contact point vs. time.

2.2 Impact of two elastic spheres

As shown in Figure 7, two spheres are traveling at opposite directions and contacting at $t = 0$. The contact region is discretized with elements at radius 0.1, 0.2, 0.3, 0.45, 0.6, 0.8, and 1.0. Figure 8 shows the displacements of selected contact points versus time. The flat plateau represents the full contact of corresponding element edge at each contact radius. Figure 9 displays the curve of normalized displacement of contact point versus contact radius. The results are able to be compared with those of Hughes *et al.* As a complementary analysis to this example, two identical spheres are investigated. The input data of sphere 1 are used for sphere 2. The result is demonstrated in Figure 10, where the onset and completion of contact points can be clearly observed. This also proves the accuracy of DDA's block system kinematics.

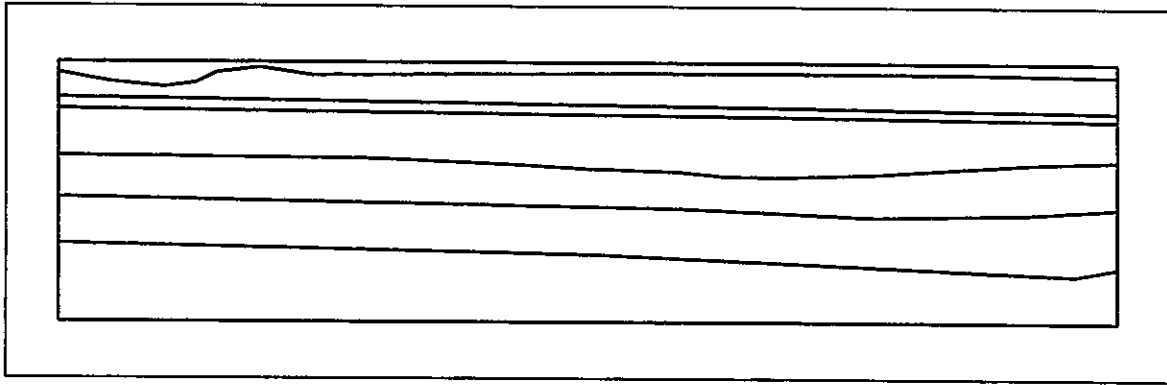


Figure 11. The discontinuous elastic media profile of seismic sounding simulation.

3 SEISMIC SOUNDING SIMULATION

The profiles of the geological structure in the mantle-crust region are of great concern to geophysics scientists and engineers. Knowing geological information can help explain the existing geological phenomenon, e.g., orogenic movements; analyze the response data received at observation stations due to earthquake excitation, e.g., seismograms; design or maintain a dam according to the geological properties of the weak zones underneath; explore for the energy or mining reservation and deposition, etc. The applications of geophysics are closely relied on the information of the geological structures (P and S wave velocities).

P and S waves traveling through the transmitting media can reflect and refract when dissimilar media or discontinuous interface is encountered. All the direct-phased and induced waves will superpose depending on the structures of the media and propagate in a complex manner. To identify the profiles of the velocity structure, seismic sounding techniques are often used. Dynamic waves generated from a shock impulse travel through media and the response data (usually, velocity records) is captured at observation stations. To analyze the captured data is difficult and complicated, in that, according to the specific profiles of the velocity structure, the arrival time of each wave can be one of the direct-phased or the combination of P and S waves.

To simulate the dynamic wave propagation problem, the configuration and profiles of velocity structure in Figures 1 and 2 are used as the numerical example. This specific example consists of discontinuous interfaces and different velocity structures identified as P and S wave velocities, and associated Poisson's ratio. The mass density of each elastic media is expressed from the following experimental formulations (Wang *et al.* in press):

$$\begin{aligned}\rho &= 2.78 + 0.56 \times (V_p - 6.0), & 6.0 > V_p \\ &= 3.07 + 0.29 \times (V_p - 7.0), & 7.5 > V_p \geq 6.0 \\ &= 3.22 + 0.20 \times (V_p - 7.5), & 8.5 > V_p \geq 7.5\end{aligned}\quad (4)$$

The proposed DDA+FEM model is applied to handle the dynamic wave propagation and discontinuous behaviors. The dimension of the example is large (in km) that, for FEM discretization to capture the high-frequency wave generated from seismic sounding, the element size will be small to make the computation almost impossible. Therefore, a scale-down configuration (in m) is presented to simulate the dynamic behaviors of the P and S waves. Figure 11 shows the configuration

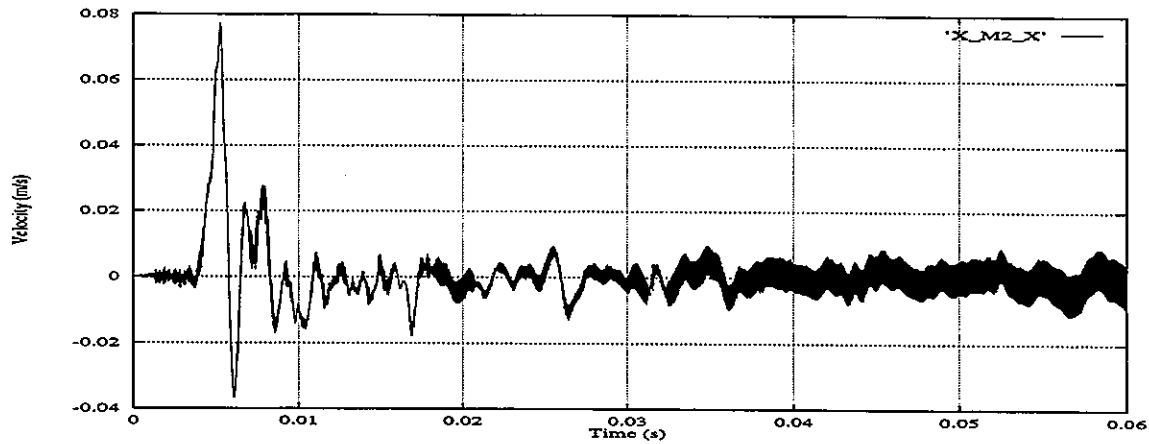


Figure 12. X-direction velocity response of station 20 m away due to x-direction shock wave.

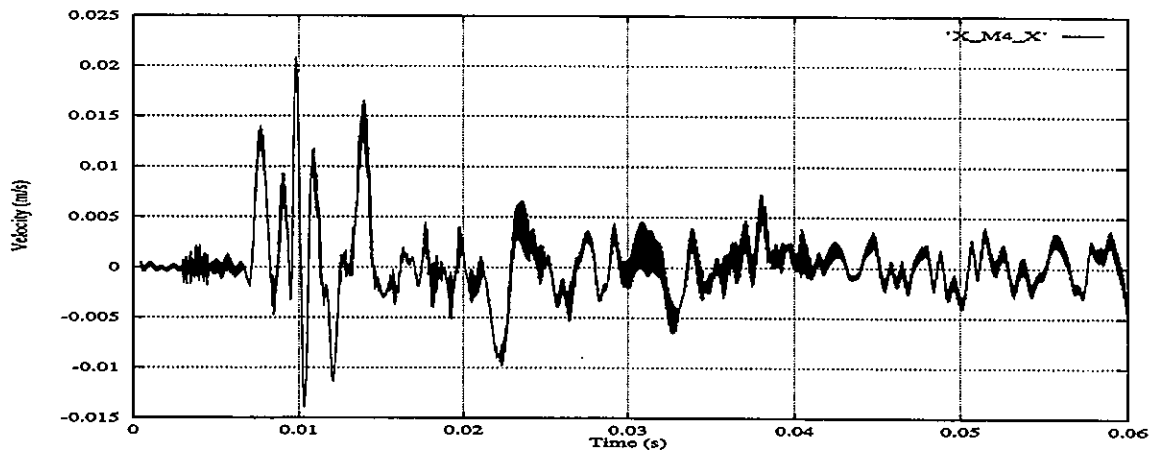


Figure 13. X-direction velocity response of station 40 m away due to x-direction shock wave.

for the numerical simulation, with the profiles of the velocity structure remaining the same. X- and y-direction shock impulse are applied separately at the location ErL and the observation stations are set at distances 20 m, 40 m, 60 m, 80 m, and 100 m from ErL (see Fig. 1). X-direction velocities at observation stations are recorded due to x-direction impulse; while y-direction velocities are recorded due to y-direction impulse.

After gravity settlement (overburden pressure build-up), dynamic calculations were performed. Figures 12 and 13 illustrate the velocity response at stations 20 m and 40 m away due to x-direction impulse. From the figures, several peaks, which represent the arrival of different waves that are either direct-phased or combined P and S waves, can be observed. For example, in Figure 12, the direct-phased ground level P wave should arrive around $t = 0.005$ s, and direct-phased ground level S wave should arrive around $t = 0.00866$ s. While other peaks can be identified as the arrival of the other direct-phased waves, P-S, or S-P (transformation from P to S or S to P) reflection and refraction waves. All the identifications are based on the information on the velocity structures. For Figure 13, the direct-phased ground level P wave and S wave should arrive around $t = 0.01$ s, and $t = 0.0173$ s respectively. Other peaks may be identified as the reflection and refraction waves from other velocity structures. Because the velocities of the P wave are higher at deeper media,

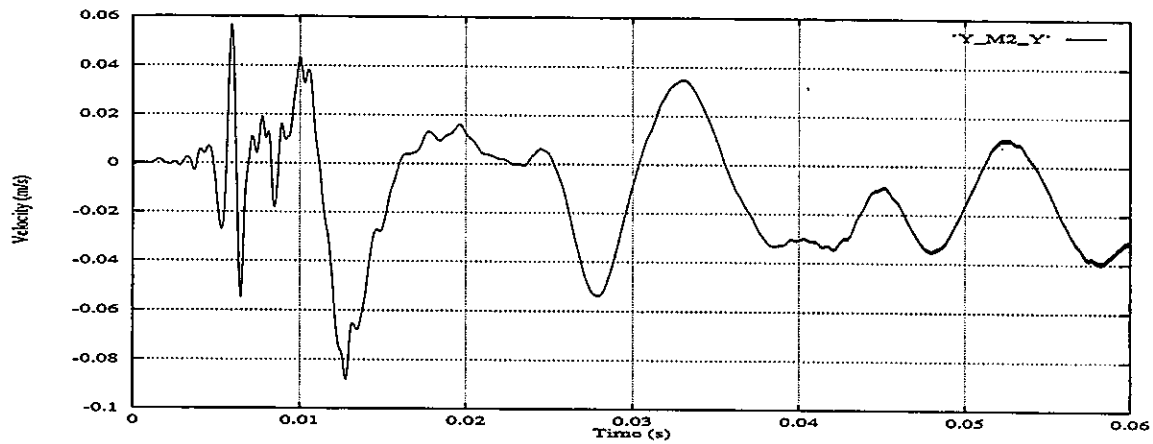


Figure 14. Y-direction velocity response of station 20 m away due to y-direction shock wave.

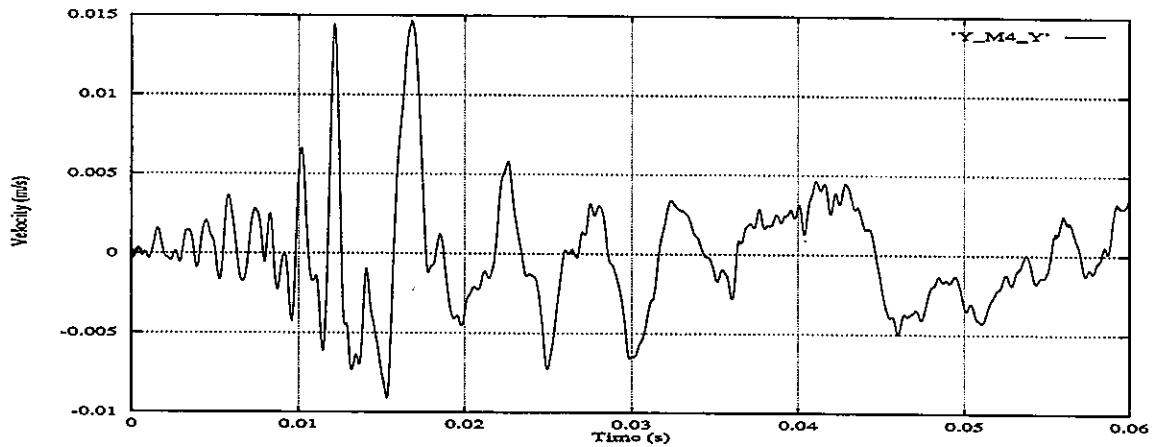


Figure 15. Y-direction velocity response of station 40 m away due to y-direction shock wave.

there are peaks in between direct-phased ground level arrivals.

Similarly, Figures 14 and 15 show the velocity response at stations 20 m and 40 m away due to y-direction impulse. In Figure 14, the direct-phased ground level S wave should arrive around $t = 0.00866$ s. The peak at $t = 0.006$ s should be identified as the arrival of P-S wave from reflection. For Figure 15, the direct-phased ground level S wave should arrive around $t = 0.017$ s. The arrival of P-S wave from reflection should be at $t = 0.01$ s.

These results demonstrate that the dynamic nature and contact mechanism of discontinuous media of DDA+FEM is well capable of describing the high-frequency dynamic wave propagation problem in a discrete multi-body system. Figures 16 and 17 also illustrate the captured data from other stations. From the figures, the delay of arrivals for each station can be clearly identified. Across the whole time span of wave travel, the reflection and refraction phenomenon are quite apparent during later stage of propagation.

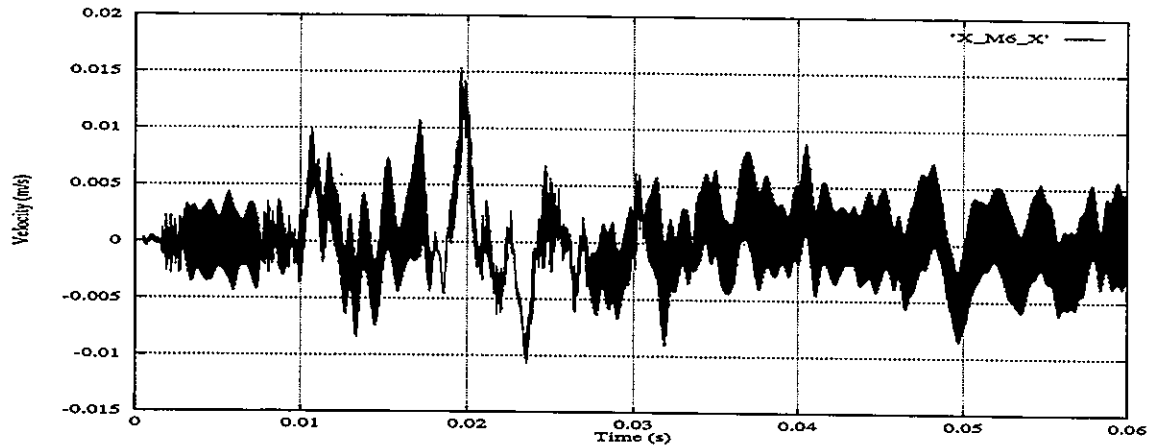


Figure 16. X-direction velocity response of station 60 m away due to x-direction shock wave.

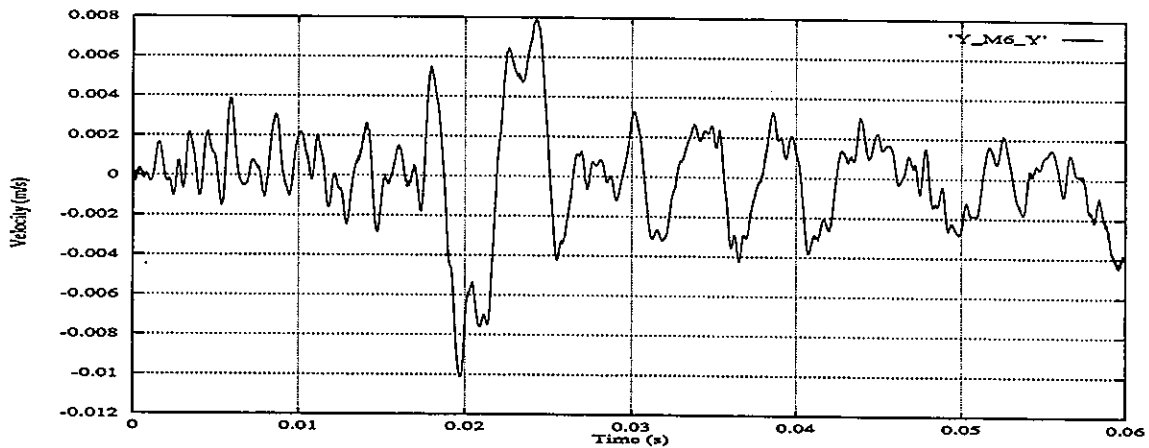


Figure 17. Y-direction velocity response of station 60 m away due to y-direction shock wave.

4 CONCLUSIONS

The objective of this paper is to demonstrate the capability of coupling Discontinuous Deformation Analysis and Finite Element Method (DDA+FEM) in the fields of geophysics. Geological knowledge is important to mankind, especially relating to energy exploration, earthquake pre-warning systems, dam engineering, nuclear waste storage, etc. One way to identify the geological information is to find the associated velocity structures in the crust-mantle region. Seismic sounding is one of the methods to utilize. Numerical simulations confirm the accuracy of DDA algorithms through classical validations, and illustrate the high-frequency wave propagation capturing by use of dynamic modeling from DDA+FEM. Most importantly, the proposed model indicates that, when the computing power is permitted, the seismic sounding technique for geophysics can be possibly simulated by comparing the response data with those from the field observation station. Therefore, the geological information survey can be more reliable and easier.

ACKNOWLEDGEMENT

The support of the National Science Foundation through contract DMI-9860244 is gratefully acknowledged. The authors will also like to thank Profs. Chun-Yong Wang and Banghui Lin for providing valuable suggestions, information and figures regarding geological structures.

REFERENCES

- Amadei, B., Lin, C. and Dwyer, J. 1996. Recent extensions to the DDA method. Proc. 1st Int. Forum Discon. Anal. 1-30.
- Chang, C.-T. 1994. Nonlinear dynamic discontinuous deformation analysis with finite element meshed block system. Ph.D. Dissertation. University of California-Berkeley, Berkeley, CA.
- Hughes, T.J.R., Taylor, R.L., Sackman, J.L., Curnier, A. and Kanoknukulchai, W. 1976. A finite element method for a class of contact-impact problems. Comput. Meth. Appl. Mech. Engng. 8: 249-276.
- Ke, T.-C. 1993. Simulated testing of two dimensional heterogeneous and discontinuous rock masses using discontinuous deformation analysis. Ph.D. Dissertation. University of California-Berkeley, Berkeley, CA.
- Koo, C.Y. and Chern, J.C. 1996. The development of DDA with third order displacement function. Proc. 1st Int. Forum Discon. Anal. 342-349.
- Lin, J.-S. and Lee, D.-H. 1996. Manifold method using polynomial basis functions of any order. Proc. 1st Int. Forum Discon. Anal. 365-372.
- Liu, L. 1996. Modeling aseismic fault slips and block deformation in Northern China by DDA. Proc. 1st Int. Forum Discon. Anal. 373-382.
- Ma, M.Y., Zaman, M and Zhu, J.H. 1996. Discontinuous deformation analysis using the third order displacement function. Proc. 1st Int. Forum Discon. Anal. 383-394.
- Shi, G. 1988. Discontinuous deformation analysis-a new numerical for the statics and dynamics of block system. Ph.D. Dissertation. University of California-Berkeley, Berkeley, CA.
- Shyu, K. 1993. Nodal-based discontinuous deformation analysis. Ph.D. Dissertation. University of California-Berkeley, Berkeley, CA.
- Wang, C.-Y., Zeng, R.-S., Mooney, W.D. and Hacker, B.R. Ultrahigh-pressure Dabie Shan orogenic belt: a crustal model derived from deep seismic-refraction profiling. J. Geophys. Res. 104: In Press.

SOIL AND ROCK ANALYSIS BY MECHANICS OF MULTIPLE CONTINUOUS BODIES

C. Shih

Purdue University, School of Civil Engineering
West Lafayette, IN 47907 USA

A. Altschaeffl

Purdue University, School of Civil Engineering
West Lafayette IN 47907 USA

E. C. Ting

Purdue university, School of Civil Engineering
West Lafayette, IN 47907 USA
National Central University, Department of Civil Engineering
Chungli, Taiwan ROC

ABSTRACT: During the last decade, we attempted to develop a finite element based algorithm to study a system of multiple continuous media of distinctly different stiffness. The algorithm is capable of predicting progressive failure according to computed stresses and failure criteria. In this paper, we report our recent work and some applications in predicting behaviors and failures of soil and rock media.

With the advancement in personalized computing power, engineers are now given the tools to approach design and analysis beyond the traditional confinement. One of the developments that may have a far-reaching impact on the engineering practice is an efficient and flexible design procedure based on a realistic assessment of the failure process. Such a procedure requires an accurate algorithm to evaluate the component reliability and to predict the progressive failure and total collapse of the component due to the changing service environment and the service load.

Finite element techniques combined with the developments in material modeling have provided a solid basis to study the stress and strain distributions in a component before it begins to fail. Because of the high redundancy built in a structure, the initial failure of the component often occurs at merely a small fraction of the ultimate component capacity. To assess the true load carrying capacity, one needs to consider the continuous changes in material property, for example the yielding and hardening of metals and microcracking of brittle and inhomogeneous materials. Part of the component may fracture and separate into multiple pieces. Due to the overall ductility, the component may be subjected to very large geometrical changes before collapse. Thus, one of the primary concerns is to find new concepts and techniques to treat large displacements, fracture, and multiple continuous bodies.

1. COMPUTATIONAL MECHANICS OF MULTIPLE CONTINUOUS BODIES

Direct numerical approaches that do not follow the traditional empirical or analytical concepts seem to show the greatest promise in the development of a viable technique to simulate component failure. Most of the advancements have been reported within the last decade. Although a satisfactory algorithm is yet to be available, significant progresses have been made in various areas. In general, such an algorithm should have the capability to handle the following basic behaviors common to most failure processes:

a. Stress Analysis of the Continuum: Numerical analysis should be convenient to handle the study of stress and strain prior to failure in the context of continuum mechanics.

b. Irreversible and Inelastic Materials and Failure Criteria: Permanent deformation and irreversible stress-strain relationship are critical behaviors to a quantitative prediction of ultimate loading capacity. The algorithm should be able to handle these properties without the need for extensive computational effort.

c. Post-fracture Material Properties: Material models should be implemented to describe the degenerated material properties according to the nature of failure and how fracture occurs.

d. Mixture of Stiff and Soft Media: Due to local failures in a continuous body, a structural member may become significantly weaker in stiffness compared to other members. Current finite element and stiffness methods have difficult handling such diversities in stiffness.

e. Large Deformations and Very Large Geometrical Changes: Before fractures to start, the local deformations near the fracture zone can be extremely large for ductile materials.

Layered structures may be subject to very large inter-layer slides. Large deformation may occur in the soft layers, while the motions of stiff layers are essentially in rigid-body motions.

Large geometrical changes also lead to complicated interaction effects. These interactions should be integrated into the algorithm as natural conclusions of the geometrical changes.

f. Impact and Dynamic Responses: Critical loading environments often involve forces applied within a very short period known as impacts and shocks. Sudden changes of the constraint and loading condition of a fragmented member may induce rapid re-distributions of the stress and strain in a manner similar to impact and shock.

g. Rigid Body Motions: Rigid body motions due to inter-layer sliding or due to fragmented components separated from the original body should be integrated into the stress analysis procedure.

h. Multiple Deformable and Free Bodies: To handle phenomena such as the break-off of a structural component, sliding between layered media and the penetration of a projectile into a structure, the algorithm should have the capability of computing stresses and motions of several interacting continuous bodies.

2. OUR EFFORT

As an initial attempt in the direction of developing a comprehensive procedure for failure prediction, an algorithm is proposed which seems to have the capability of handling a stable transition from a continuous medium to become multiple deformable bodies and free bodies. The algorithm has been implemented to study frame structures and two-dimensional solid media. We briefly summarize the essential ingredients of the algorithm.

a. A Vector Formulation of Finite Element: In the traditional finite element analysis, the stiffness and force matrices are calculated based on structural discretization. These matrices are assembled to form a system of simultaneous linear equations for the solution of nodal displacements. For dynamic problems, a similar procedure to find the mass matrix and a system of differential equations are obtained.

Instead of using the matrix formulation, we propose to adopt a transient formulation developed earlier by Key, Belytschko and Hallquist. In the formulation, the continuous medium is approximated by discrete mass particles. Using the standard finite element analysis, energy equivalent internal and external forces are found. They are the forces applied on the mass particles. Newton's law of motion and time integration complete the formulation to determine the acceleration, velocity and the displacement of each particle for a particular time increment.

b. Explicit Computation: To avoid the complexity of iteration, a simple explicit time integration formulation is suggested to find velocity and displacement for each time increment. This simplifies the implementation for complicated material models, changing constraint conditions and loading conditions. Fracture, particle collision, and penetration conditions become much simpler to incorporate. However, small time and force increments are required for numerical stability. This leads to a longer computational time in general.

c. A Convected Material Frame Formulation for Large Deformation: During the fragmental process, it is required that the large rigid body motion and the large displacement should be tracked accurately. Approximated techniques such as co-rotational formulation do not provide enough accuracy for these large geometrical changes. Errors can accumulate rapidly and cause numerical instability.

To develop a more accurate approach to handle very large deformation and yet simple in computation, a convected material frame formulation of the deformation is proposed. Instead of using the undeformed geometry as the material reference frame to calculate the deformation gradient and Lagrangian strain, we propose to use the current configuration as the material frame and adopt an incremental procedure for the deformation process. For each time or force increment, the geometry of the structural element is updated. A new material frame is defined based on the current geometry. A set of geometry shape functions can be defined to describe element geometry in terms of nodal geometry parameters such as positions and slopes.

d. Mixture of Rigid and Deformable Motions: A master node-slave node approach is proposed to monitor the motion of each rigid body imbedded in a continuous medium. The rigid bodies may be subjected to very large motions and at the same time the continuous body undergoes large deformations. A slip and frictional behavior can be introduced between different bodies.

e. Fragmentation Algorithms: Several basic algorithms are needed for the purpose of monitoring the recreation of new surfaces or new bodies. Most of them can be choices of the programmer according to how the computer codes are developed. We list a few essential choices in our programming process.

** Surface Creation or Adding Bodies:* When the element stresses or the nodal displacement values satisfy a failure criterion, new nodes are added and new free surfaces are formed. The algorithm is required to check whether a new surface is permitted to exist at that location and to determine the types of constraint conditions, which should be imposed on the new nodes.

For the new nodes, dynamic allocations and parameter storage should be adjusted accordingly.

* *Internal Force Calculations:* After an element is found to be fractured, all the internal forces should be recalculated to examine whether more fracture should occur in the elements, including those already fractured.

* *Time Increment Adjustment:* To ensure numerical stability, the size of time and load increment should be re-examined according to the dimension and the stiffness of the new structure.

* *Inter-element Collision:* Fragmented components are allowed to move freely according to the force conditions. Thus, fragments may penetrate through other elements numerically. An algorithm should be adopted to control the motions of fragmented bodies.

* *Contact and Sliding Surfaces:* The master node-slave node approach can be used to handle contact and sliding surfaces commonly encountered in the study of projectile penetrations.

* *Penetration of Projectiles:* Discretized models and material properties of the projectiles can be treated as separated inputs. Their motions can be calculated in the program as part of the multiple bodies.

3. NUMERICAL EXAMPLES

Without going through the details, we show the results of two test problems that illustrate the two major aspects in the development of the algorithm, namely a patch test for handling the extremely large deformation and a numerical verification of the algorithm with the experimental results.

Figure 1a shows the schematic model of an inclined rock layer. Between two rigid blocks, an elastic-plastic soft layer is subjected to sliding shear. Figure 1b shows the sliding mechanism as a function of time.

Figures 2 through 5 depict the comparison between the predicted results and the test data for a block of dry sand induced by the pullout of a rigid anchor. The geometry, the initial finite element mesh, and the material data of the pull-out test are taken from Dickin (1994). They are summarized in Figure 2. Figure 3 plots the comparison between the numerical results obtained by the Code STONE2D and the test data. The force-displacement curves obtained by the numerical predictions are similar to an elastic-ideally plastic behavior. Including both the fragmentation and contact behaviors, the ultimate uplift force per unit length is $F = 1.21 \text{ KN/M}$. To include fragmentation only, the medium is expected to be softer. We find $F = 1.02 \text{ KN/M}$. The averaged pull-out force obtained from the tests is $F = 1.07 \text{ KN/M}$. In Figure 3, we also show the initial fracture and the corresponding stress distribution in the sand medium. Figure 4 shows the progressive failure and the stress distributions at different stages of the failure, as the anchor being pulled out. Figure 5 plots the progressive failure pattern of the sand medium predicted by the numerical analysis. Contacts between fragments are neglected in this particular series of calculations.

REFERENCES

- Chang, J. H., Yeh, R. P. and Ting, E. C. 1998. Vectorized computation for explicit finite element approach with application to fragmentation analysis, *Journal of the Chinese Institute of Civil and Hydraulic Engineering*, vol. 10, pp.183-191.
- Dickin, E. A. 1994. Uplift Resistance of Buried Pipelines in Sand, *Soils and Foundations (Japanese Society of Soil Mechanics and Foundation Engineering)*, vol.34, no. 2, pp. 41-48.
- Rice, D. L. and Ting, E. C. 1993. Large displacement transient analysis of flexible structures, *International Journal of Numerical Methods in Engineering*, vol. 36, pp. 1541-1562.
- Rice, D. L. and Ting, E. C. 1993. Fragmentation algorithm for finite element failure simulation and analysis, *International Journal of Numerical Methods in Engineering*, vol. 36, pp. 3859-3881.
- Rice, D. L. and Ting, E. C. 1992. Transient analysis of flexible space structures, *Proceedings of the 3rd International Conference on Engineering Construction and Operation in Space*, Denver, Co.
- Shih, C., Wang, Y. K. and Ting, E. C. 1997. Behavior and analysis of deformable continuous media containing rigid discontinuous bodies, *Proceedings of the 2nd International Conference on Analysis of Discontinuous Deformation*, Kyoto, Japan.
- Ting, E. C., Wang, Y. K. and Pan, A. 1995. Algorithm for the transition from continuous to discontinuous and free bodies in finite element failure analysis, *Proceedings of the First International Conference on Analysis of Discontinuous Deformation*, Chungli.
- Ting, E. C. and Wang, Y. K. 1997. Discontinuous media and explicit finite elements, An invited paper, *Magazine of Chinese Mechanics Society*, No. 78, pp.1-5.
- Wang, Y. K. and Ting, E. C. 1998. A general curved element for very flexible beam, Technical report CE-STR-98-01, Department of Civil Engineering, National Central University.

Figure 1a. The schematic model of an inclined rock layer

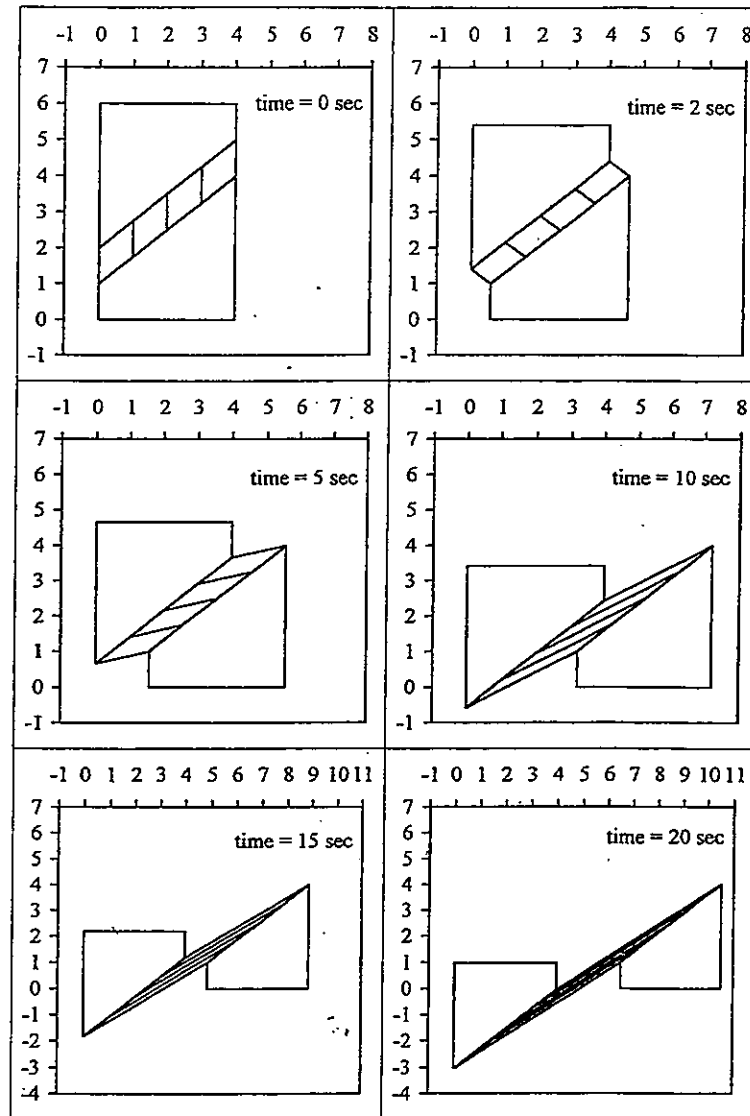
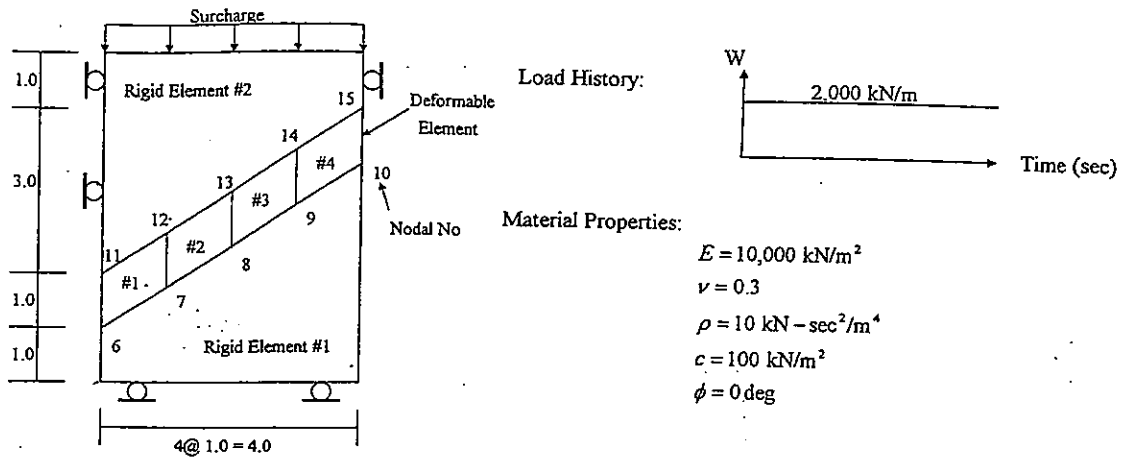
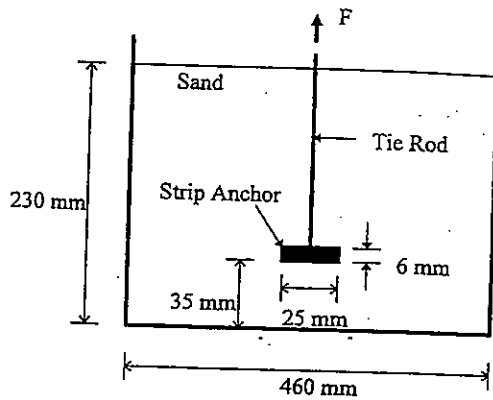
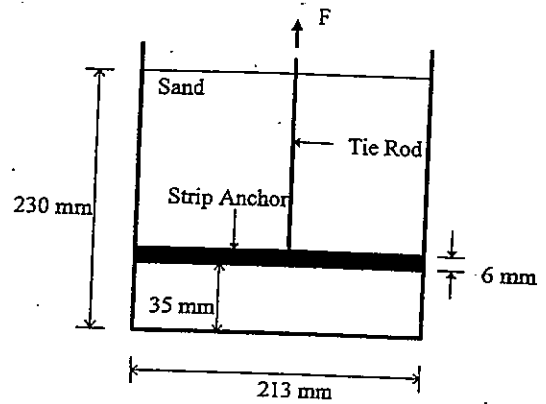


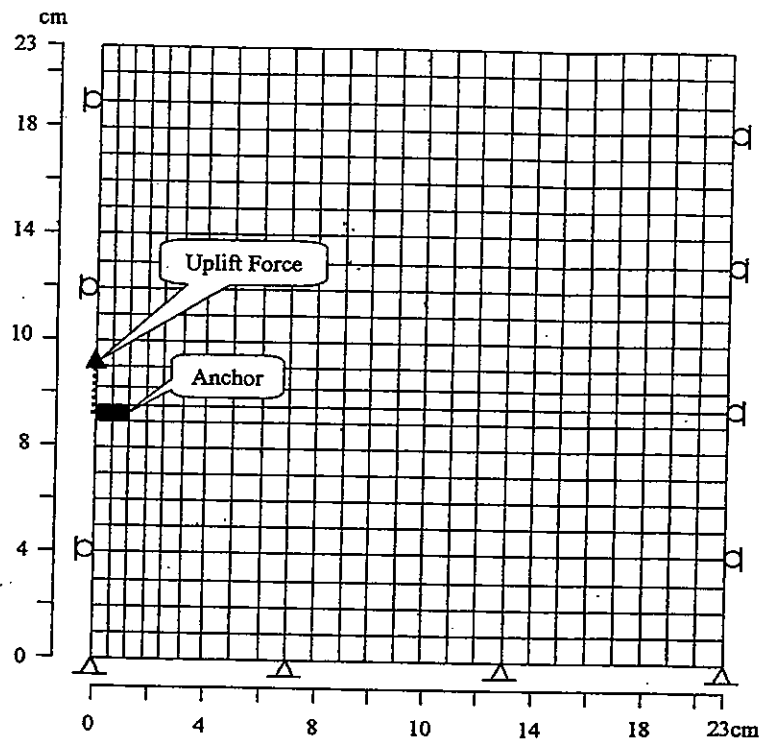
Figure 1b. Time history of the sliding of an inclined rock layer



(a)



(b)



Material Properties of Loose Sand:

Total Unit Weight, $\gamma_t = 14.5 \text{ kN/m}^3$

Elasticity Modulus, $E = 10,000 \text{ kN/m}^2$

Poisson Ratio, $\nu = 0.3$

Cohesion, $c = 0$

Internal Friction Angle, $\phi = 30 \text{ deg.}$

Mass Damping Coefficient, $\alpha = 100 \text{ sec}^{-1}$

Figure 2. The geometry (a. front view and b. side view), initial finite element mesh, and material data of a pull-out test

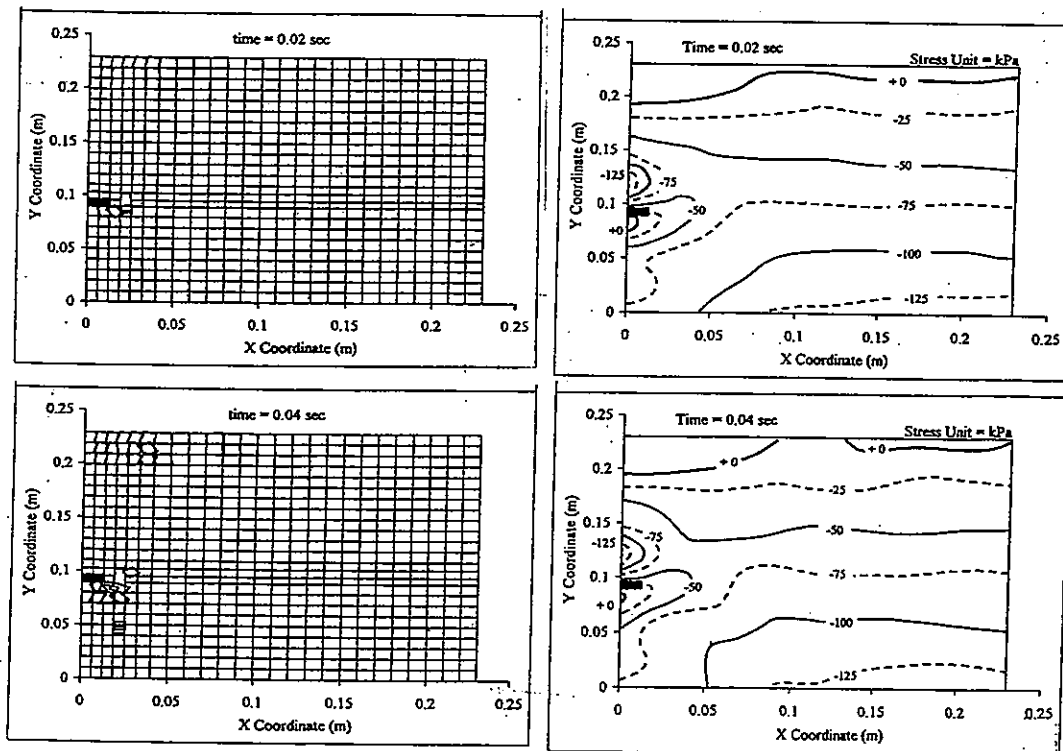
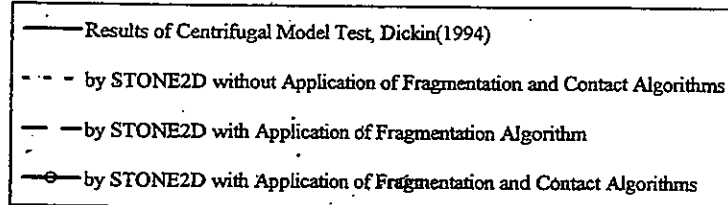
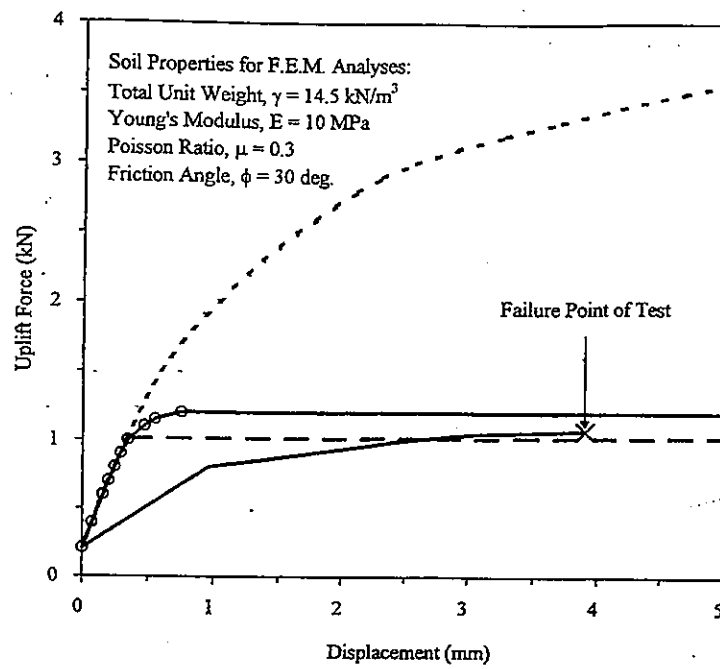


Figure 3. Comparison of the numerical results with the experimental data

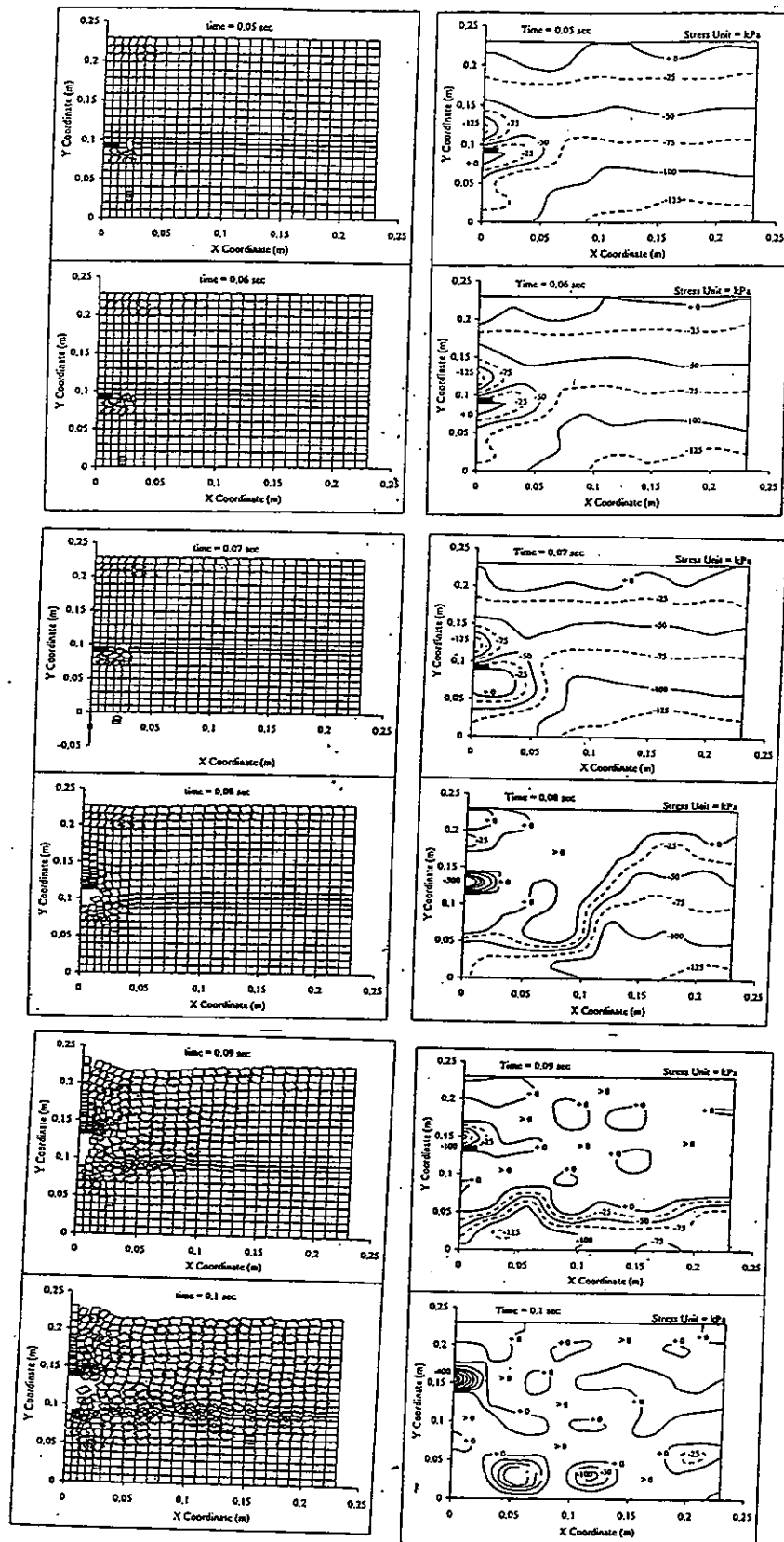


Figure 4. Progressive failure and stress distribution in the sand medium

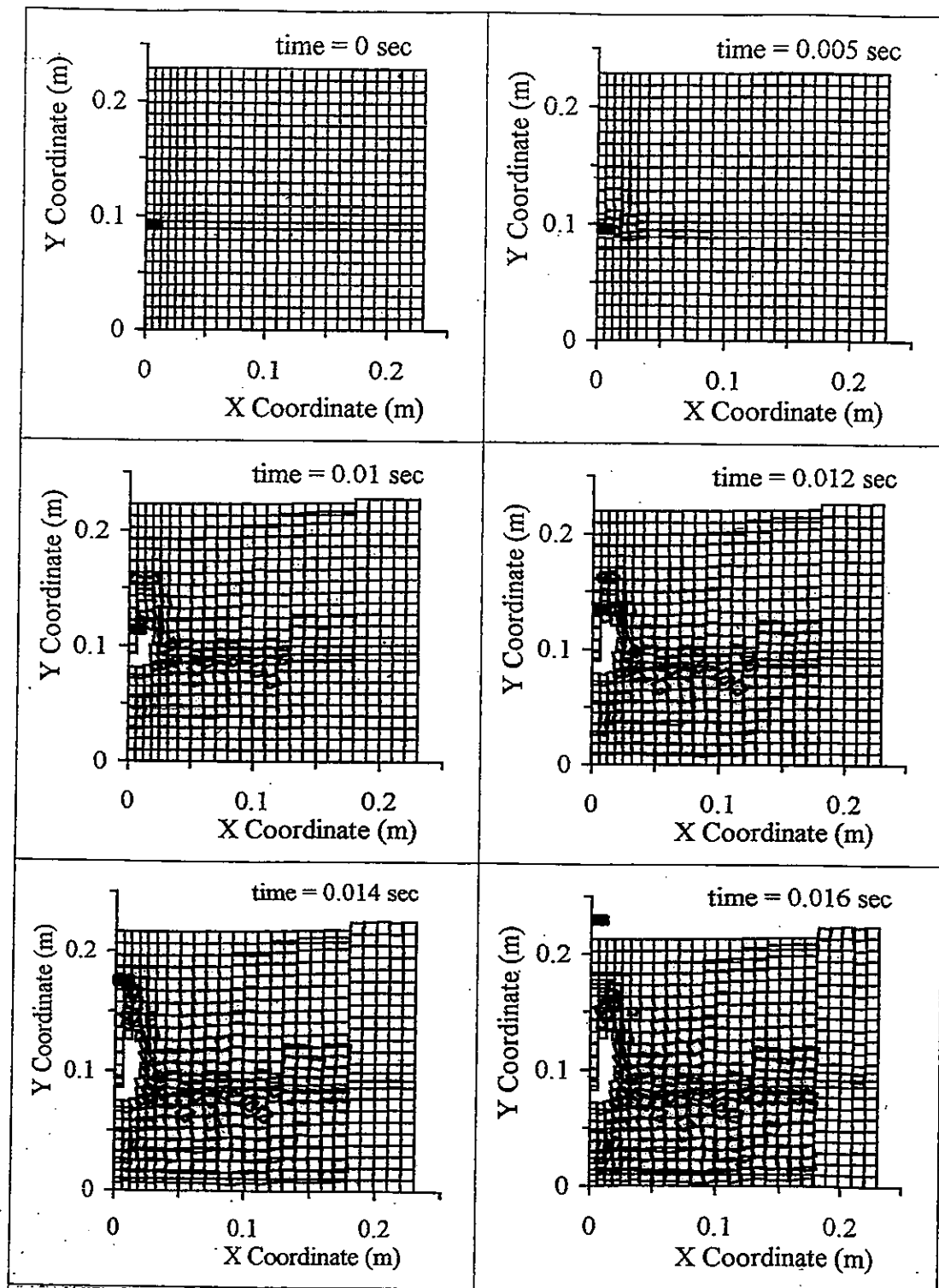


Figure 5. Progressive failure pattern (fragmentation algorithm only)

STABILITY ANALYSIS OF THE SHIP-LOCK SLOPES OF THE THREE GORGES PROJECT BY THREE-DIMENSIONAL FEM AND DEM TECHNIQUES

Weishen Zhu and Qiangyong Zhang
Institute of Rock & Soil Mechanics, Wuhan, the Chinese Academy of Sciences
Wuhan, 430071, China

Lanru Jing
Division of Engineering Geology, Royal Institute of Technology,
S-10044 Stockholm, Sweden.

ABSTRACT: The stability of the high and steep slopes formed during the excavation of the double ship-locks of the Three Gorges Hydro-Power Complex is one of the major technical concerns of the project, and many numerical analyses were performed over the years with different modelling techniques. In this contribution, three-dimensional simulations of the excavation processes of the double ship-locks were performed with both a Finite Element Method and a Distinct Element Method. Based on a constitutive model of elasto-plastic damage evolution and consideration of effects of bolt reinforcement on the fractured rocks, the FEM model tried to study the failure mechanism and deformation process of the fractured granite rocks of the slope, considering mainly the effects of several sets of secondary fractures. The DEM model using code 3DEC was applied to predict the possibility of large scale instabilities of rock movements along some large scale major fault surfaces. The two codes were applied in parallel to compare the different results by two conceptual models and the predictions indicate that large-scale instability induced by the excavations of the double ship-lock is very small. The long-term effects of rock/fault creeping were not considered in the analysis.

1 INTRODUCTION AND SITE GEOLOGY

The Three Gorges Project, the largest project of hydraulic engineering in the world today, is under construction. On the left bank a five-stage double ship-lock with a total length of 1.6 km is under construction. The widths of the two lock chambers are m each, with a central rock column separating them. On the two sides of the double ship-locks high and steep slopes are formed due to excavation of a large volume of rock, with the highest point reaching 170m. The lower parts of the slopes are the vertical walls of the lock chambers, of 50m in height. The rock is mainly granite, containing 4 to 5 sets of secondary fractures. Superimposed on the fracture sets are a number of large-scale major faults and veins in the region, which causes a major concern on their effects on the overall stability of the high and steep slope. Therefore the study of the effects of both large-scale faults/veins and secondary scale fractures sets on the slope stability is of great importance. Figure 1 shows the distribution of the major faults and veins in the ship-lock area and table 1 lists the geometrical properties of the secondary scale fractures sets. There is significant weathering at the shallow depth of 0 – 25 m, moderate weathering at depth of 25 – 40 m and slight weathering at depth of 40 – 50 m. The rocks are also heavily fractured by four sets

of non-persistent fractures and a large number of major faults and veins. All these cause complex hydro-mechanical property variations.

The in situ stress field of the region has been extensively measured over the years and analyzed, with different interpretations. The in situ stress field adopted for this study is given as

$$\sigma_x = 4.4 + 0.01168H, \sigma_y = 1.66 + 0.3039H, \tau_{xy} = 0.047 + 0.00008H \quad (1)$$

for the horizontal stress components and the vertical components corresponds to the overburden. Symbol H stands for the depth (m) and the unit of stress is MPa.

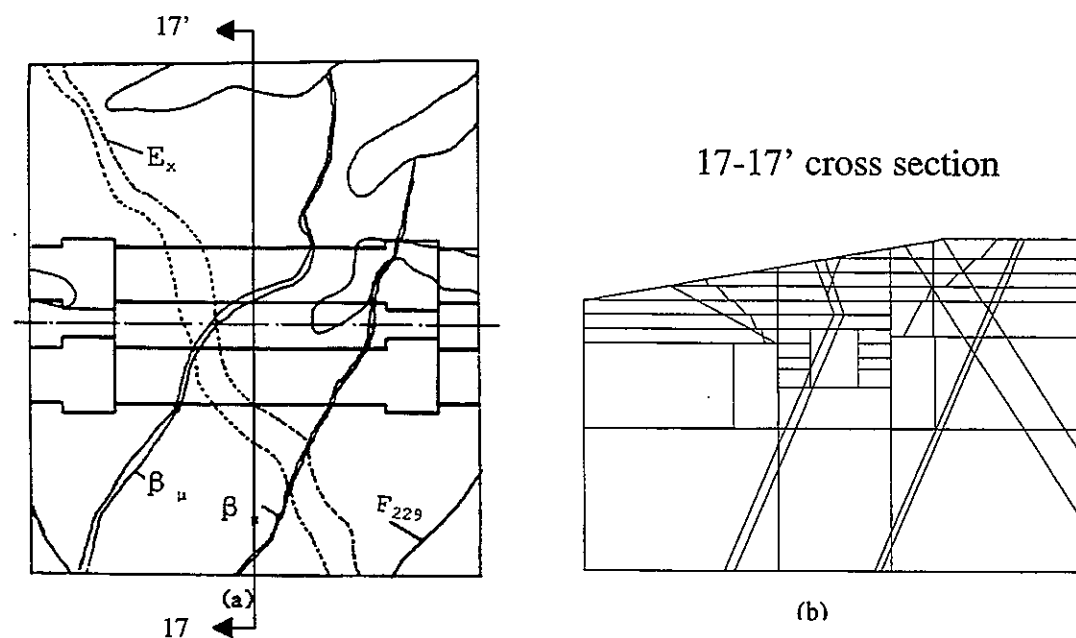


Figure 1 Major faults and veins in the ship-lock area. The dashed lines indicate the ship-lock boundaries. a) Plane view; b) Cross section at 17-17'.

Table 1. Geometrical properties of the secondary scale fractures sets

Fracture Set	Dip direction (°)		Dip angle (°)		Trace length (m)	
	Mean Value	Standard deviation	Mean value	Standard deviation	Mean value	Standard deviation
1. NEE	337	11.0	76	6.7	3.82	0.52
2. NNE	286	-	62	-	4.04	1.11
3. NNW	258	8.4	68	11.6	3.63	0.92
4. NWW	15	11.8	75	7.3	2.94	1.11

This paper presents prediction results from two numerical models applied to analyze the stability of the ship-lock slopes. The first model, the 3D FEM model, considered the influence of the 5 sets of non-penetrating fractures by means of an equivalent (smear-out) elasto-plastic damage constitutive model, with consideration of the reinforcement effects of bolt support in the equivalent properties. This 3D FEM computer code used was not optimal for including large

number of major faults or veins, and their effect on the overall stability of the slopes was investigated by analysis using a 3D DEM code 3DEC. An assumption was made that the rock mass was a simple elasto-plastic material following a Mohr-Coulomb yield criterion.

2 THE ELASTOPLASTIC DAMAGE CONSTITUTIVE MODEL

Assuming that the fractures in a rock mass are penny-shaped and applying the concept by Fanella et al. (1988), the 3-D propagation crack can be simplified to a 2-D propagation crack problem (Fig. 2). Based on these concepts, Zhang et al. (1998) proposed the following constitutive model for fractured rocks by the theory of elasto-plastic damage, given by

$$\varepsilon_{op}^{e-d} = C_{opkl}^{e-d} \sigma_{kl} = (C_{opkl}^e + C_{opkl}^{od} + C_{opkl}^{ad}) \sigma_{kl} \quad (2)$$

where

$$C_{ijkl}^e = \frac{1+\nu_0}{2E_0} (\delta_{ik}\delta_{jl} + \delta_{jk}\delta_{il}) - \frac{\nu_0}{E_0} \delta_{ij}\delta_{kl} \quad (3)$$

$$C_{opkl}^{od} = \frac{1}{E_0} \sum_{k=1}^M \{ \rho_v^{(k)} a^{(k)^3} [2G_1(1-C_v^{(k)})^2 n_o^{(k)} n_p^{(k)} n_k^{(k)} n_l^{(k)} + \frac{1}{2} G_2(1-C_s^{(k)})^2 (\delta_{kp} n_o^{(k)} n_l^{(k)} + \delta_{ko} n_p^{(k)} n_l^{(k)} + \delta_{lo} n_p^{(k)} n_k^{(k)} + \delta_{lp} n_o^{(k)} n_k^{(k)} - 4n_o^{(k)} n_p^{(k)} n_k^{(k)} n_l^{(k)})] \} \quad (4)$$

$$C_{opkl}^{ad} = \frac{1}{E_0} \sum_{k=1}^M \{ \rho_v^{(k)} a^{(k)^2} [B_1^{(k)} n_o^{(k)} n_p^{(k)} n_k^{(k)} n_l^{(k)} + B_2^{(k)} (n_o^{(k)} + n_l^{(k)} \delta_{kp} + n_p^{(k)} n_l^{(k)} \delta_{ko} + n_o^{(k)} n_k^{(k)} \delta_{lp} + n_p^{(k)} n_k^{(k)} \delta_{lo})] \} \quad (5)$$

where E_0 , ν_0 are the elastic modulus and Poisson's ratio of non-damaged rock mass respectively; M is the number of prevailing fracture sets in a unit volume of fractured rock mass; $a^{(k)}$ is the average radius of the k th fracture set in statistics; $\rho_v^{(k)}$ is average volume density of the k th fracture set; $C_v^{(k)}$ and $C_s^{(k)}$ are the pressure-transmitting and shearing-transmitting coefficients of the k th fracture set, respectively; $n_i^{(k)}$ is the unit normal vector of the k -th set of fractures; σ, τ are the projections of the applied stress tensor along the normal and tangential directions of a fracture plane respectively; and G_1 , G_2 are the coefficients given by Yang (1990). See Zhang et al. (1998) for the evaluations of functions $B_1^{(k)}$ and $B_2^{(k)}$.

From the second thermodynamic principle of irreversible process, the constitutive relation of an elastoplastic damage of the fractured rockmass, can be written, in the form of global variables,

$$\varepsilon = C^{e-d} : \sigma + \varepsilon^p \quad (6)$$

By derivation of the two sides of eq. (6) with respect to the virtual time, one obtains

$$\dot{\varepsilon}_{ij} = C_{ijkl}^{e-d} \dot{\sigma}_{kl} + C_{ijkl}^{e-d} \sigma_{kl} + \dot{\varepsilon}_{ij}^p = \dot{\varepsilon}_{ij}^e + \dot{\varepsilon}_{ij}^d + \dot{\varepsilon}_{ij}^p \quad (7)$$

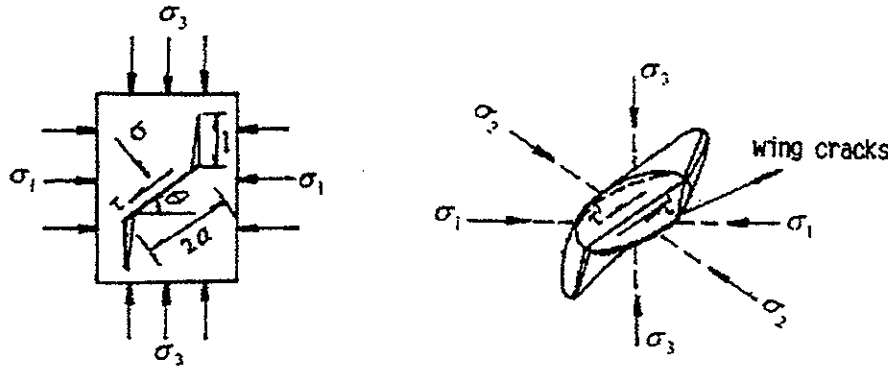


Figure 2 Simplification of a 3-D propagating crack to a 2-D propagating crack.

where $\dot{\epsilon}_{ij}^e$ is the elastic strain rate, $\dot{\epsilon}_{ij}^p$ is the plastic strain rate and $\dot{\epsilon}^d$ is the coupled damage strain rate caused by the weakening of the rockmass in its elastic properties due to damage evolution. By adopting a generalized orthogonal flow rule,

$$\dot{\sigma}_{kl} = (C_{ijkl}^{e-d})^{-1} (\dot{\epsilon}_{ij} - \lambda \frac{\partial f}{\partial \sigma_{ij}}) \quad (8)$$

the 3-D constitutive relationship of elastoplastic damage for multi-crack rockmass can be finally written (Zhang et al., 1998)

$$\dot{\sigma}_{kl} = K_{klrs} \dot{\epsilon}_{rs} \quad (9)$$

where K_{klrs} is the modulus tensor of elasto-plastic damage for multi-fractures rockmass, and whose numerical evaluation can be found in Zhang et al. (1998).

3 FORMULATION OF THE BOLT MODEL

The bolts are represented by a cylindrical damage rock-bolt element (CDRB element) to simulate reinforcement effect of bolting. Suppose that the bolt and fractured rock within a certain range comprise a CDRB element (see Fig.3a). A CDRB element is buried in a fractured rock to form a composite element of fractured rock with bolts, referred to as the BDR element in Fig.3b.

The CDRB element is assumed as orthogonal anisotropic damage medium. The contribution of CDRB element to the overall stiffness matrix of the system, i.e., the additional stiffness matrix $[K_e]_{add}$, can be derived according to the interpolation theory of FEM and the theorem of virtual work, given by Zhang et al. (1998)

$$[K_e]_{add} = [N]^T [K_e] [N] \quad (10)$$

where $[N]$ is the matrix of shape function, $[K_e]$ is the stiffness matrix of CDRB element in the global coordinate system of x - y - z , having value of

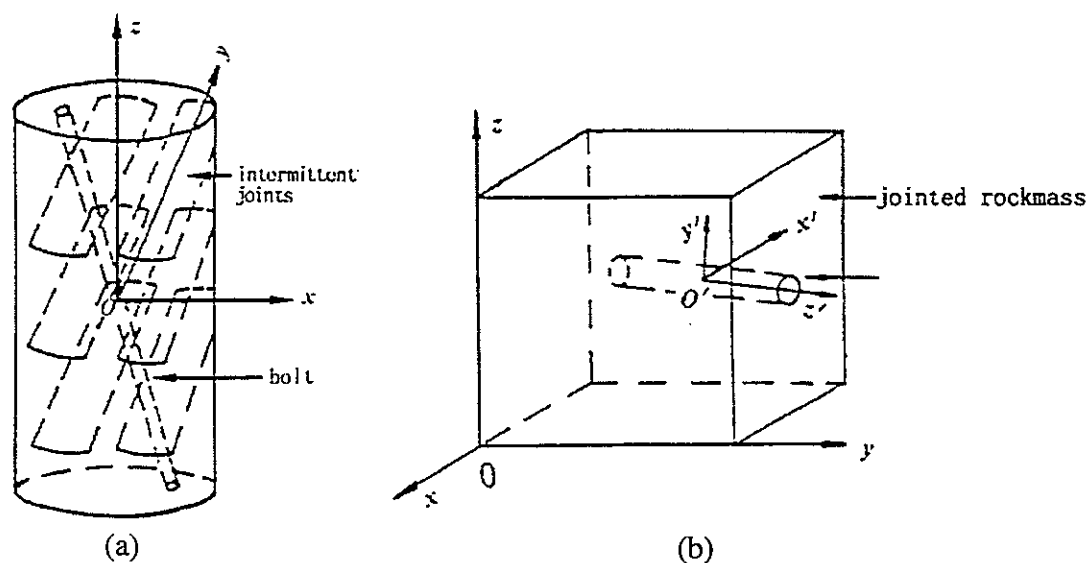


Figure 3 a) Cylindrical damage model of rock bolt element – the CDRM model; b) The damage model of bolted rock element - the BDR model.

$$[K_e] = [T]^T \left\{ \int_V [B]^T [D_e] [B] dv \right\} [T] \quad (11)$$

in which $[T]$ is the stiffness conversion matrix, $[B]$ is a geometry matrix and $[D_e]$ is the elastic damage matrix of orthogonal anisotropy for CDRB element. They are all evaluated numerically, see Zhang et al. (1998) for details.

4 THE 3D FEM MODEL OF THE SHIP-LOCK SLOPE

The 3-D FEM mesh of the problem is shown in Fig. 4a (Zhang et al. 1998). The top of the model represents the original ground surface before excavation. The boundary conditions of the model are that: i) the top surface is free; ii) the four vertical boundaries are specified with in situ stresses according to equation (1), the bottom boundary is fixed by zero displacement in normal directions. The model consists of 944 FEM element and 1972 nodes. The size of the model is 1200 m (length) x 200 m (width) x 462 m (height). The orientation of the model is parallel with the flow direction of the Yangtse River (West-East). The model contains the Gate Chamber III section of the ship-lock. Five stages of stepwise excavation procedures have been simulated, see Fig. 4b. The level which each excavation steps reached in the simulations are 170 m (Step 1), 155 m (Step 2), 140 m (Step 3), 125 m (Step 4) and 92.5 m (Step 5), respectively.

The effects of the four non-persistent fracture sets, NEE, NNE, NNW, NWW, were considered by the FEM model in the constitutive parameters for the fractured rocks. The effect of bolting was considered in the FEM model for two design options: i) 5~8m in length for the inclined slope with a spacing of 3 m x 3 m, and ii) 10~16m in length for vertical walls or middle bulk pier with a spacing of 2.5m x 2 m. Tables 2 and 3 list all mechanical properties of rocks, fractures and bolts used by the FEM model.

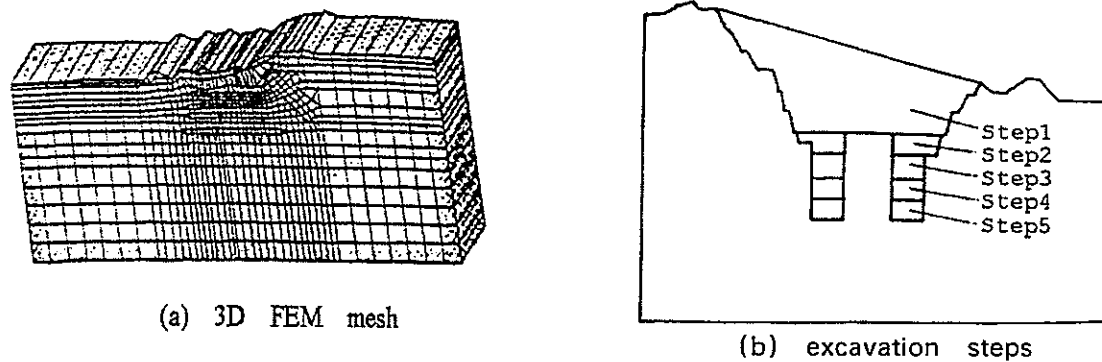


Figure 4 The 3D view of the FEM model (a) and the 5 excavation steps (b).

Table 2a. Mechanical properties of different materials

Type		E (GPa)	ν	Tan(ϕ)	C (MPa)
Rock	Strongly weathered	0.1	0.35	0.7	0.1
	Moderately weathered	1.0	0.3	1.0	0.35
	Slightly weathered	15	0.24	1.3	1.0
	No weathering	40	0.22	1.8	1.8
Bolt	(Steel)	210	0.2	-	-

Table 2b. Mechanical properties of rock fractures

Fracture	Kn (MPa/m)	Ks (MPa/m)	C (MPa)	Tan (ϕ)
Set 1	25	10	0.12	0.5
Set 2	25	10	0.12	0.5
Set 3	75	30	0.2	0.6
Set 4	75	30	0.2	0.6

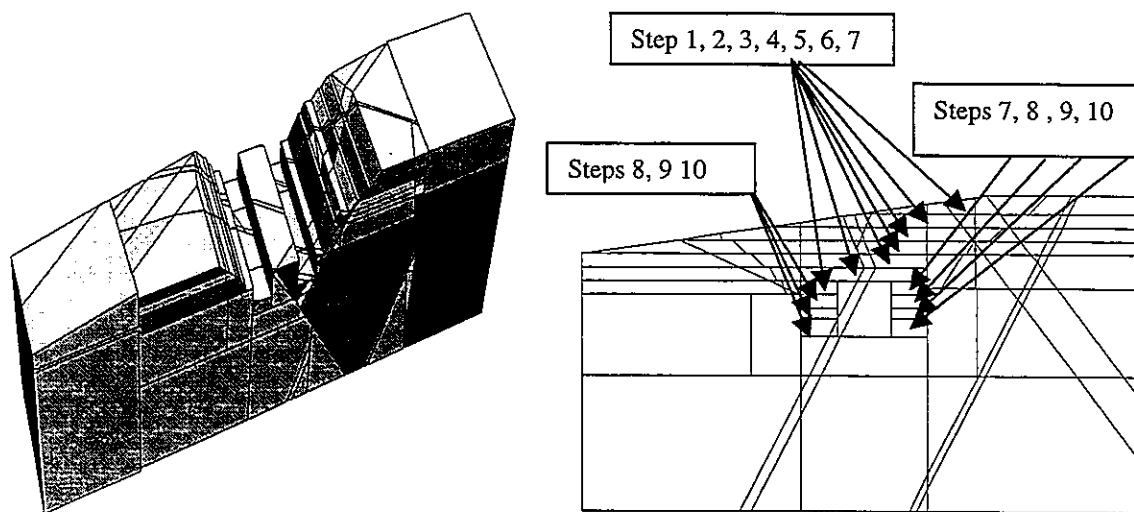
5 THE 3D DEM MODEL

The size of the DEM model is 1000×350×200m in three orthogonal directions x, y and z, respectively, with the positive y-axis pointing upward, and z-axis along the downstream of the Yangtse River, and x-axis across the Yangtse River, thus forming a left-hand co-ordinate system. The model incorporates the following structures: 1) five veins: Ex, $\beta_{\mu 1001}$, $\beta_{\mu 1003}$, $\beta_{\mu 1005}$, $\beta_{\mu 1008}$; 2) five faults: F_8 , F_{209} , F_{203} , F_{229} , F_{1009} .

The mean widths of veins were considered in the model (varying between 10 – 20m); but the widths of faults were ignored. These structural features, together with artificial discontinuities necessary for defining the slope and ship lock geometry, cut the whole problem domain into 609 blocks, which was further discretized by 18322 tetrahedral finite difference elements.

The gradual decreasing topographic heights of the ground surface was approximated by a dipping plane, starting from the exposure of the Ex vein and downstream. The slope steps and ship lock were created according to the design figures, see Fig. 5.

The boundary conditions of the DEM model are the same as that of the FEM model. The initial stress field according to equation (1) was first assigned into every elements of the model



(a) a 3D View of the DEM model.

b) Simulated excavation steps

Figure 5 Geometry and excavation steps of the DEM model (excavated volume hidden).

directly according to their depth, and the model was relaxed under the boundary stresses until an equilibrium state was reached. Excavation is simulated by removing the blocks occupying the rock volumes for the designated excavation steps in the model. This will then create an unbalanced net force which was then relaxed again by a large number of small time steps until a new equilibrium state was reached (i.e. the net unbalanced forces created by removing the concerned blocks in the model becomes negligible). In the DEM model the excavation were performed by ten steps (Fig. 5b): 1) 250 - 230 m; 2) 230 m - 215 m; 3) 215 m - 200 m; 4) 200 m - 185 m; 5) 185 m - 170 m; 6) 170 m - 155m; 7) 155 m - 140m; 8) 140 m - 125m; 9) 125 m - 112.9m; 10) 112.9 m - 92.5m. The mechanical parameters used in the DEM model are the same as that in the FEM model, with the exception that no bolt and damage evolution were considered in the DEM analysis.

6 RESULTS AND DISCUSSIONS

6.1 Displacement

Figure 6 compares the total displacement magnitudes at four monitoring points (1969, 1785, 1751 and 1707, as shown in Fig. 6a), after the excavation reached the depth of 80 m (at the end of Step 1 in the FEM model and Step 5 in the DEM model). It seems that the predicted and measured data have reasonably acceptable agreements.

After the validating of the numerical models by the above measured data, the simulations were further performed to predict the maximum accumulated total displacements in the model to see if any large scale rock movement may occur along one of the major faults or veins. Figure 7 shows the accumulated maximum displacement magnitudes at the end of the excavation by both DEM and FEM models. The DEM results show that although the maximum displacement may increase

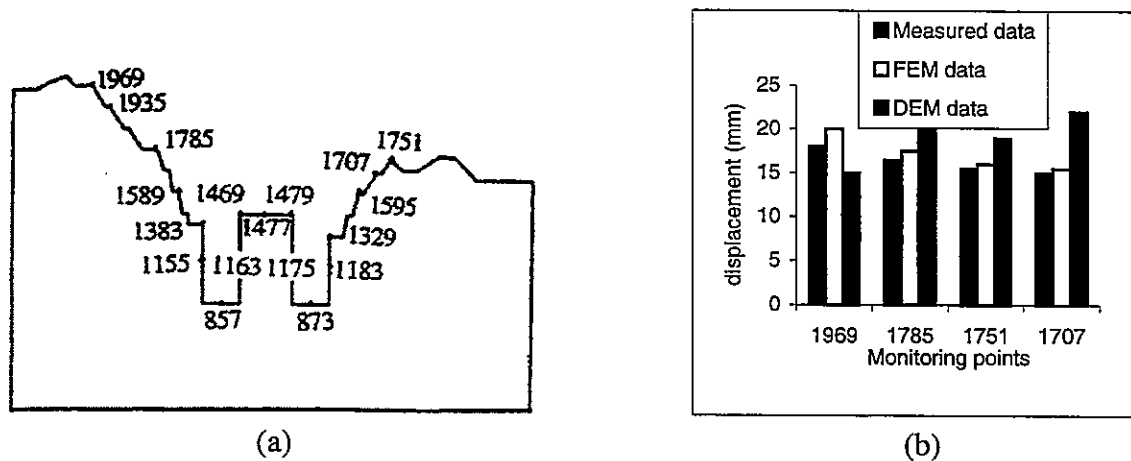


Figure 6 Measured and computed total displacement at four monitoring points. (a) The locations of the 4 points in the 20-20' cross-section. (b) FEM and DEM results, compared with measured data.

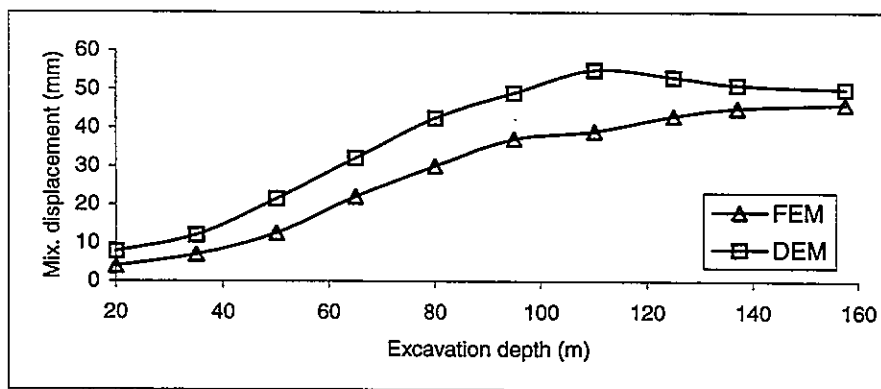


Figure 7 Maximum total displacement versus excavation depth.

with increase of the excavation depth its increases is steady and proportional to the excavated rock volume. The maximum displacement decreases after the 150 m of excavation depth, when starting excavating the ship-lock chambers, because the excavated volume becomes much smaller. The DEM model generates consistently larger displacement than its FEM counterpart, due perhaps to its accumulated large deformation algorithms.

In the DEM model, the maximum displacement appears basically at the center of the excavation, roughly along the central line of the model, and generally at the floor of the excavated area, as a floor heaving. The downwards displacements of the slopes are generally much smaller than that of the floor heaving, usually only 50-60% of the maximum total displacement. No excessive shear displacement along any of the major fault or vein was found in the DEM results. The calculated maximum horizontal shear displacement is about 10.5mm at the end of excavation of Step 8 at 125m, along the Ex and β_{1005} veins. The shear displacement magnitude is much less than that of the total displacement and will not be significant enough to cause failure. In the vertical direction, the calculated shear displacement along major faults or

veins of the slopes is also not significant. Only on the central column dividing the two ship locks, a block appears to have a shear displacement of 18.5mm along vein $\beta_{\mu 1003}$, passing through the central column (Fig.8). This shear displacement is at the same order of magnitude as the total displacement of the block.

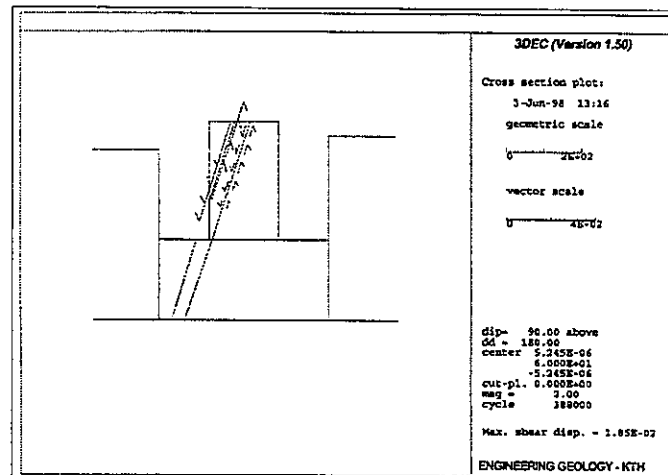


Figure 8 Shear displacements along a major fault on a vertical cross section along 17-17 line.

6.2 Stresses and failure zones

The stress tensors are dominated by the horizontal stress relieve near the excavated slope surfaces and ship lock boundaries. The stress distribution is, however, affected by the non-uniform distribution of the element sizes. Figure 9 shows the plasticity zone distribution calculated by the FEM model, before and after the reinforcement by bolts, with the latter much smaller than the former, showing significant improvement of the rock mass integrity due to bolting.

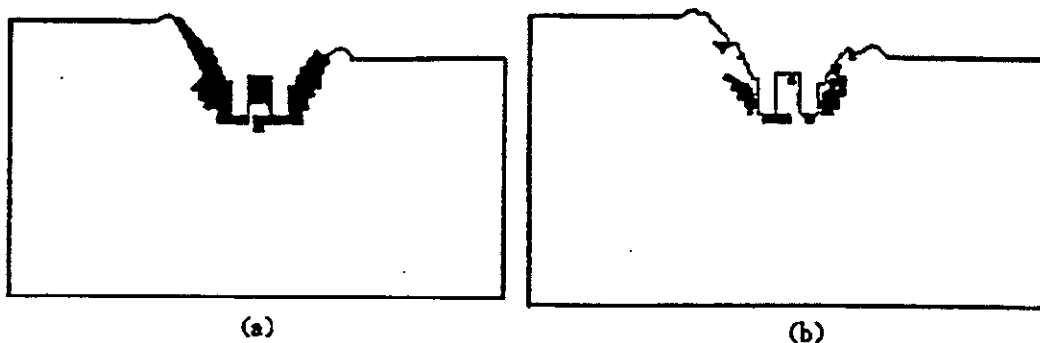


Figure 9 Plasticity zone (Black area) distribution before and after the bolting by FEM mdoel. a) Before bolting; b) after bolting.

7 CONCLUSIONS

The computed results by FEM and DEM lead to the following conclusions:

- (1) The displacements from numerical computation are, in general, in reasonably acceptable agreements compared with measured data at early excavation stage.
- (2) The numerical predictions to the complete excavation of the ship-lock slope and chambers show no large scale sliding failures of rock along any one of the major faults or veins. This may, however, change in practice due to the models' limits on the number of the faults and veins which can be included in the model due to limit in computing resources, and the limit in understanding the mechanical behaviour of the large scale faults or veins. The scale effect may also play a significant role that cannot be considered in the current FEM or DEM models.
- (3) The FEM results show that the rock-bolt supporting can increase the integraty and bearing capacity of the surrounding rock mass and decrease the damage evolution zone significantly.
- (4) From the DEM computation, although there is no indication that a large scale instability may occur in the high and steep slopes of double ship-lock area, there are possibilities of smaller scale failures of wedge sliding type on the central column, or even at some local slope surfaces. Therefore proper local reinforcement measures should be considered.

ACKNOWLEDGEMENT

The research work is financially supported by National Natural Science Foundation of China and China Yangtse Three Groges Project Development Corporation (Grant no. 59493600)

REFERENCES

- Ashby, M. F. and Hallam, S. D. 1986. The failure of brittle solids containing small cracks under compressive stress states. *Acta Metall*, 34(3): 497~510.
- Dragon, A. and Mroz, Z. 1979. A continuum model for plastic-brittle behaviour of rock and concrete. *International Journal of Science* 17: 121~137.
- Fanella, D. and Krajcinovic, D. 1988. A micromechanical model for concrete in compression. *Engineering Fracture Mechanics* 29(1): 49~66.
- Lemaitre, J. A. 1996. *Course on Damage Mechanics*. Beijing: Chinese Sciences Press.
- Li, X. and Zhu, W. 1992. The damage fracture analysis of fractured rockmass and its application in engineering. *Engineering Fracture Mechanics* 43(2): 165~170.
- Yang, Y. 1990. A fracture damage model for fractured rockmass and its application to the rock engineering. *Ph.D. dissertation*, Qinghua University, Beijing.
- Zhang, Q. 1998. Research on 3-D damage fracture model for bolted intermittent multi-cracks rockmass and its numerical simulation with application in engineering. *Ph.D. dissertation*, Institute of Rock & Soil Mechanics, the Chinese Academy of Sciences, Wuhan, China.
- Zhang, Q. and Zhu, W. 1998. Elastoplastic damage constitutive model for fractured rockmass and its rock-bolt computation. *Chinese J. of Geot. Engng.* 20(6): 90~95.

CRACK PROPAGATION BY MANIFOLD AND BOUNDARY ELEMENT METHOD

Guo-Xin Zhang

River Technology Department, I.N.A. Corporation
Sekiguchi 1-44-10, Bunkyo-ku, Tokyo, 112-8668, Japan

Yasuhito Sugiura

River Technology Department, I.N.A. Corporation
Sekiguchi 1-44-10, Bunkyo-ku, Tokyo, 112-8668, Japan

Hiroo Hasegawa

River Technology Department, I.N.A. Corporation
Sekiguchi 1-44-10, Bunkyo-ku, Tokyo, 112-8668, Japan

ABSTRACT: A second-order manifold method has been developed and is described. By means of the manifold method and a singular boundary element method proposed by the author, the failure process of a structure can be numerically analyzed. Mohr-Coulomb's law is employed as a criterion for new crack initiation, and maximum circumferential stress theory is used as criterion for the first and mixed mode (opening-shearing and closing-shearing) propagation of existing cracks. Comparison of the computed stress intensity factor with results obtained via the collocation method demonstrates the high predictive accuracy of the present method. Examples of our present method are presented.

1. INTRODUCTION

Several numerical methods are available for simulating crack propagation and the failure of structures with discontinuities. These methods include the Finite Element Method (FEM), the Boundary Element Method (BEM), the Discrete Element Method (DEM) and the Discontinuous Displacement Analysis (DDA). Although the FEM and the BEM using fine meshes with special elements can model crack propagation and the failure of structures, it is difficult to describe the discontinuities after cracks begin propagating, and small deformation restrictions are usually needed. Also the number of cracks that can be handled is limited. Therefore the behavior of failed structures and problems involving many discontinuities cannot be readily analyzed. The DEM and DDA can be utilized to model the behavior of discontinuities or block systems, but the stress distribution inside the blocks cannot be calculated properly, hence the propagation of cracks through the blocks cannot be well modeled.

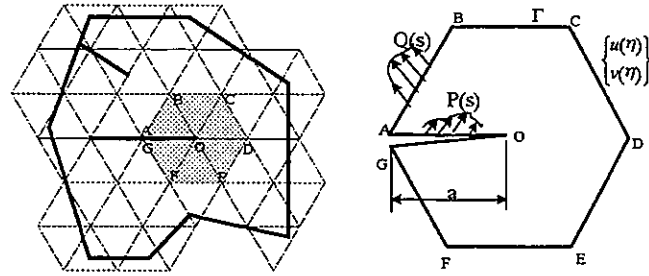
Proposed by Shi (1991), the Manifold Method (MM) is a new numerical tool for solving problems involving both continuous and discontinuous media. By introducing the concept of a cover and two sets of meshes, the manifold method combines the advantages of the FEM and DDA. It can deal with not only discontinuities, contact, large scale deformation and block movement as does the DDA, but also the stress distribution within each block as accurately as does the FEM.

To simulate crack initiation and propagation by the manifold method, Zhang et al. (1997,1998) have extended the original MM by using the Mohr-Coulomb's law to determine the fracture criterion. But a misevaluation may occur on account of the stress concentration near the crack tip. Because the stress at the crack tip is always infinite even for a small load (in the brittle

fracture problem), the crack may continue propagating indefinitely when the meshes are fine enough if the Mohr-Coulomb's criterion is utilized.

In this paper we propose a method that combines the second order MM and the singular BEM to simulate crack initiation and subsequent propagation. The stress and displacement fields are calculated via the second order MM; the Stress Intensity Factor (SIF) at the crack tip is computed using the singular BEM. The Mohr-Coulomb's fracture criterion is only used to locate the initial crack; for analyzing its subsequent propagation the SIF is the criterion used. Numerical examples are given to illustrate application of this method.

The numerical procedure for simulating crack propagation is as follows: Firstly, calculate the displacement and stresses of a structure {Fig. 1 (a)} with discontinuities using the second order manifold method. Secondly, specify a sub-region including at least one crack tip as a specific problem, solve this problem using the singular BEM. In doing this, the displacements obtained by manifold method along the boundary of sub-region is taken as the restraint conditions, and the traction free condition at the crack surface is considered {Fig. 1 (b)}. Finally, calculate the SIF at the crack tip, judge the crack to be propagating or not, reform the mathematical and physical meshes as needed and recalculate, and then move to the next region.



(a) Structure with discontinuities. (b) Sub-region containing a crack.
Figure 1. Structure containing cracks and an enlarged sub-region.

2. STRUCTURE ANALYSIS BY MANIFOLD METHOD

2.1 Basic concepts of MM

The manifold method uses the concept of cover and two sets of meshes. Cover is used to define the local function that will be described in the next section. Every cover overlays a fixed area, the size and shape of this area can be chosen arbitrarily depending on the problem to be solved. The covers overlap one another and overlay the entire physical domain.

The two sets of meshes are the physical meshes and mathematical meshes. The physical meshes describe the physical domain (including boundaries, joints and the interfaces between blocks) and define the integration areas. The mathematical meshes, on the other hand, are enclosed lines more or less arbitrarily selected for the problem. The areas enclosed by the mathematical meshes are called the mathematical covers, on which the space function is built.

For each cover, a local function can be defined, and these local functions can be combined using a weighting function to form a global function that defines the displacement and stress in the whole region. If the local cover function $u_i(x, y)$ is defined for a physical cover U_i , the global function $u(x, y)$ for the whole physical cover system can be expressed as:

$$u(x, y) = \sum_{i=1}^n w_i(x, y) u_i(x, y) \quad u_i(x, y) \quad (x, y) \in U_i \quad (1)$$

where $w_i(x, y)$ is weight function defined as:

$$w_i(x, y) \geq 0 \quad (x, y) \in U_i, \quad w_i(x, y) = 0 \quad (x, y) \notin U_i, \quad \text{with} \quad \sum_{(x, y) \in U_i} w_i = 1.$$

The simultaneous equilibrium equation takes the form:

$$\left\{ \frac{2}{\Delta t^2} [M] + \frac{2}{\Delta t} [C] + [K] \right\} \{\Delta D\} = \frac{2}{\Delta t} [M] \{\dot{D}\} + [\Delta F], \text{ with } u_i(x, y) = \begin{Bmatrix} u_i \\ v_i \end{Bmatrix} = \{D_i\} \quad (2)$$

where Δt is a time step, $[M]$ is the inertia matrix, $[C]$ is the viscosity matrix, $[K]$ is the global stiffness matrix (including element stiffness, penetration of the contact point and the stiffness of the fixed point), $\{\Delta D\}$ is the increment of displacement, $\{\dot{D}\}$ is the velocity vector, $\{\Delta F\}$ is the load increment including initial stress, body force, point load, bonding force and penetration force of contact. A detailed discussion of Equation (2) can be found in papers reported by Shi(Shi 1991).

With the cover concept and the definitions of local and global functions, the MM can model a wide variety of continuous and discontinuous structures. The FEM and DDA can be regarded as special cases of it.

2.2 Second-order MM

The original first-order MM uses the constant cover displacement $u_i(x, y)$ and the linear weight function $w_i(x, y)$ to construct the global displacement function. Use of a linear global function reduces the accuracy of the MM in simulating crack propagation. To increase the predictive accuracy a second-order MM is introduced here by constructing a second-order global function.

A second-order displacement function can be built in either of two ways: (a) the linear weight function $w_i(x, y)$ and the linear cover function $u_i(x, y)$ (Chen et al 1997), (b) the second-order weight function $w_i(x, y)$ and the constant cover function $u_i(x, y)$. We follow the latter one here and consider the six node finite elements forming the mathematical meshes. The second-order weight function is:

$$w_i(x, y) = f_{i1} + f_{i2}x + f_{i3}y + f_{i4}x^2 + f_{i5}xy + f_{i6}y^2 \quad (i=1, 2 \dots 6). \quad (3)$$

The global function of second-order is Equation (3) together with Equation (1) for the constant local function $u_i(x, y)$.

A computational example is given here to compare the predictive performance of the original MM and our second-order MM. Figure 2(a) shows a 2m×0.5m cantilever loaded by $P = 980$ kN. The Young's modulus and Poisson's ratio for the cantilever are 98 MPa and 0.24, respectively. Computed displacements at points A, B and C are compared with the analytical solutions in Table 1. The calculation meshes and the deformations of the cantilever by the first-order MM and the second-order MM are shown in Figure 2{(b)-(d)}. The results confirm a drastic improvement in predictive accuracy with the second order MM.

Table 1. Comparison of computed displacements with analytical solutions.

Point \ Method	Analytical (mm)	First Order MM (mm)	Second Order MM (mm)
A	0	0	0
B	84	23	84.4
C	264	85	266.8

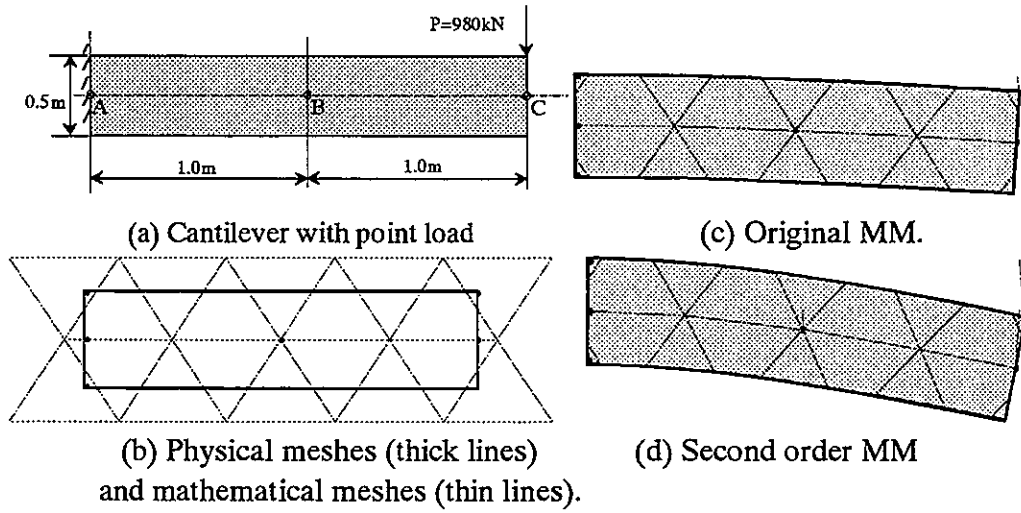


Figure 2. Deformation of cantilever by the Manifold Method.

3. SUB-REGION ANALYSIS USING SINGULAR BEM

The sub-region with a crack {Fig. 1(b)} and the known boundary displacement $\bar{u}(\eta), \bar{v}(\eta)$ can be regarded as a boundary value problem and can be solved by an indirect boundary element method. In order to form the integral equations, necessary for solving the problem, two kinds of fundamental solutions are required.

3.1 Static mechanical fundamental solution for an infinite continuous region

When a complex point force $Q = \frac{F_x + iF_y}{2\pi(1+\kappa)}$ is applied at point $z = s$ on

a complex plane (Fig. 3), the stresses and displacements in the x_1-y_1 coordinate system which makes an angle α with the x direction at point z can be obtained from the Kelvin solution (Zhang et al 1992):

$$\sigma_{y_1}^{*(1)} - i\tau_{xy_1}^{*(1)} = -Q \left[\frac{1}{z-s} - \kappa e^{-2i\alpha} \frac{1}{\bar{z}-s} \right] - \bar{Q} \left[\frac{1}{\bar{z}-s} - e^{-2i\alpha} \frac{(z-s)}{(\bar{z}-s)^2} \right]$$

$$\sigma_{x_1}^{*(1)} + \sigma_{y_1}^{*(1)} = -2Q \frac{1}{z-s} - 2\bar{Q} \frac{1}{\bar{z}-s}$$

$$u_1^{*(1)} + v_1^{*(1)} = \frac{e^{-i\alpha}}{2\mu} \left\{ -\kappa Q [\ln(z-s) + \ln(\bar{z}-s) + 1] + \bar{Q} \frac{z-s}{\bar{z}-s} \right\}$$

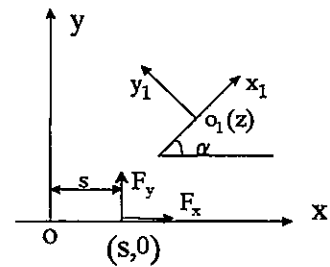


Figure 3. Infinite plane with point load at $(s, 0)$.

where μ is the shear modulus, $\kappa = 3-4\nu$ for the plane strain and $\kappa = (3-\nu)/(1+\nu)$ for the plane stress.

3.2 Fundamental solution of a point force on crack surface

In order to fix the singularity at the crack tip, a singular fundamental solution should be used. For an infinite region with a crack of length $2a$ subjected to a paired point force $P = F_y - iF_x$ at $z=s$, as shown in Figure 4, the stresses and displacements in the x_1-y_1 coordinate system can be obtained by solving the Cauchy problem (Zhang et al 1996):

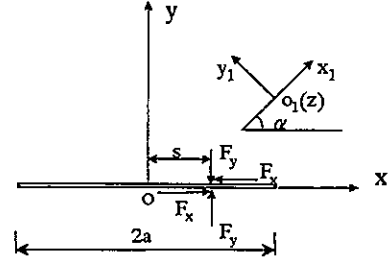


Figure 4. Infinite plane with crack, and the point load $P = F_y - iF_x$

$$\begin{aligned} \sigma^{*(2)}_{y_1} - i\tau^{*(2)}_{x_1 y_1} &= PC(z, a, s, \alpha) + \bar{P}D(z, a, s, \alpha) \\ \sigma^{*(2)}_{x_1} + \sigma^{*(2)}_{y_1} &= -2 \frac{\sqrt{a^2 - s^2}}{\pi} \operatorname{Re} \left[\frac{P}{(z-s)\sqrt{z^2 - a^2}} \right] \quad (5) \\ u_1^{*(2)} + v_1^{*(2)} &= \frac{e^{-i\alpha}}{4\pi\mu} \left\{ \frac{P[\bar{f}_1(z, a, s) - \kappa f_1(z, a, s)]}{+ \bar{P}(z - \bar{z})\sqrt{a^2 - s^2} G(z, a, s)} \right\} \end{aligned}$$

where:

$$\begin{aligned} G(z, a, s) &= \frac{1}{(z-s)\sqrt{z^2 - a^2}} \\ f_1(z, a, s) &= i \left[\ln \left(\frac{\sqrt{z^2 - a^2} + i\sqrt{a^2 - s^2}}{z-s} - \frac{is}{\sqrt{a^2 - s^2}} \right) - \ln \left(1 + \frac{s}{\sqrt{s^2 - a^2}} \right) \right] \\ C(z, a, s, \alpha) &= -\frac{1}{2\pi} \sqrt{a^2 - s^2} [G(z, a, s) + e^{-2i\alpha} \overline{G(z, a, \alpha)}] \\ D(z, a, s, \alpha) &= -\frac{1}{2\pi} \sqrt{a^2 - s^2} \left[\overline{G(z, a, s)}(1 - e^{-2i\alpha}) + e^{-2i\alpha} (z - \bar{z}) \overline{G'(z, a, \alpha)} \right] \end{aligned}$$

3.3 Boundary integral equations

Returning to the sub-region problem shown in Figure 1(b), we assume a distributed fictitious force $Q(s)$ is applied to the boundary Γ and the fictitious force $P(s)$ acts on the crack surface. The stresses and displacements at point z in the sub-region can be defined by integrating Equations (4) and (5):

$$\begin{aligned} u_1(z, \alpha) + iv_1(z, \alpha) &= \int_{\Gamma} \{ u_1^{(0)}[Q(s), z, \alpha] + iv_1^{(0)}[Q(s), z, \alpha] \} ds + \int_{-a}^a \{ u_1^{(2)}[P(s), z, \alpha] + iv_1^{(2)}[P(s), z, \alpha] \} ds \\ \sigma_{x_1}(z, \alpha) + \sigma_{y_1}(z, \alpha) &= \int_{\Gamma} \{ \sigma_{x_1}^{(0)}[Q(s), z, \alpha] + \sigma_{y_1}^{(0)}[Q(s), z, \alpha] \} ds + \int_{-a}^a \{ \sigma_{x_1}^{(2)}[P(s), z, \alpha] + \sigma_{y_1}^{(2)}[P(s), z, \alpha] \} ds \quad (6) \\ \sigma_{x_1}(z, \alpha) - i\tau_{x_1 y_1}(z, \alpha) &= \int_{\Gamma} \{ \sigma_{x_1}^{(0)}[Q(s), z, \alpha] - i\tau_{x_1 y_1}^{(0)}[Q(s), z, \alpha] \} ds + \int_{-a}^a \{ \sigma_{x_1}^{(2)}[P(s), z, \alpha] - i\tau_{x_1 y_1}^{(2)}[P(s), z, \alpha] \} ds \end{aligned}$$

Suppose the displacement on boundary Γ calculated by the MM is $\bar{u}(\eta) + i\bar{v}(\eta)$, where $\bar{u}(\eta)$ and $\bar{v}(\eta)$ denote the normal and tangential displacements at point η on Γ . Let point z in

the first formula of Equation (6) approach the point η on the boundary Γ , i.e., $(u(z) + iv(z))|_{z \rightarrow \eta} = \bar{u}(\eta) + i\bar{v}(\eta)$, an integral equation that satisfies the known displacement condition on Γ can be obtained:

$$\int_{\Gamma} \left\{ \mu_1^{(1)} [Q(s), \eta, \beta_{\eta}] + i\nu_1^{(1)} [Q(s), \eta, \beta_{\eta}] \right\} ds + \int_{-a}^a \left\{ \mu_1^{(2)} [P(s), \eta, \beta_{\eta}] + i\nu_1^{(2)} [P(s), \eta, \beta_{\eta}] \right\} ds = \bar{u}(\eta) + i\bar{v}(\eta). \quad (7a)$$

Another integral equation can be reached by using the crack surface condition. It is different from the mode of fracture problem.

For first and opening-shearing mode fracture problem, the traction free condition on the crack surface both in normal and tangential direction should be satisfied. The equation can be obtained by letting point z in the third formula of Equation (6) approach the point ξ on the crack surface in a similar way with formula (7a) and let the normal and shear stress on crack surface to be zero as:

$$P(\xi) + \int_{\Gamma} \left\{ \sigma_{y_1}^{(1)} [Q(s), \xi, \beta_{\xi}] - i\tau_{xy_1}^{(1)} [Q(s), \xi, \beta_{\xi}] \right\} ds + \int_{-a}^a \left\{ \sigma_{y_1}^{(2)} [P(s), \xi, \beta_{\xi}] - i\tau_{xy_1}^{(2)} [P(s), \xi, \beta_{\xi}] \right\} ds = 0 + i0 \quad (7b)$$

For the closing-shearing problem, the normal displacement of upper and lower crack surface should be the same, the traction free condition should be satisfied only in tangential direction as:

$$F_x(\xi) + \operatorname{Re} \left\{ \int_{\Gamma} \tau_{xy_1}^{(1)} [F_x(s), \xi, \beta_{\xi}] ds + \int_{-a}^a \tau_{xy_1}^{(2)} [F_x(s), \xi, \beta_{\xi}] ds \right\} = 0 \quad (7c)$$

where $\beta_{\eta} = \alpha_{\eta} - \alpha_s$.

Solving Equation (7) by the boundary element method yields solutions for $Q(s)$ and $P(s)$. The stress intensity factors K_I and K_{II} at the crack tip can then be calculated from Equation (8) (Zhang et al. 1992):

$$K_I - iK_{II} = -\frac{1}{\sqrt{\pi a}} \int_{-a}^a P(s) \sqrt{\frac{a+s}{a-s}} ds. \quad (8)$$

In calculating the SIF using a traditional numerical method like the FEM, fine meshes near the crack tip are usually necessary in order to capture the stress concentration there. But actually the singular area is restrained to a small region near the crack tip, and its influences on the stress and displacement in the far area are not significant. In the present method, the stress and displacement are firstly calculated by the second-order manifold method and their precision far from the crack tip can be ensured. The SIF is computed by the singular BEM based on the stress and displacement obtained. Therefore higher accuracy in the calculation of the SIF can be ensured even when relatively coarse meshes are used near the crack tip.

In order to examine the accuracy of the method, we compute the SIF of the edge and central cracks in a rectangular plate here. The results are compared with the collocation method (Marukami 1987). Figure 5 shows the meshes used in the calculation. The results are given in Figure 6. It can be seen that the SIF calculated by the present method agrees quite well with that obtained via the collocation method. For the central crack with $a/w = 0.25$ the error is less than 5.5% although only two elements are set on the crack. Further calculation shows that the error reduces to less than 0.5% if four elements are used for the crack.

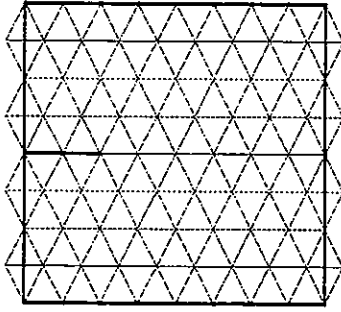
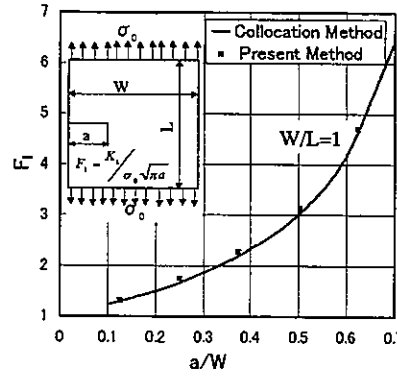
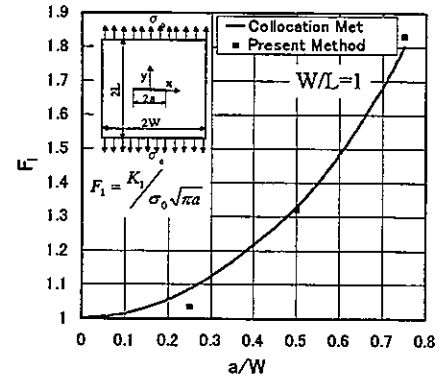


Figure 5. Meshes used in the analysis.



(a) SIF of an edge crack.



(b) SIF of a central crack.

Figure 6. SIF of cracks in rectangular plate.

4. CRACK MODELING

Manifold method provides an easier way to simulate crack propagation. Crack can propagate in any direction independent of the meshes. When a crack grows, the work needed to be done is only add a new cover to cover system and refresh the physical mesh by adding the new crack to boundary lines.

Different criteria are used in the new crack initiation and the growth of existing cracks. Fracture criteria using the SIF can only be used for existing cracks. For the initiation of new cracks, a stress-based criterion should be considered. In this paper, Mohr-Coulomb's law with three parameters is taken as the failure criterion for new cracks. It is assumed that new cracks start appearing if: (a) the first principle stress is larger than the tensile strength of the material, or (b) the maximum shear stress is larger than the shear strength of the material. Take σ_1 and σ_3 to indicate the first and third principal stresses, the failure criterion can then be expressed as:

$$\begin{aligned} \text{Tensile failure: } \sigma_1 &= T_0. \\ \text{Shearing failure: } \frac{(\sigma_1 - \sigma_3)}{2} &= C \quad \text{if } \frac{(\sigma_1 + \sigma_3)}{2} > 0 \text{ and } 0 < \sigma_1 < T_0, \\ &= C \cos \phi - \frac{(\sigma_1 + \sigma_3)}{2} \sin \phi \quad \text{if } \frac{(\sigma_1 + \sigma_3)}{2} < 0 \text{ and } 0 < \sigma_1 < T_0, \end{aligned} \quad (9)$$

where T_0 is the tension strength of the material, C is the cohesion and ϕ is the friction angle.

For existing cracks, the fracture toughness K_{IC} of material is taken as the fracture criterion, and the maximum circumferential stress theory (Erdogan et al 1963) is adopted to determine the direction of crack growth measured from the current crack line θ :

$$K_I \sin \theta + K_{II} (3 \cos \theta - 1) = 0. \quad (10)$$

The fracture criterion for mix mode problem takes the form as:

$$\cos \frac{\theta_0}{2} (K_I \cos^2 \frac{\theta_0}{2} - \frac{3}{2} K_{II} \sin \theta_0) = K_{IC}. \quad (11)$$

The present research assumes no energy loss in the fracture process, that is, the total energy of the cover before fracture has to equal to the energy of the two covers after the fracture. In order to ensure energy conservation during fracture, new-formed covers are forced to have the same velocity, stresses and coordinate as the original ones.

5. APPLICATION EXAMPLES

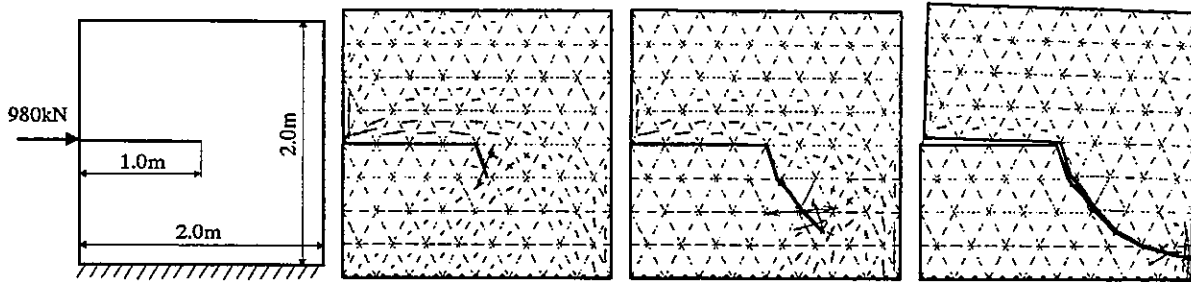
5.1 Failure of point-loaded block with edge crack

This example simulates crack propagation in a 2m×2m block with a 1m long crack. A load of $H = 980$ kN acts horizontally. Figure 7(a) shows a diagram of the block and load. The material properties and calculation conditions are listed in Table 2.

Figure 7 depicts the principal stress field and the crack propagation process in the block. In the calculation, the load H is divided into 10 sequential steps. With each step, an additional 98 kN load is added. For the first and second (loading) steps, the stresses in the block and the SIF at the crack tip are not large enough to initiate new cracks or propagate existing cracks. At the third step, the SIF at the crack tip reaches the fracture criterion {Equation (11)}. The crack starts propagating {Fig. 7(b)} in a direction that is about 70 degrees with the horizontal. The crack continues propagating and changes its propagation direction and finally penetrates the whole block {Fig. 7(c) and (d)}.

Table 2. Material properties and calculation conditions.

Elastic Modulus	19600 MPa
Poisson's Ratio	0.24
Fracture Toughness	490 N/cm ^{3/2}
Unit Mass	23.52kN/m ³
Tension Strength T_0	0.98 MPa
Cohesion C	2.94 MPa
Friction Angle ϕ	30 degree
Calculation Mode	Static
Penalty (kN/m)	4900000000



(a) shape and load. (b) beginning of propagation. (c) crack growth (d) crack penetration.

Figure 7. Crack propagation in block.

5.2 Failure of bending beam

A beam of 3m×1m with two vertical loads $P = 490$ kN at points 0.3m far from the central line of its upper surface. A crack of 0.125m long is pre-made at the central of the lower surface (See Fig. 8). The Young's modulus and Poisson's ratio of the beam are 19600 MPa and 0.2 respectively. The unit weight of material is 19.6 kN/m³. Other parameters and computational conditions are the same as those used in the previous example. The static mode is also used in this example. The load P is subdivided into four loading steps. The principal stress distribution, the crack propagation and the displacement of the beam at loading step 2 are shown in Figure 9.

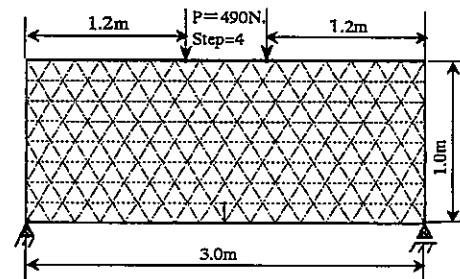


Figure 8. Four-point bending beam.

Figure 9 shows that the stress is concentrated near the two restraint points, the loading points and the crack tip. At the second (loading) step, the SIF reaches the failure criterion and the crack starts to growth {Fig. 9 (a)}. The crack propagates until the beam ruptures {Fig. 9(c)}. The direction of crack propagation is nearly along the vertical before the length of crack is less than two third of the depth of beam. Cataclastic failure occurs on the middle of upper surface after the crack penetrates the beam {Fig. 9(d)}.

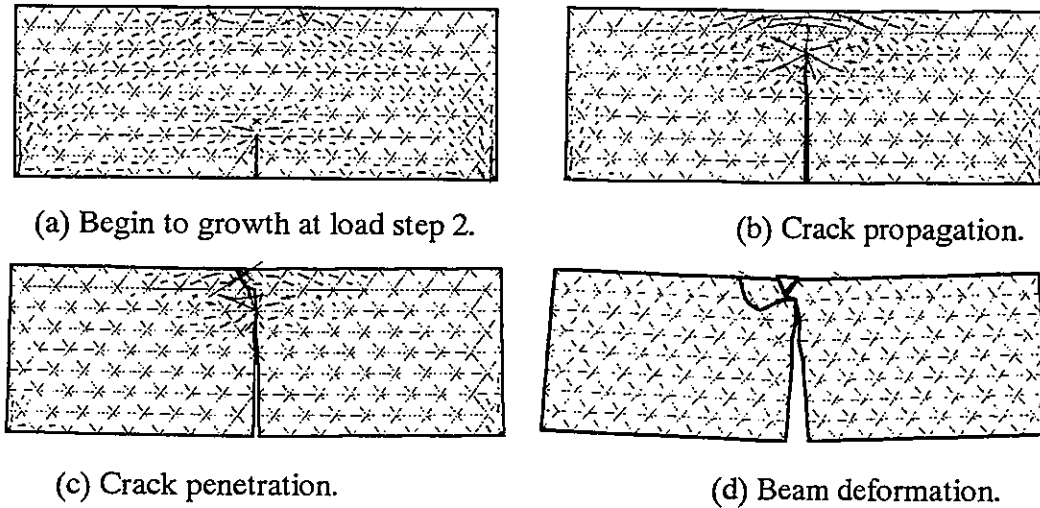


Figure 9. Principal stress distribution and crack propagation three point bending beam.

5.3 Failure of structure and the movement of blocks

Figure 10 shows another computational example of the failure of a structure and the movement of blocks. The structure is loaded by a horizontal point load $P = 196$ kN. The load P is subdivided into four loading steps for the calculation. At the third loading step, the crack begins to form at the left corner {Fig. 11(a)} and propagates into the block until the structure is broken into two [Fig. 11{(b)-(d)}]. The upper block starts to move with a continued application of the load {Fig. 11(e)}.

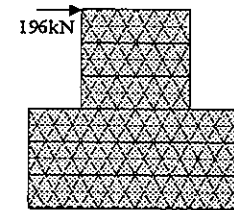


Figure 10. Mesh and load

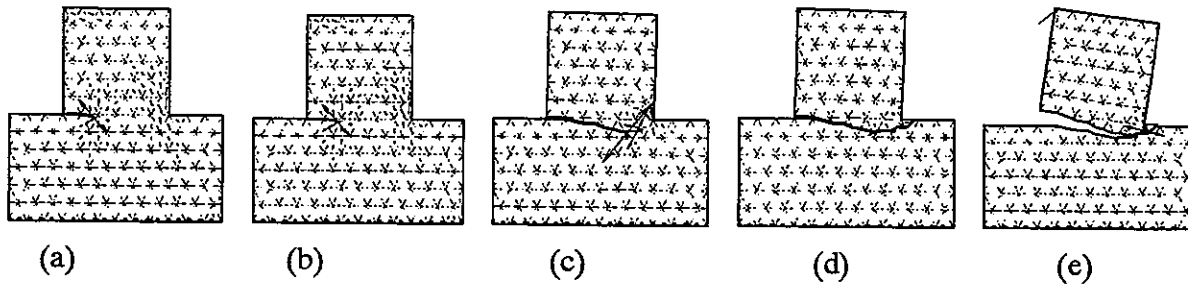


Figure 11. Failure of structure and movement of block

5.4 Example of closing-shearing problem

Figure 12 gives an example to show the application to closing-shearing problem. A rectangle sample with a crack, which lays 45° with horizontal, is shown in Figure 12 (a). The bottom is fixed and the top is forced to displace downward. The material properties are also listed in Table 2. Because the two surface of original crack is closed together and can transfer normal compression stress, the first mode SIF K_I is zero, the crack begins to propagate as shown in Figure 12(b). The crack gradually grows until it penetrates the whole sample {Fig. 12 (c), (d)}, and new cracks occur at other place. At last the sample is broken by cracks almost parallel to the direction of loading. This kind of failure pattern agrees with compression test of rock or concrete (Charles Jaeger 1972).

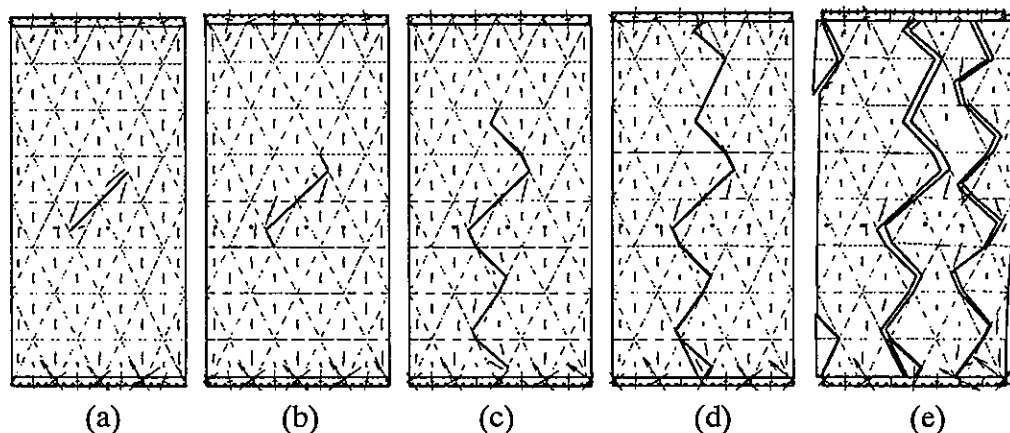


Figure 12. Compression failure of cample with crack.

6. CONCLUSION

The second-order manifold method can be used to calculate the displacement and stresses of structure with discontinuities accurately. Together with singular BEM and fracture theory, the SIF at crack tips can be predicted precisely and the crack propagation can be well simulated. Manifold method is less mesh-dependant than the FEM, the simulated crack growth is independent of mesh. Given examples have demonstrated the versatility of this method for simulating first and mixed mode fracture problem, and can also be used in closing-shearing fracture problem.

REFERENCES

- Charles Jaeger. 1972. Rock mechanics and engineering. Cambridge University Press.
- Chen, G., Ohnishi, Y. and Ito, T. 1997. Development of high order manifold method. *Proceedings of the Second International Conference on Analysis of Discontinuous Deformation*. Kyoto, Japan, pp. 132-154.
- Erdogan, F. and Sih, G. C. 1963. On the crack extension in plates under plane loading and transverse shear. *ASCE, J. Basic Engng.* Vol. 85, pp. 519-525.
- Murakami, Y. 1987. *Stress intensity factor handbook (vol. 1)*, Pergamon Books Ltd., Great Britain.
- Shi, G. H., Manifold method of material analysis. *Proceedings of Ninth Army Conference on Applied Mathematics and Computing*. Minnesota, U.S.A., pp. 51-76, 1991.
- Zhang, G. X., Sugiura, Y. and Hasegawa, H. 1997. Crack propagation and thermal fracture analysis by Manifold Method. *Proceedings of the Second International Conference on Analysis of Discontinuous Deformation*. Kyoto, Japan, pp. 282-297.
- Zhang, G. X., Sugiura, Y. and Saito, K. 1998. Failure simulation of foundation by manifold method and comparison with experiment. *Journal of Applied Mechanics (JSCE)*. Vol. 1, pp.427-436.
- Zhang, G. X. and Liu, G. T. 1992. Thermally stressed multiple system in steady state. *Theoret. Fracture Mech.* Vol. 17, pp. 69-81.
- Zhang, G. X. and Liu, G. T. 1996. Harmonic thermal fracture of multiple crack system and the stability of cracks in RCC arch dam. *Engng. Fracture Mech.* Vol. 54, No. 5, pp. 653-656.

CRACK PROPAGATION USING MANIFOLD METHOD COUPLED WITH ELEMENT FREE METHOD

Zhou Weiyuan,
Department of hydraulic Engineering
Tsinghua University Beijing China
100084

Kuo Xiaodong
Department of hydraulic Engineering
Tsinghua University Beijing China
100084

Yang Roqiong
Department of hydraulic Engineering
Tsinghua University Beijing China
100084

ABSTRACT: In rock concrete like materials, generally there appear fractures and fissures of different sizes, and their failures under stress undergo initiations, propagation, nucleation and fracture. To trace crack behaviors in rock mass, manifold and element free methods are coupled and used. Afore the crack tips, a process zone is presented, and the cracks propagate under the fracture criterion. In the paper, MM coupled with EFM crack propagation analysis is presented.

1 INTRODUCTION

Crack propagation problems are vital to the structure analysis such as in arch dams, slopes, etc. Rock cracks, generally cause failure in the abutments of dams. So far, no valid measures can be adopted for analyzing crack propagation.

FEM has the difficulties in mesh regeneration. It is far more time consuming and expensive task than assembly and solution of finite element equation. To simulate crack propagation, mesh regeneration is required for preparation of data. The authors have studied diffused element method, to calculate the crack propagation. The interpolation functions are polynomials which are fitted to the nodal values by moving least-square approximations,

The method could be used to simulate the crack tip stress field and incorporate an interface prior to the crack tips. To couple with diffused element, the manifold method is introduced to modify the discontinuous interfaces and coalescence of fissures.

Manifold method coupled with diffused element method may be effectively used to analyze progressive failure during rock failure involving discontinuous and continuous media. It may be widely used in solving geotechnique problems.

In this paper, crack propagation in rock-like material is described and novel technique is

presented.

2 MANIFOLD AND DIFFUSED ELEMENT METHOD COUPLED IN APPLICATION

In the domain Ω , deformation function $u(x)$ is assumed, where point coordinate: $\bar{x} = (x, y)^T$

$u(x)$ has n nodal values in the field:

$$u(x_i) = u_i \quad i=1, 2, \dots, n \quad (1)$$

An approximate function of $u(x)$ is denoted as

$$G u(x) = \sum_{j=1}^m P_j(x) a_j(x) = P^T(x) a(x) \quad (2)$$

Where $a(x)$ is a m dimension coefficient, $P(x)$, m dimension basic vectors

By moving least squares method formula (2) may be written as

$$G u(x) = \sum_{i=1}^n n_i(x) u_i \quad (3)$$

$$n_i(x) = \sum_{j=1}^m P_j(x) [A^{-1}(x) B(x)]_{ji}$$

$$A(x) = \sum w_i(x) P(x_i) P^T(x_i) \quad (4)$$

$$B(x) = [w_1(x) P(x_1), \dots, w_n(x) P(x_n)]$$

Where $w_i(x)$ are weighted functions at point $(x, y)^T$.

From (4), differentiation of shape functions are given as:

$$n_{i,k} = \sum \left\{ P_{j,k} [A^{-1} B]_{ji} + P_j [A_{,k}^{-1} B + A^{-1} B_{,k}]_{ji} \right\} \quad (5)$$

$$A_{,k}^{-1} = -A^{-1} A_{,k} A^{-1} \quad (6)$$

3 WEIGHTED FUNCTIONS

In the domain, manifold covers overlape together and weighted coefficients of cover functions, are given below

$$w_i(r_i) = \begin{cases} \frac{r_{mi}^2}{r_i^2 + \varepsilon^2 r_{mi}^2} \left(1 - \frac{r_i^2}{r_{mi}^2} \right)^k & r_i \leq r_{mi} \\ 0 & r_i > r_{mi} \end{cases} \quad (7)$$

Where $r_i = \|x - x_i\|$ define the influence domain of the cover function.

From variational principle,

Where

$$\begin{aligned}\delta\pi &= 0 \\ \pi &= \pi_\varepsilon + \pi_{\sigma_0} + \pi_f + \pi_u \\ \pi_\varepsilon &= \int_{\Omega} \frac{1}{2} \varepsilon^T \sigma d\Omega \\ \pi_{\sigma_0} &= \int_{\Omega} \varepsilon^T \sigma_0 d\Omega \\ \pi_f &= - \int_{\Omega} d^T \bar{f} d\Omega - \int_{\Gamma} d^T \bar{t} dr - \sum_{i=1}^{n_i} d^T(x_i') \bar{T}(x_i')\end{aligned}\quad (8)$$

$\bar{f}(x), \bar{t}(x), \bar{T}(x)$ are denoted with volume force, surface force and concentrated forces respectively.

Finally $k_n = f$ is established. The coupled MM, and diffused element methods are implemented as:

- (1) To establish M,M mesh
- (2) Any crack is traced by diffused element method and discriminated by fracture criterion
- (3) Coalescence of cracks form an interface of MM.

4 SIMULATION OF DISCONTINUOUS INTERFACE.

The fundamental theory about diffuse element method has been given in the paper[1]. Here elucidate the mathematics formation of discontinuous interface.

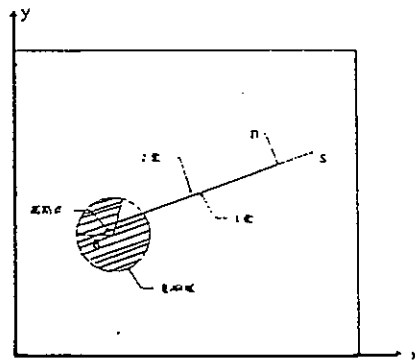


Fig1 Discontinuous interface

As shown in Fig(1), in domain Ω , the two discontinuous interfaces denoted with face1 and face2. Assuming local axis s and global axis $x-y$, k_n , k_s are given to the point as shear stiffness and normal stiffness, which make contributions to the global stiffness of the structure.

Shear stress and normal stress are shown as following equations

$$\begin{Bmatrix} \tau_s \\ \sigma_n \end{Bmatrix} = \begin{bmatrix} k_s & 0 \\ 0 & k_n \end{bmatrix} \begin{bmatrix} u_s^{(2)} - u_s^{(1)} \\ u_n^{(2)} - u_n^{(1)} \end{bmatrix} = P \begin{Bmatrix} \Delta u_s \\ \Delta u_n \end{Bmatrix} \quad (9)$$

On assuming $(u, v)^T$ as deformation at joint point, then

$$\begin{Bmatrix} \Delta u_s \\ \Delta u_n \end{Bmatrix} = \begin{bmatrix} \cos \theta & \sin \theta \\ -\sin \theta & \cos \theta \end{bmatrix} \begin{Bmatrix} \Delta u \\ \Delta v \end{Bmatrix} = T \begin{Bmatrix} \Delta u \\ \Delta v \end{Bmatrix} \quad (10)$$

$$\begin{Bmatrix} \Delta u \\ \Delta v \end{Bmatrix} = \begin{bmatrix} u^{(2)} \\ v^{(2)} \end{bmatrix} - \begin{bmatrix} u^{(1)} \\ v^{(1)} \end{bmatrix} = (N^{(2)} - N^{(1)}) d \quad (11)$$

Where d denotes deformation tensor, N shape function. The potential energy from the joint is

$$\begin{aligned} \pi_c &= \int_s \frac{1}{2} \begin{bmatrix} \Delta u_s & \Delta u_n \end{bmatrix} \begin{bmatrix} k_s & 0 \\ 0 & k_n \end{bmatrix} \begin{bmatrix} \Delta u_s \\ \Delta u_n \end{bmatrix} ds \\ &= \frac{1}{2} \int d^T (N^{(1)} - N^{(2)})^T T^T P^T T (N^{(2)} - N^{(1)}) d \cdot d_s \end{aligned} \quad (12)$$

Let $A = T^T P T$ then

$$\partial \pi_c = \partial d^T \int_s (N^{(1)T} A N^{(1)} + N^{(2)T} A N^{(2)} - N^{(1)T} A N^{(2)} - N^{(2)T} A N^{(1)}) ds \cdot d$$

The stiffness contribution made by k_n, k_s are given as below.

$$\begin{aligned} \int_s N_i^{(1)T} A N_j^{(1)} ds &= K_{ij} \\ \int_s N_i^{(2)T} A N_j^{(2)} ds &= K_{ij} \\ - \int_s N_i^{(1)T} A N_j^{(2)} ds &= K_{ij} \\ - \int_s N_i^{(2)T} A N_j^{(1)} ds &= K_{ij} \end{aligned}$$

For discontinuous interface or cracks, whether they are driven to propagate by fracture forces, Mohr-Coulomb criterion is used to make investigation:

$$\begin{aligned} \text{Tensile failure } \sigma &> 0 & k_n &= 0, k_s = 0 \\ \text{Shear failure } \tau_n &> 0 & k_s &= 0 \end{aligned} \quad (13)$$

5 FRACTURE DISCRIMINATION AND CRACK

Here the criterion for fracture: is implemented as maximum peripheral tensile stress criterion. It includes:

(1) Initiation of fracture

$$K_\theta = \frac{1}{2} \cos \frac{\theta}{2} [K_I (1 + \cos \theta) - 3 K_{II} \sin \theta] \geq K_{IC} \quad (14)$$

(2) Fracture Orientation

$$\begin{aligned}
K_I \sin \vartheta + K_{II} (3 \cos \vartheta - 1) &= 0 \\
K_I \cos \frac{\vartheta}{2} (3 \cos \theta - 1) - K_{II} \sin \frac{\vartheta}{2} (9 \cos \theta + 5) &> 0
\end{aligned} \tag{15}$$

6 CASE STUDY

As shown in Fig(2), in square plate with side length $L = 10$ m a crack emerged in its center ; its length is 0.5 m. $H = 0.5$ m $W = 1.0$,

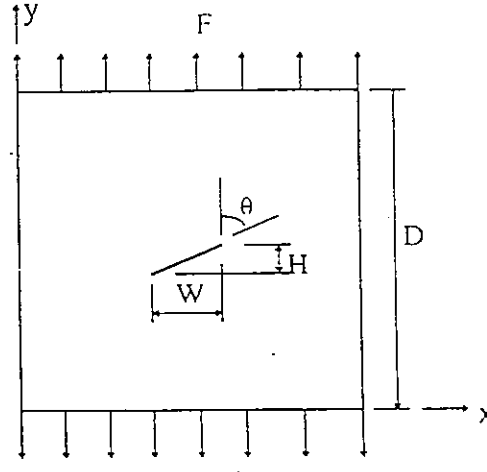


Fig 2. Crack in plate

As in Fig3(a),3(b),3(c)there are three samples:

- 3(a) with coarse mathematics covers and 403 nodes
- 3(b) with dense mathematics covers and 1605 nodes
- 3(c) with radial mathematics covers and 1655 nodes

Here basic functions of one order are adopted. These sample are applied by both tensile and compressive stresses,

For tensile condition , at the crack tip

$$\begin{aligned}
K_I &= F \sin 2\theta \sqrt{\pi \alpha} \\
K_{II} &= F \sin \theta \cos \theta \sqrt{\pi \alpha}
\end{aligned}$$

For compressive stress condition

$$\begin{aligned}
K_I &= 0 \\
K_{II} &= \begin{cases} 0 \\ F \sin \theta \cos \theta - (F \sin^2 \theta) \sqrt{\pi \alpha} \end{cases}
\end{aligned}$$

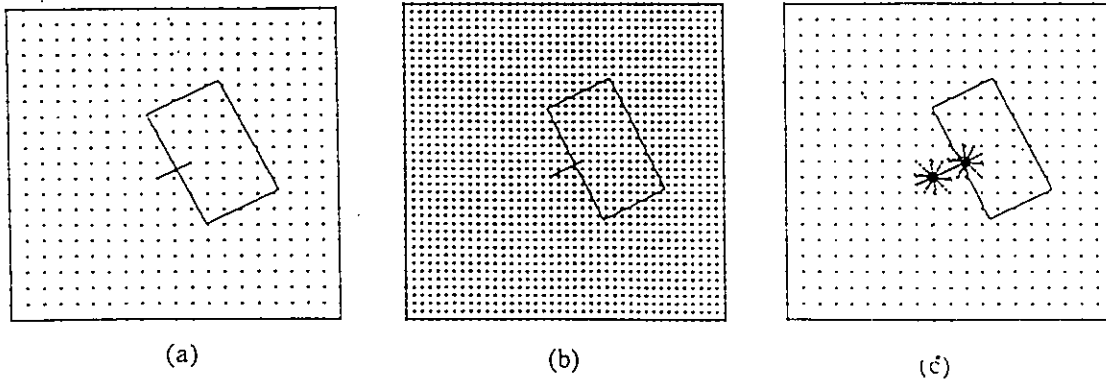


Fig 3. Crack propagation

After computation the data for fracture intensity factors are present in Tab 1.

Table 1

Unit: $\text{N} / \text{m}^{3/2}$

Loading condition	Tensile stress $F=1000 \text{ Pa}$					
Node distribution	Fig3(a)		Fig3(b)		Fig3(c)	
Element free method calculation value	K_I	K_{II}	K_I	K_{II}	K_I	K_{II}
	1143	613	1115	556	1115	542
Relative error	7.7%	15.7%	5.2%	4.9%	5.2%	2.3%
Loading condition	Shear stress $F= -1000 \text{ Pa}$					
Node distribution	Fig3(a)		Fig3(b)		Fig3(c)	
Element free method calculation value	K_I	K_{II}	K_I	K_{II}	K_I	K_{II}
	-208	-359	-96	-307	-27	-286
Relative error	—	35.5%	—	15.8%	—	7.9%

In Tab 1, the accuracy from Fig(3), is presented. The mesh should be regenerate at the fracture tip, in order to trace the crack propagate

The crack propagations are shown as in Fig(4). As shown in 4(a), tensile load $F = 1000 \text{ Pa}$, $P = 0$, in 4(b) Varies with crack length.

For Fig 4(c), 4(d), 4(e) $F = -1000 \text{ Pa}$, $P = 100 \text{ Pa}$, 0 , -100 Pa . And K_θ varies with $L_{(m)}$ and could be seen in Fig(4f).

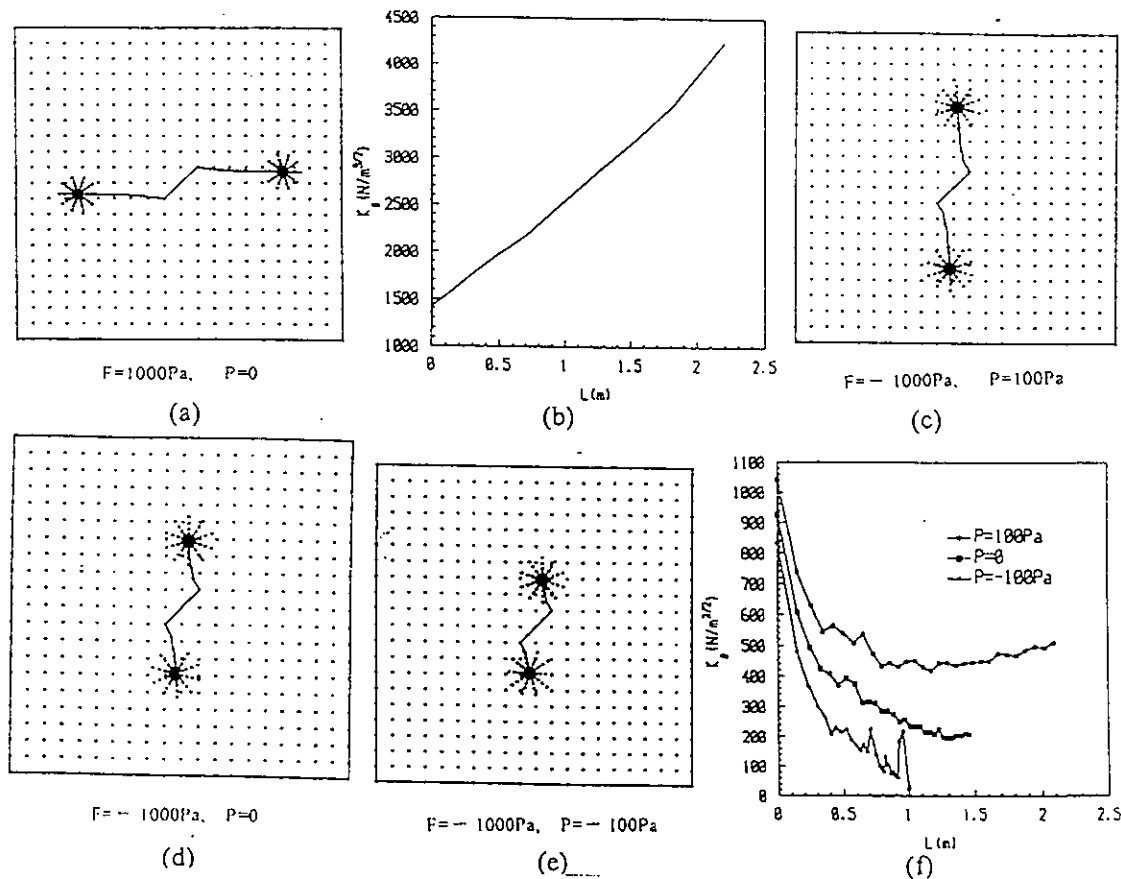


Fig 4. Crack propagation

7 CONCLUSIONS

The MM coupled with diffused element method (Element Free method) to trace crack propagation were verified effectively. They are much simpler in mesh generation, and have high accuracy. The authors introduce several samples in the paper to verify their correctness. The method may be used in a popular way in Engineering.

REFERENCES

- Aoki.S. , Kishimoto.K. and Sakata.M. , *Finite element computation of dynamic stress intensity factor for a rapidly propagation crack using J-intergart*, Comput.Mech., 2, 54~62, 1987
- Koh.H.M, Lee.H.S and Haber, R.B, *Dynamic crack propagation analysis using Eulerian-languangain. Kinematic descriptions*. Compute Mech.,3,141~155,1988.
- Wawrzynek.P.A. and Ingreffea.A.R., *Interactive finite element analysis of fracture processes and integrated approach* ,Theor.Appl.Fracture Mech.,8,137~150,1987.
- Gerstle.W.H.,Matha.L.and Ingraffea.A.R, *Finite and boundary element modeling of crack propagation in two-and three-dimensions*. Engrg. with Computers,2,167~183,1987.